

TABLE OF CONTENTS

	Page
INTRODUCTION	1
CHAPTER 1 A REVIEW OF CONSTITUTIVE SOIL MODELS	3
1.1 Introduction.....	3
1.2 Constitutive soil model	3
1.2.1 Hyperbolic model.....	5
1.2.2 Hardening soil model.....	13
1.2.3 Hardening soil-small strain model	21
CHAPTER 2 COMPARISON AMONG DIFFERENT CONSTITUTIVE SOIL MODELS THROUGH TRIAXIAL AND OEDOMETER TESTS.....	23
2.1 Introduction.....	23
2.2 Triaxial test	23
2.3 Finite element modeling	24
2.3.1 Geometry of model and boundary conditions in Plaxis.....	24
2.3.2 Geometry of model and boundary condition in Zsoil.....	26
2.4 Experimental data	27
2.5 Application of constitutive soil models	29
2.5.1 Mohr–Coulomb model.....	29
2.5.2 Hardening soil model.....	34
2.5.3 Hardening small strain soil model	38
2.5.4 Duncan–Chang soil model.....	41
2.6 Comparison between constitutive soil models.....	45
2.7 Oedometer test	50
2.8 Finite element modeling	51
2.8.1 Geometry of model and boundary conditions in Plaxis.....	51
2.8.2 Model geometry and boundary conditions in Zsoil	52
2.9 Experimental data	53
2.10 Application of constitutive soil models	55
2.10.1 Duncan–Chang Model	55
2.10.2 Hardening soil model.....	57
2.10.3 Hardening small strain constitutive soil model.....	59
2.11 Comparison between constitutive soil models.....	61
2.12 Updated mesh results for triaxial test.....	64
CHAPTER 3 NUMERICAL SIMULATIONS FOR DAM-X	73
3.1 Introduction.....	73
3.2 Asphalt core dam	73
3.3 Dam-X.....	74
3.4 Typical cross section.....	75
3.5 Soil parameters.....	77

3.6	Instrumentation	80
3.7	Finite element modeling	80
3.8	Displacement contours at the end of construction	84
3.9	Comparison between measured data and numerical simulations after construction	88
3.9.1	Comparison between measured and computed displacements after construction (inclinometer INV-01)	88
3.9.2	Comparison between measured and computed displacements after construction (inclinometer INV-02)	90
3.9.3	Comparison between measured and computed displacements after construction (inclinometer INV-03)	92
3.9.4	Comparison between measured and computed displacements after construction (INH-01 and INH-02)	94
3.10	Comparison between Plaxis and Zsoil	97
3.11	Numerical simulation procedure for wetting	101
3.11.1	Justo approach.....	102
3.11.2	Nobari–Duncan approach	102
3.11.3	Escuder Procedure	105
3.11.4	Plaxis Procedure.....	109
3.12	Results after impoundment	110
3.12.1	Comparison between measured and computed displacements after impoundment (inclinometer INV-01)	113
3.12.2	Comparison between measured and computed displacements after impoundment (inclinometer INV-02)	116
3.12.3	Comparison between measured and computed displacements after impoundment (inclinometer INV-03)	118
3.12.4	Comparison between measured and computed displacements after impoundment (inclinometer INH-01)	120
3.13	Shear wave velocity measurement.....	121
3.13.1	Material properties for zone 3O and 3P	121
3.13.2	Comparison between measured and computed displacements	127
3.14	Concluding remarks	132
	CONCLUSION.....	135
	RECOMMENDATIONS.....	137
	APPENDIX I.....	139
	APPENDIX II.....	165
	BIBLIOGRAPHY.....	177

LIST OF TABLES

		Page
Table 1.1	Summary of Hyperbolic parameters (Wong et Duncan, 1974)	8
Table 1.2	Summary of Hyperbolic parameters (Duncan, Wong et Mabry, 1980)	11
Table 2.1	Mesh size influences on deviatoric stress for the Hardening soil model in Plaxis software	26
Table 2.2	Mesh size influences on deviatoric stress for the Hardening soil model in Zsoil software.....	27
Table 2.3	Soil properties used in the MC model for loose sand	30
Table 2.4	Soil properties used in the MC model for dense sand	31
Table 2.5	Soil properties used in the HS model for dense and loose sand (Brinkgreve, 2007)	34
Table 2.6	Supplemental HS Small soil parameters for loose and dense Hostun sand (Brinkgreve, 2007).....	38
Table 2.7	Soil properties used in the model for dense and loose sand	42
Table 3.1	Hardening soil model parameters used for rockfill dam simulation.....	78
Table 3.2	Mohr-Coulomb soil model parameters used for rockfill dam simulation	79
Table 3.3	Duncan-Chang soil model parameters used for rockfill dam simulation	79
Table 3.4	Mesh size influences on total displacement in Plaxis software	82
Table 3.5	Absolute maximum horizontal and vertical displacement resulted by FE analysis at section INV-1.....	90
Table 3.6	Absolute maximum horizontal and vertical displacement resulted by FE analysis at section INV-2.....	92
Table 3.7	Absolute maximum horizontal and vertical displacement resulted by FE analysis at section INV-3.....	94

Table 3.8	Absolute maximum vertical displacement resulted by FE analysis at section INH-1	95
Table 3.9	Absolute maximum vertical displacement resulted by FE analysis at section INH-2	96
Table 3.10	Associated bounds (Simon Grenier, 2010)	107
Table 3.11	Absolute maximum horizontal and vertical displacement resulted by FE analysis at section INV-1	115
Table 3.12	Absolute maximum horizontal and vertical displacement resulted by FE analysis at section INV-2	117
Table 3.13	Absolute maximum horizontal and vertical displacement resulted by FE analysis at section INV-3	119
Table 3.14	Absolute maximum vertical displacement resulted by FE analysis at section INH-1	121
Table 3.15	Mohr-Coulomb soil model parameters used for rockfill dam simulation at zone 3O	124
Table 3.16	Mohr-Coulomb soil model parameters used for rockfill dam simulation at zone 3P	124
Table 3.17	HS soil model parameters used for rockfill dam simulation at zone 3O	125
Table 3.18	HS soil model parameters used for rockfill dam simulation at zone 3P	125
Table 3.19	HSS soil model parameters used for rockfill dam simulation at zone 3O	126
Table 3.20	HSS soil model parameters used for rockfill dam simulation at zone 3P	126

LIST OF FIGURES

		Page
Figure 1.1	Comparison of typical stress and strain curve with hyperbola (Al-Shayea et al., 2001)	5
Figure 1.2	Transformed Hyperbolic stress- strain curve (Duncan et Chang, 1970)	6
Figure 1.3	Mohr envelope for Oroville dam core material (Wong et Duncan, 1974).....	9
Figure 1.4	Hyperbolic axial strain – radial strain curve (Wong et Duncan, 1974).....	10
Figure 1.5	Variation of bulk modulus with confining pressure (Duncan, Wong et Mabry, 1980)	12
Figure 1.6	Hyperbolic stress-strain relationship for a standard drained triaxial test in primary loading (Brinkgreve et Broere, 2006)	14
Figure 1.7	Explanation of <i>Eoedref</i> in the oedometer test (Brinkgreve et Broere, 2006)	16
Figure 1.8	Dilatancy cut-off (Brinkgreve et Broere, 2006).....	19
Figure 1.9	Yield surface of the hardening soil model in p-q plane (Brinkgreve et Broere, 2006)	20
Figure 1.10	The yield contour of the hardening soil model in stress space (Brinkgreve et Broere, 2006)	20
Figure 1.11	Schematic presentation of the HS model, stiffness-strain behavior (Obrzud, 2010).....	22
Figure 2.1	Triaxial loading condition (Surarak et al., 2012).....	24
Figure 2.2	Plot of the mesh in Plaxis.....	25
Figure 2.3	Plot of the mesh in Zsoil	27
Figure 2.4	Results of drained triaxial test on loose Hostun sand (Brinkgreve, 2007).....	28
Figure 2.5	Results of drained triaxial test on dense Hostun sand, deviatoric stress versus axial strain (Brinkgreve et Broere, 2006)	28

Figure 2.6 Results of drained triaxial test on dense Hostun sand, volumetric strain versus axial strain (Brinkgreve et Broere, 2006)29

Figure 2.7 The initial stiffness, E_0 and the secant modulus, E_{50} (Brinkgreve et Broere, 2006)30

Figure 2.8 Deviatoric stress vs axial strain for the MC model in dense sand32

Figure 2.9 Volumetric strain vs axial strain for the MC model in dense sand32

Figure 2.10 Deviatoric stress vs axial strain for the MC model in loose sand33

Figure 2.11 Volumetric strain vs axial strain for the MC model in loose sand33

Figure 2.12 Deviatoric stress vs axial strain for the HS model in dense sand36

Figure 2.13 Volumetric strain vs axial strain for the HS model in dense sand36

Figure 2.14 Deviatoric stress vs axial strain for the HS model in loose sand37

Figure 2.15 Volumetric strain vs axial strain for the HS model in loose sand37

Figure 2.16 Deviatoric stress vs axial strain for the HSS model in dense sand39

Figure 2.17 Volumetric strain vs axial strain for the HSS model in dense sand40

Figure 2.18 Deviatoric stress vs axial strain for the HSS model in loose sand40

Figure 2.19 Volumetric strain vs axial strain for the HSS model in loose sand41

Figure 2.20 Deviatoric stress vs axial strain for the Duncan-Chang model in dense sand43

Figure 2.21 Volumetric strain vs axial strain for the Duncan-Chang model in dense sand43

Figure 2.22	Deviatoric stress vs axial strain for the Duncan-Chang model in loose sand.....	44
Figure 2.23	Volumetric strain vs axial strain for the Duncan-Chang model in loose sand.....	44
Figure 2.24	Deviatoric stress vs axial strain for the HSS, HS and MC soil models in dense sand modeled by Plaxis.....	46
Figure 2.25	Deviatoric stress vs axial strain for the Duncan, HSS, HS and MC soil models in dense sand modeled by Zsoil	47
Figure 2.26	Volumetric strain vs axial strain for the Duncan, HSS, HS and MC soil models in dense sand modeled by Zsoil	47
Figure 2.27	Volumetric strain vs axial strain for the HSS, HS and MC soil models in dense sand modeled by Plaxis	48
Figure 2.28	Deviatoric stress vs axial strain for the Duncan, HSS, HS and MC soil models in loose sand modeled by Zsoil.....	48
Figure 2.29	Deviatoric stress vs axial strain for the HSS, HS and MC soil models in loose sand modeled by Plaxis.....	49
Figure 2.30	Volumetric strain vs axial strain for the Duncan, HSS, HS and MC soil models in loose sand modeled by Zsoil.....	49
Figure 2.31	Volumetric strain vs axial strain for the HSS, HS and MC soil models in loose sand modeled by Plaxis.....	50
Figure 2.32	Oedometer loading condition.....	51
Figure 2.33	Oedometer simulation in Plaxis	52
Figure 2.34	Plot of the mesh in Plaxis.....	52
Figure 2.35	Oedometer simulation in Zsoil.....	53
Figure 2.36	Results of oedometer test on dense Hostun sand (Brinkgreve, 2007).....	54
Figure 2.37	Results of oedometer test on loose Hostun sand (Brinkgreve, 2007).....	54
Figure 2.38	Vertical stress vs axial strain for the Duncan-Chang model in dense sand.....	56

Figure 2.39	Vertical stress vs axial strain for the Duncan-Chang model in loose sand	56
Figure 2.40	Vertical stress vs. axial strain for the HS model in dense sand	58
Figure 2.41	Vertical stress vs. axial strain for the HS model in loose sand	58
Figure 2.42	Unloading and reloading for dense Hostun sand	59
Figure 2.43	Result of oedometer test (HSS Model) on dense Hostun sand, vertical stress vs. axial strain.....	60
Figure 2.44	Result of oedometer test (HSS Model) on loose Hostun sand, vertical stress vs. axial strain.....	60
Figure 2.45	Vertical stress vs axial strain for the HSS, HS and Duncan-Chang soil models in dense sand modeled by Plaxis	62
Figure 2.46	Vertical stress vs axial strain for the HSS, HS and Duncan-Chang soil models in dense sand modeled by Zsoil	62
Figure 2.47	Vertical stress vs axial strain for the HSS, HS and Duncan-Chang soil models in loose sand modeled by Zsoil	63
Figure 2.48	Vertical stress vs axial strain for the HSS, HS and Duncan-Chang soil models in loose sand modeled by Plaxis.....	63
Figure 2.49	Deviatoric stress vs axial strain for the Hardening soil model in dense sand	65
Figure 2.50	Volumetric strain vs axial strain for the Hardening soil model in dense sand	65
Figure 2.51	Deviatoric stress vs axial strain for the Hardening soil model in loose sand.....	66
Figure 2.52	Volumetric strain vs axial strain for the Hardening soil model in loose sand.....	66
Figure 2.53	Deviatoric stress vs axial strain for the Hardening small strain soil model in dense sand	67
Figure 2.54	Volumetric strain vs axial strain for the Hardening small strain soil model in dense sand	67
Figure 2.55	Deviatoric stress vs axial strain for the Hardening small strain soil model in loose sand	68

Figure 2.56 Volumetric strain vs axial strain for the Hardening small strain soil model in loose sand68

Figure 2.57 Deviatoric stress vs axial strain for the Mohr–Coloumb model in dense sand69

Figure 2.58 Volumetric strain vs axial strain for the Mohr–Coloumb model in dense sand69

Figure 2.59 Deviatoric stress vs axial strain for the Mohr–Coloumb model in loose sand.....70

Figure 2.60 Volumetric strain vs axial strain for the Mohr–Coloumb model in loose sand.....70

Figure 2.61 Deviatoric stress vs axial strain for the Duncan–Chang model in dense sand71

Figure 2.62 Volumetric strain vs axial strain for the Duncan–Chang model in dense sand71

Figure 2.63 Deviatoric stress vs axial strain for the Duncan–Chang model in loose sand.....72

Figure 2.64 Volumetric strain vs axial strain for the Duncan–Chang model in loose sand.....72

Figure 3.1 The Dam-X hydroelectric complex (Vannobel, 2013)75

Figure 3.2 Cross section of the Dam-X(Cad drawing, Hydro-Quebec).....76

Figure 3.3 Plot of the mesh in Zsoil82

Figure 3.4 Plot of the mesh in Plaxis.....83

Figure 3.5 Simplified dam cross section83

Figure 3.6 Contour of horizontal displacement (Mohr-Coulomb model)85

Figure 3.7 Contour of vertical displacement (Mohr-Coulomb model)85

Figure 3.8 Contour of horizontal displacement (Duncan-Chang model).....86

Figure 3.9 Contour of vertical displacement (Duncan-Chang model)86

Figure 3.10 Contour of horizontal displacement (HS model)87

Figure 3.11 Contour of vertical displacement (HS model)87

Figure 3.12	Accumulated horizontal displacements at section (INV-01).....	89
Figure 3.13	Vertical displacements at section (INV-01).....	89
Figure 3.14	Accumulated horizontal displacements at section (INV-02).....	91
Figure 3.15	Vertical displacement at section (INV-02).....	91
Figure 3.16	Accumulated horizontal displacements at section (INV-03).....	93
Figure 3.17	Vertical displacements at section (INV-03).....	93
Figure 3.18	Vertical displacements at section (INH-01).....	95
Figure 3.19	Vertical displacements at section (INH-02).....	96
Figure 3.20	Comparison between Plaxis and Zsoil for vertical displacement at section INV-01.....	97
Figure 3.21	Comparison between Plaxis and Zsoil for relative horizontal displacement at section INV-01.....	98
Figure 3.22	Comparison between Plaxis and Zsoil for vertical displacement at section INV-02.....	98
Figure 3.23	Comparison between Plaxis and Zsoil for relative horizontal displacement at section INV-02.....	99
Figure 3.24	Comparison between Plaxis and Zsoil for vertical displacement at section INV-03.....	99
Figure 3.25	Comparison between Plaxis and Zsoil for relative horizontal displacement at section INV-03.....	100
Figure 3.26	Comparison between Plaxis and Zsoil for vertical displacement at section INH-01.....	100
Figure 3.27	Comparison between Plaxis and Zsoil for vertical displacement at section INH-02.....	101
Figure 3.28	Amount of compression under confinement stress (Simon Grenier, 2010).....	103
Figure 3.29	Evaluation of stress relaxation for wetting condition (Nobari et Duncan, 1972).....	105
Figure 3.30	Solving flowchart (Simon Grenier, 2010).....	108

Figure 3.31	Applying a volumetric strain to a cluster.....	110
Figure 3.32	Horizontal displacement after watering analyzed based on the Mohr-Coulomb model.....	111
Figure 3.33	Vertical displacement after watering analyzed based on the Mohr-Coulomb model.....	112
Figure 3.34	Horizontal displacement after watering analyzed based on the Hardening soil model.....	112
Figure 3.35	Vertical displacement after watering analyzed based on the Hardening soil model.....	113
Figure 3.36	Vertical displacements after watering resulted by FE analysis and inclinometer (INV-01).....	114
Figure 3.37	Horizontal displacements after watering resulted by FE analysis and inclinometer (INV-01).....	115
Figure 3.38	Vertical displacements after watering resulted by FE analysis and inclinometer (INV-02).....	116
Figure 3.39	Horizontal displacements after watering resulted by FE analysis and inclinometer (INV-02).....	117
Figure 3.40	Vertical displacements after watering resulted by FE analysis and inclinometer (INV-03).....	118
Figure 3.41	Horizontal displacements after watering resulted by FE analysis and inclinometer (INV-03).....	119
Figure 3.42	Vertical displacements after watering resulted by FE analysis and inclinometer (INH-01).....	120
Figure 3.43	Normalized shear wave velocity at zones 3O and 3P(Guy Lefebure, 2014).....	127
Figure 3.44	Inclinometers placement (Vannobel, 2013).....	128
Figure 3.45	Accumulated horizontal displacements at section (INV-01).....	128
Figure 3.46	Vertical displacements at section (INV-01).....	129
Figure 3.47	Accumulated horizontal displacements at section (INV-02).....	129
Figure 3.48	Vertical displacements at section (INV-02).....	130

Figure 3.49	Accumulated horizontal displacements at section (INV-03).....	130
Figure 3.50	Vertical displacements at section (INV-03).....	131
Figure 3.51	Vertical displacements at section (INH-01).....	131
Figure 3.52	Vertical displacements at section (INH-02).....	132

LIST OF ABBREVIATIONS

a	Parameter of the Hyperbolic model (Kondner, 1963); coefficient in Justo method
b	Parameter of the Hyperbolic model (Kondner, 1963)
B	Bulk modulus
c	Cohesion in Mohr-Coulomb failure criteria
d	Poisson's ratio parameter in Hyperbolic model
e_{max}	Maximum void ratio
E_i	Initial Young's modulus in Hyperbolic formulation
E_{50}^{ref}	Reference secant stiffness in standard drained triaxial test in HS soil model
E_{50}	Secant stiffness in standard drained triaxial test in HS soil model
E_{ur}^{ref}	Reference Young's modulus for unloading and reloading in HS soil model
E_{ur}	Unloading and reloading stiffness in HS soil model
E_{oed}	Oedometer stiffness in HS soil model
E_{oed}^{ref}	Reference oedometer stiffness in HS soil model
E_t	Tangent Young's modulus

F	Poisson's ratio parameter in Hyperbolic model
f	Yield function
\bar{f}	Function of stress
G	Shear modulus; Poisson's ratio parameter in Hyperbolic model
k	Modulus number in Hyperbolic model
K_b	Bulk modulus number in Hyperbolic model
K_{ur}	Unloading elastic modulus number in Hyperbolic model
K_0^{nc}	Normally consolidated coefficient of lateral earth pressure
m	Bulk modulus exponent in Hyperbolic model
n	Modulus exponent in Hyperbolic model
p	Mean stress
pa	Atmospheric pressure
p _p	Pre-consolidation stress
p^{ref}	Reference stress for stiffnesses
q	Deviatoric stress

q_f	Ultimate deviatoric stress
q^{\sim}	Special stress measure for deviatoric stresses in HS soil model
R_f	Failure ratio in Hyperbolic model
φ	Friction angle in Mohr-Coulomb failure criteria
φ_m	Mobilized friction angle
φ_{cv}	Critical friction angle
$\Delta\varphi$	Change of friction angle with confining stress in Hyperbolic model
σ_1	Maximum principal stress; axial stress in triaxial setting
σ_2	Intermediate principal stress
σ_3	Minimum principal stress; radial stress in triaxial setting
σ_{1d}	Maximum principal stress in dry condition
σ_{3w}	Isotropic confinement stress after wetting
σ_{3t}	Isotropic confinement stress from which the volumetric strain begins
$\Delta\sigma_x$	Horizontal stress increment (x axis) in plane strain formulation
$\Delta\sigma_y$	Vertical stress increment (y axis) in plane strain formulation

$\sigma_1 - \sigma_3$	Deviatoric stress
$(\sigma_1 - \sigma_3)_u$	Ultimate deviatoric stress in Hyperbolic formulation
$(\sigma_1 - \sigma_3)_f$	Failure deviator stress in Hyperbolic formulation
ε	Strain
ε_r	Radial strain
ε_a	Axial strain
ε_v	Volumetric strain
ε_1	Axial principal strain
ε_{1w}	Axial principal strain after wetting
ε_{1c}	Maximum strain due to the isotropic consolidation stress
ε_{1L}	Maximum strain due to the deviatoric stress
ε_1^p	Axial plastic strain
ε_v^p	Volumetric plastic strain
ε_1^e	Axial elastic strain
$\dot{\varepsilon}_v^p$	Rate of plastic volumetric strain for triaxial test

ε_{vc}	Volumetric changes under confinement pressure
ε_{vl}	Volumetric changes under deviatoric stresses
$\Delta\varepsilon_x$	Horizontal strain increment (x axis) in plane strain formulation
$\Delta\varepsilon_y$	Vertical strain increment (y axis) in plane strain formulation
γ	Density
γ^p	Shear plastic strain
$\dot{\gamma}^p$	Rate of plastic shear strain
$\Delta\gamma_{yx}$	Shear strain increment in (x-y plane) in plane strain formulation
ϑ	Poisson's ratio
ϑ_t	Tangent Poisson's ratio
ϑ_{ur}	Unloading / Reloading Poisson's ratio
$\Delta\tau_{xy}$	Shear stress increment (in x-y plane) in plane strain formulation
Ψ_m	Mobilized dilatancy angle
Ψ	Dilatancy angle
α	Auxiliary parameter

β Parameter of Nobari-Duncan method

INTRODUCTION

Context of the research

The design of rockfill dams undergoes a numerical modeling phase to evaluate its cost and feasibility. The current modeling methods have some limitations in describing all aspects of the behavior of these dams during construction and impoundment stages. Although there are several constitutive soil models, each one has weaknesses in hypothesis. A large number of parameters in the model or their determinations through tests are not necessarily representative of actual field conditions. In addition, there are limitations and lack of judicious use of numerical tools such as whether an implicit finite element approach or explicit finite difference is appropriate or not. This specific research will undertake studies that will focus on the advancement of numerical modeling of an asphaltic core rockfill dam to achieve a better prediction of dam behavior for better dam design and safety assessment.

Objectives and scopes

The main objectives of this research are as follows:

- 1- Software validation through test cases

This objective is focused on determining the degree of precision for Zsoil and Plaxis, which are commercial finite element software applications that have been developed specifically for stability and deformation analyses in geotechnical engineering projects. They will be compared based on established benchmark tests; this will enable us to gain confidence on their accuracy and performance.

- 2- Choice of soil constitutive models

During this stage, several analyses will be undertaken to examine the performance of different soil models. The following constitutive soil models will be considered: Hardening soil (HS), Mohr–Coulomb (MC), and Duncan–Chang. The dependency of stress–strain modulus is one of the important aspects in constitutive models of granular materials. This

dependency is described with several soil parameters. A comparison with measured data will confirm the applicability of various constitutive soil models for asphalt core dams.

1- Impact of wetting condition on dam performance

Finally, the research will extend into the prediction of material behavior after impounding (transition from dry to wet condition). A comparison between the results of simulation and measured data will be conducted.

Thesis organization

This thesis is organized into three main chapters. In the first chapter, a literature review on constitutive soil models is presented; particularly, a summary related to the Duncan–Chang and HS soil models is given.

In the second chapter, the evaluation of various constitutive soil models, namely, the Duncan–Chang, MC, HS, and Hardening small strain (HSS) using triaxial and oedometer tests is explained. Two finite element software applications, namely Plaxis and Zsoil, are used for the numerical simulations and the results are compared with experimental data. Two appendices (Appendix 1 and 2) provide a tutorial on how to perform the simulation using these software applications.

Furthermore, a rockfill dam is studied, a Hydro-Québec earth dam is simulated by considering various soil models and the results are compared with measured data obtained during and after the construction stage. The results for this part of the research are presented in chapter 3. The research is extended into the prediction of the material behavior after impounding. In addition, a comparison is made between the results of the simulations with those of the MC model, HS model, and measured data. This chapter contains results of multi-modal analysis of surface wave or MMASW test. Finally, the last part of the thesis comprises the conclusions and recommendations for further research.

CHAPTER 1

A REVIEW OF CONSTITUTIVE SOIL MODELS

1.1 Introduction

Several attempts have been made to describe the stress–strain relationship of soil by using the basic soil parameters that can be determined from testing. This has resulted in the development of various constitutive soil models (Pramthawee, Jongpradist et Kongkitkul, 2011). Many researchers have focused on the properties of rockfill materials; they have tried to designate the properties of rockfill based on the procedure and concepts of soil mechanics (Jansen, 2012). However, it is difficult to adapt most soil mechanics test to rockfill sizes, which contain unsymmetrical boulders from 20 cm to 90 cm (Hunter et Fell, 2003a; Jansen, 2012).

1.2 Constitutive soil model

Various constitutive equations are used to reproduce rockfill material behavior (Costa et Alonso, 2009; Pramthawee, Jongpradist et Kongkitkul, 2011; Varadarajan et al., 2003; Xing et al., 2006). Some of them are listed below.

The Barcelona basic model has been used by Costa and Alonso to simulate the mechanical behavior of the shoulder, filter, and core materials. This constitutive soil model was used to model the Lechago dam in Spain. The impacts of suction in soil strength and stiffness were considered in this model. A good agreement was achieved between laboratory results and model simulations (Costa et Alonso, 2009).

An elastoplastic constitutive model (DSC) was applied by Varadarajan to reproduce the rockfill material characteristics. Large size triaxial tests were used to define the rockfill material parameters. As a result, it was shown that the model can provide a suitable prediction of the behavior of the rockfill materials (Varadarajan et al., 2003).

An “evaluation of the HS model using numerical simulation of high rockfill dams” had been conducted by Pramthawee (Pramthawee, Jongpradist et Kongkitkul, 2011). To make a comparison with field data, the soil model was numerically implemented into a finite element program (ABAQUS). The material parameters for the rockfill were obtained from laboratory triaxial testing data. Finally, it was shown that by using the HS constitutive model, the response of rockfills under dam construction conditions could be precisely simulated (Pramthawee, Jongpradist et Kongkitkul, 2011).

The non-linear Hyperbolic model (Duncan and Chang, 1970) was used by Feng Xing to model a reliable approximation of soil behavior. The Hyperbolic model was implemented in two-dimensional finite element software. The study focused on the “physical, mechanical, and hydraulic properties of weak rockfill during placement and compaction in three dam projects in China”. The material parameters for the rockfill were estimated from laboratory tests. Numerical analysis was conducted to evaluate the settlements and slope stability of the dams and finally, the results were compared with field measurements. Slope stability and deformation analysis indicated a satisfactory performance of concrete-faced rockfill dams by using suitable rock materials (Xing et al., 2006).

Another constitutive soil model that can be considered for further research on rockfill materials is the HSS model. This constitutive soil model can simulate the pre-failure non-linear behavior of soil. Several applications of the HSS model in numerical modeling of geotechnical structures were reported by Obrzud (Obrzud et Eng, 2010).

1.2.1 Hyperbolic model

This section summarizes the Hyperbolic model. In 1963, Kondner proposed using the Hyperbolic constitutive model for cohesive soil (Kondner, 1963). Duncan and Chang in their publication, “Non-linear analysis of stress and strain in soils,” indicated that the stress and strain relationship in soils could be better estimated by considering a hyperbolic equation. As shown in figure 1.1, the stress–strain curve in the drained triaxial test can be estimated accurately by a hyperbola (Kondner, 1963). The stress–strain approach in a triaxial test is compatible with a two-constant hyperbolic equation (equation 1.1) (Duncan et Chang, 1970):

$$\sigma_1 - \sigma_3 = \frac{\varepsilon}{a + b \cdot \varepsilon} \quad (1.1)$$

where $\sigma_1 - \sigma_3$ is the deviator stress, and σ_1 and σ_3 are the major and minor principal stresses, respectively. ε is the axial strain, and constants a and b are material parameters (Kondner, 1963).

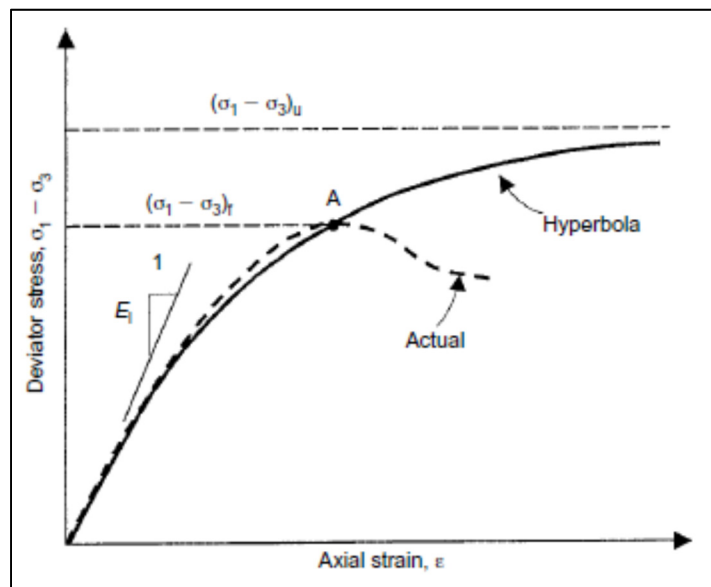


Figure 1.1 Comparison of typical stress and strain curve with hyperbola (Al-Shayea et al., 2001)

The constants, a and b , will be more understandable if the stress–strain data are drawn on transformed axes as shown in figure 1.2. The parameters a and b are the intercept and slope of the straight line, respectively. In 1970, Duncan and Chang extended the hyperbolic constitutive model in conjunction with confining pressure and several other parameters (Duncan et Chang, 1970).

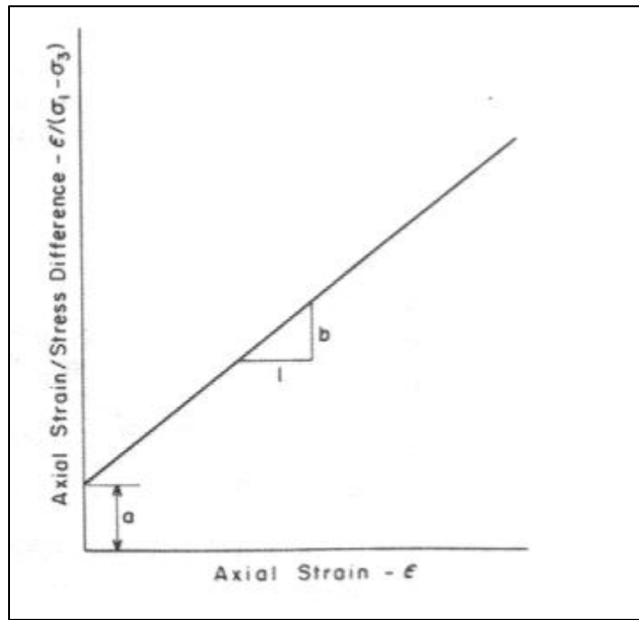


Figure 1.2 Transformed Hyperbolic stress-strain curve (Duncan et Chang, 1970)

The initial tangent modulus is defined below:

$$E_i = kpa \left(\frac{\sigma_3}{pa} \right)^n \quad (1.2)$$

where pa is the atmospheric pressure, k is a modulus number, and n is the exponent determining the rate of variation of E_i with σ_3 . By substituting the parameters a and b , equation 1.1 can be rewritten as

$$(\sigma_1 - \sigma_3) = \frac{\varepsilon}{\frac{1}{E_i} + \frac{\varepsilon}{(\sigma_1 - \sigma_3)u}} \quad (1.3)$$

where $(\sigma_1 - \sigma_3)$ is the deviator stress; σ_1 and σ_3 are the major and minor principal stresses; ε is the axial strain; E_i is the initial tangent modulus, and $(\sigma_1 - \sigma_3)_u$ is the ultimate deviator stress.

The hyperbola is supposed to be reliable up to the actual soil failure, which is denoted by point A in figure 1.1 (Al-Shayea et al., 2001). The ratio failure is defined as the proportion between the actual failure deviator stress $(\sigma_1 - \sigma_3)_f$ and the ultimate deviator stress $(\sigma_1 - \sigma_3)_u$, as indicated in equation 1.4.

$$R_f = \frac{(\sigma_1 - \sigma_3)_f}{(\sigma_1 - \sigma_3)_u} \quad (1.4)$$

The variation of the deviator stress with confining stress can be represented by the well-known MC relationship as indicated in equation 1.5.

$$(\sigma_1 - \sigma_3)_f = \frac{2C \cos \varphi + 2\sigma_3 \sin \varphi}{1 - \sin \varphi} \quad (1.5)$$

where c is the cohesion, and φ is the friction angle.

In addition, Duncan and Chang represented the tangent Young's modulus as

$$E_t = \left[1 - \frac{Rf(1 - \sin \varphi)(\sigma_1 - \sigma_3)}{2c \cos \varphi + 2\sigma_3 \sin \varphi} \right]^2 K \cdot pa \left(\frac{\sigma_3}{pa} \right)^n \quad (1.6)$$

Wong and Duncan in 1974 developed the previous works by adding other parameters related to the Poisson's ratio. Totally, nine parameters, which are listed in table 1.1, are defined.

Table 1.1 Summary of Hyperbolic parameters (Wong et Duncan, 1974)

Parameter	Name	Function
K, K_{ur}	Modulus number	Relate E_i and E_{ur} to σ_3
n	Modulus exponent	
c	Cohesion intercept	Relate $(\sigma_1 - \sigma_3)$ to σ_3
φ	Friction angle	
R_f	Failure ratio	Relate $(\sigma_1 - \sigma_3)u$ to $(\sigma_1 - \sigma_3)_f$
G	Poisson's ratio parameter	Value of ϑ_i at $\sigma_3 = pa$
F	Poisson's ratio parameter	Decrease in ϑ_i for tenfold increase in σ_3
d	Poisson's ratio parameter	Rate of increase of ϑ_t with strain

The Mohr envelopes for most of the soils are curved as shown in figure 1.3. Specifically for cohesionless soils, such as rockfills or gravels, this curvature makes it hard to choose a single value of the friction angle, which can be illustrative of the whole range of pressures of interest. To overcome such difficulty, the friction angle can be calculated for values that change with confining stress using equation 1.7 (Wong et Duncan, 1974).

$$\varphi = \varphi_0 - \Delta\varphi \log_{10} \left(\frac{\sigma_3}{pa} \right) \quad (1.7)$$

where φ_0 is the value of φ for σ_3 equal to pa , and $\Delta\varphi$ is the reduction in φ for a tenfold increase in σ_3 . The values of φ obtained from equation 1.7 are used in equation 1.6 to determine the tangent modulus (Wong et Duncan, 1974).

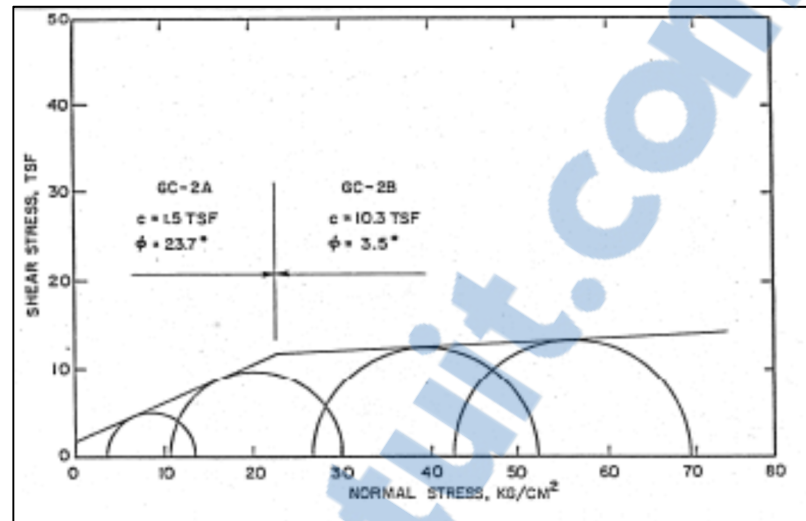


Figure 1.3 Mohr envelope for Oroville dam core material (Wong et Duncan, 1974)

The variation of axial strain with radial strain can be calculated by means of a hyperbolic equation, i.e., equation 1.8 (Naylor, 1975).

$$-\frac{\varepsilon_r}{\vartheta_i - d\varepsilon_r} = \varepsilon_a \quad (1.8)$$

In the equation above, ϑ_i is the initial Poisson's ratio when the strain is zero, and d is a parameter representing the changes in the value of Poisson's ratio with the radial strain. Figure 1.4 shows the variation of ε_a with ε_r . In addition, Poisson's ratio can be estimated for values that vary with the confining stress using equation 1.9.

$$\vartheta_i = G - F \log_{10} \left(\frac{\sigma_3}{pa} \right) \quad (1.9)$$

where G is the value of ϑ_i for σ_3 equal to pa , and F is the reduction in Poisson's ratio for a tenfold increase in σ_3 (Naylor, 1975).

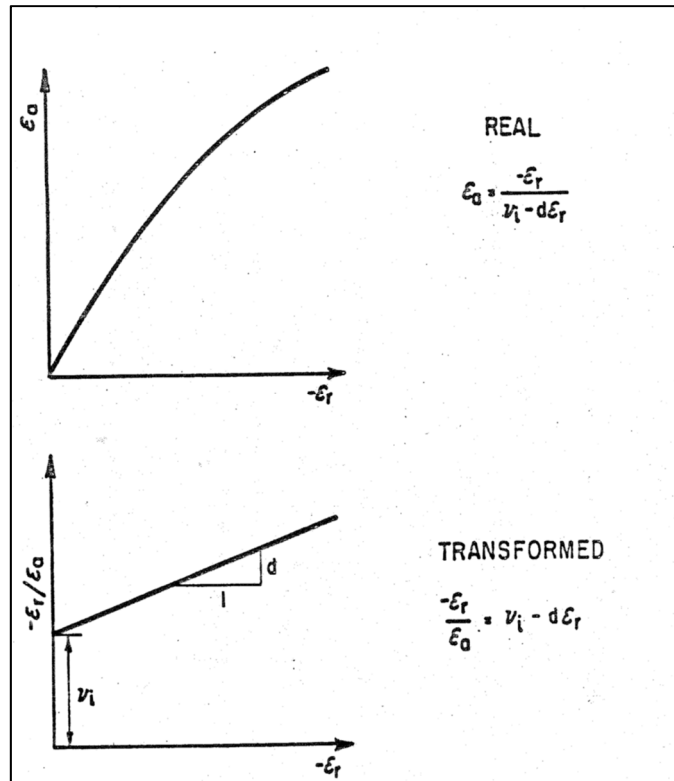


Figure 1.4 Hyperbolic axial strain – radial strain curve (Wong et Duncan, 1974)

Moreover, the volume change behavior of soils can be modeled by the bulk modulus, which varies with the confining pressure (Duncan, Wong et Mabry, 1980).

The following equation was presented by Duncan (1980) to calculate bulk modulus.

$$B = K_b p_a \left(\frac{\sigma_3}{p_a} \right)^m \quad (1.10)$$

where K_b and m are bulk modulus parameters. These parameters can be used instead of the Poisson parameters given in table 1.1.

Equation 1.11 expresses the relationship between the bulk modulus and Poisson's ratio (Duncan, Wong et Ozawa, 1980):

$$\nu = \frac{3B-E}{6B} \quad (1.11)$$

Table 1.2 Summary of Hyperbolic parameters (Duncan, Wong et Mabry, 1980)

Parameter	Name	Function
K, K_{ur}	Modulus number	Relate E_i and E_{ur} to σ_3
n	Modulus exponent	
c	Cohesion intercept	Relate $(\sigma_1 - \sigma_3)$ to σ_3
$\varphi, \Delta\varphi$	Friction angle parameters	
R_f	Failure ratio	Relate $(\sigma_1 - \sigma_3)u$ to $(\sigma_1 - \sigma_3)_f$
k_b	Bulk modulus number	Value of B/pa at $\sigma_3 = pa$
m	Bulk modulus exponent	Change in B/pa for tenfold increase in σ_3

In addition, several finite element programs, such as ISBILD and FEADAM (Duncan, Wong et Ozawa, 1980; Naylor, 1975; Ozawa et Duncan, 1973) were developed to predict the behavior of rockfill dams. The hyperbolic model, as a popular constitutive model, is used to suitably estimate the non-linear and stress dependent stress-strain properties of soils in these programs (Duncan, Wong et Ozawa, 1980; Naylor, 1975; Ozawa et Duncan, 1973).

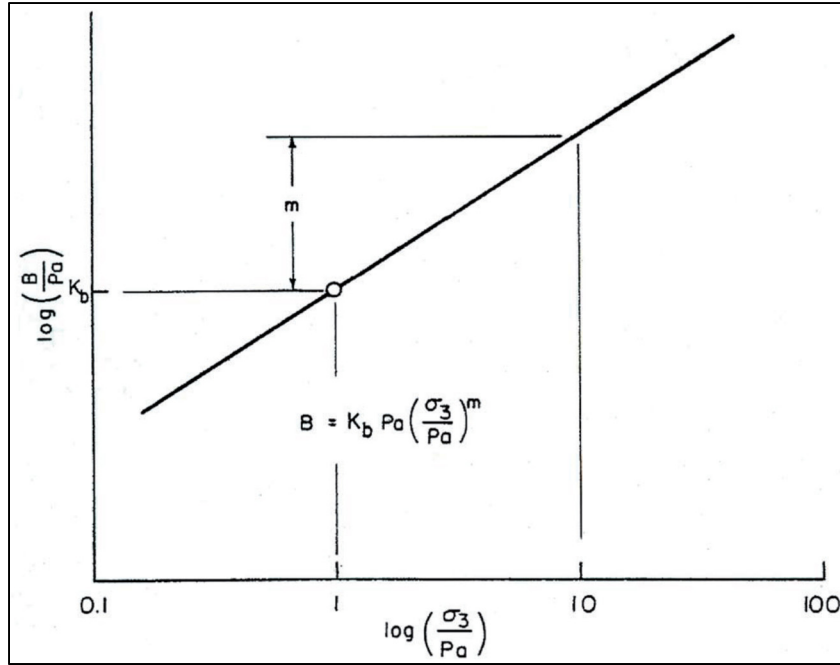


Figure 1.5 Variation of bulk modulus with confining pressure (Duncan, Wong et Mabry, 1980)

The soil stress–strain relationship for each load increment of the analysis is considered to be linear. The relation between stress–strain is supposed to obey Hook’s law of elastic deformation.

$$\begin{Bmatrix} \Delta\sigma_x \\ \Delta\sigma_y \\ \Delta\tau_{xy} \end{Bmatrix} = \frac{E_t}{(1+\vartheta_t)(1-2\vartheta_t)} \begin{bmatrix} (1-\vartheta_t) & \vartheta_t & 0 \\ \vartheta_t & (1-\vartheta_t) & 0 \\ 0 & 0 & (1-2\vartheta_t)/2 \end{bmatrix} \begin{Bmatrix} \Delta\varepsilon_x \\ \Delta\varepsilon_y \\ \Delta\gamma_{yx} \end{Bmatrix} \quad (1.12)$$

where $\Delta\sigma_x$, $\Delta\sigma_y$, and $\Delta\tau_{xy}$ are stress increments during a step of the analysis, and $\Delta\varepsilon_x$, $\Delta\varepsilon_y$, and $\Delta\gamma_{yx}$ are the corresponding strain increments. E_t is the tangent Young’s modulus and ϑ_t is the tangent Poisson’s ratio. During each step of the analysis, the value of E_t and ϑ_t will be adjusted with calculated stresses in elements (Seed, Duncan et Idriss, 1975).

By considering the bulk modulus, the stress–strain relationship (equation 1.12) can be rewritten as (Duncan, Wong et Mabry, 1980):

$$\begin{pmatrix} \Delta\sigma_x \\ \Delta\sigma_y \\ \Delta\tau_{xy} \end{pmatrix} = \frac{3B}{9B-E} \begin{bmatrix} (3B+E) & (3B-E) & 0 \\ (3B-E) & (3B+E) & 0 \\ 0 & 0 & E \end{bmatrix} \begin{pmatrix} \Delta\varepsilon_x \\ \Delta\varepsilon_y \\ \Delta\gamma_{yx} \end{pmatrix} \quad (1.13)$$

where E is the stiffness modulus and B is the bulk modulus.

The major inconsistencies of the Hyperbolic constitutive model are specified by Seed et al. (Seed, Duncan et Idriss, 1975) as follows:

- 1- Since the Hyperbolic model is based on Hook's law, it cannot show accurately the soil behavior at and after failure when a plastic deformation occurs.
- 2- The constitutive model does not take into account volume changes owing to shear stress or "shear dilatancy."
- 3- The soil model parameters are not fundamental soil properties but are empirical parameter coefficients that depict the soil behavior such as water content, soil density, range of pressure during testing, and drainage on limited conditions. These parameters vary as the physical condition changes.

The advantages of the Hyperbolic constitutive model are listed below (Seed, Duncan et Idriss, 1975):

- 1- The conventional triaxial test can be used to determine the parameter values.
- 2- "The same relationships can be applied for effective stress and total stress analyses".
- 3- Parameter values can be achieved for different soils; this information can be used in cases where the available data are not sufficient for defining the dam parameters.

1.2.2 Hardening soil model

The formulation of the HS model is based on the Hyperbolic model as indicated in equation 1.14 (Schanz, Vermeer et Bonnier, 1999). However, the HS soil model has some advantages compared to the Hyperbolic model, such as using the theory of plasticity, allowing for soil

dilatancy, and considering the yield cap (Brinkgreve et Broere, 2006). Equation 1.14 indicates the relation between the axial strain, ε_1 and deviatoric strain shown in figure 1.6.

$$\text{For } q < q_f \quad \varepsilon_1 = \frac{1}{2E_{50}} \frac{q}{1 - \frac{q}{q_a}} \quad (1.14)$$

where q is the deviatoric stress. The ultimate deviatoric stress, q_f and the asymptotic value of the shear strength, q_a are shown in figure 1.6. E_{50} is the confining stress-dependent stiffness modulus, which can be calculated using equation 1.15:

$$E_{50} = E_{50}^{ref} \left(\frac{c \cos\varphi - \sigma_3 \sin\varphi}{c \cos\varphi + p^{ref} \sin\varphi} \right)^m \quad (1.15)$$

E_{50}^{ref} is the secant stiffness in standard drained triaxial test and corresponds to the reference confining pressure. The quantity of stress dependency is defined by the power m (Brinkgreve et Broere, 2006). The value of m is considered equal to 0.5 (Janbu, 1963) while Von Soos (Soos et Bohac, 2001) reported different values in the range between 0.5 and 1.

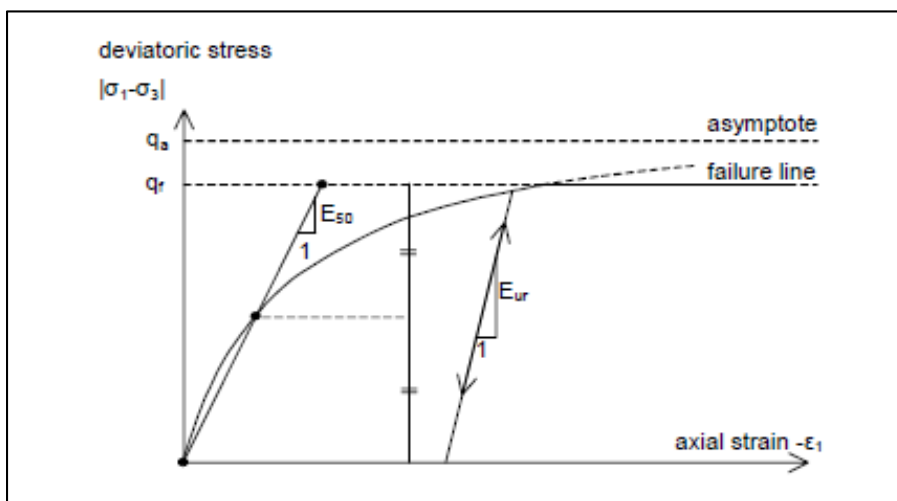


Figure 1.6 Hyperbolic stress-strain relationship for a standard drained triaxial test in primary loading (Brinkgreve et Broere, 2006)

The ultimate deviatoric stress, q_f and asymptotic stress, q_a shown in figure 1.6, are calculated using equations 1.16 and 1.17:

$$q_f = (ccot\varphi - \sigma_3) \frac{2\sin\varphi}{1-\sin\varphi} \quad (1.16)$$

$$q_a = \frac{q_f}{R_f} \quad (1.17)$$

In the equations above, R_f is the failure ratio. C , φ , and σ_3 are the cohesion, friction angle, and minor principal stress, respectively.

Another stiffness, E_{ur} is defined for unloading and reloading stress path as indicated in equation 1.18.

$$E_{ur} = E_{ur}^{ref} \left(\frac{c \cos\varphi - \sigma_3 \sin\varphi}{c \cos\varphi + p^{ref} \sin\varphi} \right)^m \quad (1.18)$$

where E_{ur}^{ref} is the reference Young's modulus that corresponds to the reference pressure for unloading and reloading.

The oedometer stiffness is defined by equation 1.19:

$$E_{oed} = E_{oed}^{ref} \left(\frac{c \cos\varphi - \sigma_3 \sin\varphi}{c \cos\varphi + p^{ref} \sin\varphi} \right)^m \quad (1.19)$$

where E_{oed}^{ref} is a tangent stiffness modulus at a vertical stress of $\sigma_1 = p^{ref}$ as shown in figure 1.7.

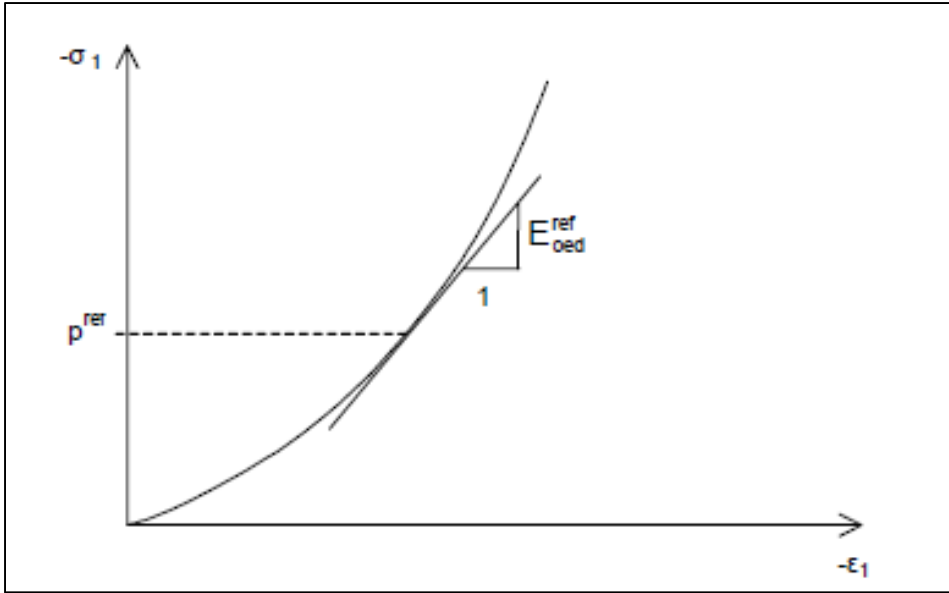


Figure 1.7 Explanation of E_{oad}^{ref} in the oedometer test
(Brinkgreve et Broere, 2006)

The hardening yield function for shear mechanism is defined as

$$f = \bar{f} - \gamma^p \quad (1.20)$$

where \bar{f} is a function of stress, and γ^p is a function of the plastic strain, as indicated in equations 1.21 and 1.22, respectively (Brinkgreve et Broere, 2006).

$$\bar{f} = \frac{1}{E_{50}} \frac{q}{1 - q/q_a} - \frac{2q}{E_{ur}} \quad (1.21)$$

where q is the deviatoric stress, and q_a is the asymptotic value of the shear strength. E_{ur} and E_{50} are the unloading and reloading stiffness and the secant stiffness modulus, respectively, as indicated in equations 1.15 and 1.18.

$$\begin{aligned} \gamma^p &= \varepsilon_1^p - \varepsilon_2^p - \varepsilon_3^p \\ \varepsilon_v^p &= \varepsilon_1^p + \varepsilon_2^p + \varepsilon_3^p \\ \gamma^p &= (2\varepsilon_1^p - \varepsilon_v^p) \approx 2\varepsilon_1^p \end{aligned} \quad (1.22)$$

where

ε_1^p is the axial plastic strain. The plastic volume change, ε_v^p is relatively small (Brinkgreve et Broere, 2006; Obrzud, 2010); therefore, for the equation above, we can assume $\gamma^p \approx 2\varepsilon_1^p$.

The axial elastic strain is approximated using equation 1.23:

$$\varepsilon_1^e = \frac{q}{E_{ur}} \quad (1.23)$$

Considering the yield condition $f = 0$, we have $\bar{f} = \gamma^p$.

$$\varepsilon_1^p = \frac{1}{2}\bar{f} = \frac{1}{2}\left(\frac{1}{E_{50}}\frac{q}{1-q/q_a} - \frac{2q}{E_{ur}}\right) \quad (1.24)$$

Combining equations 1.23 and 1.24 will lead to equation 1.25. For the triaxial test, the axial strain is the summation of the elastic and plastic components as indicated in equation 1.25.

$$\varepsilon_1 = \varepsilon_1^e + \varepsilon_1^p = \frac{q}{E_{ur}} + \frac{1}{2}\left(\frac{1}{E_{50}}\frac{q}{1-q/q_a} - \frac{2q}{E_{ur}}\right) = \frac{1}{2E_{50}}\frac{q}{1-q/q_a} \quad (1.25)$$

The shear plastic strain is given by equation 1.22. The volumetric plastic strain is explained as follows. The plastic flow rule is derived from the plastic potential defined by equation 1.26 (Obrzud, 2010). The rate of plastic volumetric strain for triaxial test can be calculated using equation 1.27, and as can be observed, the relationship is linear.

$$g_1 = \frac{\sigma_1 - \sigma_3}{2} + \frac{\sigma_1 + \sigma_3}{2} \sin\Psi_m \quad (1.26)$$

$$\dot{\varepsilon}_v^p = \sin\Psi_m \dot{\gamma}^p \quad (1.27)$$

where Ψ_m is the mobilized dilatancy angle and can be calculated using the following equation:

$$\sin\Psi_m = \frac{\sin\phi_m - \sin\phi_{cv}}{1 - \sin\phi_m \sin\phi_{cv}} \quad (1.28)$$

where

φ_m is the mobilized friction angle:

$$\sin\varphi_m = \frac{\sigma'_1 - \sigma'_3}{\sigma'_1 + \sigma'_3 - 2c \cot\varphi} \quad (1.29)$$

φ_{cv} is the critical state friction angle, and is defined as

$$\sin\varphi_{cv} = \frac{\sin\varphi - \sin\psi}{1 - \sin\varphi \sin\psi} \quad (1.30)$$

The HS model considers the dilatancy cut-off. While dilating materials after an extensive shearing reach a state of critical density, dilatancy arrives at an end as shown in figure 1.8.

To define this behavior, the initial void ratio, e_{init} , and the maximum void ratio, e_{max} for materials should be assigned. When the maximum void ratio appears, the mobilized dilatancy angle, Ψ_{mob} , is set to zero (Brinkgreve et Broere, 2006).

For $e < e_{max}$

$$\sin\Psi_{mob} = \frac{\sin\varphi_{mob} - \sin\varphi_{cv}}{1 - \sin\varphi_{mob} \sin\varphi_{cv}} \quad (1.31)$$

$$\sin\varphi_{cv} = \frac{\sin\varphi - \sin\psi}{1 - \sin\varphi \sin\psi} \quad (1.32)$$

For $e > e_{max}$ $\Psi_{mob} = 0$

Equation 1.33 shows the relationship between void ratio and volumetric strain.

$$-(\varepsilon_v - \varepsilon_v^{init}) = \ln\left(\frac{1+e}{1+e_{init}}\right) \quad (1.33)$$

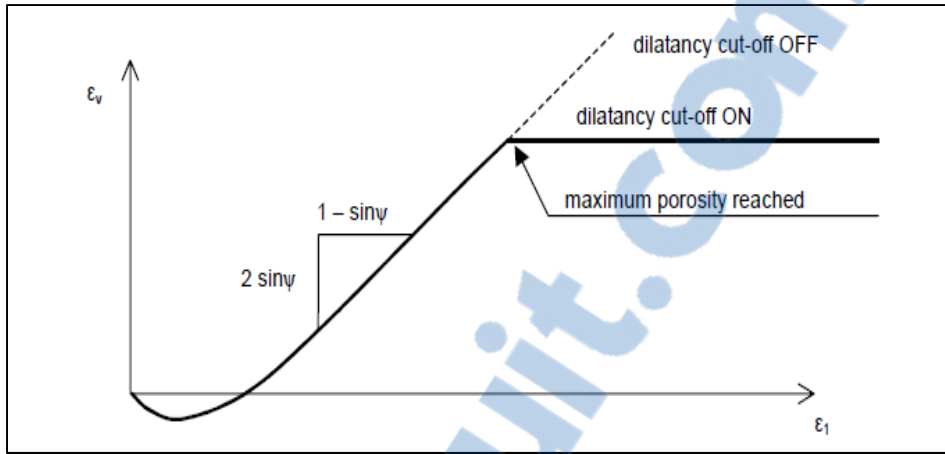


Figure 1.8 Dilatancy cut-off (Brinkgreve et Broere, 2006)

The shear yield surface, which is shown in figure 1.9, does not consider the plastic volume strain calculated in isotropic compression. Hence, “a second yield surface is assumed to close the elastic region in the direction of p axis (figure 1.9). This cap yield surface, makes it possible to formulate a model with independent parameters, E_{50}^{ref} and E_{oed}^{ref} ” (Brinkgreve et Broere, 2006). The shear yield surface is regulated by the triaxial modulus, E_{50}^{ref} , and the oedometer modulus, E_{oed}^{ref} , controls the cap yield surface. The yield cap is defined as (Brinkgreve et Broere, 2006):

$$f^c = \frac{q^{\sim 2}}{\alpha^2} + p^2 - p_p^2 \quad (1.34)$$

where p_p is the preconsolidation stress. α is an auxiliary parameter, which is related to K_0^{nc} , the normally consolidated coefficient of lateral earth pressure. Other parameters in the equation above are defined as

$$p = -\frac{(\sigma_1 + \sigma_2 + \sigma_3)}{3} \quad (1.35)$$

$$q^{\sim} = \sigma_1 + (\delta - 1)\sigma_2 - (\delta)\sigma_3 \quad (1.36)$$

$$\delta = \frac{(3 + \sin \varphi)}{(3 - \sin \varphi)} \quad (1.37)$$

The following advantages of the HS constitutive model are mentioned by Schanz et al. (Schanz, Vermeer et Bonnier, 1999):

- 1- “In contrast to an elastic-perfectly plastic model, the yield surface of the HS model is not constant in the principal stress space; it can expand owing to plastic straining”.
- 2- The HS model comprises two types of hardening, that is, shear hardening and compression hardening. Shear hardening is applied to simulate irreversible strain caused by primary deviatoric loading. Compression hardening is applied to simulate irreversible plastic strain caused by primary compression in oedometer loading.

The HS constitutive model limitations are listed below (Obrzud et Eng, 2010):

- 1- The model is not capable of reproducing softening impacts.
- 2- The model cannot reproduce the hysteretic soil behavior during cyclic loading.
- 3- The model considers elastic material behavior during unloading and reloading, while the strain range in which the soil can behave as elastic is considerably small and limited.

1.2.3 Hardening soil-small strain model

The HSS model is a revision of the HS model that considers the increased stiffness of soils at small strains. Generally, soils show more stiffness at small strains when compared with stiffness at engineering strains, as shown in figure 1.11. The stiffness at small strain levels changes non-linearly with strains. The HSS model uses almost the same parameter as the HS model. Two additional parameters i.e. G_0^{ref} and $\gamma_{0.7}$ are required to define the HSS model, where G_0 is the small strain shear modulus, and $\gamma_{0.7}$ is the strain level at which the shear modulus has reduced to 70% of the small strain shear modulus (Brinkgreve et Broere, 2006). As an enhanced version of the HS model, the HSS model can account for small strain stiffness and it is capable to reproduce hysteric soil behavior under cyclic loading conditions (Obrzud, 2010).

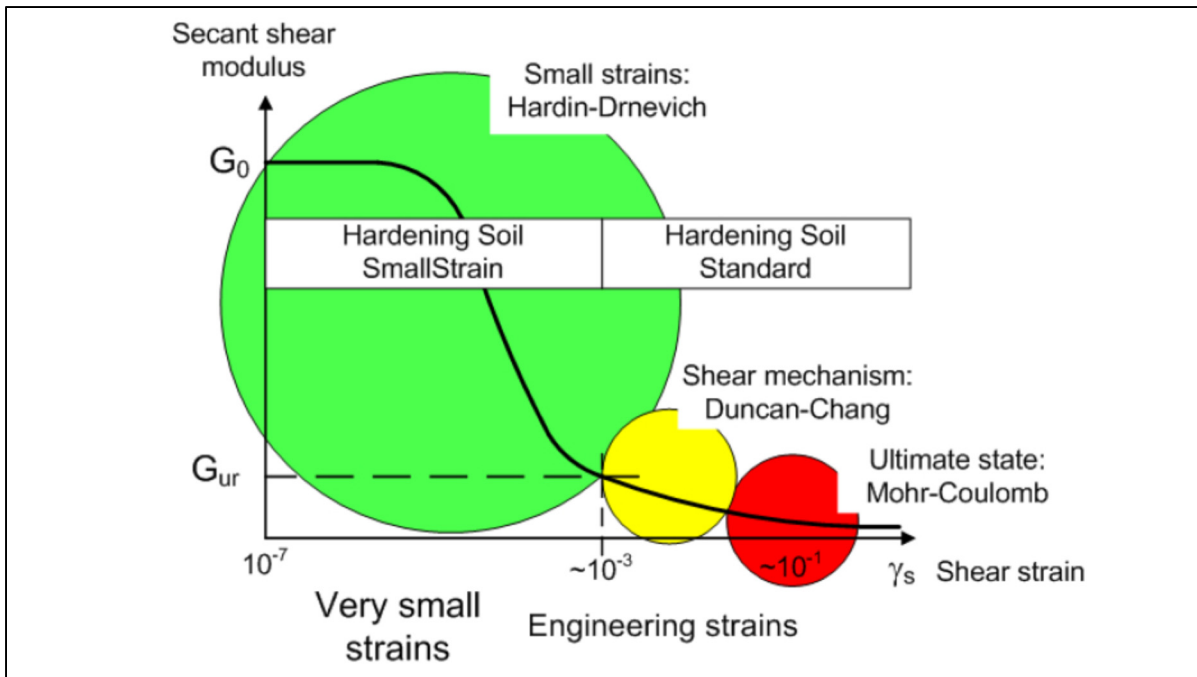


Figure 1.11 Schematic presentation of the HS model, stiffness-strain behavior (Obrzud, 2010)

CHAPTER 2

COMPARISON AMONG DIFFERENT CONSTITUTIVE SOIL MODELS THROUGH TRIAXIAL AND OEDOMETER TESTS

2.1 Introduction

Choosing an appropriate soil constitutive model is one of the most important elements of a successful finite element or finite difference analysis of soil behavior. There are several soil constitutive models; however, none of them can reproduce all aspects of real soil behavior (Brinkgreve, 2007). In this chapter, various constitutive soil models, namely, Duncan–Chang, MC, HS, and HSS are studied through triaxial and oedometer tests. Two finite element software, Plaxis and Zsoil, are used for the numerical tests. The triaxial and oedometer numerical simulation procedures using Plaxis and Zsoil are explained in sections 2.3 and 2.8, respectively. The studies have focused on Hostun sand (Benz, 2007; Brinkgreve et Broere, 2006; Obrzud, 2010). The standard drained triaxial test is conducted on loose and dense specimens, and experimental tests results are shown in figures 2.4 to 2.6. Finally, the data obtained from Plaxis, Zsoil, and experimental tests are compared with each other.

2.2 Triaxial test

The triaxial test is one of the most popular and reliable methods for calculating soil shear strength parameters. In this test, a specimen that has experienced confining pressure by the compression of fluid in triaxial chamber is subjected to continuously rising axial load to observe the shear failure. This stress can be loaded using two methods. The first method is a stress-controlled test wherein the dead weight is increased in equal increments until the specimen fails. In this method, the axial strain due to the load is measured using a dial gauge. The second method is a strain-controlled test, where the axial deformation is increased at a constant rate. Based on drainage, three types of tests are defined, namely, consolidated-drained, consolidated-undrained, and unconsolidated-undrained (Das et Sobhan, 2013). In this study, the implemented simulations are conducted in consolidated-drained condition.

2.3 Finite element modeling

In this section, the consolidated-drained triaxial test is modeled and the geometry and boundary conditions, which are used to simulate the model through Plaxis and Zsoil, are presented.

2.3.1 Geometry of model and boundary conditions in Plaxis

A consolidated-drained triaxial test was implemented on the geometry shown in figure 2.1. An axisymmetric model was used. The left and bottom sides of the model were constrained in the horizontal and vertical direction, respectively. The rest of the boundaries were assumed free to move. For simplicity, a $1\text{ m} \times 1\text{ m}$ unit square was used to simulate the test; these dimensions are not real. This model represents a quarter of the specimen test. As the soil weight was not considered, the dimensions of the model had no impact on the results. The initial stress and steady pore pressure were not taken into account. Furthermore, the deviator stress and confining pressure were simulated as uniformly distributed loads (Brinkgreve, 2007).

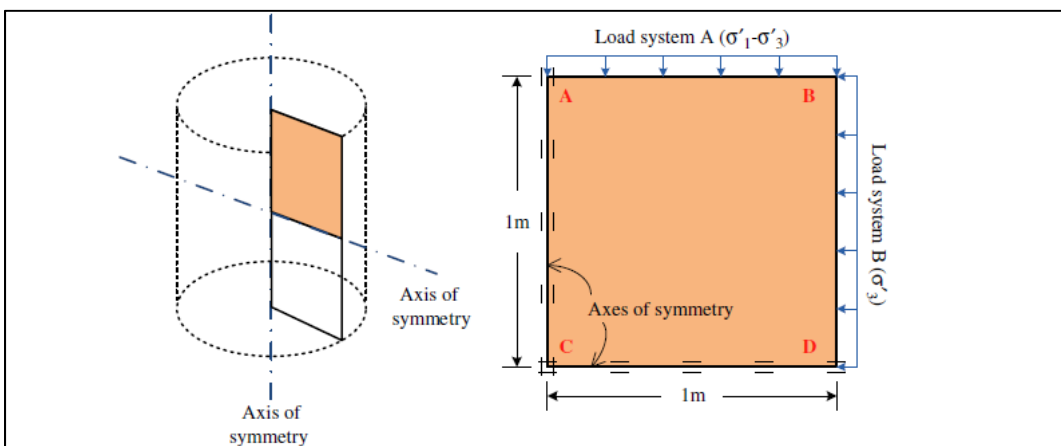


Figure 2.1 Triaxial loading condition (Surarak et al., 2012)

In the first phase, the model was exposed to a confining pressure, $\sigma_3 = -300$ kPa to allow consolidation. In the second stage, the model was loaded vertically up to failure, whereas the horizontal confining pressure was kept unchanged.

A fifteen-node triangular element was used. It is crucially important to use a sufficient number of refined meshes to ensure that the results from the finite element software are precise. To observe the influence of mesh size on the stress–strain graph, several analyses were implemented using Plaxis. Table 2.1 shows that decreasing the mesh size has no significant influence on the maximum deviatoric stress. As the modeled test has a relatively simple geometry, decreasing the mesh size has no significant influence on the test results (Brinkgreve, 2007).

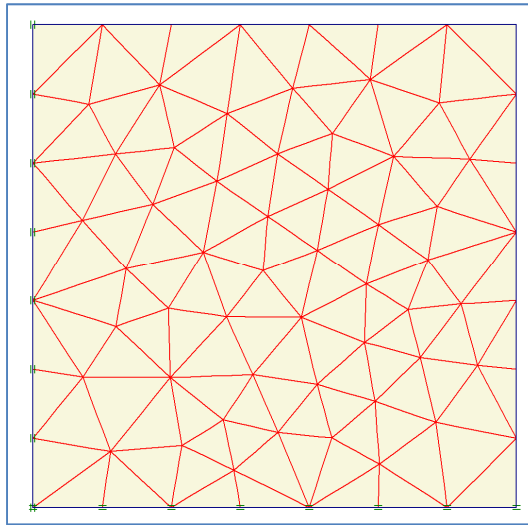


Figure 2.2 Plot of the mesh in Plaxis

Table 2.1 Mesh size influences on deviatoric stress for the Hardening soil model in Plaxis software

Average element size (mm)	Number of nodes	Maximum deviatoric stress
91.29	1017	1164.98
61.78	2177	1165.75
41.81	4689	1165.75

2.3.2 Geometry of model and boundary condition in Zsoil

A compressive triaxial test can be simulated by using an axisymmetric geometry of unit dimension, $1 \text{ m} \times 1 \text{ m}$, that represents a quarter of the soil sample (Brinkgreve, 2007). As the weight was not considered, the dimensions of the model had no impact on the results. The initial stresses were set to a uniform compressive pressure of 300 kPa for all three directions to account for the consolidation under confining pressure. As the strain control test was performed, the load was imposed as vertical displacement on the top nodes while the bottom nodes were fixed in the vertical direction. The displacement magnitude of top nodes was defined as a load–time function. Horizontal confining pressure was applied on the right side, while the left side was kept fixed horizontally. Various mesh sizes were used to model the test; however, as can be observed in table 2.2, refining the mesh size has no significant influence on the results owing to the relatively simple geometry of the triaxial test. Four-node quadrilateral elements were used for meshing as shown in figure 2.3.

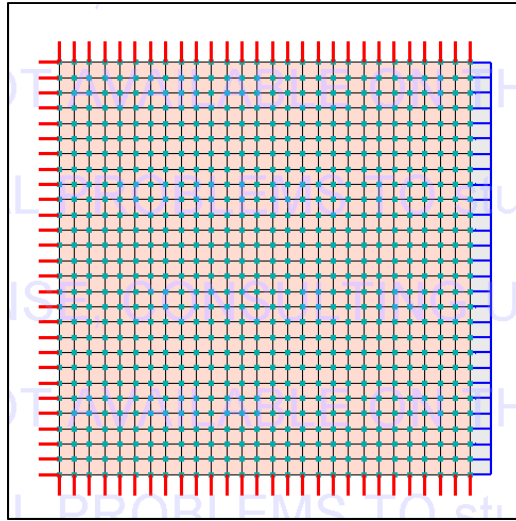


Figure 2.3 Plot of the mesh in Zsoil

Table 2.2 Mesh size influences on deviatoric stress for the Hardening soil model in Zsoil software

Number of elements	Number of nodes	Maximum deviatoric stress
1	4	1144.49
81	100	1144.51
729	784	1144.52

2.4 Experimental data

Experimental data on dense and loose Hostun sand available from reports (Benz, 2007; Brinkgreve et Broere, 2006; Obrzud, 2010) were used to obtain the parameters. Consolidated-drained triaxial tests at a fixed pressure of $\sigma_3 = -300$ kPa were conducted on loose and dense sand. Furthermore, four control tests were performed to check the possibility of reproducing the test results (Schanz et Vermeer, 1996). The results are shown in figures 2.4 and 2.5, where the deviatoric stress-axial-strain and volumetric strain-axial-strain curves are illustrated. As shown, the reproducibility of results is satisfactory (Schanz et Vermeer, 1996).

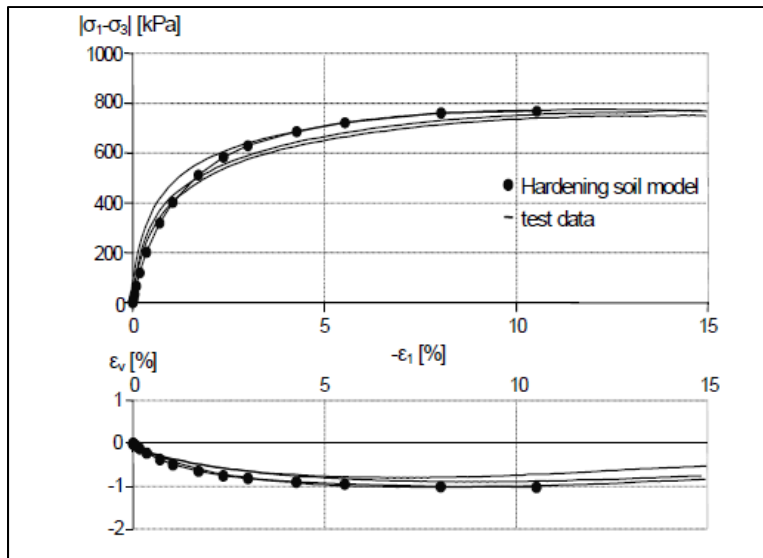


Figure 2.4 Results of drained triaxial test on loose Hostun sand (Brinkgreve, 2007)

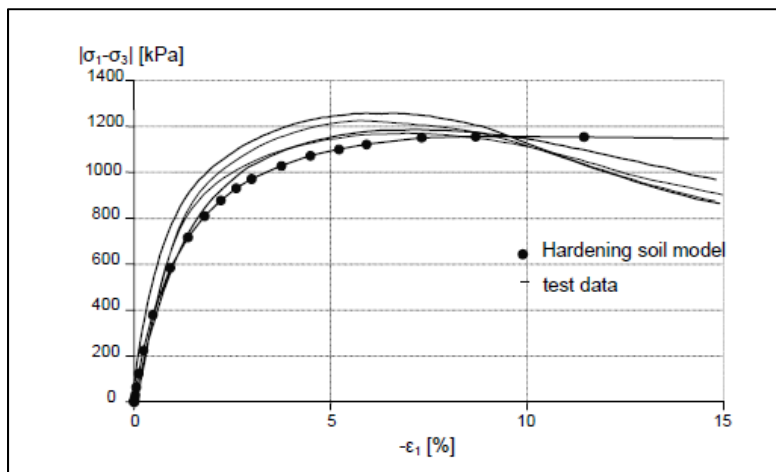


Figure 2.5 Results of drained triaxial test on dense Hostun sand, deviatoric stress versus axial strain (Brinkgreve et Broere, 2006)

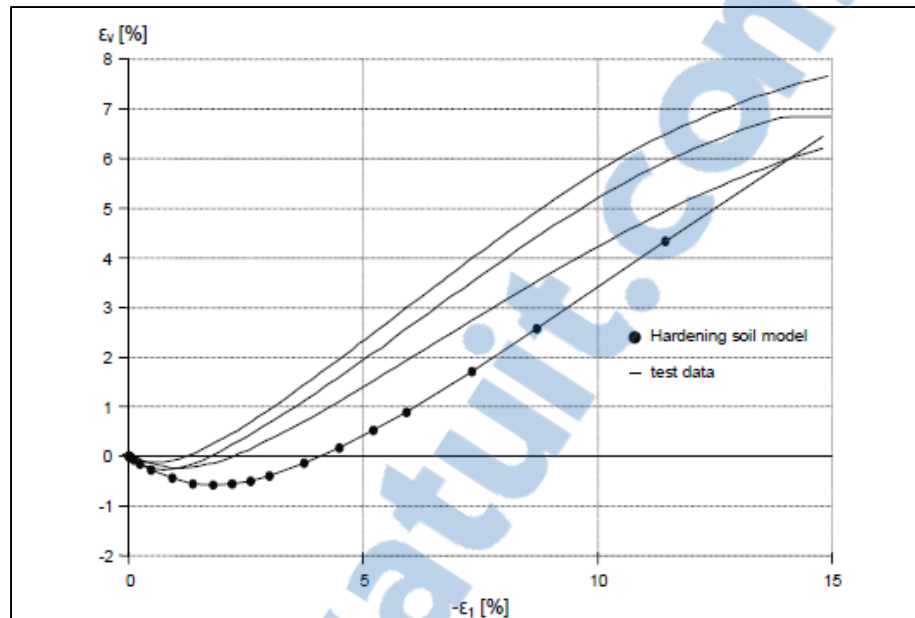


Figure 2.6 Results of drained triaxial test on dense Hostun sand, volumetric strain versus axial strain (Brinkgreve et Broere, 2006)

2.5 Application of constitutive soil models

The stress–strain relationship for Hostun sand was modeled using various constitutive models in Plaxis and Zsoil. The results of Zsoil and Plaxis for different models were compared with experimental data, as shown in figures 2.4 to 2.6, to determine the most appropriate model.

2.5.1 Mohr–Coulomb model

The MC model is a linear elastic-perfectly plastic model used to depict the soil response when subjected to shear stress (Ti et al., 2009). The linear region is based on Hooke's law of isotropic elasticity, while the plastic region is attributed to the MC failure criterion (Ti et al., 2009). Five parameters are required to define the MC soil model (table 2.3). For real soil, the stiffness modulus is not constant and depends on the stress. E_0 is the initial stiffness and E_{50} is the secant modulus at 50% of the soil strength as shown in figure 2.7. For a material with an extended elastic range, using the initial stiffness, E_0 seems appropriate; however, using E_{50}

for loading of soils is generally acceptable (Brinkgreve et Broere, 2006). E_{50} is used for this modeling. For the MC model in many cases, it is suggested to consider a Poisson's ratio between 0.3 and 0.4 (Brinkgreve et Broere, 2006); hence a Poisson's ratio of 0.35 is assumed.

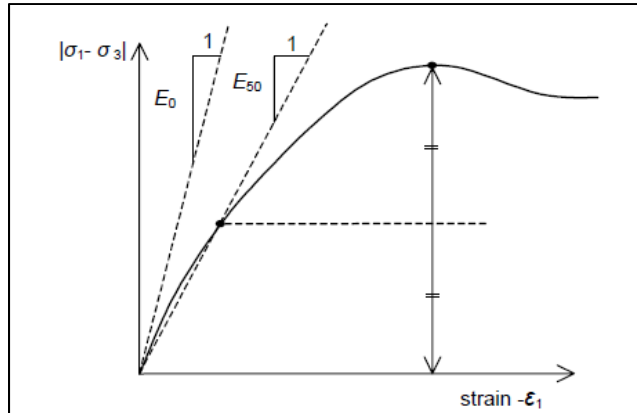


Figure 2.7 The initial stiffness, E_0 and the secant modulus, E_{50} (Brinkgreve et Broere, 2006)

Table 2.3 Soil properties used in the MC model for loose sand

Material	Model	Data group	Properties	Unit	Value
Hostun loose sand	Mohr-Coulomb	Elastic	E	[KN/m ²]	20000
			ϑ	-	0.35
		Density	γ	[KN/m ³]	17
			γf	[KN/m ³]	10
		Nonlinear	φ	[degree]	34
			ψ	[degree]	0
			C	[KN/m ²]	0

Table 2.4 Soil properties used in the MC model for dense sand

Material	Model	Data group	Properties	Unit	Value
Hostun dense sand	Mohr-Coulomb	Elastic	E	[KN/m ²]	37000
			ϑ	-	0.35
		Density	γ	[KN/m ³]	17.5
			γf	[KN/m ³]	10
		Nonlinear	φ	[degree]	41
			ψ	[degree]	14
			C	[KN/m ²]	0

Numerical analyses conducted on the MC model are shown in figures 2.8 to 2.11. This model consists of elastic and plastic portions. The results shown in figures 2.8 to 2.11 do not indicate good agreement between experimental tests and simulated results. The experimental result shows a curved shape, whereas the MC simulation result in the elastic part is linear (figures 2.8 and 2.10). Consequently, the simulation implemented using the MC model cannot demonstrate softening behavior in dense sand as shown in figure 2.8. Simulation results and experimental results for loose sand as shown in figure 2.10 are more compatible. Finally, it can be clearly observed that the simulation results using Plaxis and Zsoil (figures 2.8 to 2.11) are in agreement.

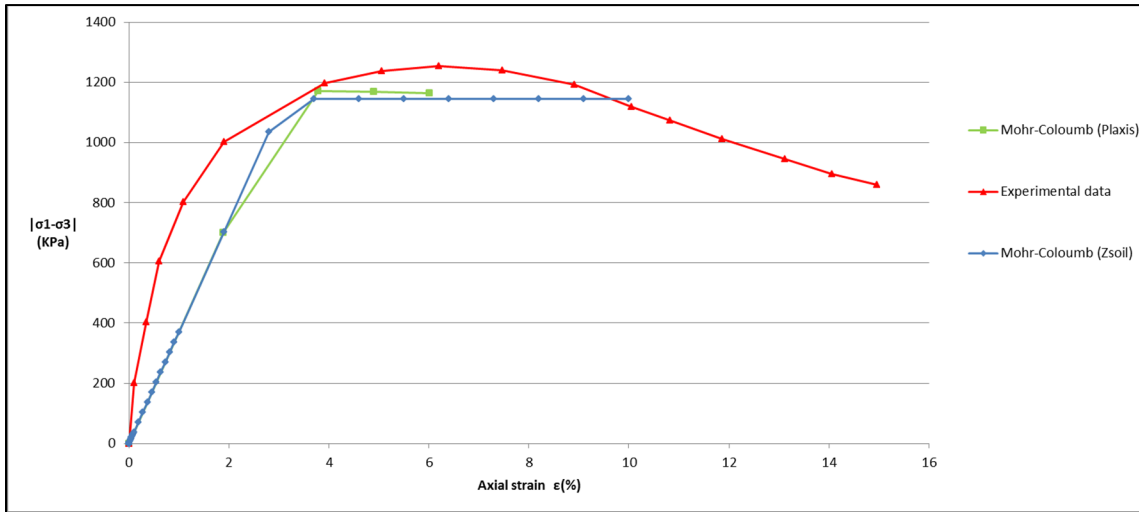


Figure 2.8 Deviatoric stress vs axial strain for the MC model in dense sand

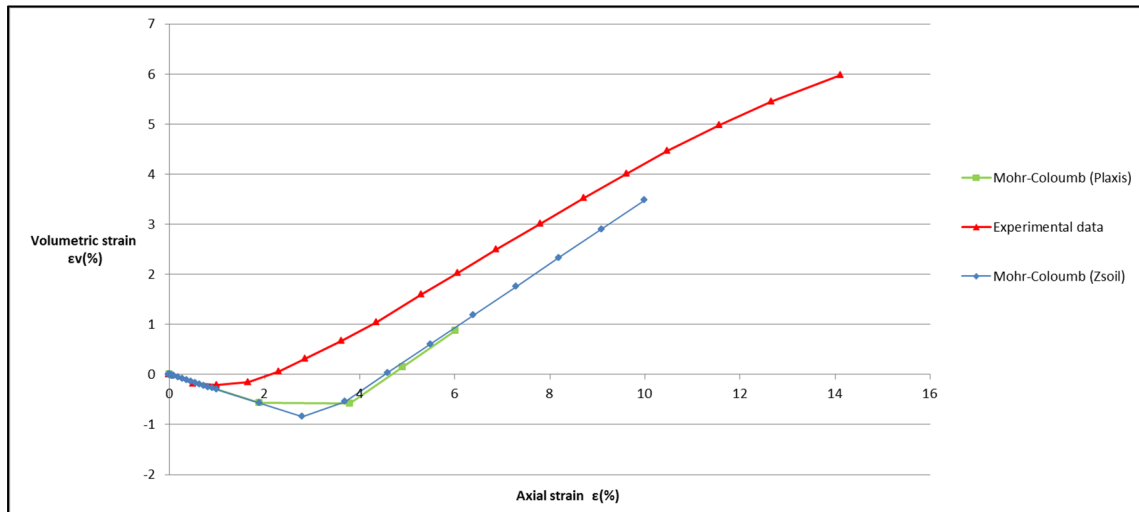


Figure 2.9 Volumetric strain vs axial strain for the MC model in dense sand

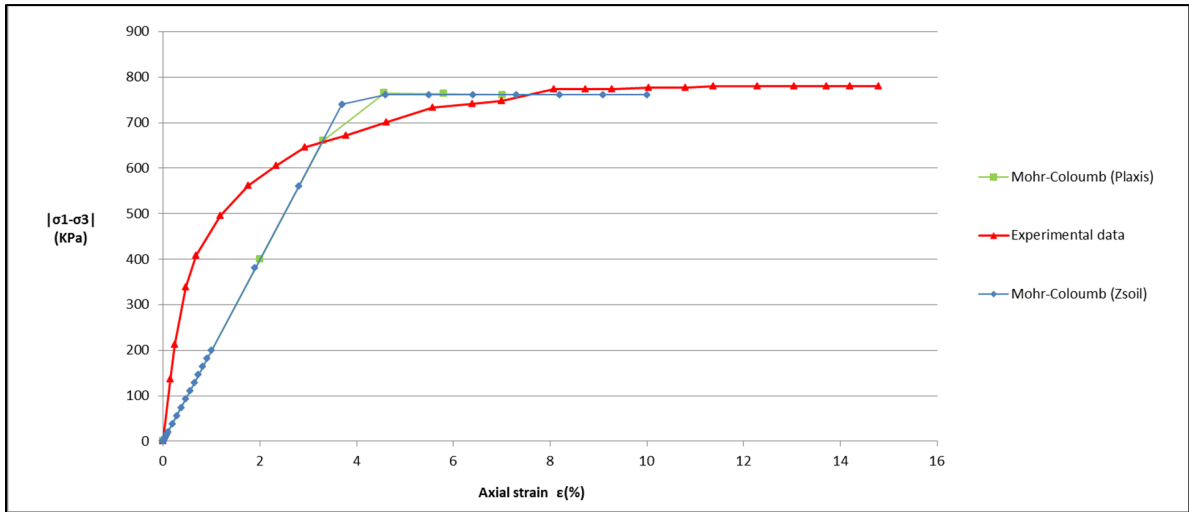


Figure 2.10 Deviatoric stress vs axial strain for the MC model in loose sand

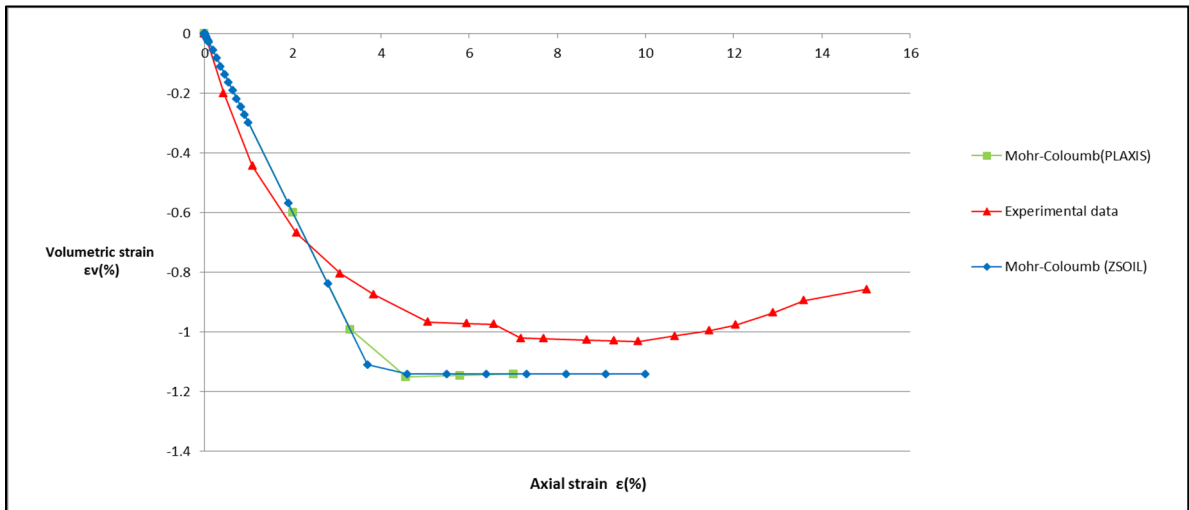


Figure 2.11 Volumetric strain vs axial strain for the MC model in loose sand

2.5.2 Hardening soil model

In this section, the HS model is used to simulate the drained triaxial test. In contrast to the MC model, the soil stiffness in this model is defined more precisely by using three modulus stiffnesses, namely, the triaxial loading stiffness, triaxial unloading stiffness, and oedometer loading stiffness (Brinkgreve, 2007). A summary of the HS model parameters for Hostun sand is presented in table 2.5.

Table 2.5 Soil properties used in the HS model for dense and loose sand (Brinkgreve, 2007)

Material	Model	Properties	Unit	Dense sand	Loose sand
Hostun sand	Hardening	E_{50}^{ref}	[KN/m ²]	37000	20000
		E_{ur}^{ref}	[KN/m ²]	90000	60000
		E_{oed}^{ref}	[KN/m ²]	29600	16000
		ϑ_{ur}	-	0.2	0.2
		γ	[KN/m ³]	17.5	17
		γf	[KN/m ³]	10	10
		φ	[degree]	41	34
		ψ	[degree]	14	0
		C	[KN/m ²]	0	0
		m	-	0.5	0.65
		Failure ratio	-	0.9	0.9
		k_0^{nc}	-	0.34	0.44

The theoretical solution for failure of a sample is calculated based on the MC model (equation 2.1):

$$f = \frac{|\sigma_1 - \sigma_3|}{2} + \frac{\sigma_1 + \sigma_3}{2} \sin \varphi - c \cdot \cos \varphi = 0 \quad (2.1)$$

The failure due to compression is calculated as

$$\text{For dense soil} \quad \sigma_1 = \sigma_3 \cdot \frac{1 + \sin \varphi}{1 - \sin \varphi} - 2c \cdot \frac{\cos \varphi}{1 - \sin \varphi} = 1455.8 \quad (2.2)$$

$$|\sigma_1 - \sigma_3| = 1155.8 \text{ kpa}$$

$$\text{For loose soil} \quad \sigma_1 = \sigma_3 \cdot \frac{1 + \sin \varphi}{1 - \sin \varphi} - 2c \cdot \frac{\cos \varphi}{1 - \sin \varphi} = 1063$$

$$|\sigma_1 - \sigma_3| = 763 \text{ kpa}$$

The confining pressure, σ_3 is assumed as 300 kPa. The deviator stress values ($\sigma_1 - \sigma_3$) for dense and loose sand, calculated theoretically using equation 2.2, are in good agreement with the results of Plaxis, Zsoil, and the results obtained from experimental tests.

As shown in figure 2.12, for both experimental test data (dense Hostun sand) and numerical analysis conducted based on the HS constitutive model, a hyperbolic relationship can be observed between the deviatoric stress (principal stress difference) and the vertical strain. The stress–strain relationship of soil in the HS model before reaching failure is based on the hyperbolic model (Schanz, Vermeer et Bonnier, 1999). A good agreement is indicated in figure 2.12 between the first hyperbolic part of the simulation conducted using Plaxis and Zsoil and the experimental data. The HS model does not include any softening behavior (Obrzud et Eng, 2010); hence, the second part of the graph stays constant and cannot completely show the same experimental results. In figure 2.14, it can be observed that the triaxial test results (for loose Hostun sand) based on the HS constitutive model calculation are in good agreement with experimental test results. Finally, it is evident that the ultimate shear strength for dense sand is higher than loose sand; this can be observed in figures 2.12 and 2.14. A good agreement is observed between Plaxis and Zsoil test results.

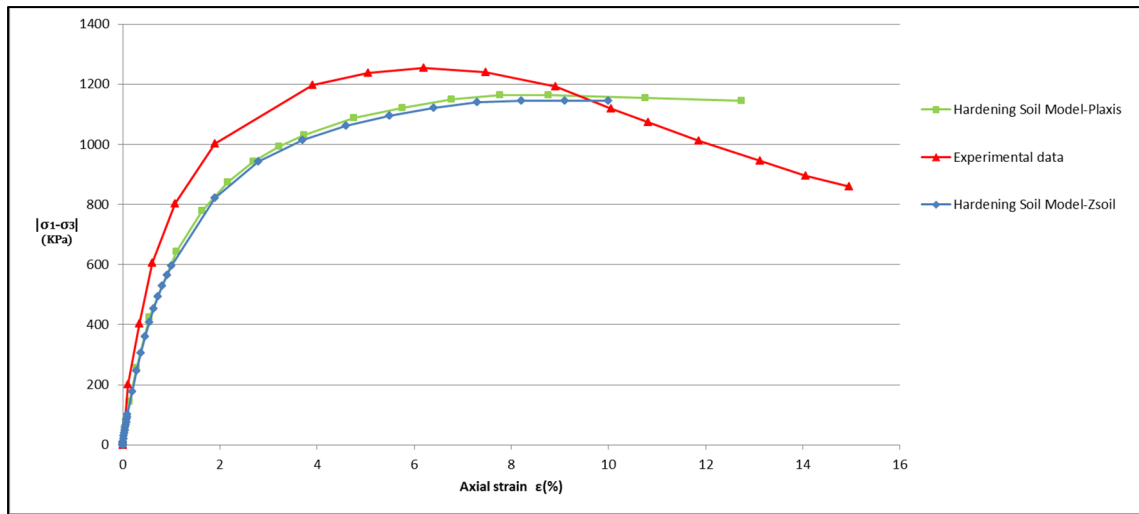


Figure 2.12 Deviatoric stress vs axial strain for the HS model in dense sand

Figures 2.13 and 2.15 show the volumetric strain versus axial strain. Dilation can be observed in figure 2.13 for dense sand, where sand particles are moved out of voids due to increasing shear force. In figure 2.15, negative dilation can be observed as sand particles continue to move into larger voids until failure (Towhata, 2008).

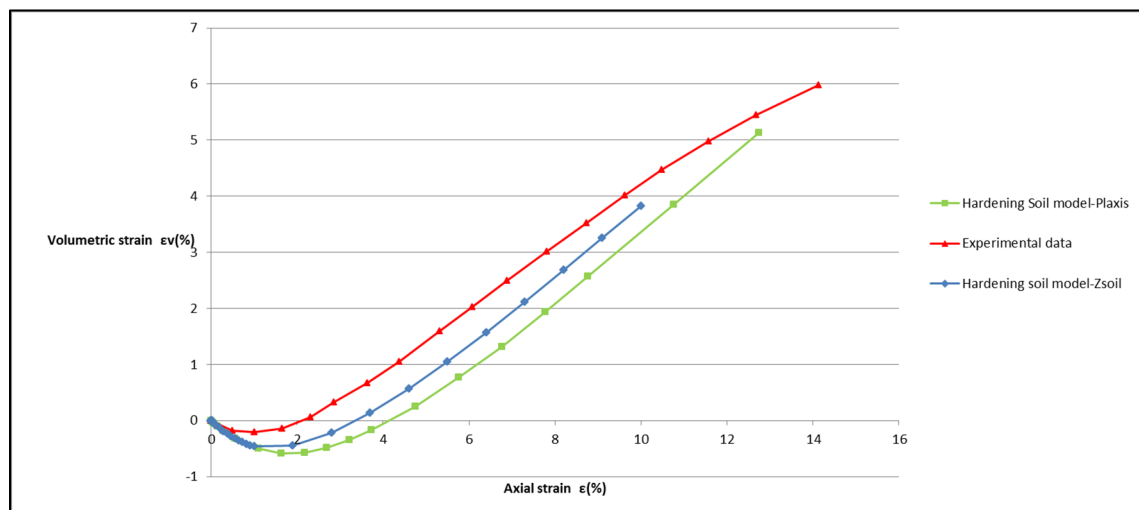


Figure 2.13 Volumetric strain vs axial strain for the HS model in dense sand

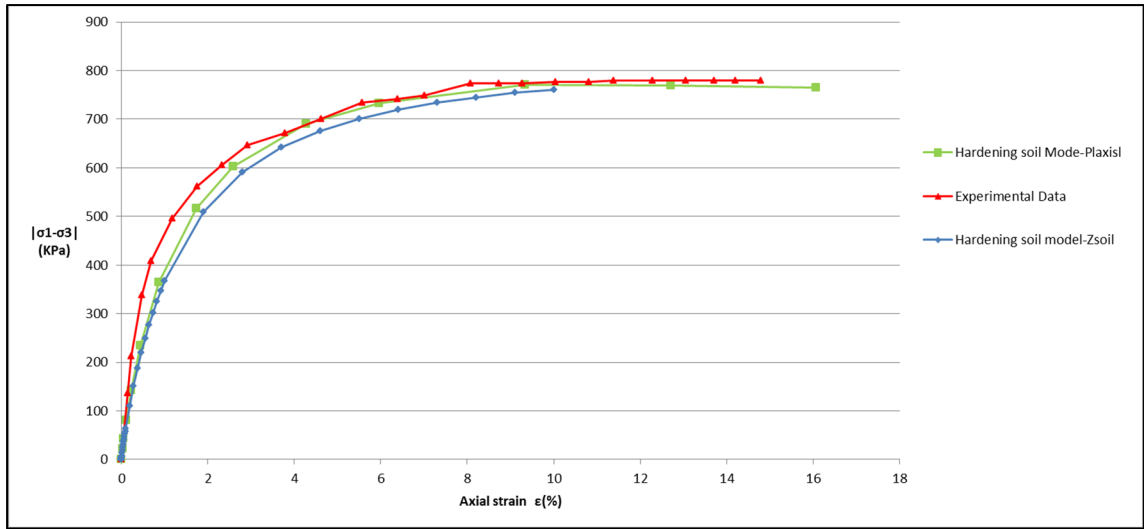


Figure 2.14 Deviatoric stress vs axial strain for the HS model in loose sand

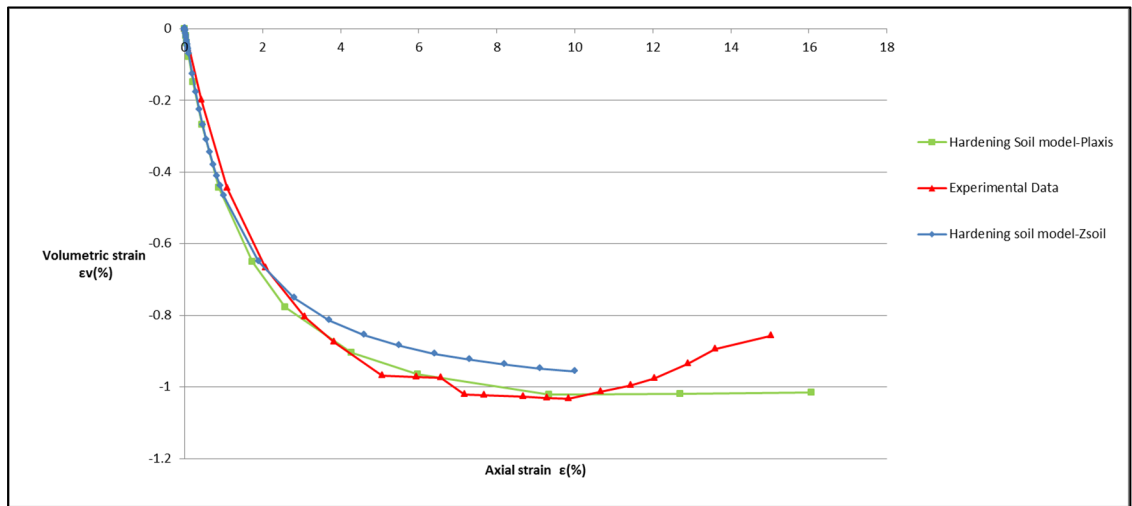


Figure 2.15 Volumetric strain vs axial strain for the HS model in loose sand

2.5.3 Hardening small strain soil model

In this section, the HSS model is studied to simulate the soil behavior in drained triaxial tests. For HSS modeling, two extra parameters are required apart from those required in the HS model; their values are given in table 2.6.

Table 2.6 Supplemental HS Small soil parameters for loose and dense Hostun sand (Brinkgreve, 2007)

Parameters	Loose sand	Dense sand
$G_0^{\text{ref}}(p_{\text{ref}}=100\text{kpa})$	70000	112500
Shear strain	0.0001	0.0002

For loose sand (figure 2.18), the deviatoric stress increases with axial strain until a failure shear stress is reached. After reaching that point, the shear resistance is approximately constant with further increase in axial strain. In dense sand (figure 2.16), the deviatoric stress rises with increasing axial strain before reaching the peak stress after which a decrease in deviatoric stress is observed. The analysis implemented using the HSS soil model can reproduce the same trends except the softening behavior in dense sand. Furthermore, a good agreement was found between Plaxis and Zsoil results.

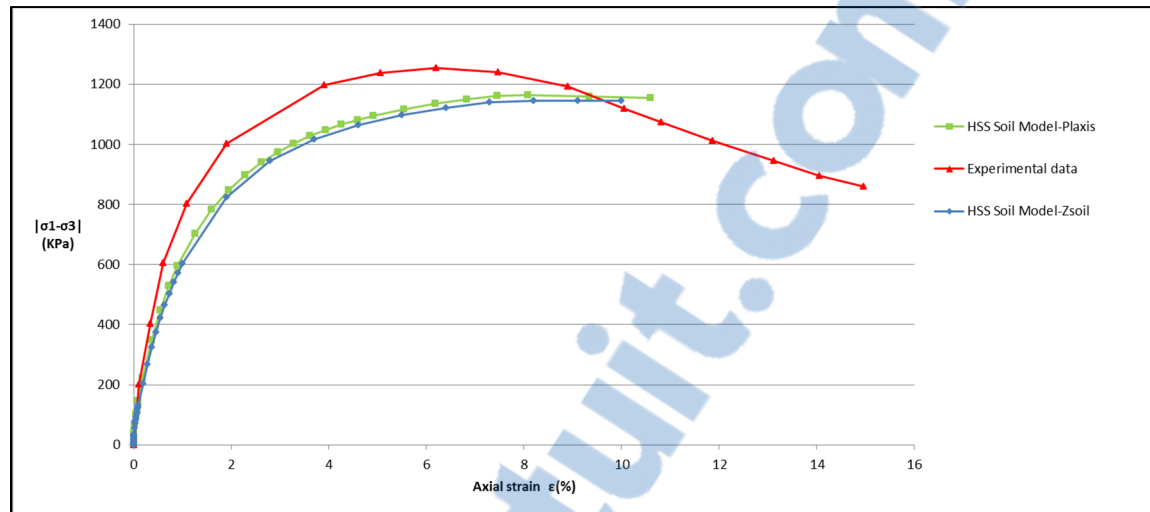


Figure 2.16 Deviatoric stress vs axial strain for the HSS model in dense sand

Increase in shear force is often accompanied by an increase in volume of the system for dense sand, which is referred to as dilatancy. This is the result of change in alignment of soil particles. An increased shear force moves the soil particles inside the voids resulting in a decrease of volume or negative dilatancy as can be observed in figure 2.19 and the starting region in figure 2.17 (Towhata, 2008). For dense sand, as the shear force continues to rise, the particles instead of being pushed in are pushed out of the intergranular spaces leading to increase in volume of the system (Towhata, 2008) as can be observed in figure 2.17. Since the HSS model accounts for dilatancy, it can be observed in the result of Zsoil and Plaxis (figures 2.17 and 2.19). Zsoil correctly shows dilatancy in dense and loose sands and has an acceptable deviation from the real test results.

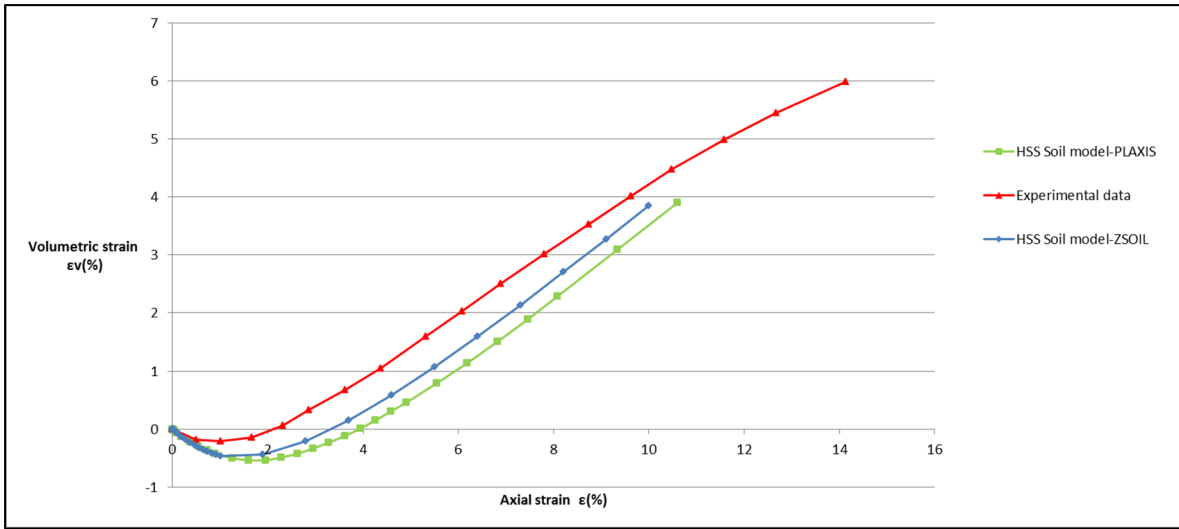


Figure 2.17 Volumetric strain vs axial strain for the HSS model in dense sand

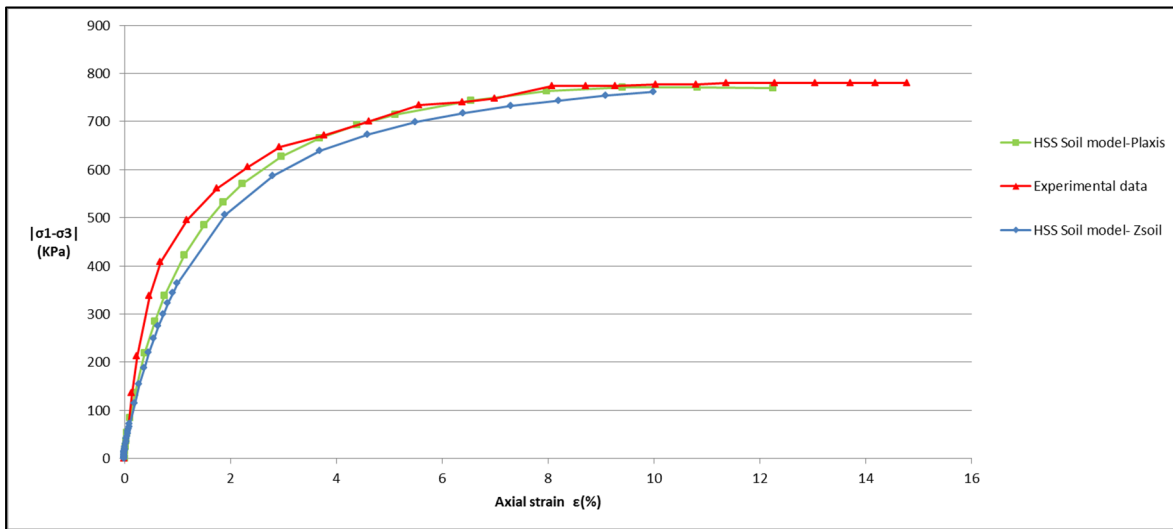


Figure 2.18 Deviatoric stress vs axial strain for the HSS model in loose sand

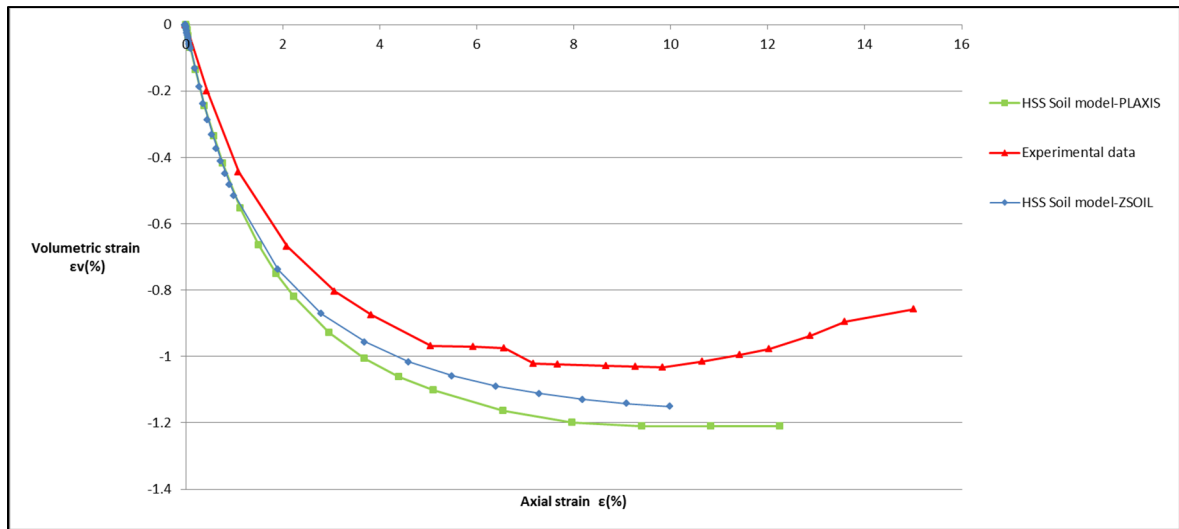


Figure 2.19 Volumetric strain vs axial strain for the HSS model in loose sand

2.5.4 Duncan–Chang soil model

In this section, the Duncan–Chang soil model is used to simulate the drained triaxial test. This constitutive soil model is a non-linear elastic model based on a hyperbolic stress–strain relationship. The parameters employed to depict the hyperbolic stress–strain relation are k (modulus number), n (modulus exponent), R_f (failure ratio), and G , F , d (Poisson’s ratio parameters). A summary of the Duncan–Chang soil model parameters for Hostun sand is presented in table 2.7.

Table 2.7 Soil properties used in the model for dense and loose sand

Material	Model	Properties	Unit	Dense sand	Loose sand
Hostun sand	Duncan- Chang	γ	[KN/m ³]	17.5	17
		γf	[KN/m ³]	10	10
		φ	[degree]	41	34
		C	[KN/m ²]	0	0
		n	-	0.5	0.65
		R_f (Failure ratio)	-	0.8	0.8
		k	-	740	400
		G	-	0.3065	0.38
		F	-	0.02	0.013
		d	-	9.24	3.85

Numerical analyses implemented on the Duncan–Chang model are shown in figures 2.20 to 2.23. The confining pressure, σ_3 is assumed as 300 kPa. For both experimental test data (dense Hostun sand) and numerical analysis, a hyperbolic relationship can be observed between the deviatoric stress (principal stress difference) and the vertical strain (figure 2.20). The Duncan–Chang model was formulated in order to exhibit an appropriate and fit result on the data. A good agreement is indicated in figure 2.20 between the first hyperbolic part of the simulation conducted using Zsoil and experimental data.

The Duncan–Chang soil model does not include softening behavior; hence, the second part of the graph cannot completely depict the experimental results. From figure 2.22, it can be observed that the simulations (for loose Hostun sand) closely agree with experimental test results.

For the volumetric strain versus axial strain, it is shown that the simulation cannot describe the soil volumetric–axial strain relation for dense sand (figure 2.21). As the Duncan–Chang

soil model does not consider dilatancy parameter, a remarkably large difference can be observed between the simulation and experimental data.

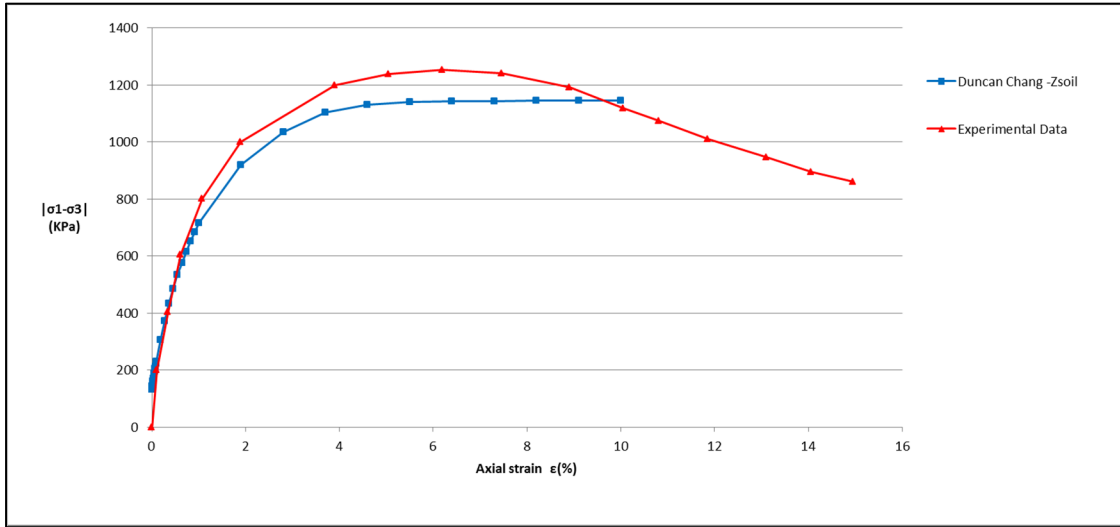


Figure 2.20 Deviatoric stress vs axial strain for the Duncan-Chang model in dense sand

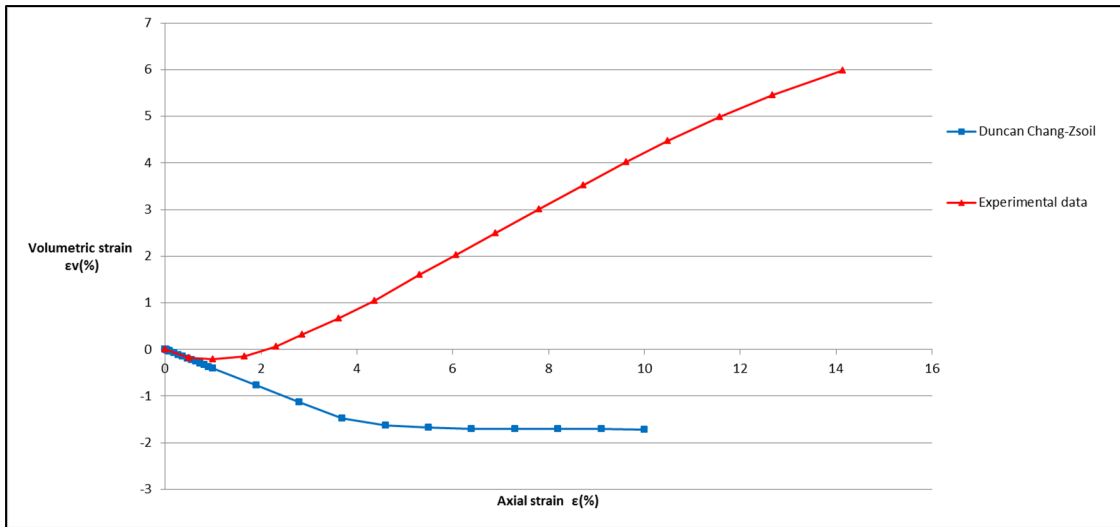


Figure 2.21 Volumetric strain vs axial strain for the Duncan-Chang model in dense sand

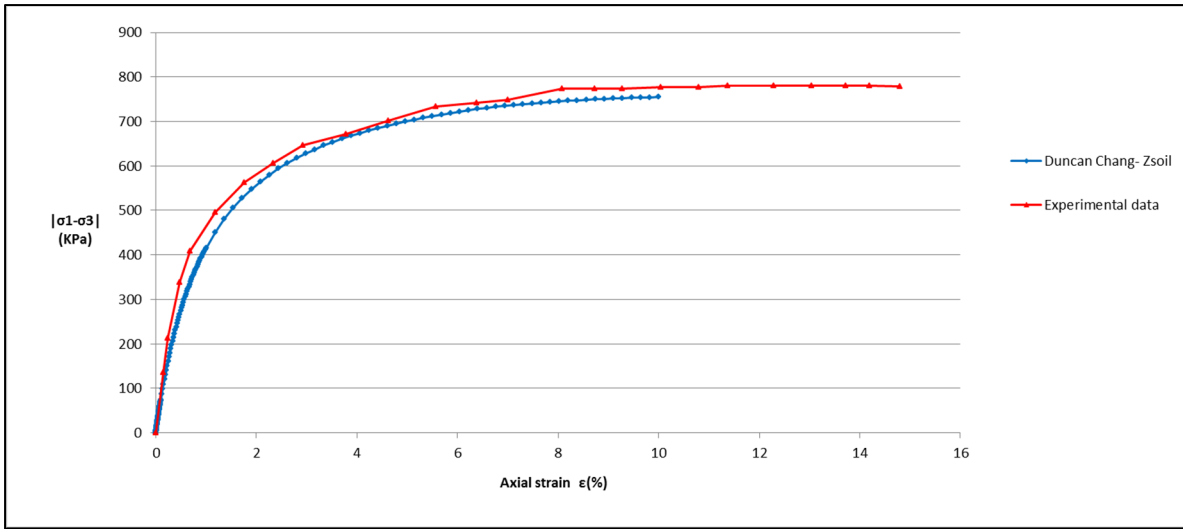


Figure 2.22 Deviatoric stress vs axial strain for the Duncan-Chang model in loose sand

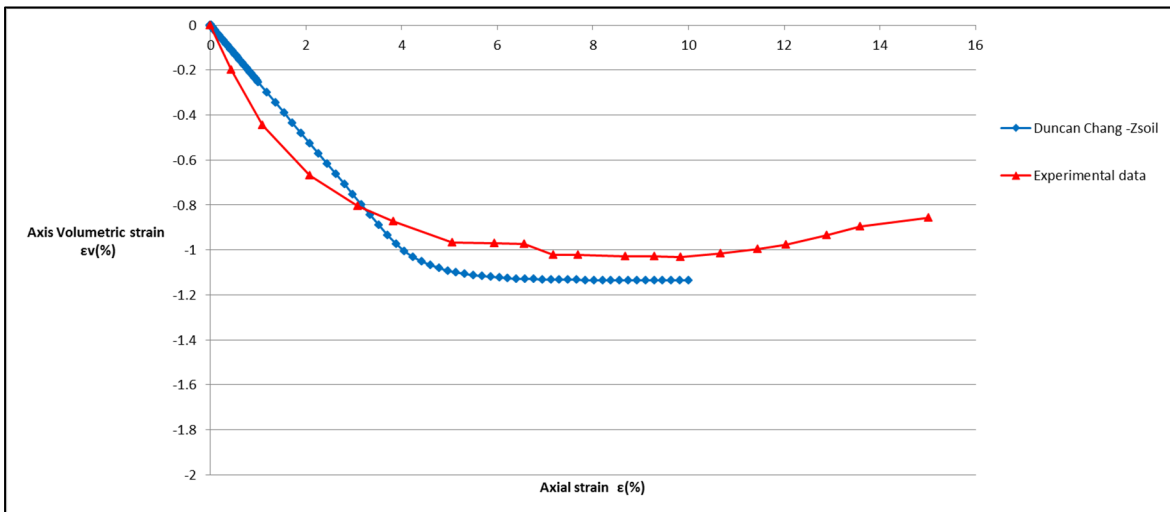


Figure 2.23 Volumetric strain vs axial strain for the Duncan-Chang model in loose sand

2.6 Comparison between constitutive soil models

In this chapter, the data reported from earlier experiments (Brinkgreve, 2007; Schanz et Vermeer, 1996) were used to obtain the parameters for modeling and to compare the different constitutive models, i.e., Duncan–Chang, MC, HS, and HSS in Zsoil and Plaxis. The comparison was conducted by modeling a consolidated drained triaxial test. It can be observed from figures 2.24, 2.25, 2.28, and 2.29 that a simple linear function as in the MC model is not sufficient to describe the soil stress–strain relation completely. The hyperbolic relation implemented in the Duncan–Chang and HS models provide a better fit for the soil stress–strain relation as can be observed in figures 2.24, 2.25, 2.28, and 2.29.

As sand soil is subjected to shear strains, it may expand or contract due to changes in granular interlocking. If the sand soil volume increases, the peak strength will be followed by a reduced shear strength due to reduced density. This lowering of shear strength is known as strain softening. A constant stress–strain relationship is obtained when the expansion or contraction of material ends, and when interparticle bonds are fragmented. When the soil reaches a state where its shear strength and density do not change, then it is said to have reached the critical state (Roscoe, Schofield et Wroth, 1958).

“A loose soil will contract in volume on shearing, and may not develop any peak strength above the critical state” (Roscoe, Schofield et Wroth, 1958). From figures 2.28 and 2.29, it can be observed that the results using the Duncan–Chang, MC, HS, and HSS models correctly show the critical strength.

In dense soil (figures 2.24 and 2.25), contraction is prevented once granular interlocks are formed. To overcome this, additional shear force is required to dilate the soil and peak shear strength can be observed. After reaching the peak strength, the shear strength of soil declines (softening) as the soil expands. Strain softening will continue until the critical state is reached and the volume becomes constant (Roscoe, Schofield et Wroth, 1958).

As can be observed from figures 2.24 and 2.25, the graphs of HS and HSS overlap with each other and provide a better fit when compared with that of MC. For all the models, the peak and critical state coincide and reach the same peak stress. None of the models is able to display the softening phenomenon.

From figures 2.26, 2.27, 2.30, and 2.31, it can be observed that MC, HS, and HSS accurately show the dilatant behavior of soil (Roscoe, Schofield et Wroth, 1958). HS and HSS provide better results as compared with MC for both types of soils. HS and HSS have identical plots in case of dense sand (figures 2.26 and 2.27), whereas in case of loose soil, the plot using HS model is closer to the experimental results by a narrow margin (figures 2.30 and 2.31). Additionally, the Duncan–Chang soil model does not consider dilatancy; hence, a large difference can be observed between the simulation and experimental data for dense sand (figure 2.26).

Overall, the Duncan–Chang, HS, and HSS provide a better fitting stress–strain curve in comparison with MC; however, they fail to account for softening in case of dense sand. For the volumetric strain versus axial strain, both HS and HSS results have acceptable accuracy, which are better than those of MC and Duncan–Chang.

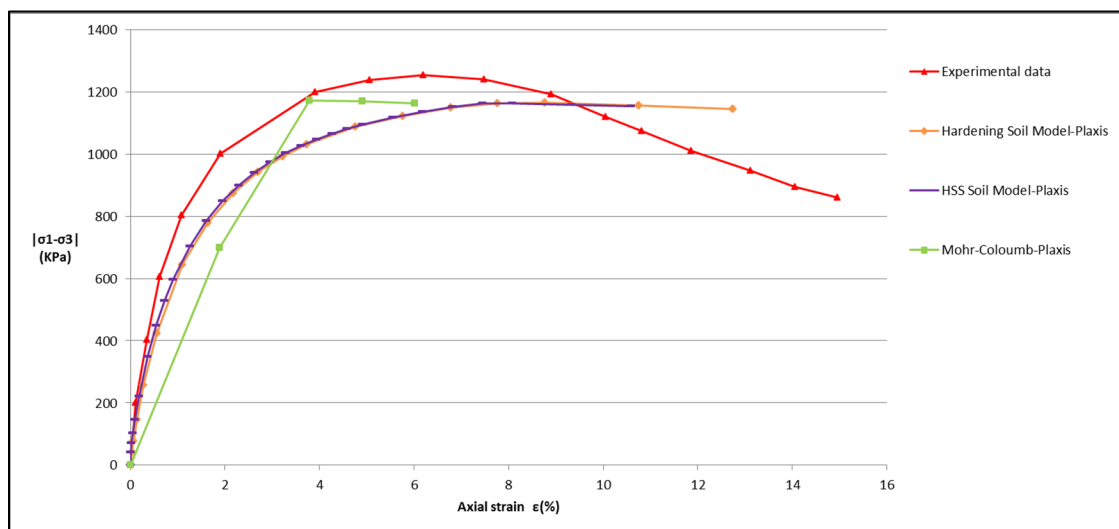


Figure 2.24 Deviatoric stress vs axial strain for the HSS, HS and MC soil models in dense sand modeled by Plaxis

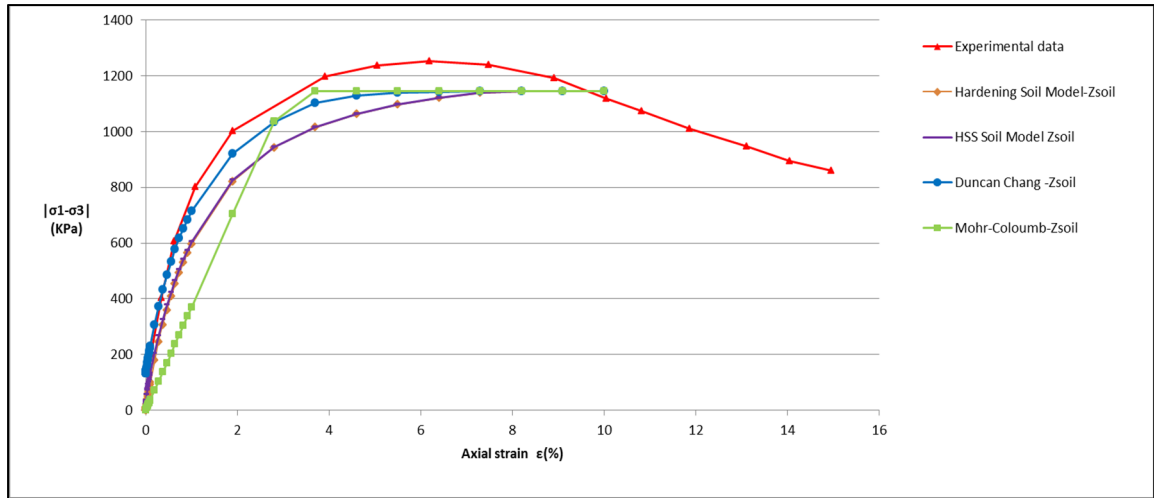


Figure 2.25 Deviatoric stress vs axial strain for the Duncan, HSS, HS and MC soil models in dense sand modeled by Zsoil

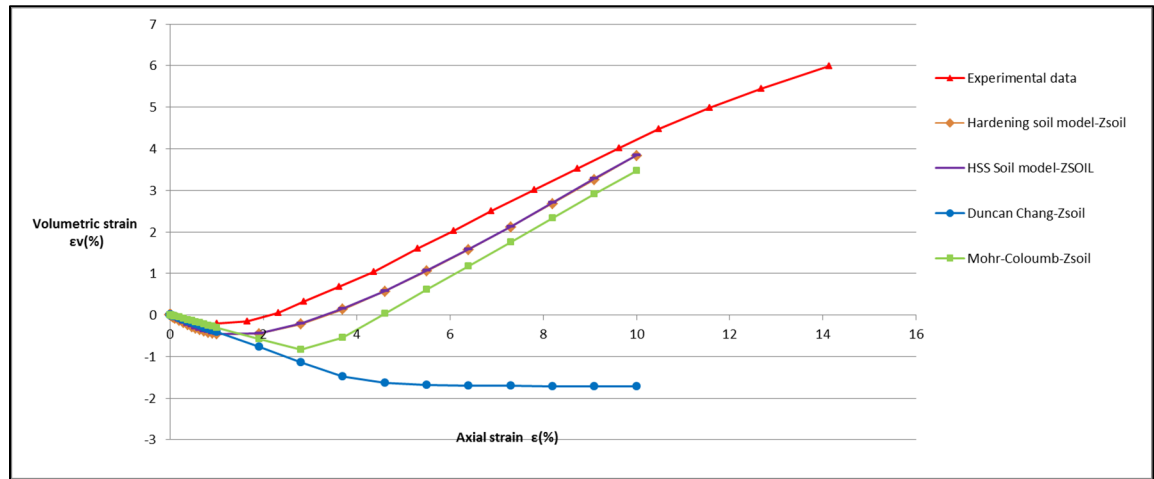


Figure 2.26 Volumetric strain vs axial strain for the Duncan, HSS, HS and MC soil models in dense sand modeled by Zsoil

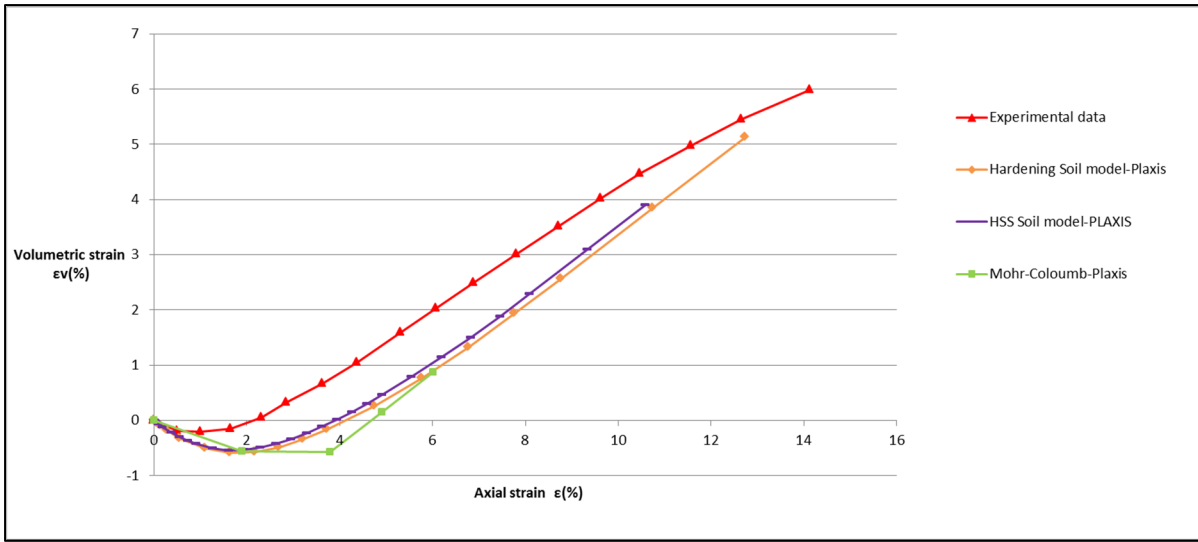


Figure 2.27 Volumetric strain vs axial strain for the HSS, HS and MC soil models in dense sand modeled by Plaxis

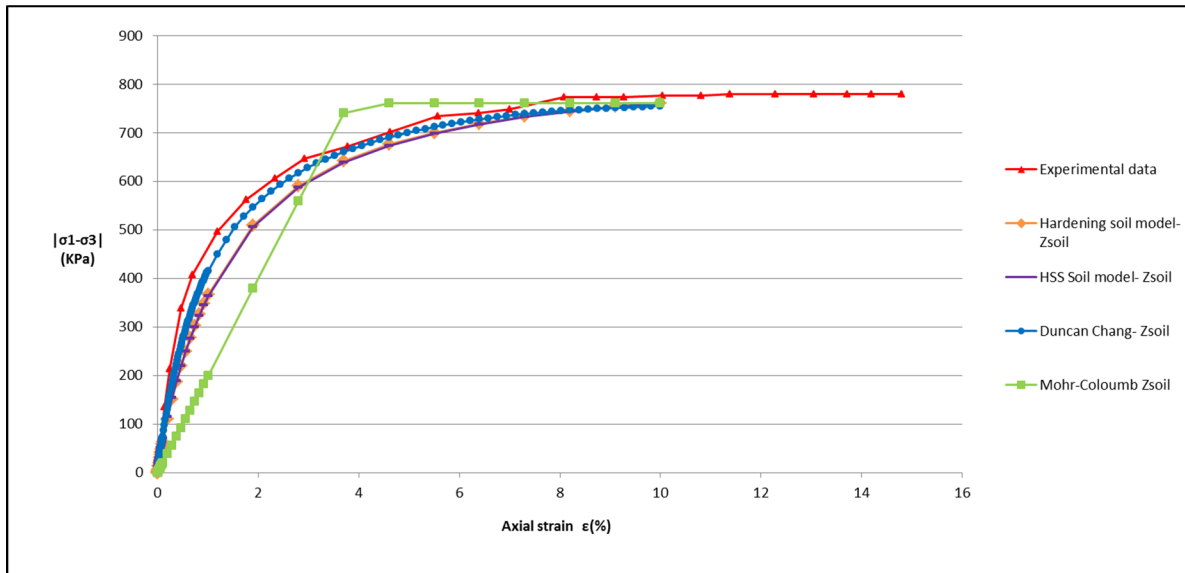


Figure 2.28 Deviatoric stress vs axial strain for the Duncan, HSS, HS and MC soil models in loose sand modeled by Zsoil

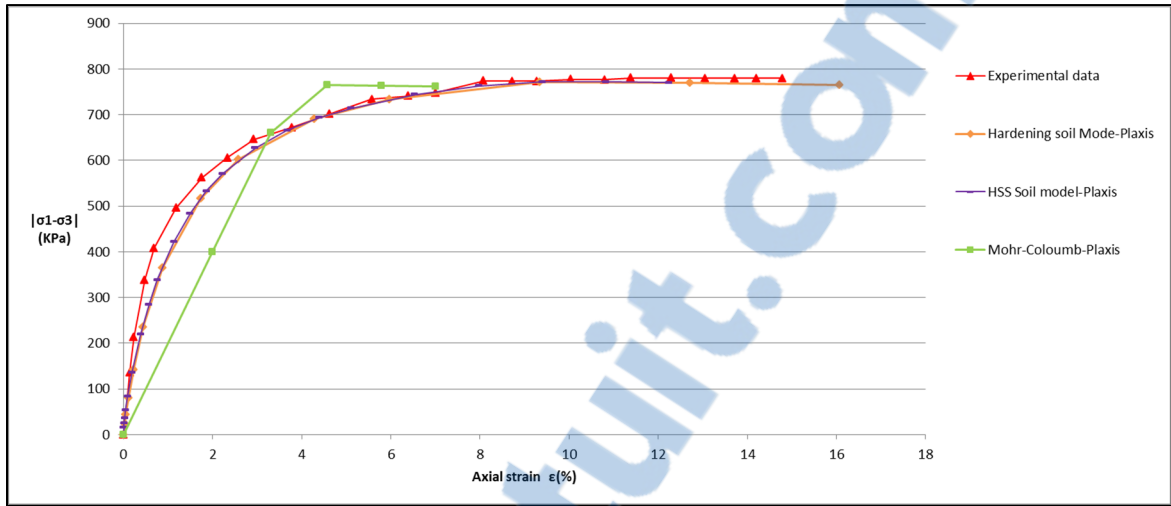


Figure 2.29 Deviatoric stress vs axial strain for the HSS, HS and MC soil models in loose sand modeled by Plaxis

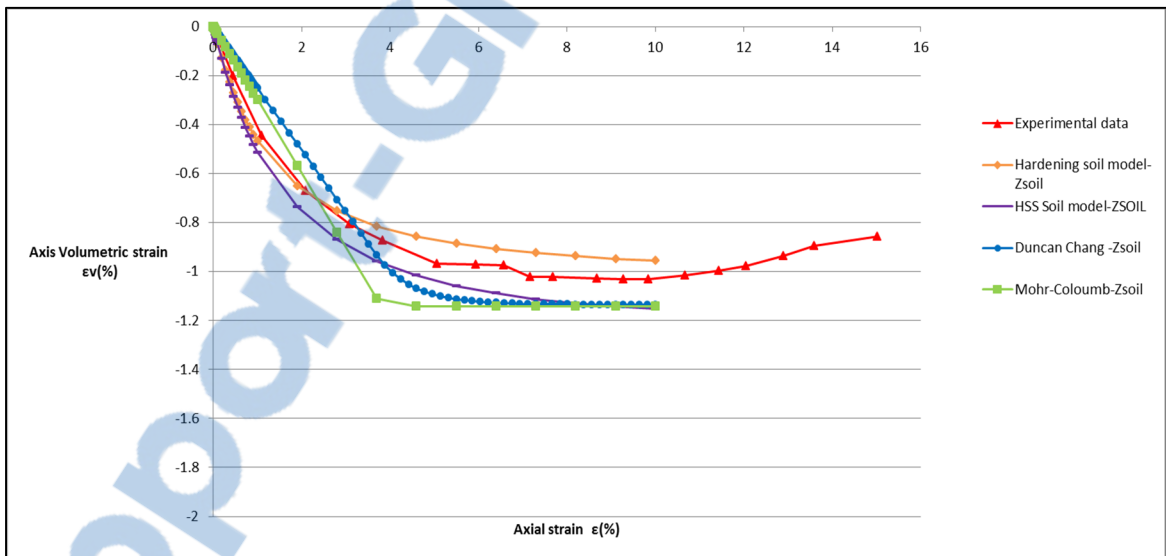


Figure 2.30 Volumetric strain vs axial strain for the Duncan, HSS, HS and MC soil models in loose sand modeled by Zsoil

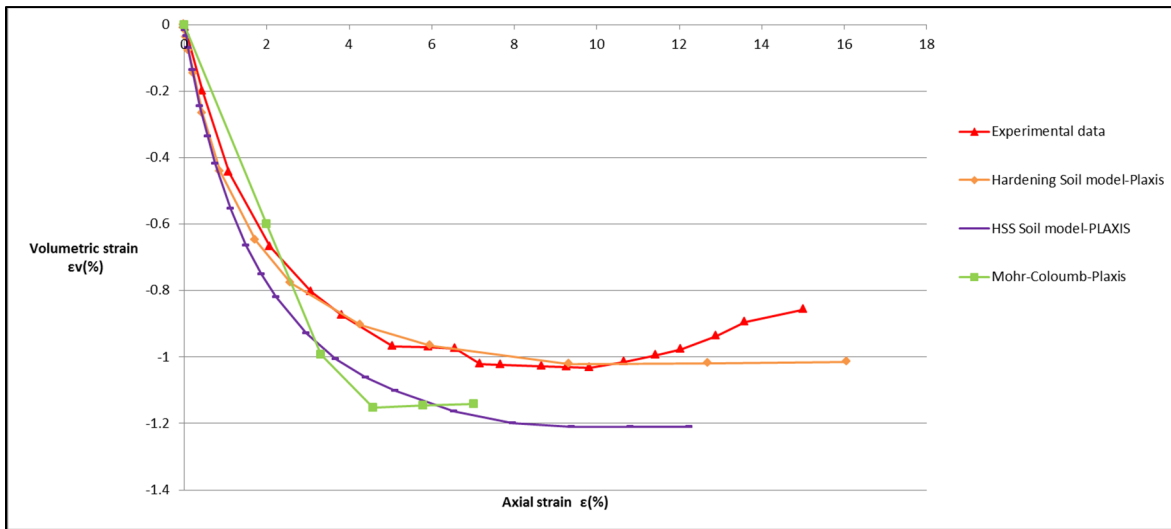


Figure 2.31 Volumetric strain vs axial strain for the HSS, HS and MC soil models in loose sand modeled by Plaxis

2.7 Oedometer test

The test specimen is a disc contained in a stiff metal cylinder. The sample is laid between two porous discs at the top and bottom, where the upper one can move inside the ring (Atkinson, 2007; Craig, 2004). During the test, load is imposed on the specimen along the vertical axis, whereas strain in the other direction (horizontal) is prevented (Lambe et Whitman, 2008). As the soil sample is laterally confined, the radial strains are zero and the axial strain is equal to the volumetric strain (Atkinson, 2007; Lambe et Whitman, 2008).

Pressure can be applied by adding or removing weight on the specimen through a metal loading cap, which is fixed over the top disc (Atkinson, 2007; Craig, 2004). The load is applied through a lever arm and each load is maintained for 24 hours (Das et Sobhan, 2013). Compression of the sample can be studied through successive increases in the applied load; usually, the previous load is doubled (Das et Sobhan, 2013). In the conventional oedometer test apparatus, the porous discs at the top and bottom behave as drains; hence, seepage is vertical and one-dimensional (Atkinson, 2007). Axial strain can be measured by using a dial gauge installed on the loading cap (Atkinson, 2007).

2.8 Finite element modeling

In this section, the oedometer test result is analyzed, and the geometry and boundary conditions used to simulate the model through Plaxis and Zsoil are described.

2.8.1 Geometry of model and boundary conditions in Plaxis

A one-dimensional compression test (Oedometer test) was carried out on the geometry shown in figure 2.32. An axisymmetric model was used. The left and right sides of the model were constrained horizontally, while the bottom side was constrained in the vertical direction. The top boundary was assumed free to move. For simplicity, a 1×1 m unit square was considered to simulate the test. As the soil weight was not considered, the dimensions of the model did not change the results. The initial stress and steady pore pressure were not taken into account. Moreover, the applied load on the top boundary (figure 2.33) was simulated as uniformly distributed loads. The dense soil model was loaded at 50 kPa, 100 kPa, 200 kPa, and 400 kPa, consecutively. Similarly, the loose soil model was loaded at 25 kPa, 50 kPa, 100 kPa, and 200 kPa. After imposing the load, the model was unloaded and reloaded successively (Atkinson, 2007). A fifteen-node triangular element was used (figure 2.34).

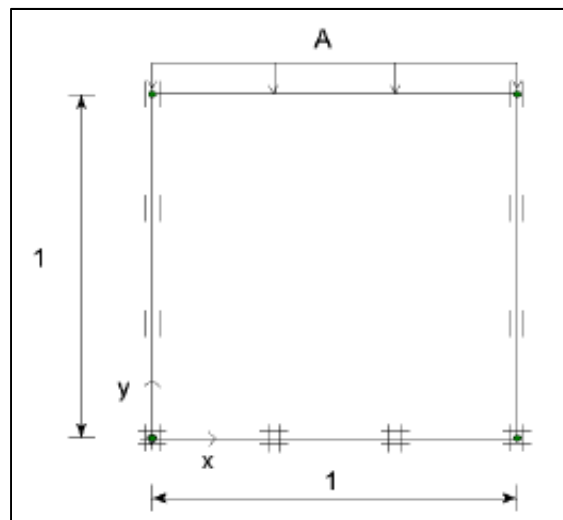


Figure 2.32 Oedometer loading condition



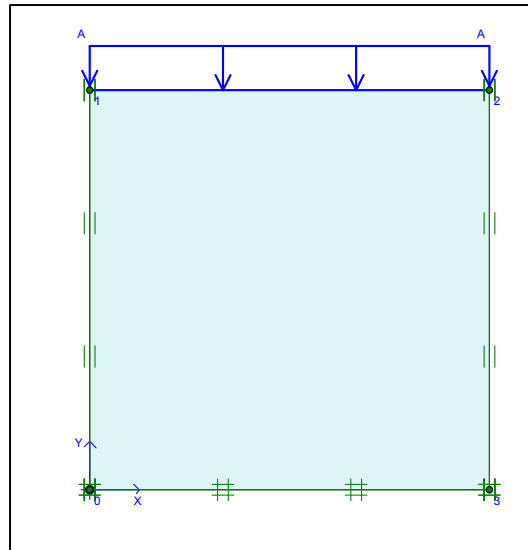


Figure 2.33 Oedometer simulation in Plaxis

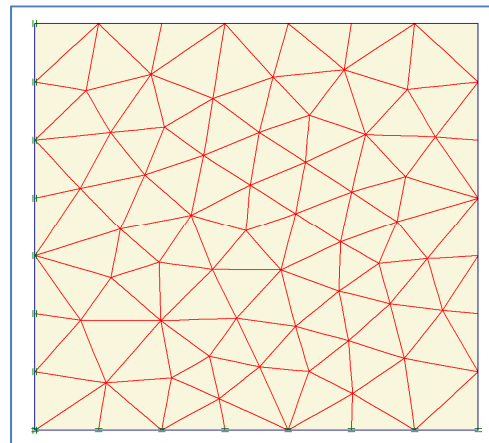


Figure 2.34 Plot of the mesh in Plaxis

2.8.2 Model geometry and boundary conditions in Zsoil

An oedometer test can be simulated by using an axisymmetric geometry of one dimension as shown in figure 2.35 (Brinkgreve, 2007). As the weight was not considered, the model dimensions did not affect the results. The load was imposed on top nodes while the bottom nodes were fixed in the vertical direction. The right and left sides were fixed horizontally. The applied load on the top nodes was defined as a load–time function. A four-node

quadrilateral element was used as shown in figure 2.35 (one element was used). The dense sand was loaded at 50 kPa, 100 kPa, 200 kPa, and 400 kPa, consecutively. Similarly, the loose sand was loaded at 20 kPa, 50 kPa, 100 kPa, and 200 kPa. The model was unloaded and reloaded after each loading step.

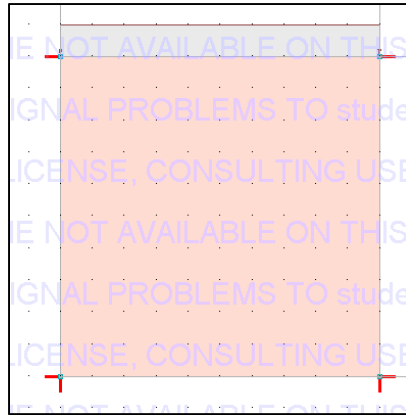


Figure 2.35 Oedometer simulation in Zsoil

2.9 Experimental data

The experimental data on dense and loose Hostun sand available from reports were used to obtain the parameters (Benz, 2007; Brinkgreve, 2007). Oedometer tests were implemented on loose and dense Hostun sand. During the test, samples were loaded, unloaded, and reloaded successively. Figures 2.36 and 2.37 show the results; the vertical stress and axial strain curves ($\sigma_{yy} - \varepsilon_{yy}$) are illustrated. For both graphs, it can be observed that the curves (original loading portions) are concaved upward. Thus, the soil becomes stiffer as the stress level rises (Lambe et Whitman, 2008).

As shown in figures 2.36 and 2.37, the model is unloaded and reloaded consecutively. “The rebound upon unloading is due to the elastic energy stored within individual particles during loading”. However, not all the strain that occurs during the loading can be obtained during subsequent unloading. The strains caused by sliding between particles or due to fracturing of particles are largely irreversible (Lambe et Whitman, 2008). Moreover, experimental data shown through unloading indicate that for stresses less than the maximum stress of the

loading, the soil is much stiffer. As potential sliding between particles occurs during the first loading, the sand exhibits more stiffness during subsequent reloadings. In contrast, the stress–strain curves show the same stiffness when the soil is reloaded to stresses more than the maximum stress of the first loading (Lambe et Whitman, 2008).

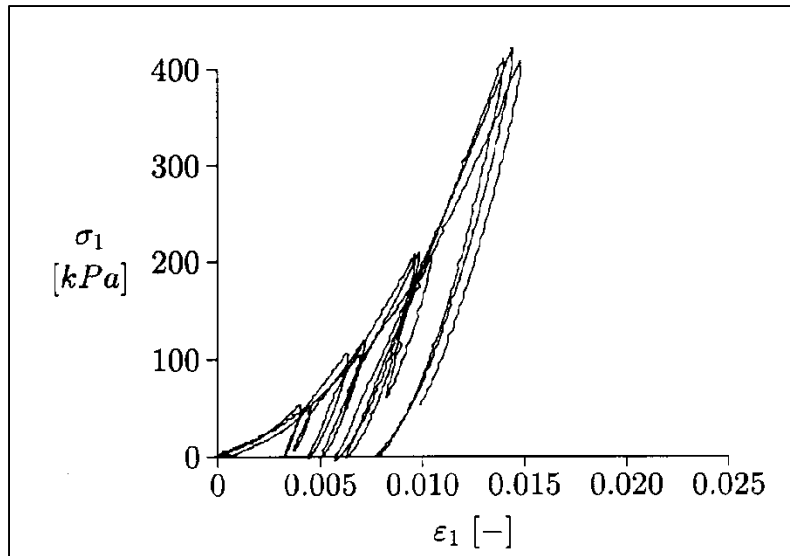


Figure 2.36 Results of oedometer test on dense Hostun sand (Brinkgreve, 2007)

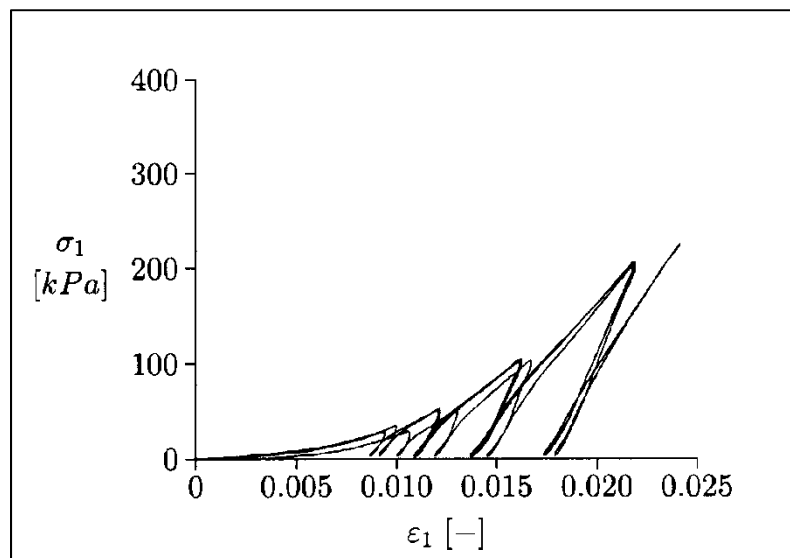


Figure 2.37 Results of oedometer test on loose Hostun sand (Brinkgreve, 2007)

2.10 Application of constitutive soil models

The stress–strain relationship ($\sigma_{yy} - \varepsilon_{yy}$) for Hostun sand was modeled using various constitutive models in Plaxis and Zsoil. To determine the most appropriate soil constitutive model, the results of Zsoil and Plaxis for various soil models were compared with experimental data as shown in figures 2.36 and 2.37.

2.10.1 Duncan–Chang Model

Numerical analyses implemented using the Duncan–Chang model are shown in figures 2.38 and 2.39. The Duncan–Chang model is a non-linear elastic model based on a hyperbolic relationship between stress and strain (Duncan, Wong et Mabry, 1980). This type of constitutive model was formulated in order to depict an appropriate and fit result on the data from different laboratory experiments (e.g., triaxial or oedometer tests) (Duncan, Wong et Mabry, 1980). However, as mentioned in chapter 1, some limitations and restrictions, such as plasticity and dilatancy can be observed in this model (Seed, Duncan et Idriss, 1975).

Two different material sets (dense Hostun sand and loose Hostun sand) were used. The properties of these materials are listed in table 2.7. The results shown in figures 2.38 and 2.39 do not indicate a good agreement between the experimental test and simulation. The experimental results exhibit a permanent strain after each loading and unloading (deformation results in irreversible plastic strain), whereas the Duncan–Chang simulation displays elastic behavior. For the simulation conducted using the Duncan–Chang model, unloading and reloading curves coincide with the loading curve during different loading steps.

From figures 2.38 and 2.39, it can be observed that the simulation and experimental results for loose and dense sand are not compatible. The Duncan–Chang model cannot provide a satisfactory prediction behavior of the stress–strain relationship ($\sigma_{yy} - \varepsilon_{yy}$) under loading and unloading cycles.

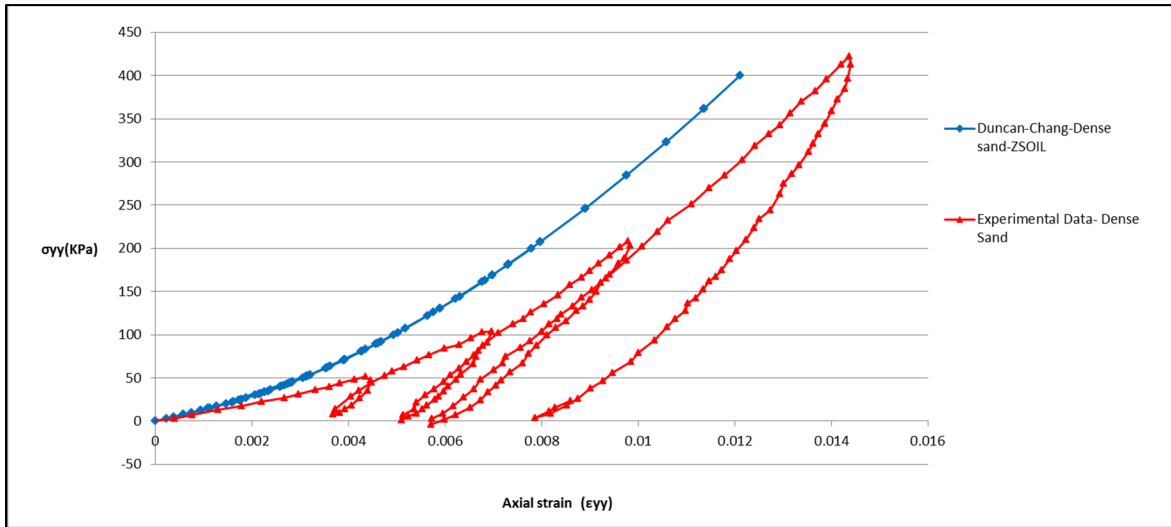


Figure 2.38 Vertical stress vs axial strain for the Duncan-Chang model in dense sand

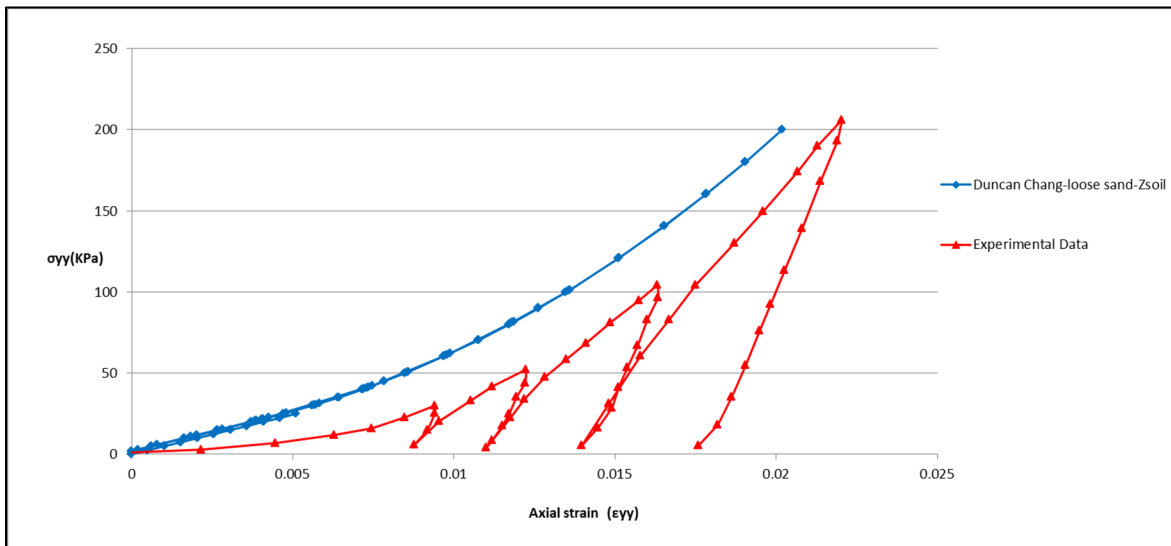


Figure 2.39 Vertical stress vs axial strain for the Duncan-Chang model in loose sand

2.10.2 Hardening soil model

In this section, the HS model is used to simulate the oedometer test. A summary of the HS model parameters for Hostun sand is presented in table 2.5. For the non-linear original loading portions shown in figures 2.40 and 2.41 (loose and dense sand), a good agreement is shown between the simulation results conducted using Plaxis and Zsoil, and experimental data. For ease of understanding, a schematic diagram of loading, unloading, and reloading is shown in figure 2.42.

The experimental data shown in figures 2.42, 2.36, and 2.37 indicate that the unloading behavior is concave upward while reloading is concaved downward. As the unloading and reloading curves (figures 2.40 and 2.41) are different, a hysteresis loop can be observed (figure 2.42, point A to B and B to A). Furthermore, for the loose Hostun sand experimental data (figure 2.41), the reloading curve cannot intersect the unloading curve at the maximum stress level that was reached during original loading (figure 2.42, points A' and A). In addition, the reloading curve (figure 2.41) exhibits more strain than the original loading curve at the same stress level (refer to the schematic diagram, figure 2.42, points A and A').

In contrast, the HS model considers an elastic material behavior during unloading and reloading (figures 2.40 and 2.41), and the reloading curve can intersect the unloading curve at the maximum stress level that was reached during original loading (figures 2.40 and 2.41). In other words, points A and A' are concurrent. In the HS model, the unloading and reloading processes are approximately linear, while the strain range in which the soil can behave as elastic is negligible and limited (Obrzud et Eng, 2010).

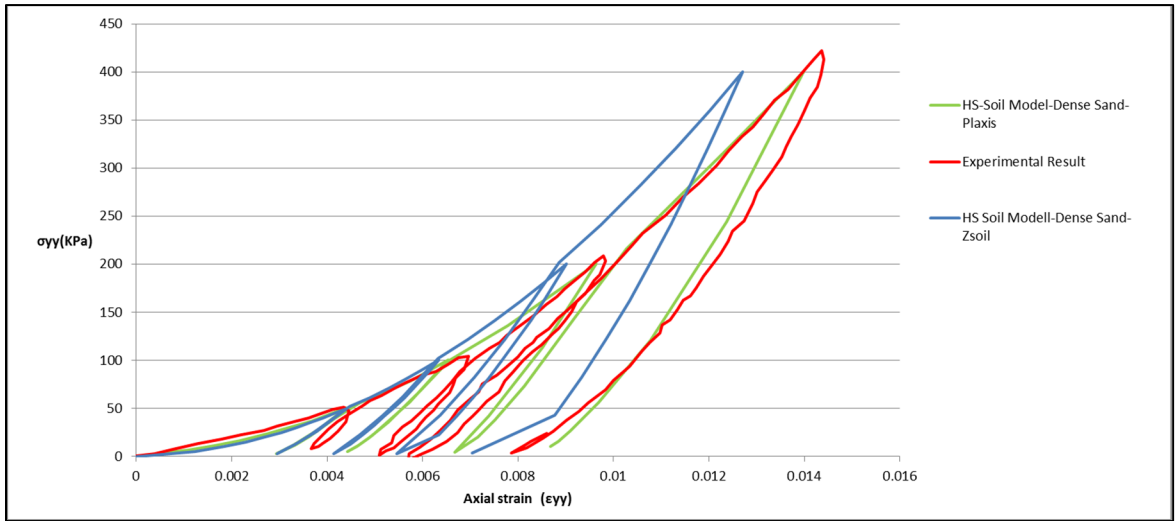


Figure 2.40 Vertical stress vs. axial strain for the HS model in dense sand

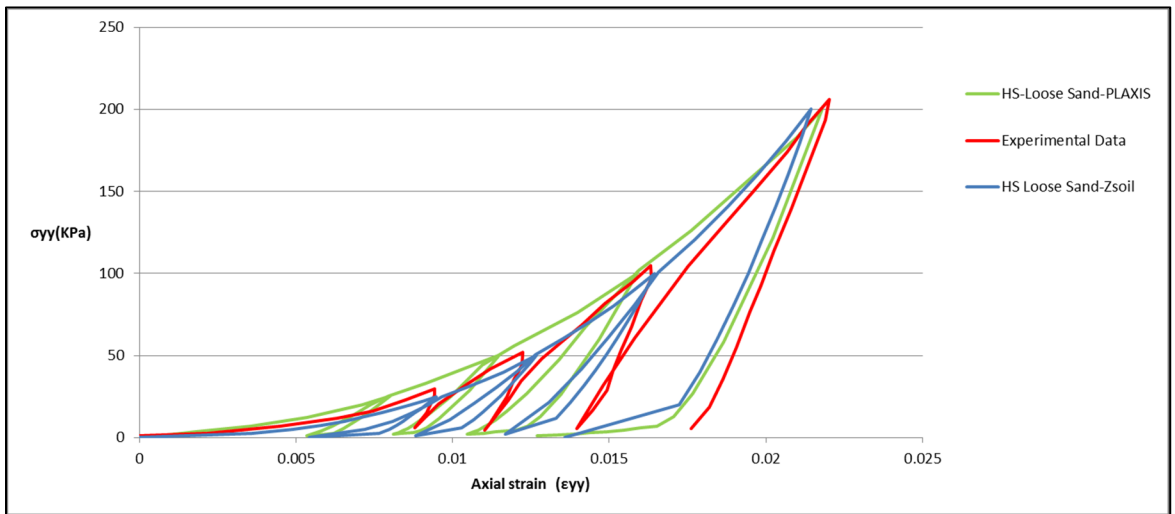


Figure 2.41 Vertical stress vs. axial strain for the HS model in loose sand

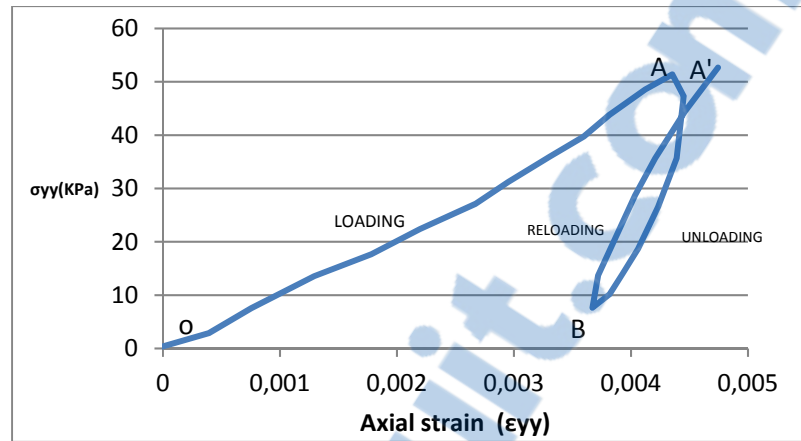


Figure 2.42 Unloading and reloading for dense Hostun sand

2.10.3 Hardening small strain constitutive soil model

In this section, the HSS model is studied to simulate the soil behavior in the oedometer test. For HSS modeling, two extra parameters are required apart from those required in the HS model; their values are indicated in table 2.6. Figures 2.43 and 2.44 show the results of the simulation implemented using the HSS model and experimental results. For the non-linear original loading portion, a good agreement is observed between Plaxis and Zsoil results.

Moreover, hysteretic soil behavior can be observed in the simulation generated using the HSS soil model. The HSS model as an advanced version of the HS soil model takes into account small strain stiffness; hence, it can produce hysteretic soil behavior under different cyclic loading (Obrzud et Eng, 2010).

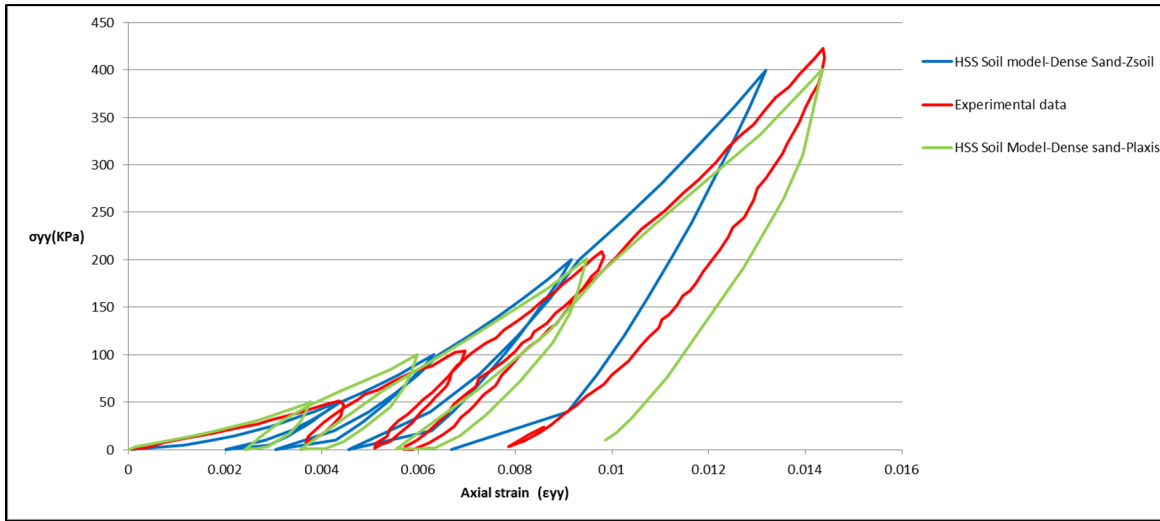


Figure 2.43 Result of oedometer test (HSS Model) on dense Hostun sand, vertical stress vs. axial strain

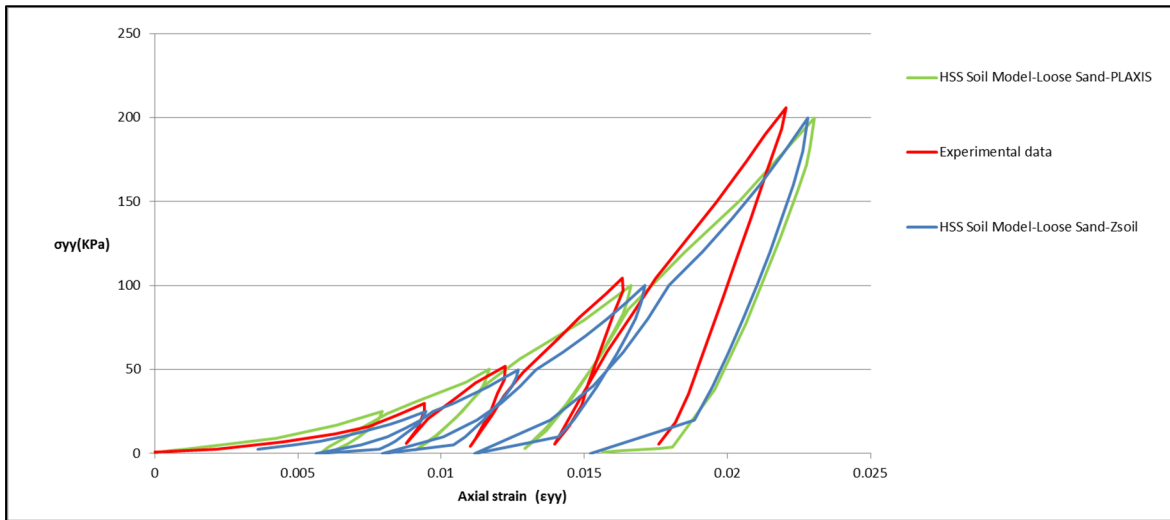


Figure 2.44 Result of oedometer test (HSS Model) on loose Hostun sand, vertical stress vs. axial strain

2.11 Comparison between constitutive soil models

In this section, the data from previous experiments available in reports (Benz, 2007; Brinkgreve, 2007) were used to obtain the parameters for modeling and to compare the different constitutive models, i.e., the Duncan–Chang, HS, and HSS in Zsoil and Plaxis. The comparison was conducted by simulating an oedometer test. It can be observed from figures 2.45, 2.46, 2.47, and 2.48 that a non-linear elastic soil model, such as the Duncan–Chang model is not sufficient to predict the soil stress–strain relation (vertical stress vs. axial strain) completely. The experimental results exhibit a permanent strain after each loading and unloading; whereas, the Duncan–Chang model displays an elastic behavior and deformation that do not comprise irreversible plastic strain.

Furthermore, for the simulation implemented using the Duncan–Chang model, unloading on the stress–strain curve coincides with the loading during different loading steps. An accurate simulation needs the application of advanced constitutive models that can estimate the stress–strain relationship more precisely than the simple non-linear elastic model (Duncan–Chang model). Hence, the HS and HSS soil models have been studied. It is shown that both these models can reproduce the non-linear original loading portion (figures 2.45 to 2.48). Moreover, the HS and HSS models can differentiate between loading and unloading.

However, the HS standard model cannot generate hysteretic soil behavior, which can be observed during cyclic loading in the experimental test (figure 2.45). In contrast, the results (figure 2.45) indicate that the HSS can produce more precise and consistent estimation of the stress–strain analysis (simulating hysteretic soil behavior), which can be used for dynamic and unloading problem calculations, e.g., excavations (Obrzud et Eng, 2010).

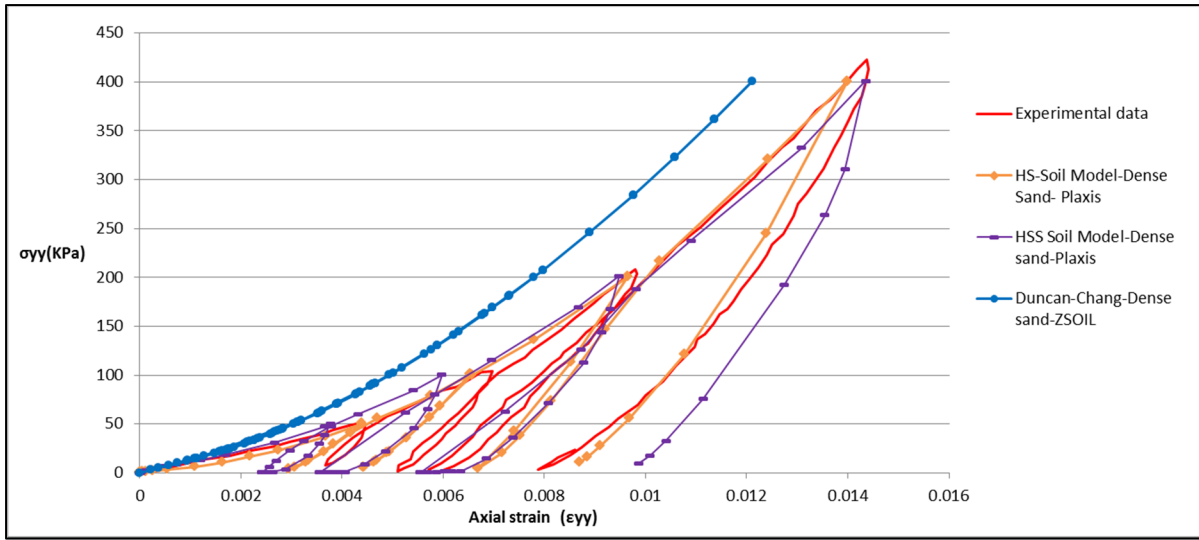


Figure 2.45 Vertical stress vs axial strain for the HSS, HS and Duncan-Chang soil models in dense sand modeled by Plaxis

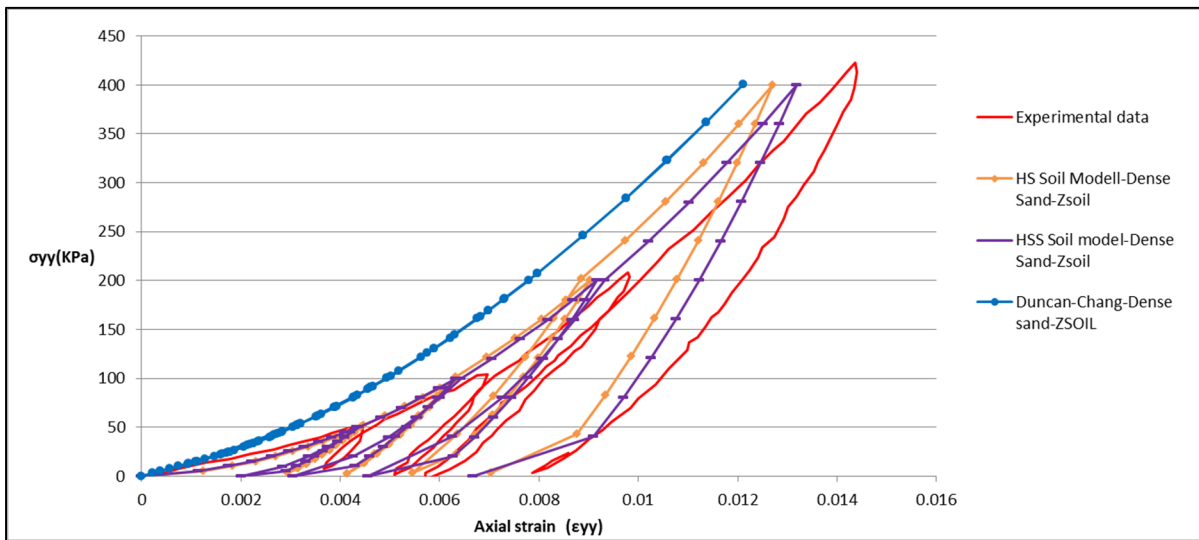


Figure 2.46 Vertical stress vs axial strain for the HSS, HS and Duncan-Chang soil models in dense sand modeled by Zsoil

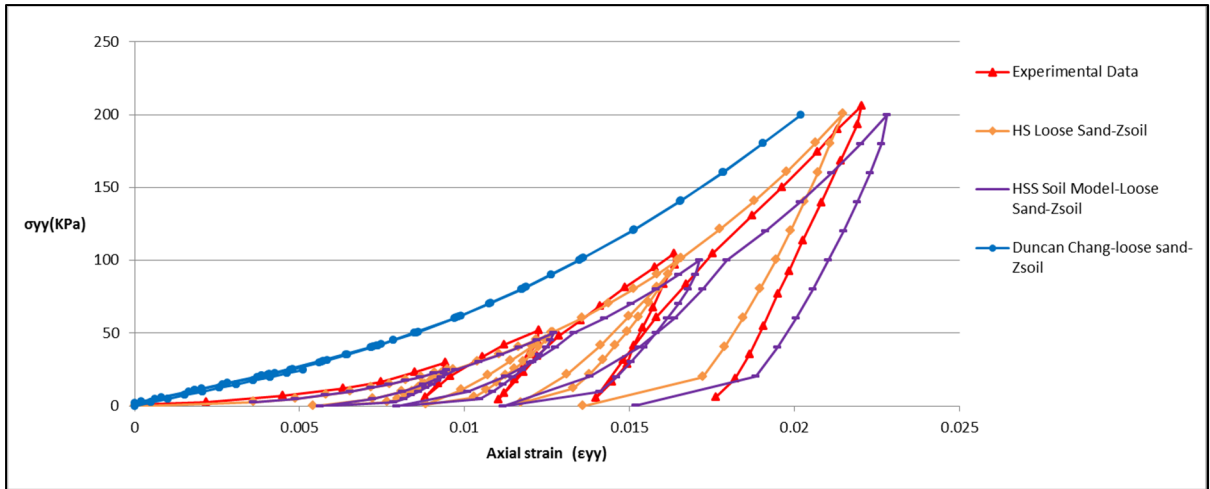


Figure 2.47 Vertical stress vs axial strain for the HSS, HS and Duncan-Chang soil models in loose sand modeled by Zsoil

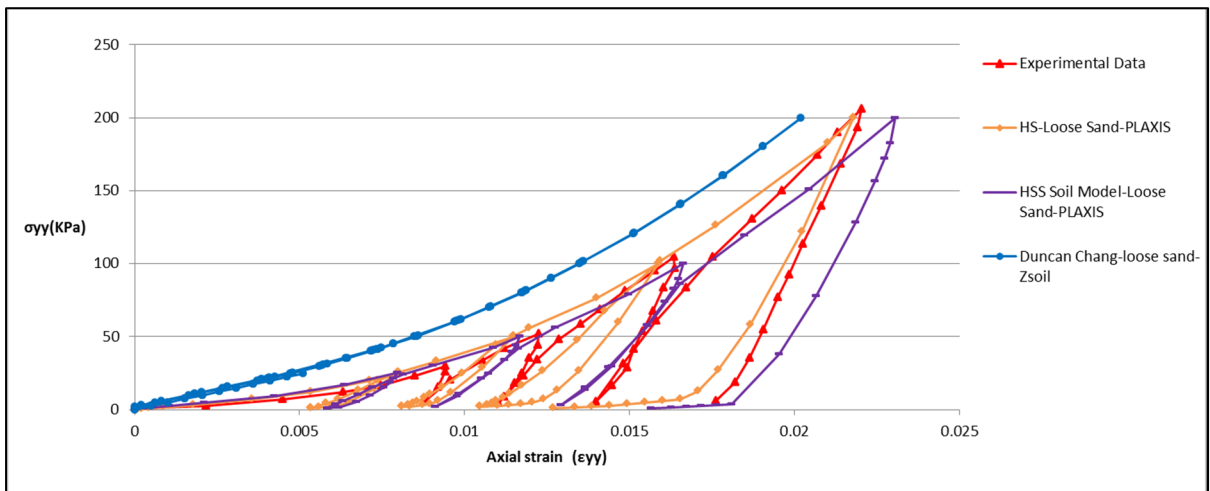


Figure 2.48 Vertical stress vs axial strain for the HSS, HS and Duncan-Chang soil models in loose sand modeled by Plaxis

2.12 Updated mesh results for triaxial test

“The influence of the geometry change of the mesh at equilibrium condition” is not considered in conventional finite element analysis (Brinkgreve, 2007). This assumption can be a good estimation when the studied problem has small deformation (generally, for most engineering problems, this case is acceptable). Nevertheless, in some cases where large deformation occurs, it is essential to adjust the mesh because a Lagrangian kinematic formulation is used (Brinkgreve, 2007).

It is important to take into account some specific features when the large deformation theory is used. Supplementary terms should be incorporated in the stiffness matrix to model the influence of large deformation on the finite element equations. Furthermore, a process needs to be included to simulate the changes in stress when finite element rotations happen. In addition, as the calculation proceeds, the finite element mesh has to be updated (Brinkgreve, 2007).

As illustrated in section 2.4, the soil has settled 10%. To consider the effect of large deformation, updating of the mesh is considered. This can be simulated in Zsoil by the UPDATE mesh option. For the triaxial test, the effect of using this option was investigated and a comparison was made between the two different calculation methods (with update mesh and without update mesh). The results are shown in figures 2.49 to 2.64. It can be observed that the update mesh results for loose soil (HS, HSS, and MC soil models) exhibit smaller volumetric strain ($\varepsilon_v - \varepsilon_a$) in comparison to calculations without update mesh. Furthermore, for the deviatoric stress versus axial strain, the update mesh calculations show a smaller value for the maximum shear stress ($\sigma_1 - \sigma_3$).

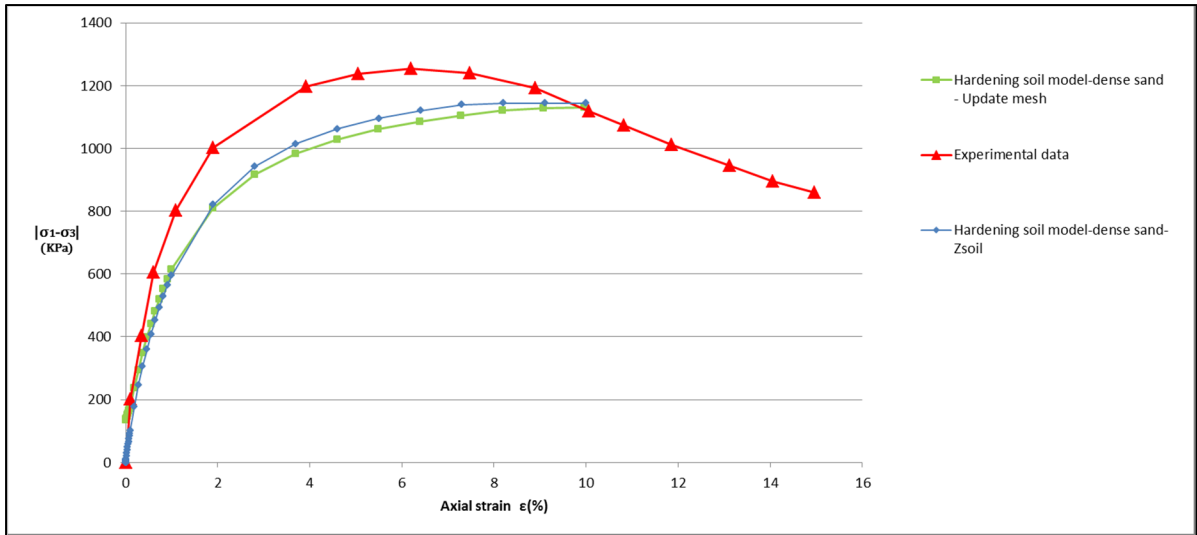


Figure 2.49 Deviatoric stress vs axial strain for the Hardening soil model in dense sand

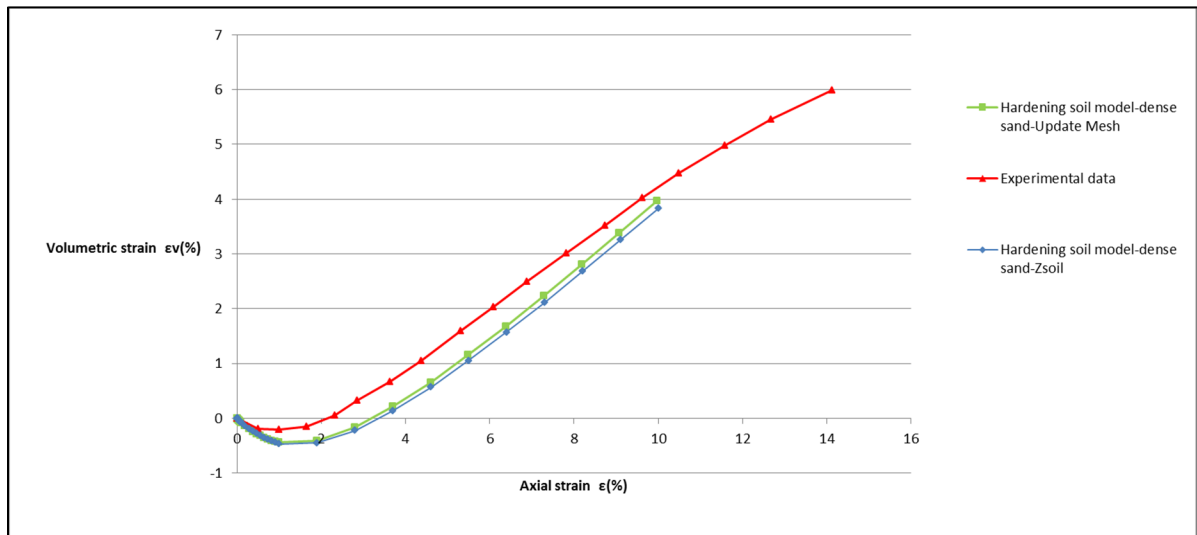


Figure 2.50 Volumetric strain vs axial strain for the Hardening soil model in dense sand

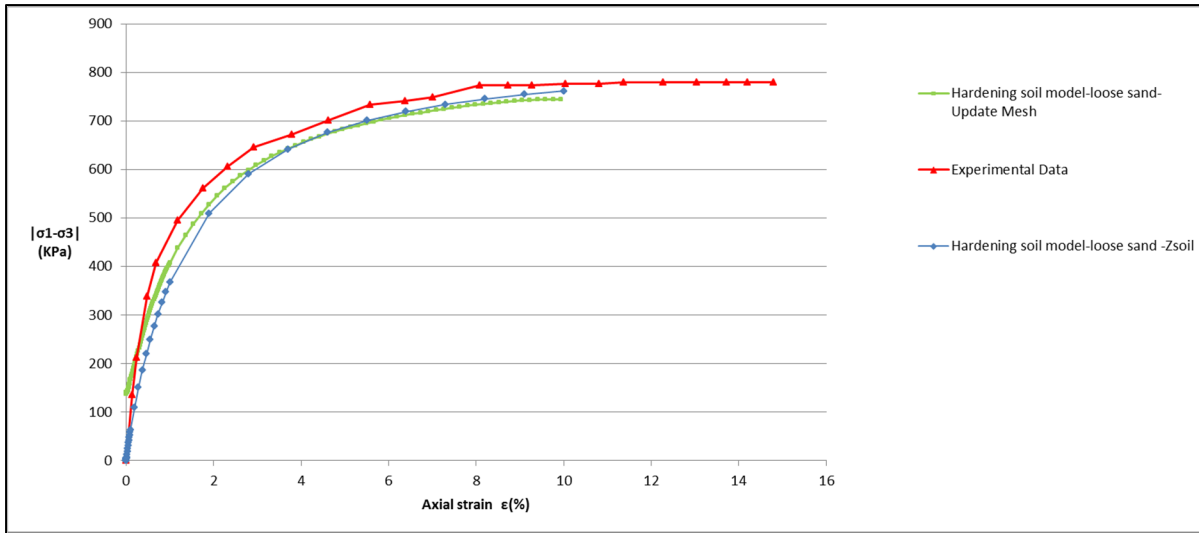


Figure 2.51 Deviatoric stress vs axial strain for the Hardening soil model in loose sand

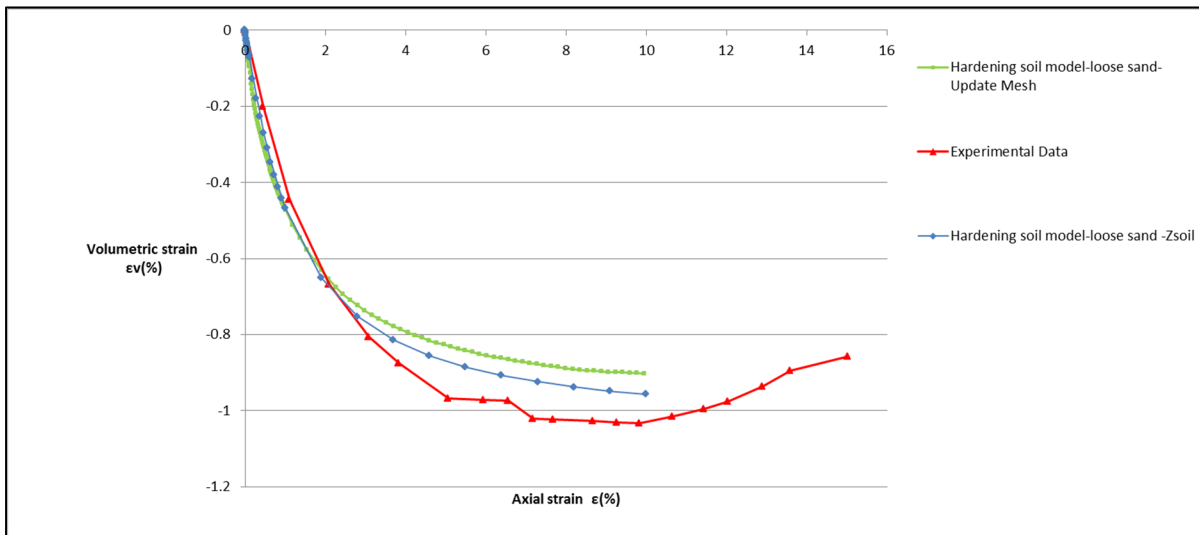


Figure 2.52 Volumetric strain vs axial strain for the Hardening soil model in loose sand

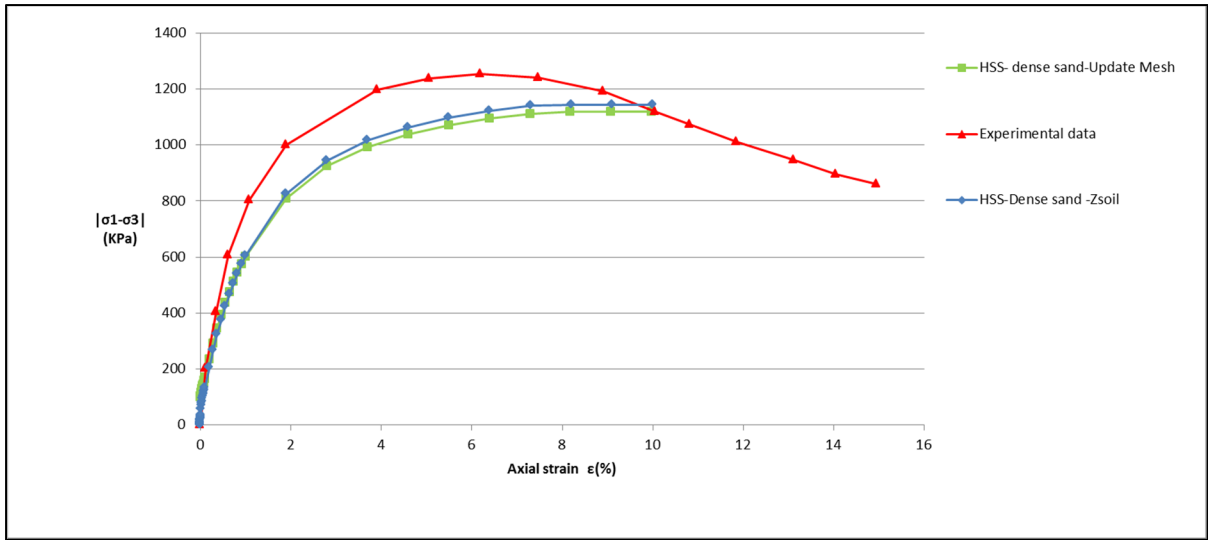


Figure 2.53 Deviatoric stress vs axial strain for the Hardening small strain soil model in dense sand

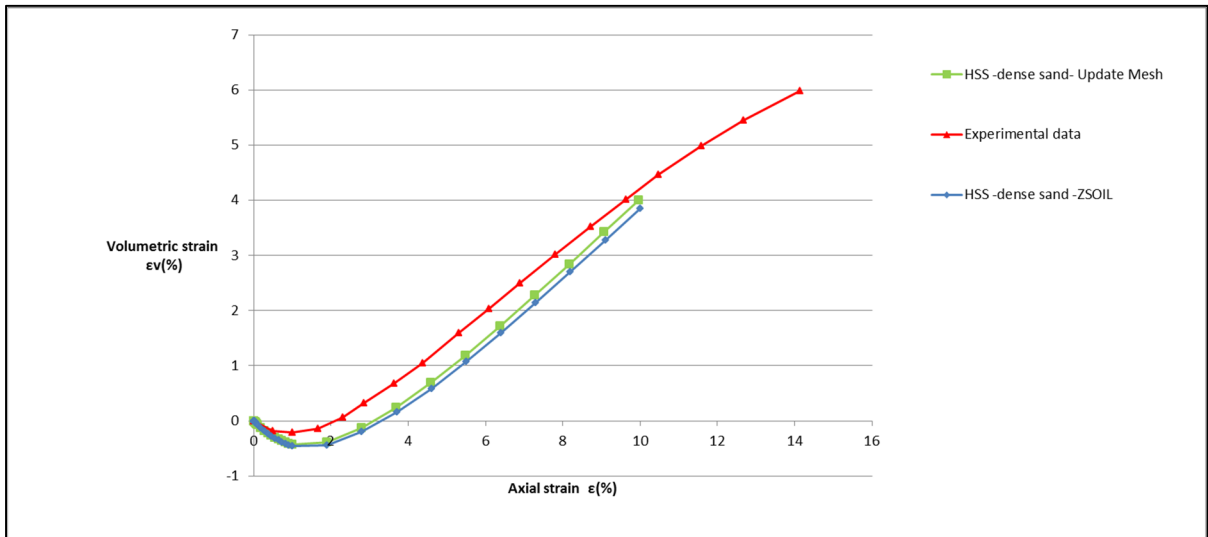


Figure 2.54 Volumetric strain vs axial strain for the Hardening small strain soil model in dense sand

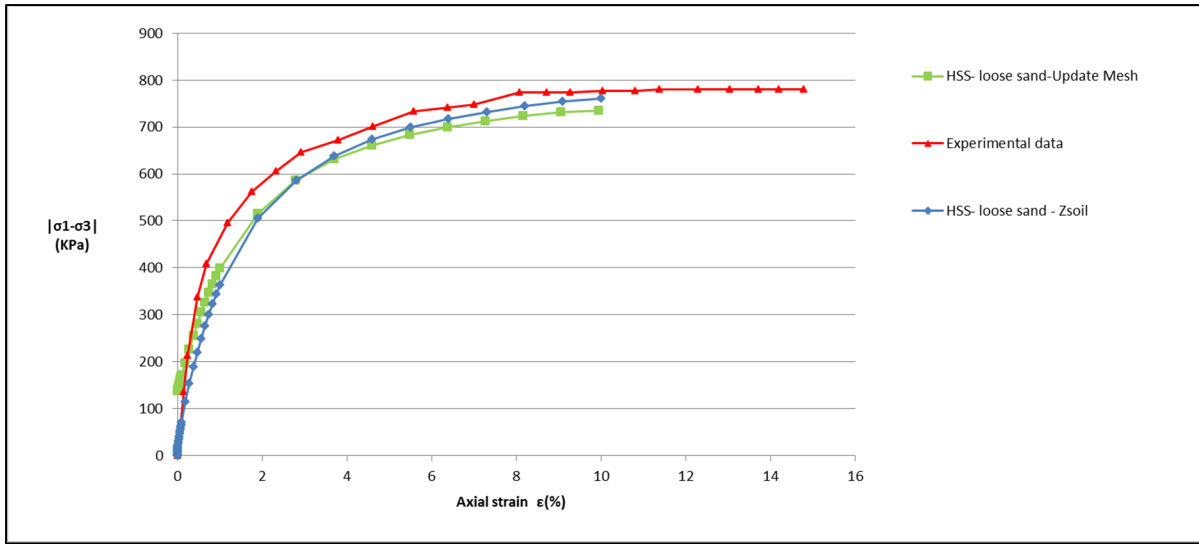


Figure 2.55 Deviatoric stress vs axial strain for the Hardening small strain soil model in loose sand

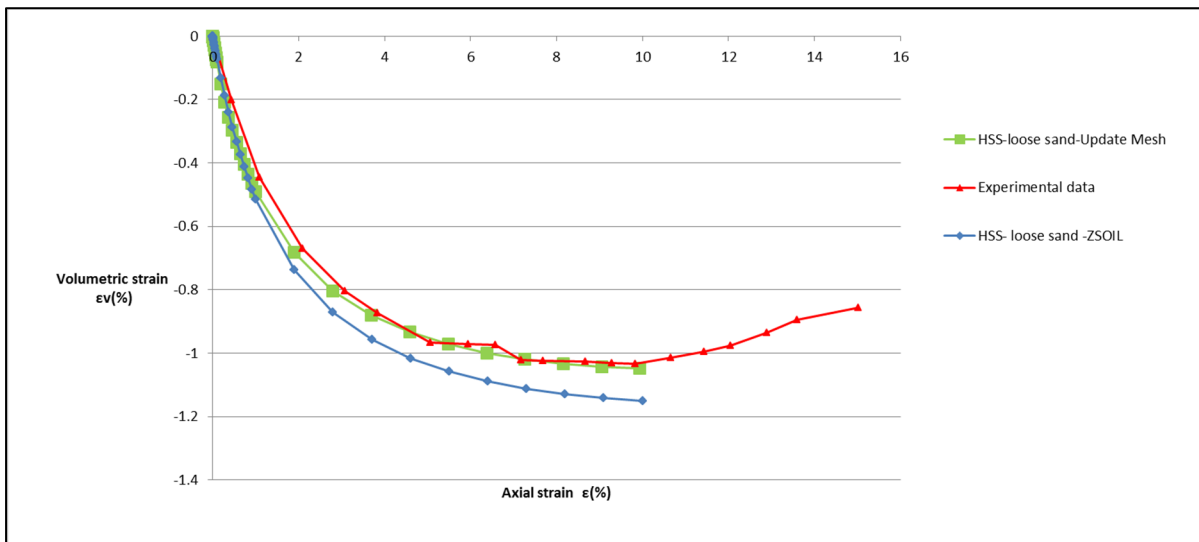


Figure 2.56 Volumetric strain vs axial strain for the Hardening small strain soil model in loose sand

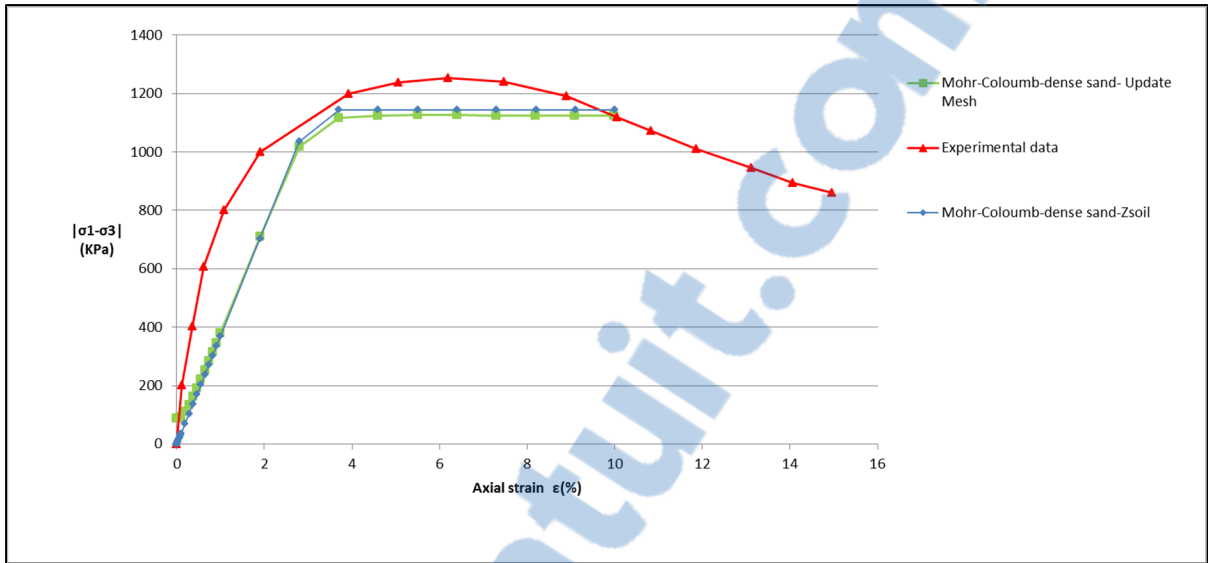


Figure 2.57 Deviatoric stress vs axial strain for the Mohr–Coloumb model in dense sand

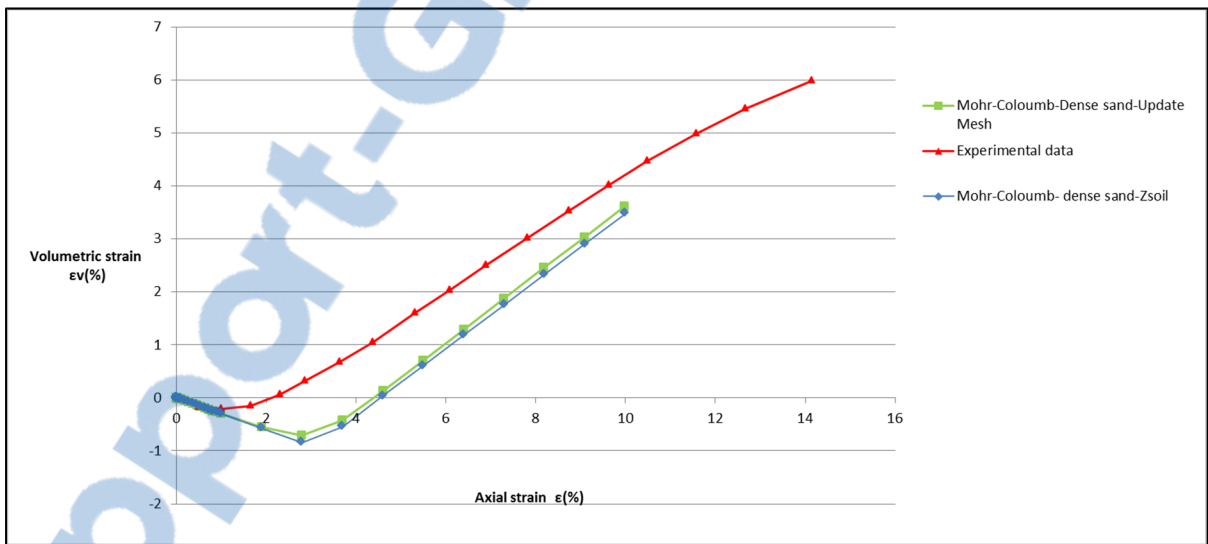


Figure 2.58 Volumetric strain vs axial strain for the Mohr–Coloumb model in dense sand

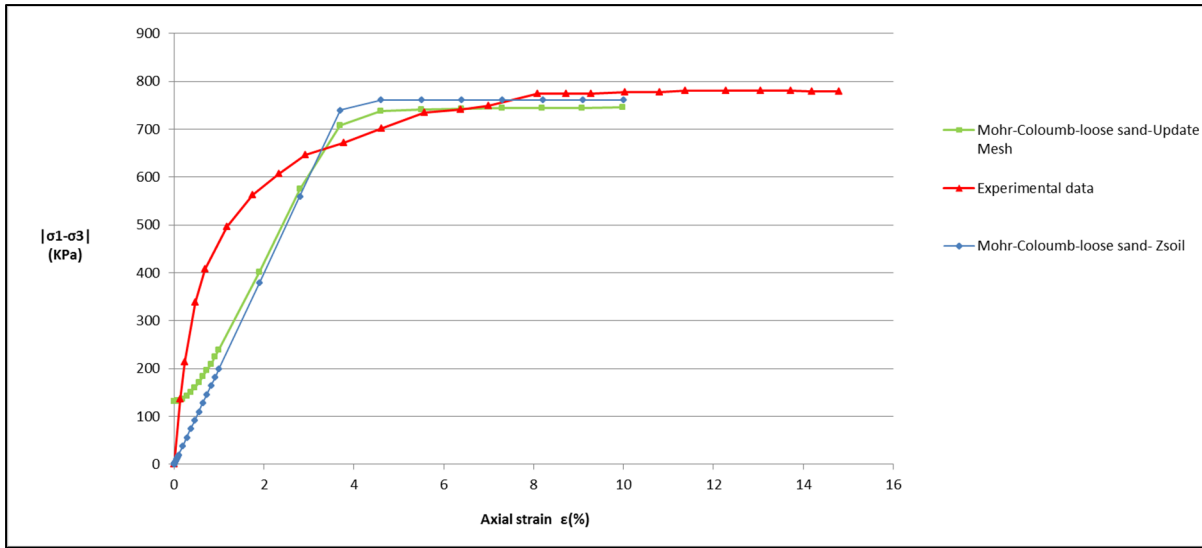


Figure 2.59 Deviatoric stress vs axial strain for the Mohr-Coloumb model in loose sand

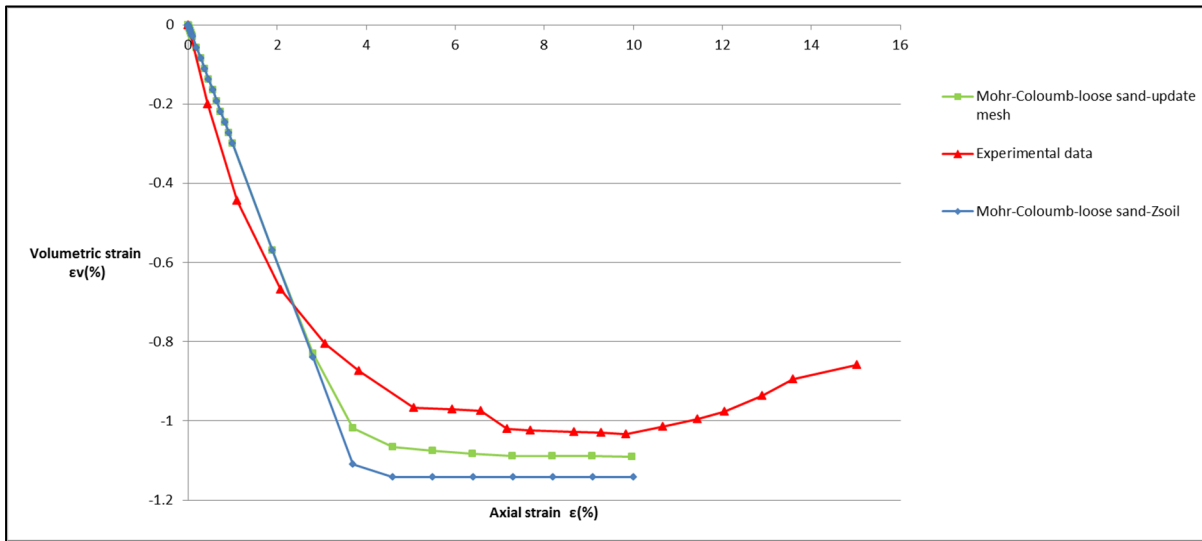


Figure 2.60 Volumetric strain vs axial strain for the Mohr-Coloumb model in loose sand

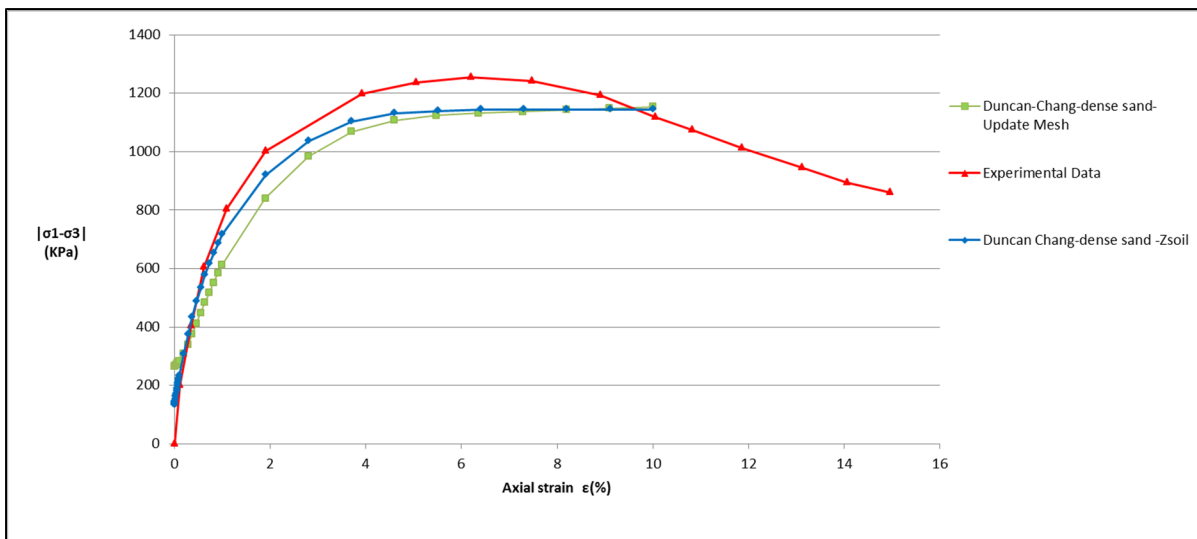


Figure 2.61 Deviatoric stress vs axial strain for the Duncan–Chang model in dense sand

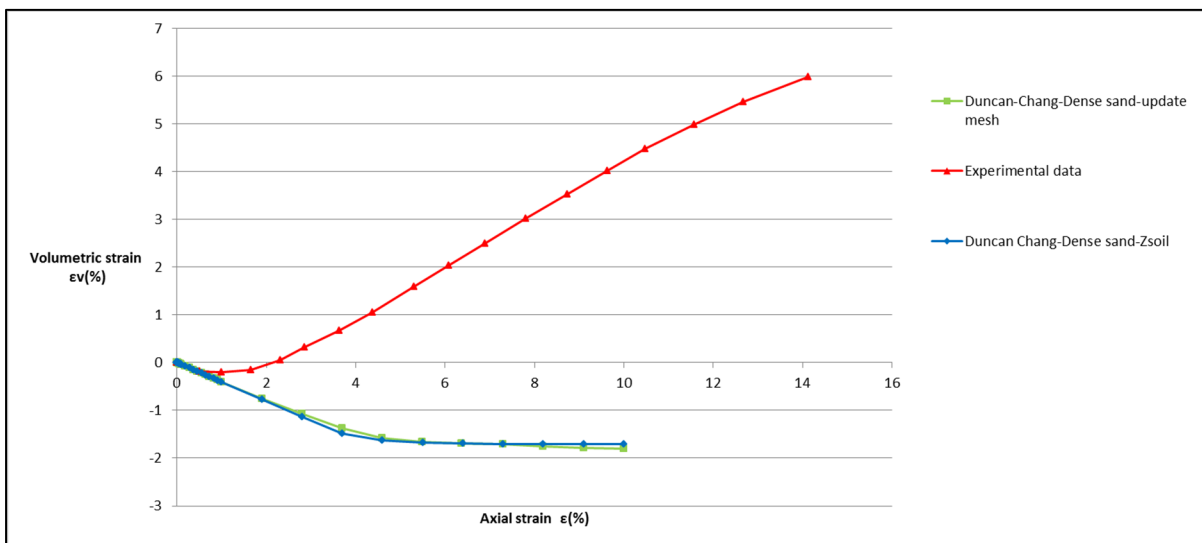


Figure 2.62 Volumetric strain vs axial strain for the Duncan–Chang model in dense sand

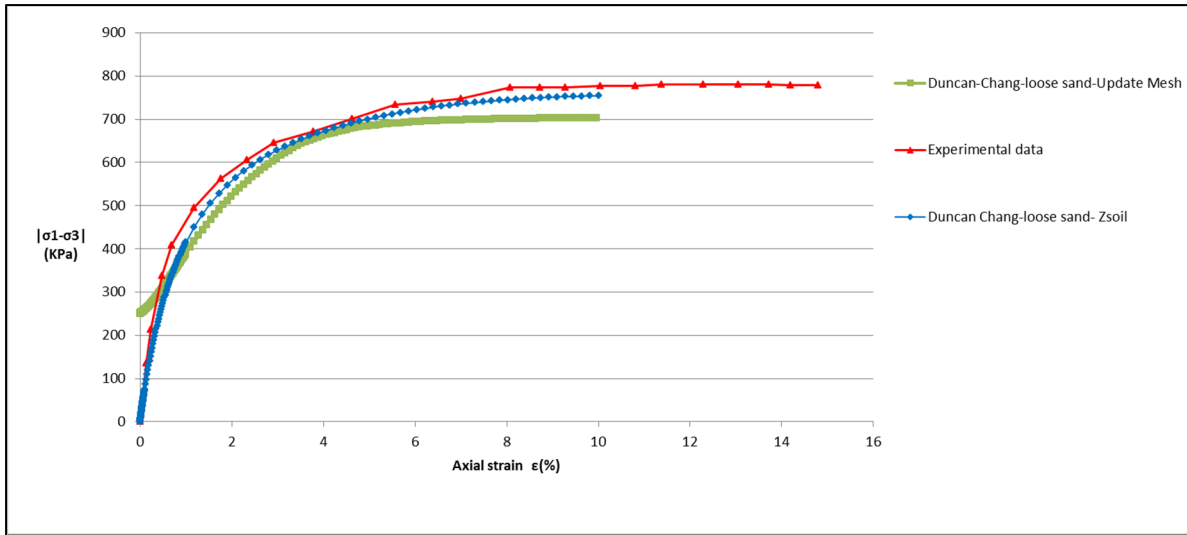


Figure 2.63 Deviatoric stress vs axial strain for the Duncan–Chang model in loose sand

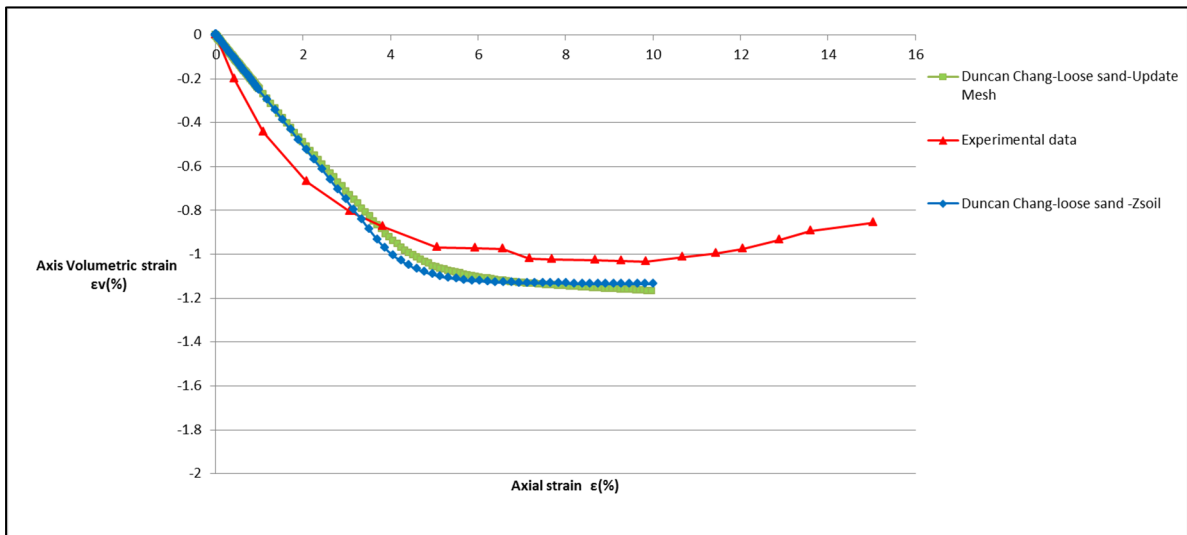


Figure 2.64 Volumetric strain vs axial strain for the Duncan–Chang model in loose sand

CHAPTER 3

NUMERICAL SIMULATIONS FOR DAM-X

3.1 Introduction

In this chapter, various constitutive soil models, namely, the Hyperbolic (Duncan-Chang 1970), MC, and HS are applied to analyze the construction and watering stages of the Dam-X. The Dam-X was recently constructed in Quebec, Canada, with 110 m height and 514 m crest length. The computations are conducted using finite element commercial software. In this study, 2D static analyses based on the plane-strain condition are assumed. The plane-strain assumption is acceptable for long dams (Feizi-Khankandi et al., 2009).

The monitoring program, which is necessary for the safety of the earth dam, is extensively emphasized. The monitoring provides information for a comprehensive understanding of the ongoing dam performance (Stateler, 2013). In this chapter, the simulation results and measured data are compared in order to determine the applicability of various constitutive models for rockfill dam simulations.

3.2 Asphalt core dam

The history of earth dams constructed using different bituminous core types, hand-placed and machine-placed, from 1948 to 1991, has been mentioned in ICOLD Bulletin 84 (Stateler, 2013). In 1962, the first earth dam with a machine compacted asphalt core was constructed in Germany (Höeg et al., 2007). Since 1962, more than 100 asphalt core dams have been constructed (Alicescu, Tournier et Yannobel, 2008; Gopi, 2010). A list of asphalt-concrete core dams built in different countries can be found in *Hydropower and Dams* journal. Several dams of this type were built in Europe, and worldwide, there have been constructions in China, Brazil, Iran, Canada, etc. Satisfactory operation of asphalt-concrete core dams has been reported in various references (Höeg, 1993). The important properties of asphalt-concrete are “impermeability, flexibility, resistance to erosion, and self-healing” (Saxegaard,

2003). The well-behaved operation of this type of dam is mainly due to the viscoelastic plastic properties of the asphalt-concrete core, which can adjust to induced deformation as a whole, or due to the foundation settlement (Creegan et Monismith, 1996; Gopi, 2010). Noticeably, the asphalt-concrete core is sufficiently resistant to sustain earthquake excitations without cracking and material degradation (Hoeg, 2005). Numerous numerical simulations have been conducted to evaluate the performance of the asphalt-concrete core dam under earthquake movements (Akhtarpour et Khodaii, 2009; Höeg, 1993; Vannobel, 2013).

3.3 Dam-X

The Dam-X has been constructed across a River in the northern part of Québec province. The project involves building of six dikes up to 80 m high. From a hydrological study at full supply level of 243.8 m, the total reservoir area is approximately 81 km². The Dam-X with 514 m length has a maximum height of 110 m. The Dam-X is a zoned rockfill with asphalt-concrete core. Owing to the deficiency of the fill material in the area, the asphaltic core was considered for the dam (Vannobel, 2013). The dam reservoir is shown in figure 3.1. The dam has a fill volume of approximately 4 475 500 m³ and during flood condition, the spillway has a capacity of 2976 m³/s (Vannobel, 2013).

The rockfill dam region in geological reports is depicted as a “rugged and a jagged bedrock”, which is severely impacted by glacial erosion. The foundation of the dam is composed mainly of quartz monzonite and monzonite (Vannobel, 2013).

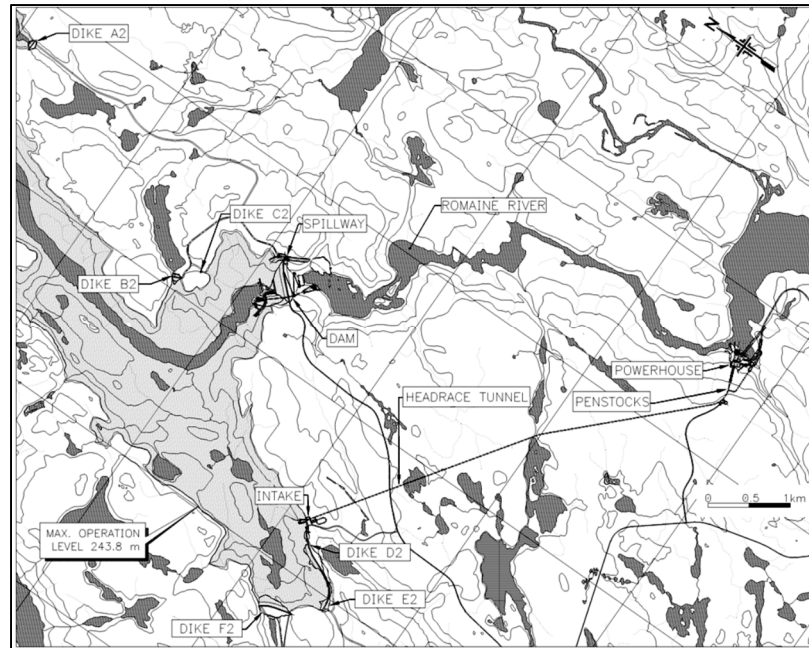


Figure 3.1 The Dam-X hydroelectric complex (Vannobel, 2013)

3.4 Typical cross section

Figure 3.2 illustrates a cross section of the rockfill dam. The upstream and downstream slopes are 1:1.6 and 1:1.45, respectively. The core and bedrock are connected by a continuous concrete sill, and the grout curtain was installed in the bedrock under the sill (Vannobel, 2013).

The asphalt core is built vertically and centered on the dam axis. Corresponding to the applied hydraulic head, the asphalt core as a watertight element has 85 cm width at the base, which changes to 50 cm at the dam crest (Vannobel, 2013). The asphalt core is surrounded on both sides by transitions and filters, i.e., zone 3M and zone 3N as shown in figure 3.3. Zone 3M contains crushed stone with a maximum particle size of 80 mm, and the transition (zone 3N) consists of crushed stone with a maximum particle size of 200 mm. Moreover, the shells on both sides of the dam consist of compacted rockfill inner zone (zone 3O with a maximum size of 600 mm) and the outer zone (zone 3P with a maximum size of 1200 mm) (Vannobel, 2013).

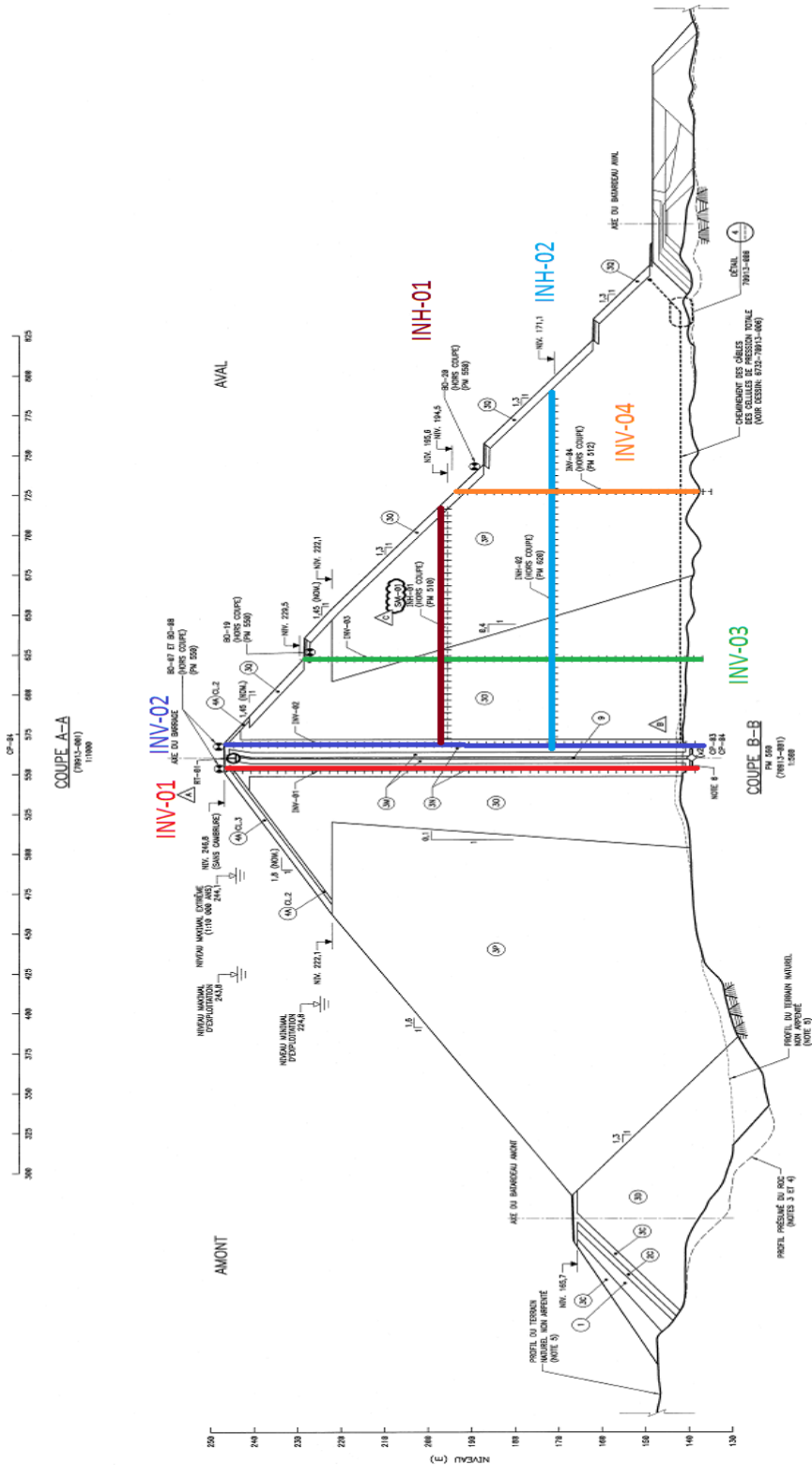


Figure 3.2 Cross section of the Dam-X(Cad drawing, Hydro-Quebec)

3.5 Soil parameters

Various constitutive soil models, namely, the hyperbolic (Duncan & Chang, 1970), MC, and HS models are used to analyze the construction and impoundment stages of the Dam-X. Tables 3.1 to 3.3 presents the different soil model parameters used for the dam simulation.

The Norwegian Geotechnical Institute (NGI) standard (Benoit Mathieu, 2012), as a suitable reference for material properties of tall dams (dams with dikes higher than 50 m), is considered (Daniel Verret, 2013). The parameters used for zone 3M and 3N are chosen based on the recommended Storvatn dam material properties (NGI, 1987). However, for the shell materials (zone 3O and 3P), higher stiffness values compared with NGI are assumed. The asphalt core material properties are extracted from the Dam-X design report (Benoit Mathieu, 2012).

Both elastic and plastic strains in the HS soil model depend on the unloading and reloading stiffness parameters in equations 3.1 and 3.2 (Brinkgreve et Broere, 2006). Plastic strains in the HS model emerge only in the primary loading, whereas elastic strains appear in both primary loading and reloading/unloading. Hence, different unloading and reloading stiffness values in the range of ($E_{ur}^{ref} = E_{50}^{ref}$) and ($E_{ur}^{ref} = 3E_{50}^{ref}$) are presumed in the study of this soil model (figures 3.13, 3.15, and 3.17). Table 3.1 presents the HS model properties for unloading and reloading stiffness equal to three times the secant stiffness ($E_{ur}^{ref} = 3E_{50}^{ref}$).

Equation 3.1 represents the axial plastic strain.

$$-\varepsilon_1^p = \frac{1}{2E_{50}} \frac{q}{1 - q/q_a} - \frac{q}{E_{ur}} \quad (3.1)$$

Elastic strain can be calculated as

$$-\varepsilon_1^e = \frac{q}{E_{ur}}, \quad -\varepsilon_2^e = -\varepsilon_3^e = -\nu_{ur} \frac{q}{E_{ur}} \quad (3.2)$$

Table 3.1 Hardening soil model parameters used for rockfill dam simulation

Properties	Unit	material				
		Asphalt core	3M	3N	3O	3P
E_{50}^{ref}	[KN/m ²]	21500	280000	170000	110000	80000
E_{ur}^{ref}	[KN/m ²]	64500	840000	510000	330000	240000
E_{oed}^{ref}	[KN/m ²]	21500	252000	137700	89100	72000
ϑ_{ur}	-	0.45	0.3	0.3	0.33	0.33
γ	[KN/m ³]	24.5	23.6	23.7	22.5	22.5
φ	[degree]	32.6	47	47	45	43
C	[KN/m ²]	0	0	0	0	0
ψ	[degree]	0	15	15	10	10
m	-	0.5	0.18	0.23	0.4	0.4
Failure ratio	-	0.9	0.9	0.9	0.9	0.9

where E_{50}^{ref} is the secant stiffness, E_{ur}^{ref} is the reference Young's modulus for unloading and reloading stiffness, E_{oed}^{ref} is the reference Young's modulus used to define the oedometer stiffness, ϑ is the Poisson's ratio, φ is the friction angle, γ is the specific weight of the material, C is the cohesion, ψ is the dilation angle, m is an exponent (power for stress-level dependency of stiffness), and R_f is the failure ratio.

Table 3.2 Mohr-Coulomb soil model parameters used for rockfill dam simulation

Properties	Unit	material				
		Asphalt core	3M	3N	3O	3P
E	[KN/m ²]	21500	280000	170000	110000	80000
ϑ	-	0.45	0.33	0.33	0.2	0.2
γ	[KN/m ³]	24.5	23.6	23.7	22.5	22.5
φ	[degree]	32.6	47	47	45	43
ψ	[degree]	0	15	15	10	10
C	[KN/m ²]	0	0	0	0	0

where E is the Young's modulus, ϑ is the Poisson's ratio, ϕ is the friction angle, γ is the specific weight of the material, C is the cohesion, and ψ is the dilation angle.

Table 3.3 Duncan-Chang soil model parameters used for rockfill dam simulation

Properties	Unit	material				
		Asphalt core	3M	3N	3O	3P
k		215	2800	1700	1100	800
γ	[KN/m ³]	24.5	23.6	23.7	22.5	22.5
φ	[degree]	32.6	47	47	45	43
C	[KN/m ²]	0	0	0	0	0
n	-	0.5	0.18	0.23	0.4	0.4
Failure ratio	-	0.8	0.6	0.6	0.7	0.7

where k is the modulus number, n is the modulus exponent, φ is the friction angle, C is the cohesion, γ is the specific weight of the material, and R_f is the failure ratio.

3.6 Instrumentation

Inclinometers are used widely to measure ground deformations in abutments, foundations, embankments, and structures. Vertical inclinometers are used specifically to measure any possible horizontal and vertical deformations, which might occur owing to the valley asymmetry (Vannobel, 2013).

The monitoring program consists of vertical inclinometers on both sides of the core (INV-01 and INV-02), vertical and horizontal inclinometers in the downstream shells (INV-03, INV-04, INH-01, and INH-02), total pressure cells alongside the contact between the core and concrete sill, survey monuments along the crest and downstream slope, survey pins installed on top of the core, measuring weir, thermistor cables in the upper part of the crest, and accelerographs (Vannobel, 2013). Figure 3.2 shows the vertical and horizontal inclinometer positions inside the Dam-X. The horizontal and vertical displacements measured from these devices are shown in figures 3.12 to 3.19.

3.7 Finite element modeling

In this section, the rockfill dam is modeled, and the geometry and boundary conditions, which are used to simulate the model through Zsoil and Plaxis, are described. A two-dimensional plane-strain model is used to analyze the dam at the highest elevation of the crest as shown in figure 3.2. Simulations are performed for 81 stages, including the end of construction and impoundment.

The simulations are conducted using stage construction in 55 different layers. Increasing the number of layers helps to reduce the height of the elements, which consequently leads to results closer to reality (Qoreishi, 2013). Each of these layers consists of five zones. The asphalt core is located at the dam center and has been protected by transition (zones 3M & 3N) and rockfill shells (zones 3O & 3P) on either side of the dam. Tables 3.1 to 3.3 present the assigned model parameters for the elements of each zone. Figure 3.5 shows the simplified

geometry of the dam. Owing to the high rigidity of the bedrock, the bottom boundary of the model is constrained in the horizontal and vertical directions.

A multistage modeling technique is used to simulate an increase of water level behind the dam. Corresponding to the raised water elevation, a new hydraulic boundary condition and a new hydrostatic pressure are applied. The flow calculation is performed based on Darcy's law.

When the geometry of the dam is completed, the finite element meshing can be performed. The positions of points and lines in the geometry are considered to implement the mesh. The mesh generation procedure can be performed using the Zsoil software, in which the geometry of the dam is divided into basic element types. Four-node quadrilateral elements are used for meshing (figure 3.3). The model consists of 10,066 nodes and 9,883 continuum 2D elements.

A fifteen-node triangular element is used in Plaxis. It is crucially important to use a sufficient number of refined mesh to ensure that the results from the finite element analysis are precise (refer to figure 3.4). Various mesh sizes are considered to establish a suitable FE mesh; particularly, the mesh size for the asphalt core elements is refined as indicated in table 3.4.

In addition, the initial conditions are considered in the simulation. The initial geometry configuration and the initial stresses, such as effective stresses and pore pressure are concluded in the initial conditions.

Table 3.4 Mesh size influences on total displacement in Plaxis software

Number of elements	Number of nodes	Number of stress points	Average element size (m)	Max total displacement of dam (cm), accumulated displacement	Max total displacement at the crest (cm), accumulated displacement
12784	102921	153408	2.26	73.493	72.35
2976	24189	35712	4.69	73.496	72.355
1731	14135	20772	6.14	73.498	72.359
512	4237	6144	11.3	73.5	72.378
384	3173	4608	13	73.507	72.39

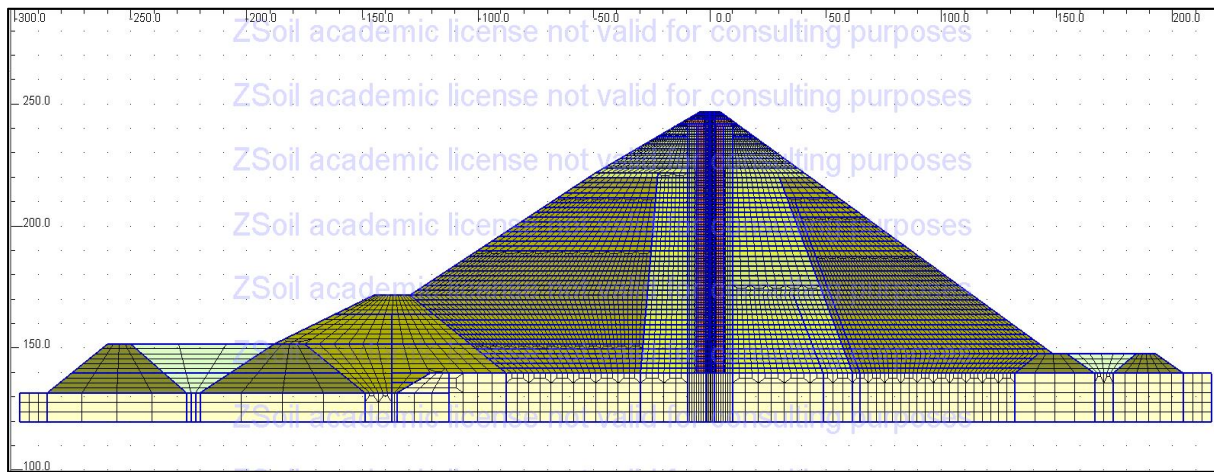


Figure 3.3 Plot of the mesh in Zsoil

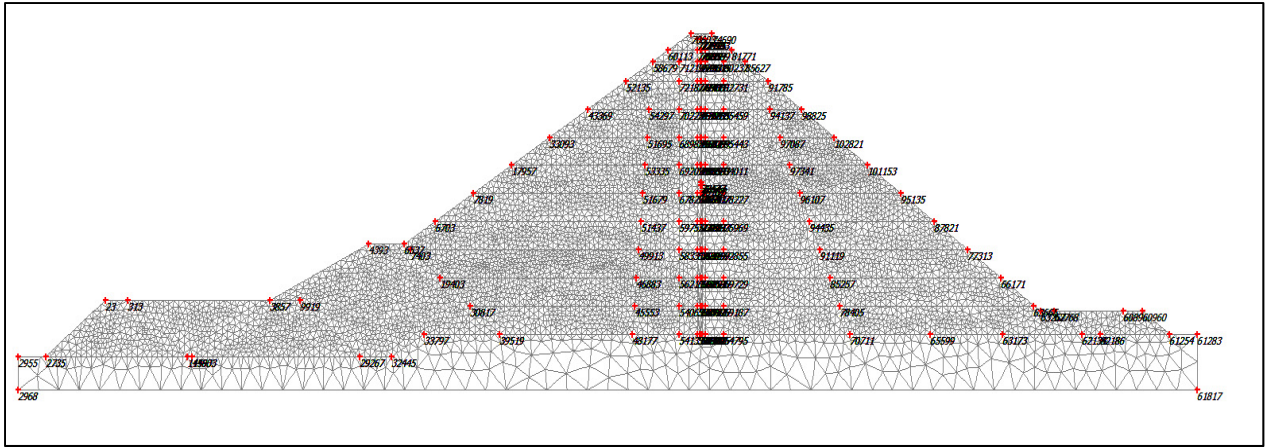


Figure 3.4 Plot of the mesh in Plaxis

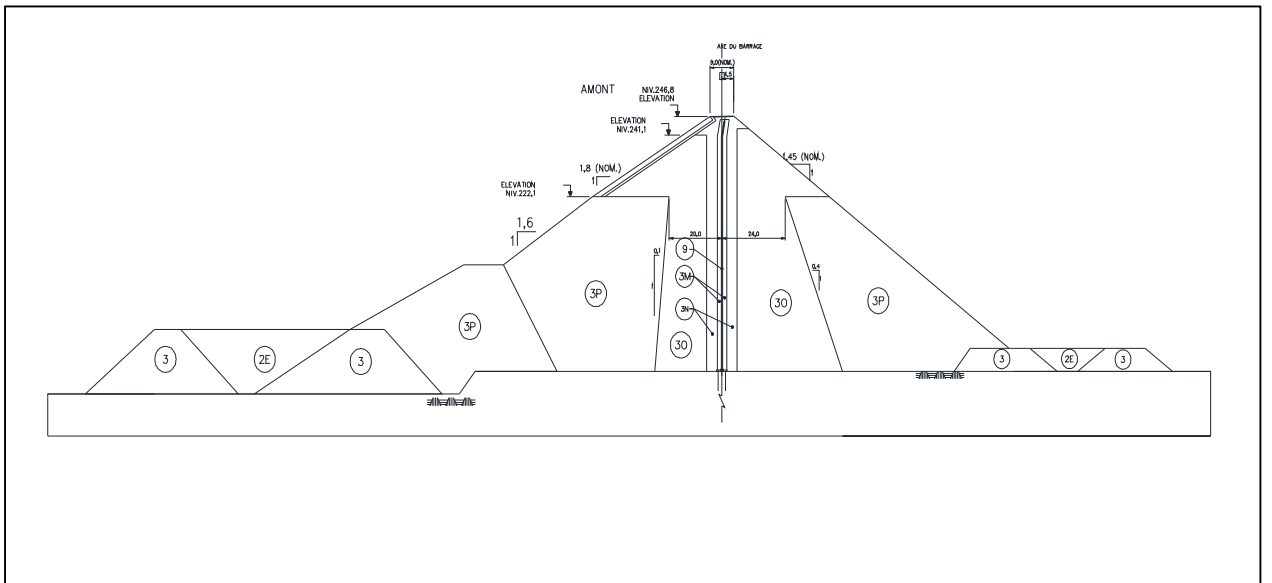


Figure 3.5 Simplified dam cross section

3.8 Displacement contours at the end of construction

In this chapter, the finite element (FE) as an efficient method is used to study the dam performance. The FE method can be effective if a reliable stress–strain relationship and appropriate model parameters are used (Kim et al., 2014). The Dam-X simulation is implemented using the Hyperbolic (Duncan & Chang, 1970), HS, and MC models. Both construction and impoundment analyses are performed, and a comparison is made between the monitoring data and simulation results.

The horizontal and vertical displacement contours for the simulation using the MC model are shown in figures 3.6 and 3.7, respectively. Symmetrical horizontal displacement contours can be achieved as shown in figure 3.6. The maximum movements computed indicate a 15 cm horizontal movement and a 36 cm settlement. The maximum settlement occurs inside the shell (figure 3.7).

Figures 3.8 and 3.9 show the horizontal and vertical displacement contours for the simulation using the Duncan–Chang model. The horizontal displacement is zero at the center; this value has increased progressively when approaching the upstream and downstream side. The maximum horizontal displacement is 37 cm as shown in figure 3.8. A concentric circle shape can be achieved in the contour of the vertical movement as shown in figure 3.9. The maximum vertical displacement is 51 cm, which occurs at a height of 68% H (H = height of Dam-X) from the bottom of the dam.

The horizontal and vertical displacements for the analysis using the HS model (with $E_{ur} = 3E$) are shown in figures 3.10 and 3.11. As shown in figure 3.10, approximately 2.4 mm of horizontal displacement is calculated at the dam crest, and approximately 3.9 cm is predicted at the depth of 70 m below the crest. The maximum vertical displacement is 30 cm (0.27% H , H = dam height) as shown in figure 3.11. The general trend of the displacement after construction is similar to that of previous studies carried out by Qoreishi, Ghanooni, and Akhtarpour (Akhtarpour et Khodaii, 2009; Nahabadi, 2002; Qoreishi, 2013).

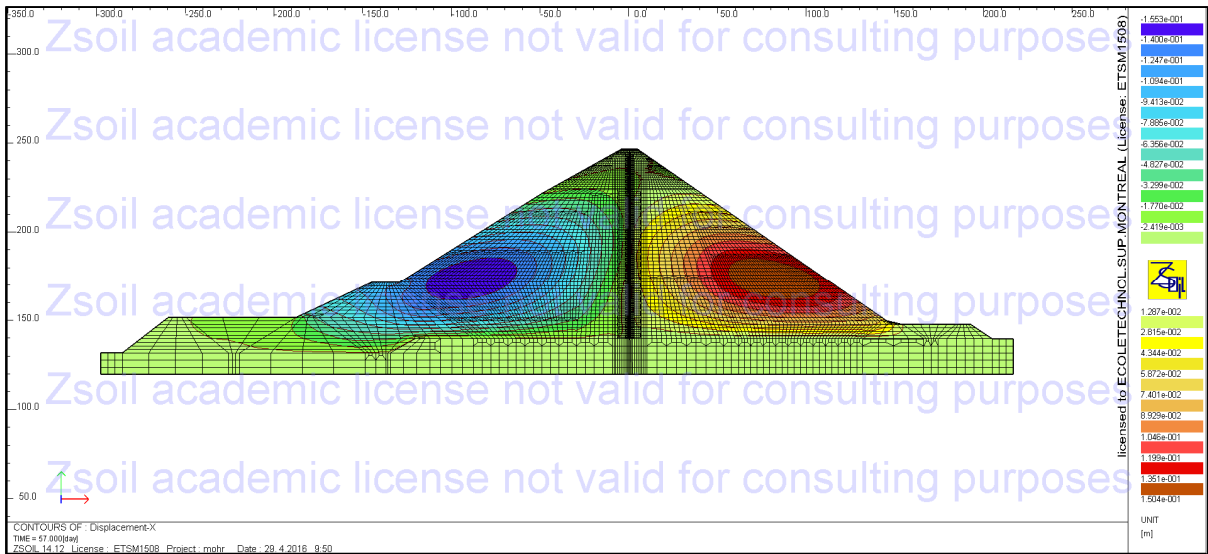


Figure 3.6 Contour of horizontal displacement (Mohr-Coulomb model)

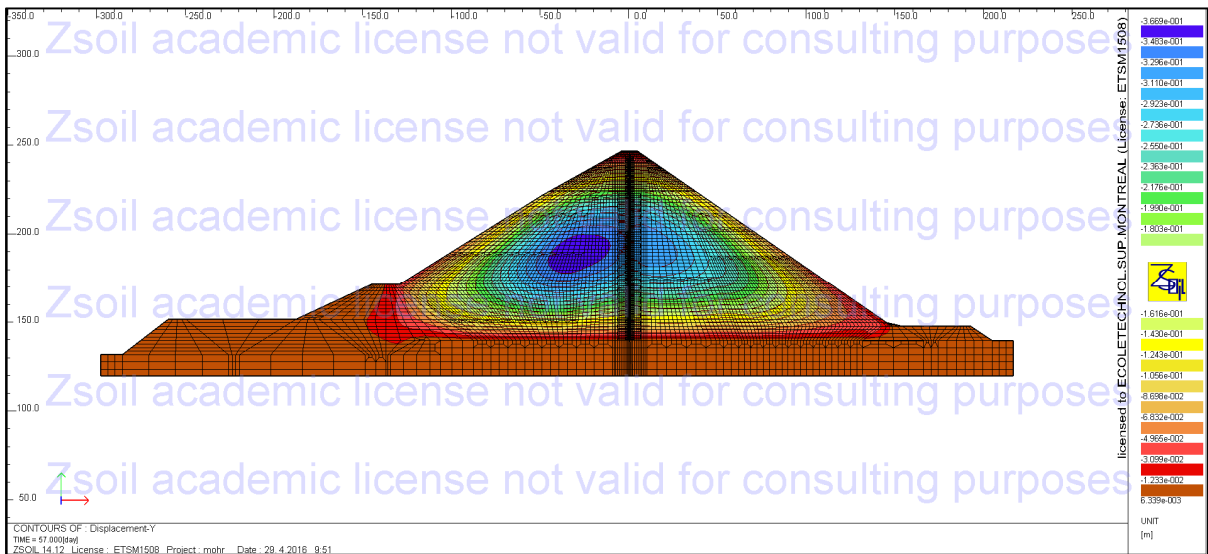


Figure 3.7 Contour of vertical displacement (Mohr-Coulomb model)

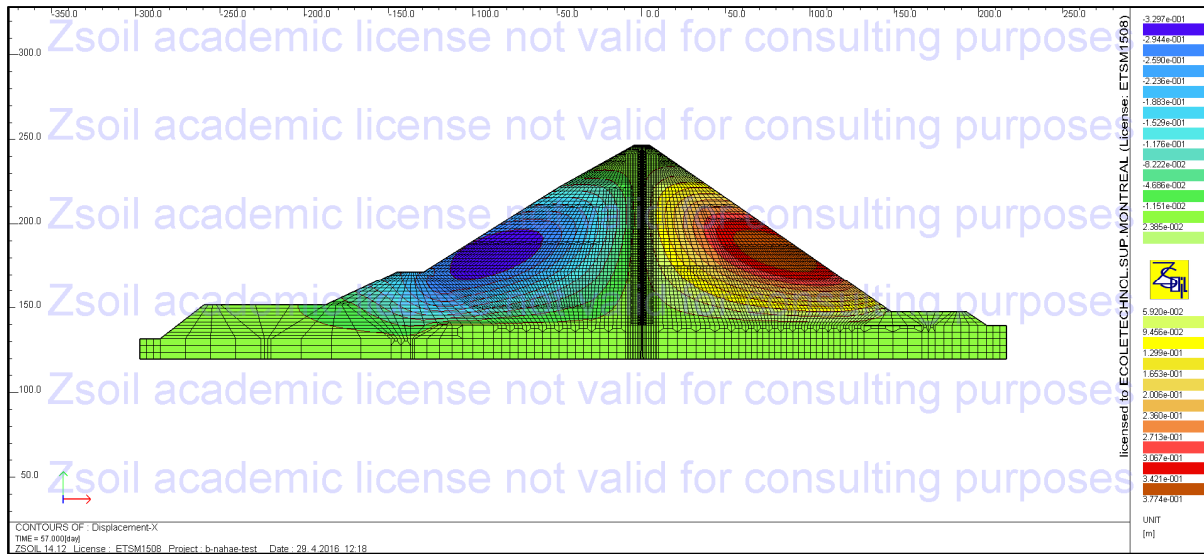


Figure 3.8 Contour of horizontal displacement (Duncan-Chang model)

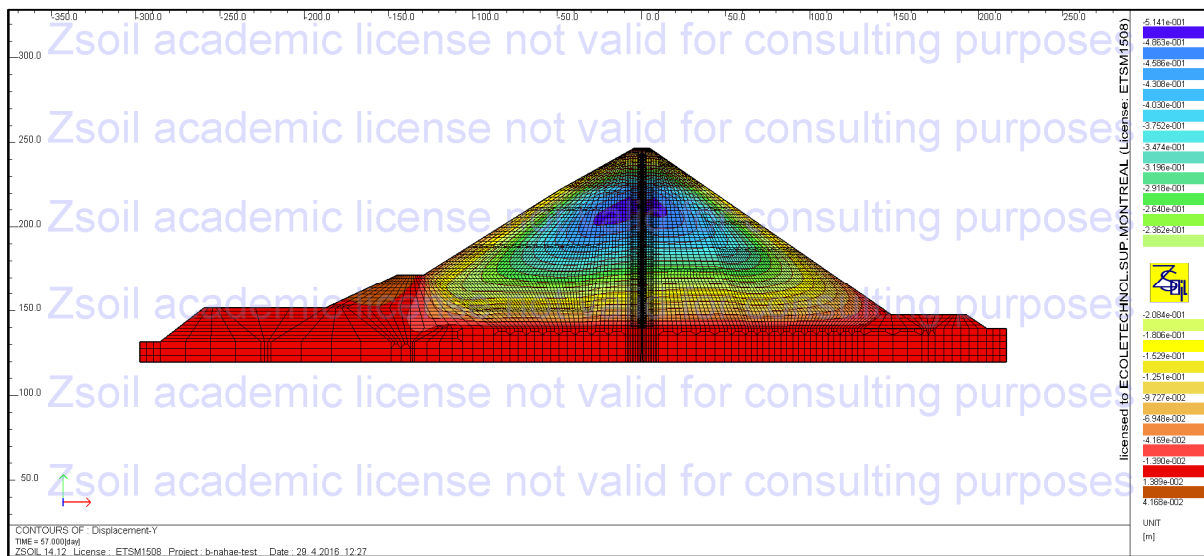


Figure 3.9 Contour of vertical displacement (Duncan-Chang model)

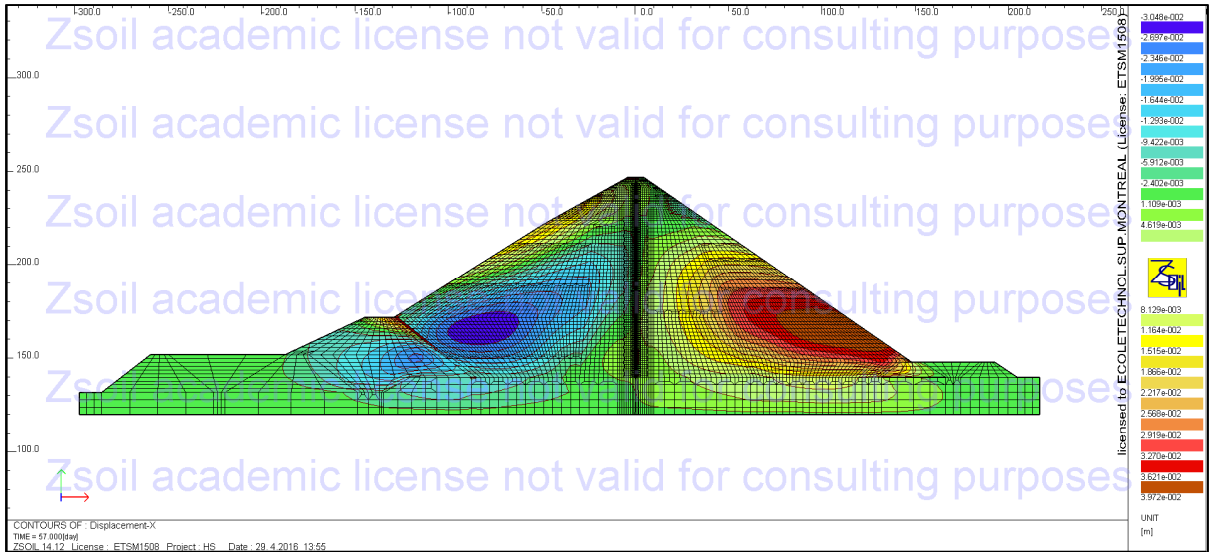


Figure 3.10 Contour of horizontal displacement (HS model)

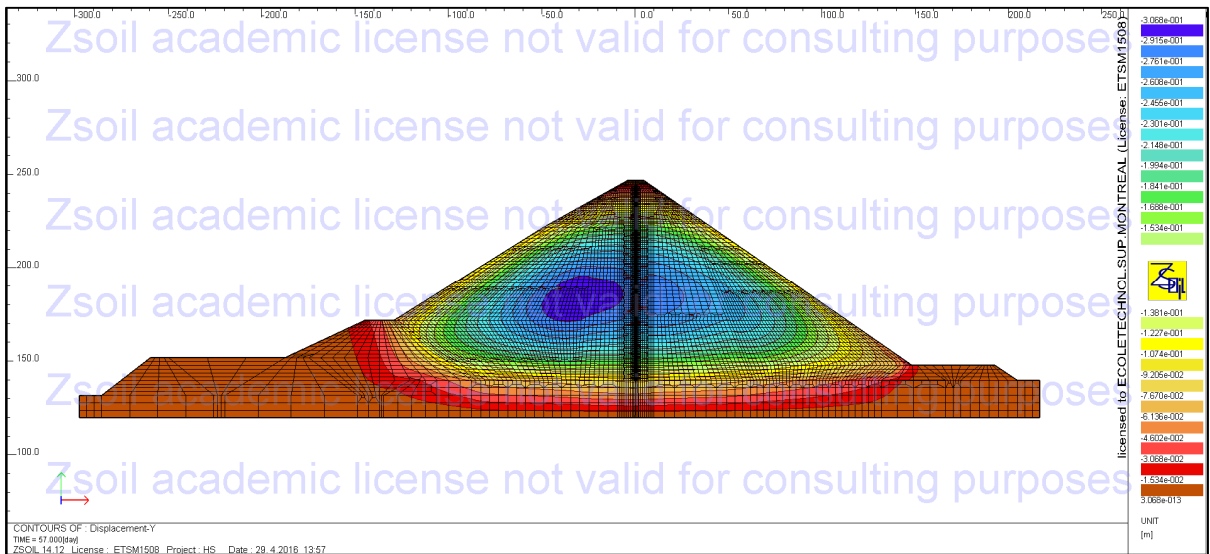


Figure 3.11 Contour of vertical displacement (HS model)

3.9 Comparison between measured data and numerical simulations after construction

This section mainly focuses on the comparison of the measured data from monitoring instruments (i.e., INV-1, INV-2, INV-03, INH-01, and INH-02) and numerical analysis of Dam-X at the end of construction (refer to figures 3.12 to 3.19).

3.9.1 Comparison between measured and computed displacements after construction (inclinometer INV-01)

To make a comparison with the field data, the MC, HS, and Duncan–Chang soil models were implemented into the finite element programs. The MC soil model is able to predict the accumulated horizontal displacement with fair accuracy; the horizontal displacement at the crest of dam is estimated as 6 cm using the MC model as shown in figure 3.12. Meanwhile, the expected horizontal displacement at the crest is slightly lower for the HS soil model, which is 2 cm. The jagged form of the measured curve is due to the variability of measurement (Vannobel, 2013). The maximum vertical displacement measured using the inclinometer (INV-01) is 45.2 cm as shown in figure 3.13. Thus, the HS and MC soil models can provide a satisfactory prediction of the behavior of rockfill materials in the vertical direction and they have an acceptable deviation from the monitoring data.

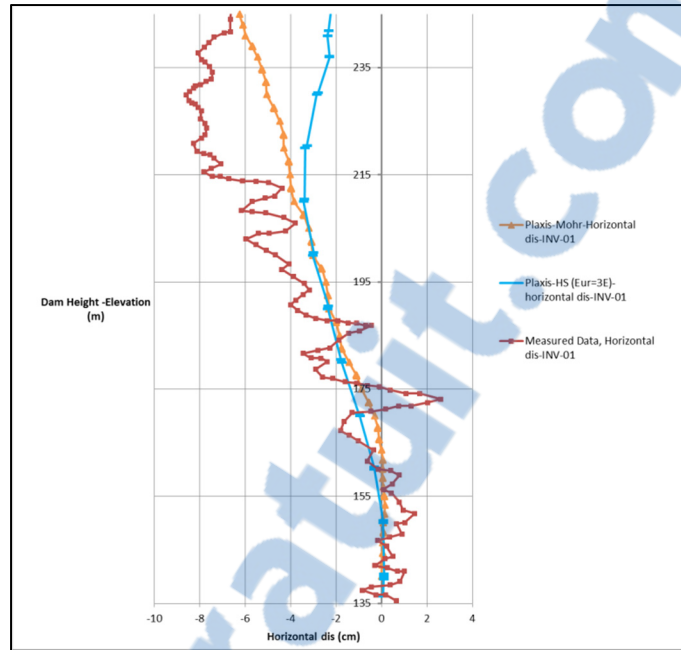


Figure 3.12 Accumulated horizontal displacements at section (INV-01)

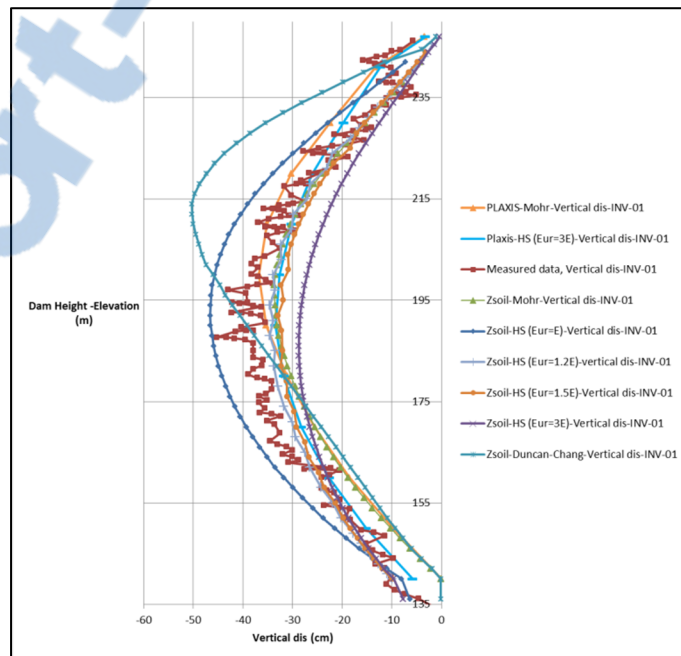


Figure 3.13 Vertical displacements at section (INV-01)

Table 3.5 Absolute maximum horizontal and vertical displacement resulted by FE analysis at section INV-1

Soil model	Absolute maximum vertical displacement (cm)	Absolute maximum horizontal displacement (cm)
M-C (PLAXIS)	36.7	6.24
M-C (ZSOIL)	33.6	-
HS- $E_{ur}=3E$ (PLAXIS)	33.4	3.43
HS- $E_{ur}=E$ (ZSOIL)	46.5	-
HS- $E_{ur}=1.2E$ (ZSOIL)	34.6	-
HS- $E_{ur}=1.5E$ (ZSOIL)	32.9	-
HS- $E_{ur}=3E$ (ZSOIL)	28.7	-
Duncan-Chang	50.2	-
Measurment	45.2	8.59

3.9.2 Comparison between measured and computed displacements after construction (inclinometer INV-02)

The entire rockfill dam is not perfectly symmetrical, thus a 4 cm horizontal displacement toward the upstream side can be observed at the crest of dam as shown in figure 3.14. The discrepancy between the internal monitoring data at section INV-02 and computations at elevation 175 to 215 m appears to be attributable to construction circumstances such as rainfall during the period of construction, a dissimilar thickness of compaction layers, and different distributions of particle size (Kim et al., 2014).

Because the rockfill materials are well compacted, the measured and computed vertical displacements are relatively small compared with the size of the dam. According to the computed settlement for MC, HS ($E = E_{ur}$), HS ($E = 3 E_{ur}$), and measured data, the relative vertical displacement can be calculated as 0.29%, 0.40%, 0.26%, and 0.365%, respectively. In addition, the graphs of HS, and MC provide a better fit when compared with that of Duncan–Chang.

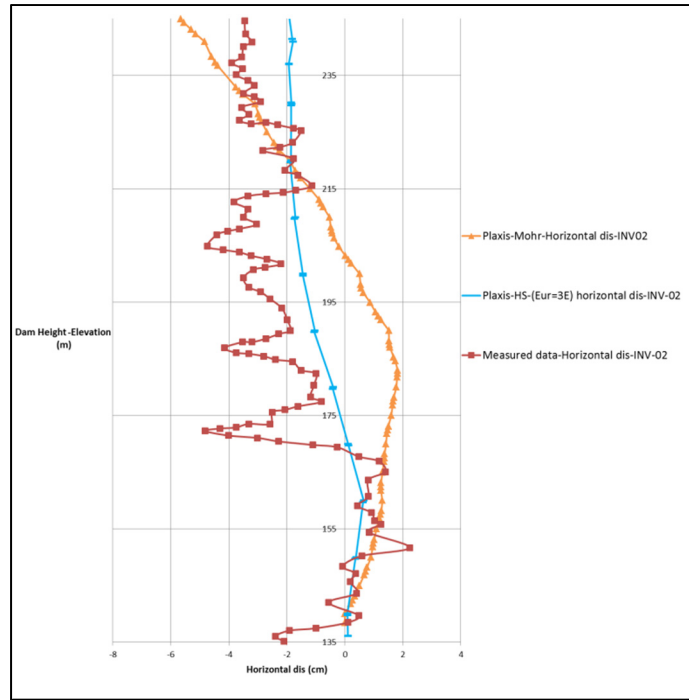


Figure 3.14 Accumulated horizontal displacements at section (INV-02)

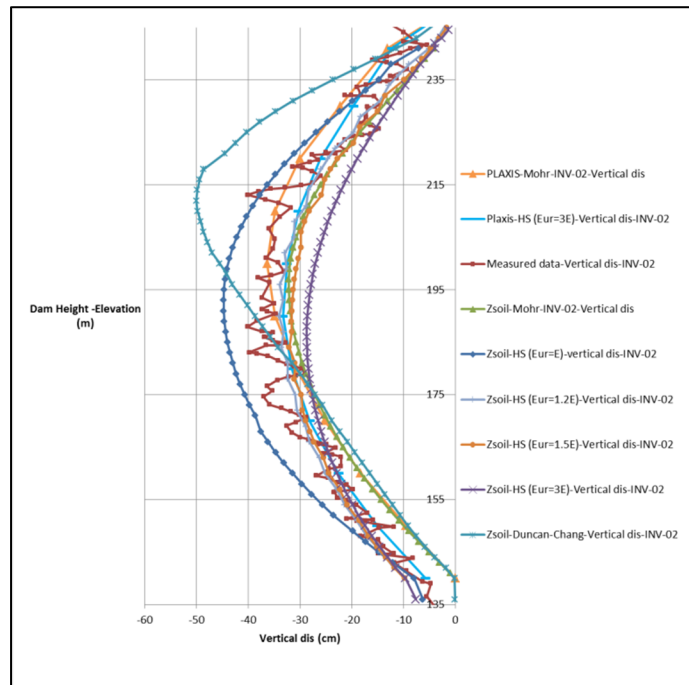


Figure 3.15 Vertical displacement at section (INV-02)

Table 3.6 Absolute maximum horizontal and vertical displacement resulted by FE analysis at section INV-2

Soil model	Absolute maximum vertical displacement (cm)	Absolute maximum horizontal displacement (cm)
M-C (PLAXIS)	36.3	5.65
M-C (ZSOIL)	32.2	-
HS- $E_{ur}=3E$ (PLAXIS)	33.3	1.9
HS- $E_{ur}=E$ (ZSOIL)	44.8	-
HS- $E_{ur}=1.2E$ (ZSOIL)	34.1	-
HS- $E_{ur}=1.5E$ (ZSOIL)	32.1	-
HS- $E_{ur}=3E$ (ZSOIL)	28.7	-
Duncan-Chang	49.9	-
Measurment	40.1	4.8

3.9.3 Comparison between measured and computed displacements after construction (inclinometer INV-03)

The inclinometer (INV-03) recorded a 10 cm horizontal displacement at the crest, which is in fair agreement with the numerical analysis using the MC model (12 cm). However, the HS soil model predicted a smaller value of approximately 3 cm.

Figure 3.17 shows the measured vertical displacement at the end of construction. The results of simulations using the MC and HS soil models in terms of the maximum vertical displacement and the location of the maximum value are almost identical to the measured data (approximately at the middle of the cross section). Conversely, the analysis using the Duncan–Chang soil model shows more settlement (43.4 cm) at a higher elevation (El 206 m).

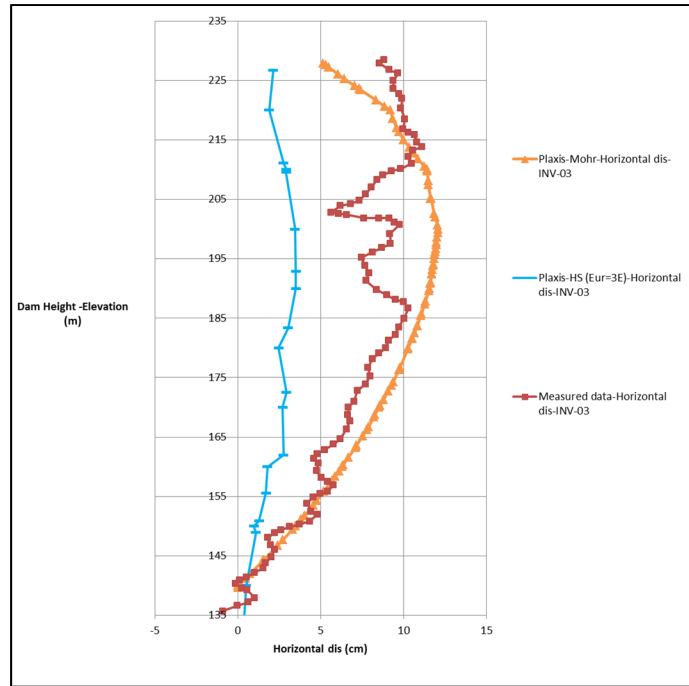


Figure 3.16 Accumulated horizontal displacements at section (INV-03)

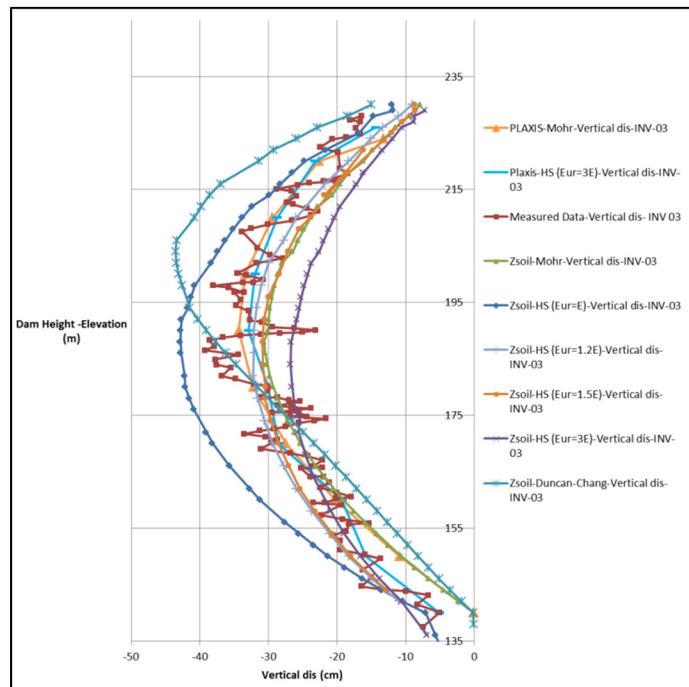


Figure 3.17 Vertical displacements at section (INV-03)

Table 3.7 Absolute maximum horizontal and vertical displacement resulted by FE analysis at section INV-3

Soil model	Absolute maximum vertical displacement (cm)	Absolute maximum horizontal displacement (cm)
M-C (PLAXIS)	34.3	12.04
M-C (ZSOIL)	30.64	-
HS- $E_{ur}=3E$ (PLAXIS)	32.9	3.44
HS- $E_{ur}=E$ (ZSOIL)	42.8	-
HS- $E_{ur}=1.2E$ (ZSOIL)	32.2	-
HS- $E_{ur}=1.5E$ (ZSOIL)	30.8	-
HS- $E_{ur}=3E$ (ZSOIL)	26.67	-
Duncan-Chang	43.4	-
Measurment	39.2	11.09

3.9.4 Comparison between measured and computed displacements after construction (INH-01 and INH-02)

Figures 3.18 and 3.19 show the settlement corresponding to inclinometers INH-01 and INH-02. There is a poor agreement between the monitoring data and the results of all assumed constitutive soil models; remarkably, a large difference can be observed between the simulation and monitoring data at zone 3O. The disagreement between the numerical simulation outcomes and measured data can be explained using MMASW tests. MMASW tests were performed on the dam to characterize the rockfill material shear wave velocity at the downstream side (Hunter et Crow, 2012). The MMASW test results are shown in section 3.13.

Overall, because of the inconsistency between actual construction circumstances and assumptions in the numerical study (i.e., the material stiffness at zone 3O), the numerical simulations obtained larger settlements compared to the measured data.

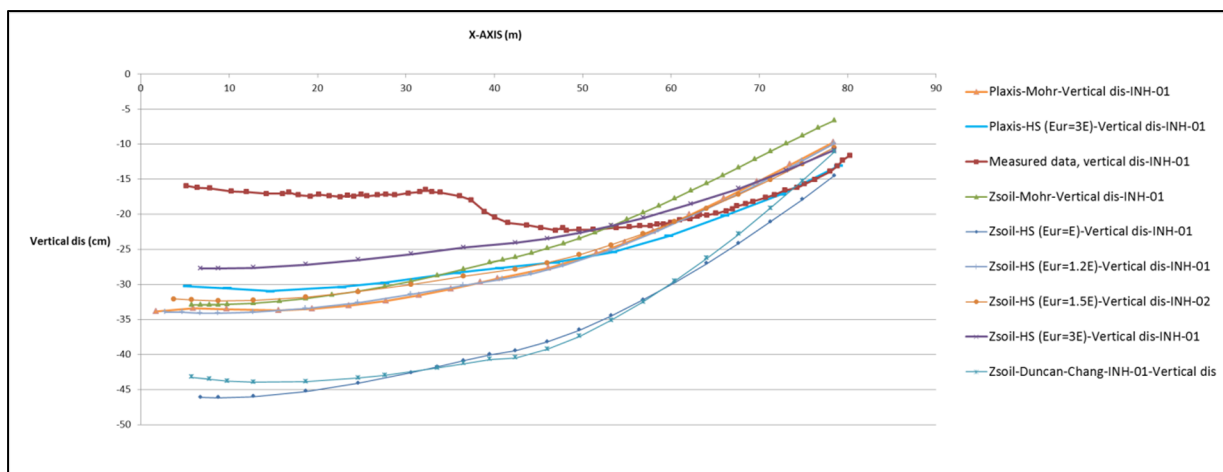


Figure 3.18 Vertical displacements at section (INH-01)

Table 3.8 Absolute maximum vertical displacement resulted by FE analysis at section INH-1

Soil model	Absolute maximum vertical displacement (cm)
M-C (PLAXIS)	33.8
M-C (ZSOIL)	32.9
HS- $E_{ur}=3E$ (PLAXIS)	30.5
HS- $E_{ur}=E$ (ZSOIL)	46
HS- $E_{ur}=1.2E$ (ZSOIL)	33.9
HS- $E_{ur}=1.5E$ (ZSOIL)	32.05
HS- $E_{ur}=3E$ (ZSOIL)	27.7
Duncan-Chang	43.9
Measurment	22.2

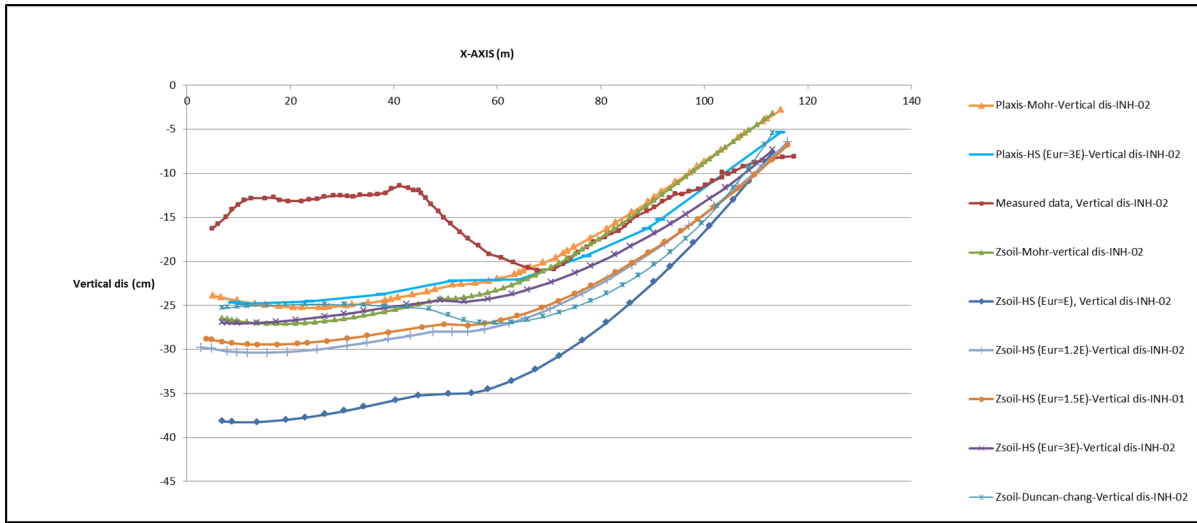


Figure 3.19 Vertical displacements at section (INH-02)

Table 3.9 Absolute maximum vertical displacement resulted by FE analysis at section INH-2

Soil model	Absolute maximum vertical displacement (cm)
M-C (PLAXIS)	25.2
M-C (ZSOIL)	27
HS- $E_{ur}=3E$ (PLAXIS)	24.8
HS- $E_{ur}=E$ (ZSOIL)	38
HS- $E_{ur}=1.2E$ (ZSOIL)	30.36
HS- $E_{ur}=1.5E$ (ZSOIL)	29.46
HS- $E_{ur}=3E$ (ZSOIL)	27
Duncan-Chang	27
Measurment	21

3.10 Comparison between Plaxis and Zsoil

Plaxis and Zsoil are finite element software applications that have been developed specifically for stability and deformation analysis in geotechnical engineering projects. Figures 3.20 to 3.27 show a comparison between Plaxis and Zsoil. As the Plaxis model has more nodes (15-node element) compared with the Zsoil model (4-node quadrilateral element), naturally, the Plaxis model can provide a better prediction. However, the difference between these two applications is almost negligible.

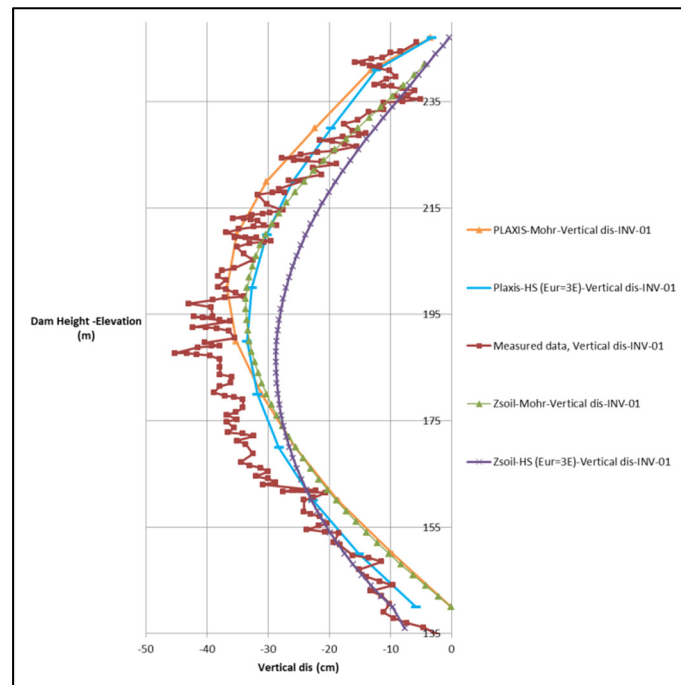


Figure 3.20 Comparison between Plaxis and Zsoil for vertical displacement at section INV-01

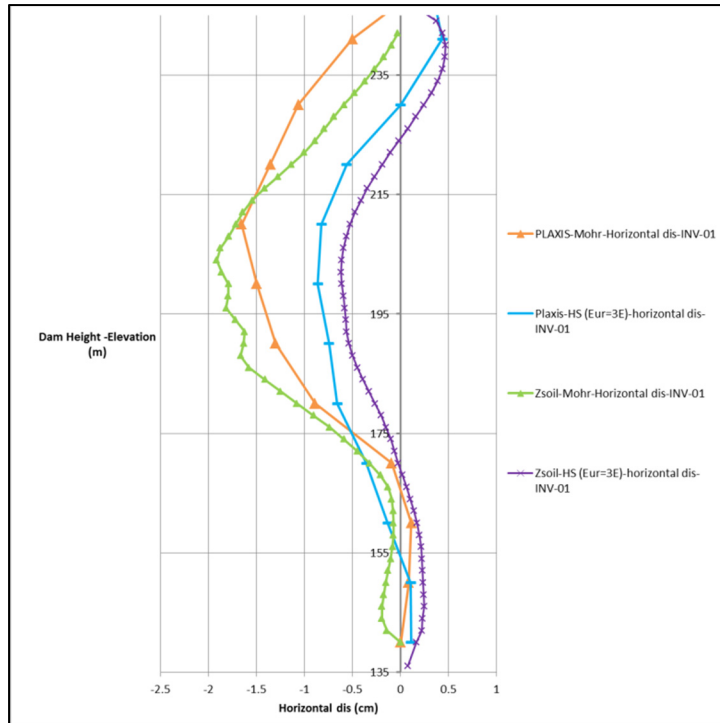


Figure 3.21 Comparison between Plaxis and Zsoil for relative horizontal displacement at section INV-01

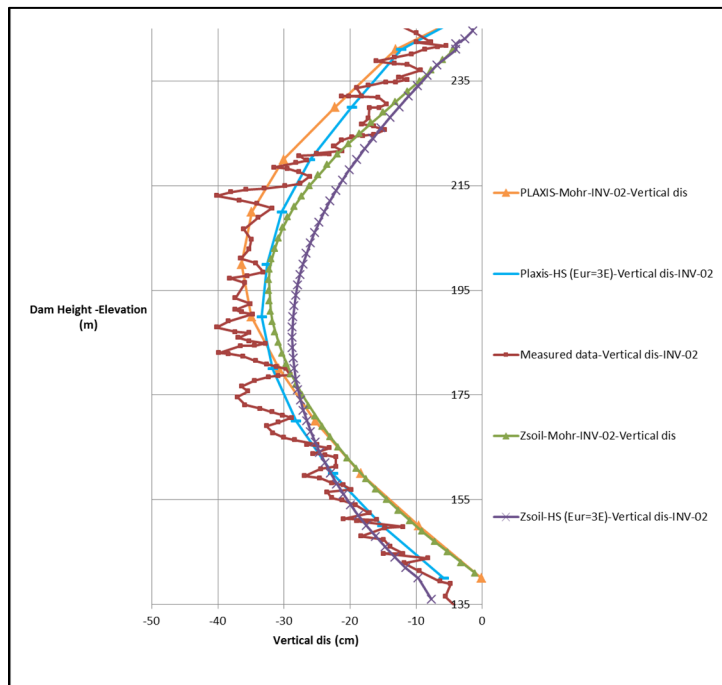


Figure 3.22 Comparison between Plaxis and Zsoil for vertical displacement at section INV-02

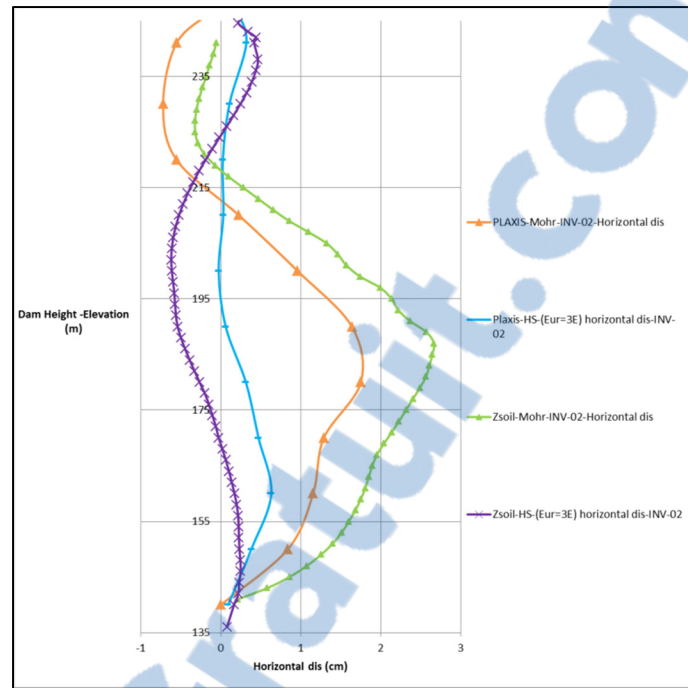


Figure 3.23 Comparison between Plaxis and Zsoil for relative horizontal displacement at section INV-02

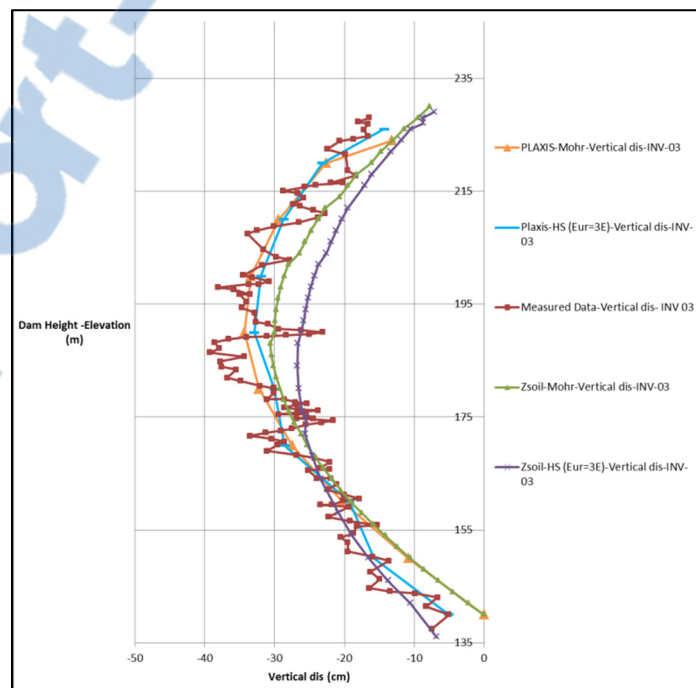


Figure 3.24 Comparison between Plaxis and Zsoil for vertical displacement at section INV-03

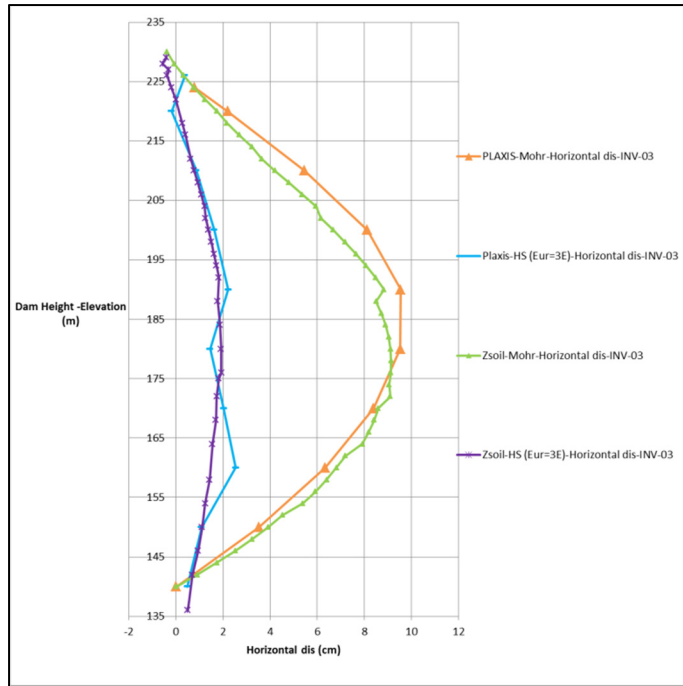


Figure 3.25 Comparison between Plaxis and Zsoil for relative horizontal displacement at section INV-03

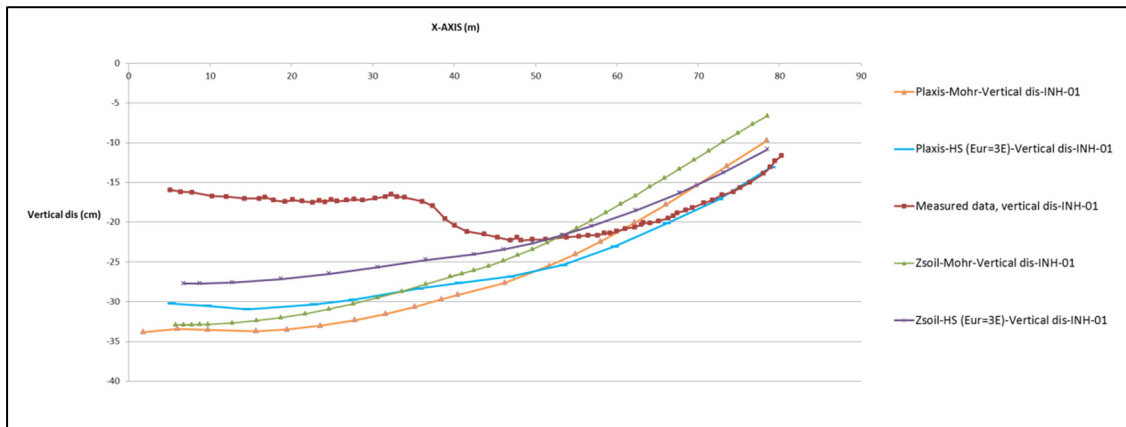


Figure 3.26 Comparison between Plaxis and Zsoil for vertical displacement at section INH-01

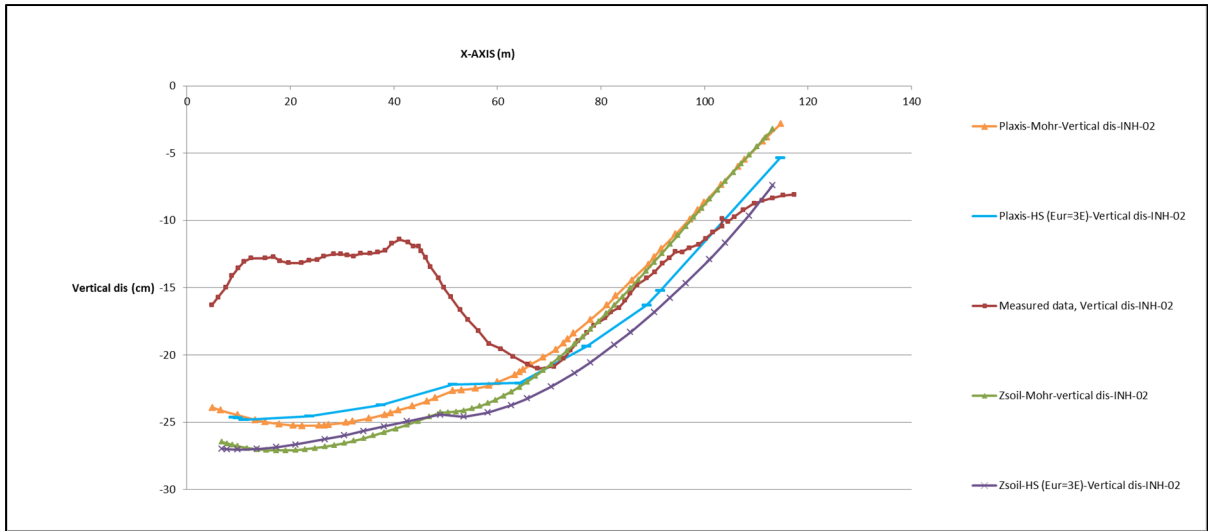


Figure 3.27 Comparison between Plaxis and Zsoil for vertical displacement at section INH-02

3.11 Numerical simulation procedure for wetting

A review of previous studies conducted by Nobari and Duncan indicates that collapse might occur in rockfill materials and clean sands when wetted. The main factors in granular material behavior when wetted are crack propagation and loss of strength between grain contact points that could be a result of increasing stress levels or even at a constant stress state over time. Furthermore, because of spreading fissures in the particles, new sliding particles inside the granular mass can be observed. The interlocks between particles shatter, and the grains look for more stable positions. The settlement in the upstream side of rockfill dams during the first impoundment would be an example of such phenomenon (Nobari et Duncan, 1972; Qoreishi, 2013; Simon Grenier, 2010).

The analytical procedures for the prediction of collapse are discussed further in this chapter. The main purpose of the numerical simulation for rockfill materials is to determine the deviatoric stress ($q = \sigma_1 - \sigma_3$), isotropic confinement stress σ_3 , and consequently calculate the strain (ϵ_1, ϵ_3) produced by rock collapse due to the wetting phenomenon. Two different procedures are described in this chapter (Simon Grenier, 2010).

3.11.1 Justo approach

This method introduces a lower deviatoric stress equal to

$$\Delta(\sigma_1 - \sigma_3) = a(\sigma_1 - \sigma_3) \quad (3.3)$$

where a is a coefficient upon wetting and is a fraction between 0 and 1 or can be defined as a proportion coefficient between $(\sigma_1 - \sigma_3)^{saturate}$ and $(\sigma_1 - \sigma_3)^{dry}$.

The value of a can be calculated from triaxial test results. This approach was investigated by Justo (Justo, 1991). Justo assumed that the Poisson's ratio remains unchanged during wetting, and to simplify the solution, the ratio between $\frac{\sigma_1}{\sigma_3}$ was considered constant. The value of a for different types of rocks was proposed by Justo (1991). The value varies between 0.26 and 0.6 (Simon Grenier, 2010).

3.11.2 Nobari–Duncan approach

Two components of volumetric strain variations as a result of wetting are assumed in the Nobari–Duncan procedure (Nobari et Duncan, 1972). These components are:

1. Volume loss (ε_{vc}) under isotropic confinement stresses

Volumetric variations because of wetting (ε_{vc}) under a confinement pressure (σ_3) is illustrated in figure 3.28. Equation 3.4 represents this parameter as

$$\varepsilon_{vc} = (\sigma_{3w} - \sigma_{3t})\beta \quad (3.4)$$

where σ_{3w} is considered as the isotropic confinement stress after wetting, and σ_{3t} can be defined as the isotropic confinement stress from which the volumetric strain begins; β is the slope of the line (figure 3.28).

2. Volume loss (ε_{vl}) under deviatoric stresses

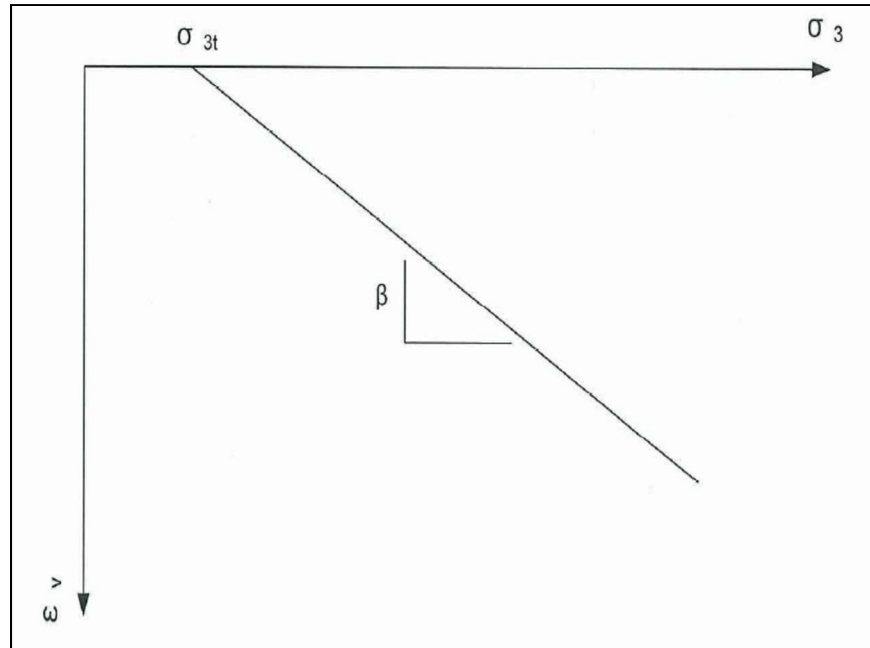


Figure 3.28 Amount of compression under confinement stress (Simon Grenier, 2010)

In order to simulate the physical phenomenon described in a numerical model, the occurrence of volume loss is prevented. For the first step, the amount of stress relaxation is calculated in case that the height and volume remain unchanged. Figure 3.29 shows the procedure for evaluating new stresses. As can be observed, “total” and “local” strains are represented for wet specimens. The total strain shown in figure 3.29 includes all strains (strain under isotropic confinement stress, ϵ_{vc} , and strain induced by deviatoric stress, ϵ_{vL}) whereas the local strain includes only the strains induced by axial loading.

The directions of principal stresses are assumed not to change during the saturation procedure or during the stress relaxation shown in figure 3.29 (Nobari et Duncan, 1972; Simon Grenier, 2010).

$$\epsilon_{1d} = (\epsilon_{1c} + \epsilon_{1L}) = \epsilon_{1w} \quad (3.5)$$

where ϵ_{1c} and ϵ_{1L} are the maximum strains due to the isotropic consolidation stress and deviatoric stress, respectively.

$$\epsilon_{vd} = (\epsilon_{vc} + \epsilon_{vL}) = \epsilon_{vw} \quad (3.6)$$

where ε_{vc} and ε_{vL} are the volumetric strains due to the isotropic consolidation and deviatoric stress, respectively.

The following equations are used for the plane strain in the orientation of the principal stresses:

$$\varepsilon_v = (\varepsilon_1 + \varepsilon_3), \quad \varepsilon_3 = -\vartheta\varepsilon_1 \quad (3.7)$$

Therefore,

$$\varepsilon_v = (1 - \vartheta)\varepsilon_1 \quad (3.8)$$

The Nobari–Duncan procedure (Nobari et Duncan, 1972) considers two main steps to solve the problem. In the first step, a new confinement stress, σ_{3w} , and $(\sigma_{1w} - \sigma_{3w})$ due to wetting will be calculated (essentially no change in the volume is assumed to reproduce the physical phenomenon in a numerical model; $\Delta\varepsilon_v = 0$ and therefore, $\varepsilon_{vd} = \varepsilon_{vw}$). In this condition, the system would not be in equilibrium; to restore equilibrium, in the second step, a load equal to the stress reduction calculated in the first step $((\sigma_{1d} - \sigma_{3d}) - (\sigma_{1w} - \sigma_{3w}))$ should be applied to the model.

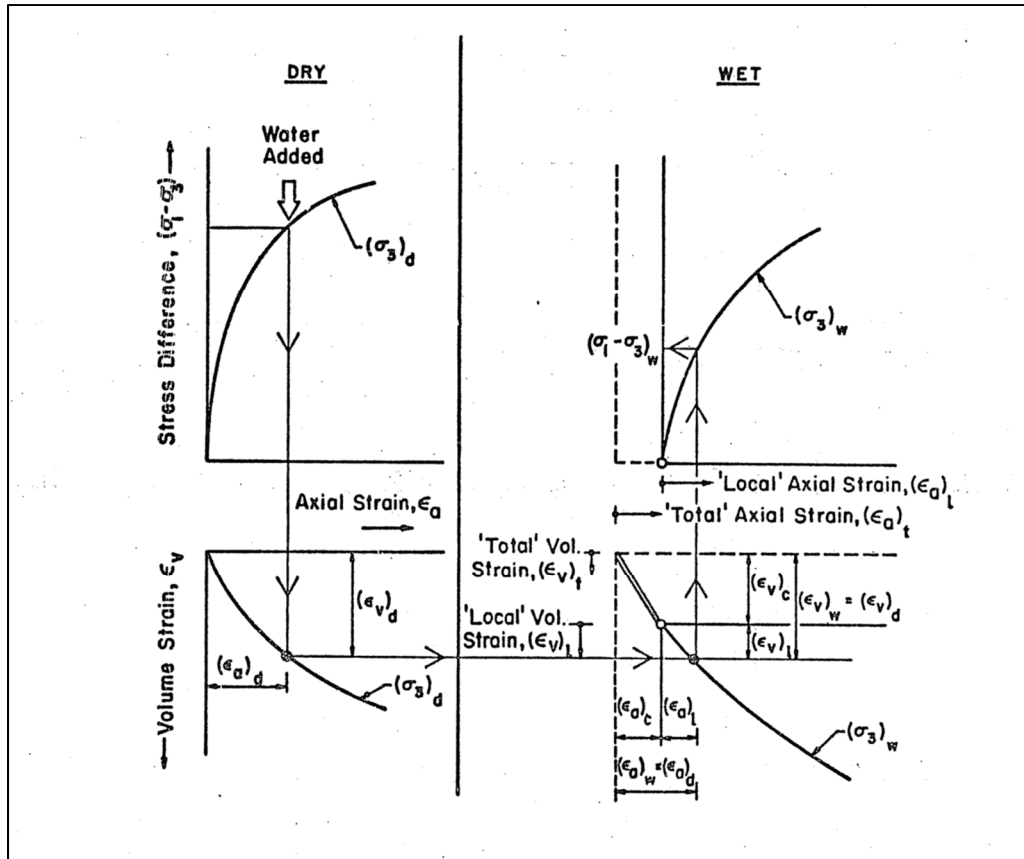


Figure 3.29 Evaluation of stress relaxation for wetting condition (Nobari et Duncan, 1972)

3.11.3 Escuder Procedure

The solution procedure for the problem explained by Nobari and Duncan (Nobari et Duncan, 1972) was used by Escuder et al. (2005) who proposed the following modified procedure. The equations used in this method are shown below.

$$\epsilon_{1d} - (\epsilon_{1c} + \epsilon_{1L}) = ERR1 \rightarrow 0 \tag{3.9}$$

where ϵ_{1d} , ϵ_{1L} , and ϵ_{1c} can be calculated using the following equations:

$$\epsilon_{1d} = \frac{(\sigma_{1d} - \sigma_{3d})}{\left[\left(1 - \frac{R_f(1 - \sin \phi)(\sigma_{1d} - \sigma_{3d})}{2 \cdot \sigma_{3d} \cdot \sin \phi} \right) \left[k \cdot p_a \left(\frac{\sigma_{3d}}{p_a} \right)^n \right] \right]} \tag{3.10}$$

$$\varepsilon_{1c} = \frac{\beta}{(1-\vartheta)} (\sigma_{3w} - \sigma_{3t}) \quad (3.11)$$

where σ_{3w} is unknown

$$\varepsilon_{1L} = \frac{(\sigma_{1w} - \sigma_{3w})}{\left[\left(1 - \frac{R_f(1-\sin\varphi)(\sigma_{1w} - \sigma_{3w})}{2\sigma_{3w}\sin\varphi}\right) \left[k.pa \left(\frac{\sigma_{3w}}{pa}\right)^n \right] \right]} \quad (3.12)$$

where σ_{3w} and $(\sigma_{1w} - \sigma_{3w})$ are unknown

$$\varepsilon_{Vd} - (\varepsilon_{Vc} + \varepsilon_{VL}) = ERR2 \rightarrow 0 \quad (3.13)$$

where ε_{Vd} , ε_{Vc} , and ε_{VL} can be calculated as

$$\varepsilon_{Vd} = (1 - \vartheta) \frac{(\sigma_{1d} - \sigma_{3d})}{\left[\left(1 - \frac{R_f(1-\sin\varphi)(\sigma_{1d} - \sigma_{3d})}{2\sigma_{3d}\sin\varphi}\right) \left[k.pa \left(\frac{\sigma_{3d}}{pa}\right)^n \right] \right]} \quad (3.14)$$

$$\varepsilon_{Vc} = \beta(\sigma_{3w} - \sigma_{3t}) \quad (3.15)$$

where σ_{3w} is unknown

$$\varepsilon_{VL} = (1 - \vartheta) \frac{(\sigma_{1w} - \sigma_{3w})}{\left[\left(1 - \frac{R_f(1-\sin\varphi)(\sigma_{1w} - \sigma_{3w})}{2\sigma_{3w}\sin\varphi}\right) \left[k.pa \left(\frac{\sigma_{3w}}{pa}\right)^n \right] \right]} \quad (3.16)$$

where σ_{3w} , and $(\sigma_{1w} - \sigma_{3w})$ are unknown.

It should be noted that Poisson's ratio also varies with respect to σ_3 ; the formula is

$$\vartheta = \frac{3B-E}{6B} \quad (3.17)$$

where B and E are functions of σ_3 and E is a function of $(\sigma_1 - \sigma_3)$

The system of equation can be solved by using the bisection method.

$$ERR1 = f(\sigma_{3w}, (\sigma_{1w} - \sigma_{3w})) \quad (3.18)$$

and

$$ERR2 = g(\sigma_{3w}, (\sigma_{1w} - \sigma_{3w})) \quad (3.19)$$

where the implicit functions, f and g , represent equations 3.9 and 3.13. The bisection method has been used to solve non-linear equations. This method always converges, although the convergence is slow. The upper and lower search variables should be defined; the values given in table 3.10 are fairly acceptable (Simon Grenier, 2010).

Table 3.10 Associated bounds (Simon Grenier, 2010)

Variable	boundaries	
	lower	higher
σ_{3w}	0	σ_{3d}
$(\sigma_{1w} - \sigma_{3w})$	0	$(\sigma_{1d} - \sigma_{3d})$

Figure 3.30 shows the solution procedure. The lower and upper bounds of the two unknown variables, i.e., σ_{3w} and $(\sigma_{1w} - \sigma_{3w})$ are considered, respectively, by using σ_{min} , σ_{max} , and by $\Delta\sigma_{min}$ and $\Delta\sigma_{max}$. Once the two roots of error functions are assessed, it is possible to change the calculated stresses before wetting with new ones (Simon Grenier, 2010).

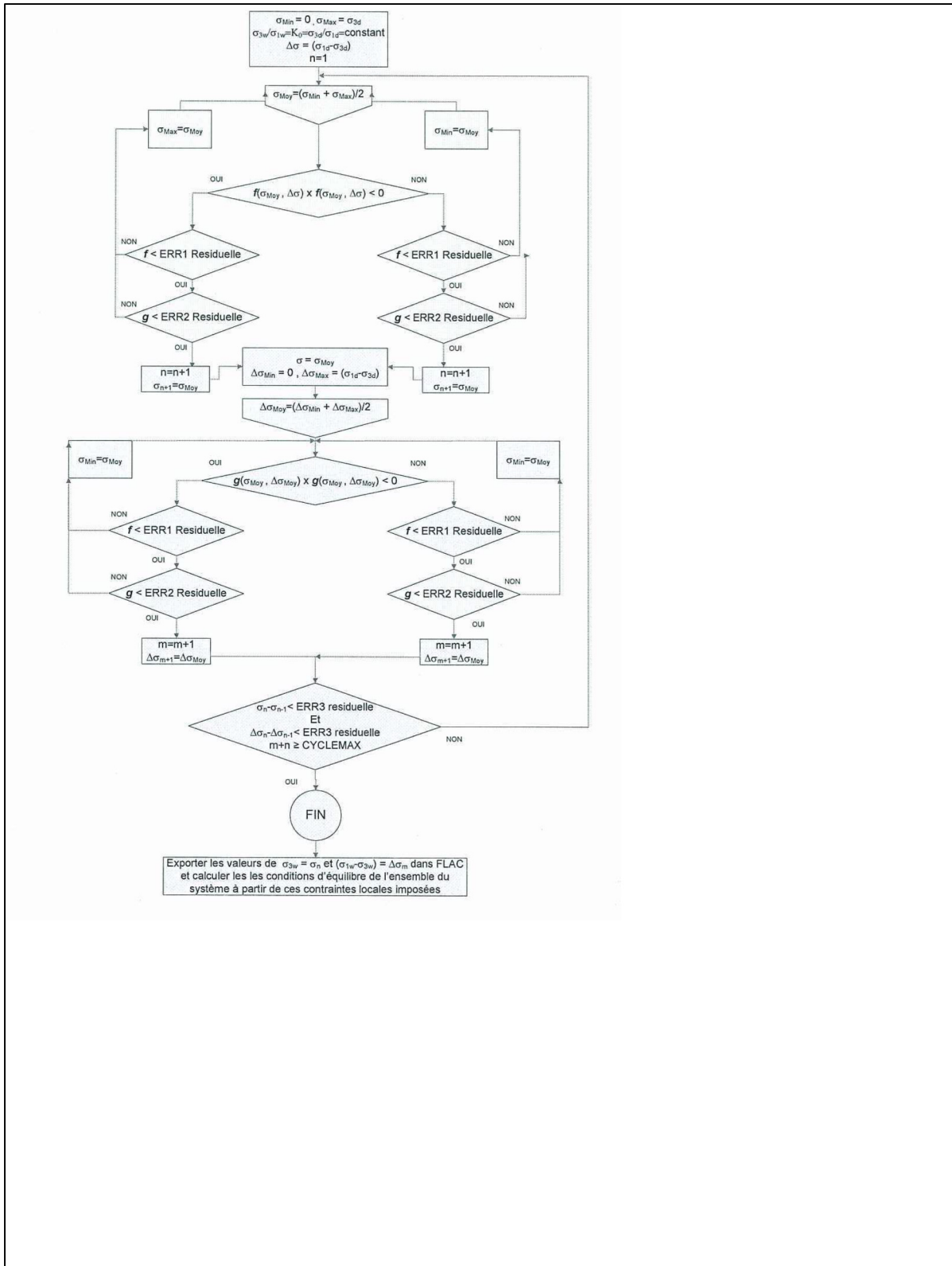


Figure 3.30 Solving flowchart (Simon Grenier, 2010)

In this part of the research, the Justo method is considered to simulate grain collapse due to wetting. Corresponding to the raised water elevation, a new stiffness is applied to each zone inside the upstream side. However, stiffness modulus variations do not affect the calculation in Zsoil. The reason is explained as follows:

This change of E modulus will not change the mechanical state of the material because the stress state is integrated in time as follows

$$\text{sig}_{n+1} = \text{sig}_n + E(t) * \text{delta-epsilon}_{n+1}$$

In this equation, $E(t)$ is changed; however, the stress state due to change of stiffness will not vary as there is no source for the lack of equilibrium that could produce some delta-epsilon; therefore, delta-epsilon is simply equal to zero.

In addition, using the Nobari–Duncan method requires programming, which demands the use of an open source software such as FLAC.

3.11.4 Plaxis Procedure

This process can be implemented by applying a volumetric strain to a cluster as shown in figure 3.31. First, the relevant cluster is exposed to contraction or expansion due to the induced strain while holding the same stress level in this cluster. Then, based on the strain changes, the reaction stress resulting from the surrounding soil and boundary conditions are calculated. Next, the imbalance caused by this reaction stress can be calculated, and in the last part, stress equilibrium is achieved in all relevant clusters and boundary conditions (Plaxis, 2014).

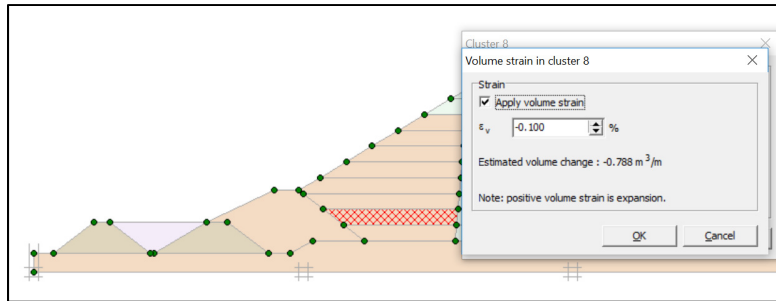


Figure 3.31 Applying a volumetric strain to a cluster

3.12 Results after impoundment

The induced deformations and stresses due to reservoir filling were computed by means of the FE method. The multistage modeling technique was used to increase the water level to an elevation of 240 m above the dam foundation. Corresponding to the raised water elevation, a new hydraulic boundary condition and hydrostatic pressure were applied. Moreover, the flow calculation was performed based on Darcy's law.

Previous studies carried out on instrumented dams imply that one of the key parameters contributing to differential displacement development during impoundment is the compression as a result of wetting (Nobari et Duncan, 1972). The behavior of rockfill materials at wetting can be explained as an irreversible deformation resulting from the lubrication and rock breakage at block contacts (Vannobel, 2013). None of the constitutive soil models (i.e., MC, HS, and Duncan–Chang) used in this study can simulate the strain softening behavior of geomaterials, collapse settlement (rock breakage), and time dependency. However, there is an alternative way to simulate grain collapse due to wetting in Plaxis software, that is, by prescribing a volume strain to the upstream shoulder cluster during the analysis.

The horizontal and vertical deformations resulting from impoundment calculation using MC and HS soil models are shown in figures 3.32 to 3.35. As a result of the hydrostatic pressure on the core, the horizontal displacement is in the downstream direction (figures 3.32 and

3.34). The largest horizontal displacement is observed approximately near the downstream crest. Correspondingly, the largest settlement due to wetting is observed near the upstream crest as shown in figures 3.33 and 3.35.

In addition, the predicted deformation mechanism of the Rankine wedge as a result of reservoir pressure on the asphalt core is shown in figures 3.33 and 3.35. Owing to buoyancy forces on the upstream side of the dam, upward movements within the saturated zones can be observed (figure 3.33). The maximum upward movement during impoundment on the upstream side of the dam calculated based on the MC model is limited to 22.5 cm.

Most of the numerical simulations based on various soil constitutive models predict some swelling movements in the upstream part, whereas such amount of upward movement usually cannot be observed in real embankment dams (Feizi-Khankandi et al., 2009). The HS soil model can consider the unloading modulus, hence a relatively lesser upward movement (4 cm) in comparison with the MC model (22.5 cm) can be observed.

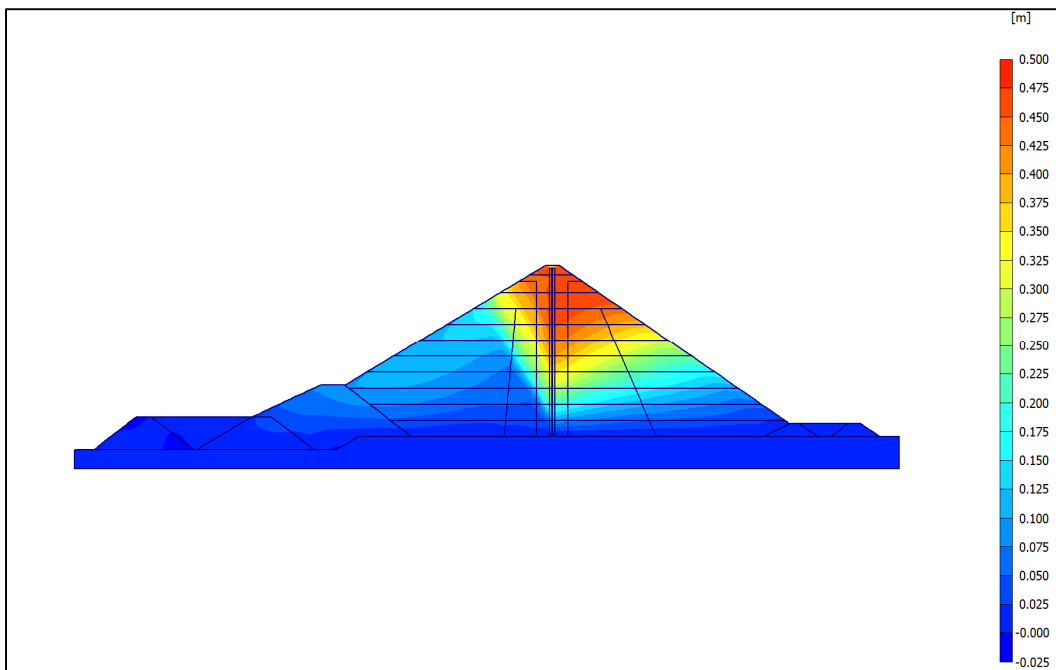


Figure 3.32 Horizontal displacement after watering analyzed based on the Mohr-Coulomb model

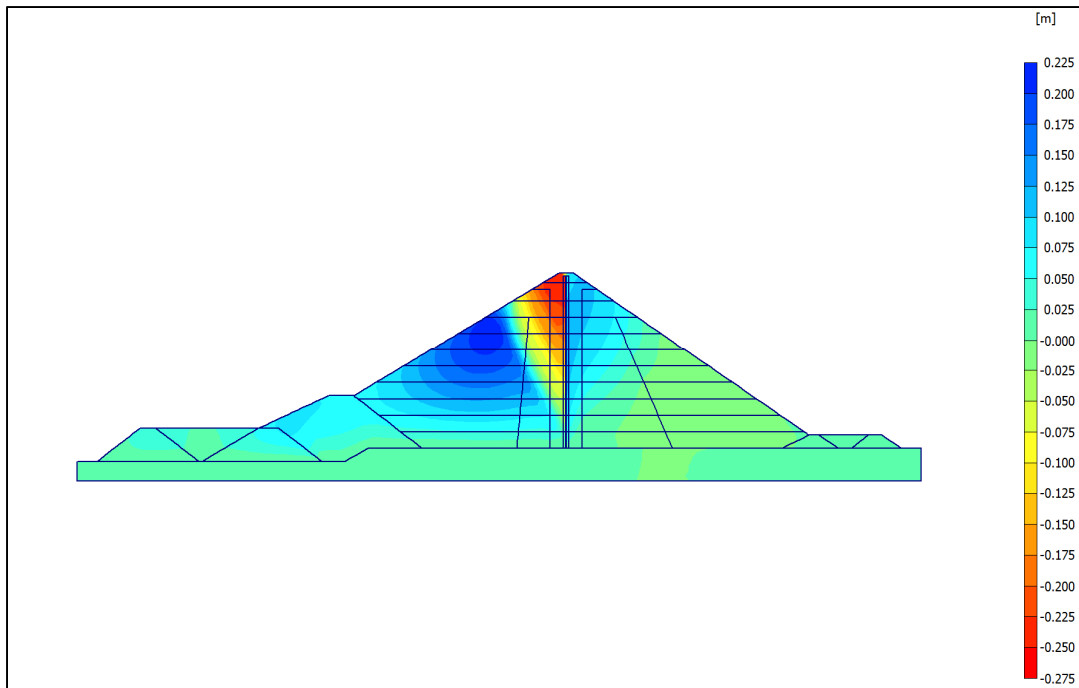


Figure 3.33 Vertical displacement after watering analyzed based on the Mohr-Coulomb model

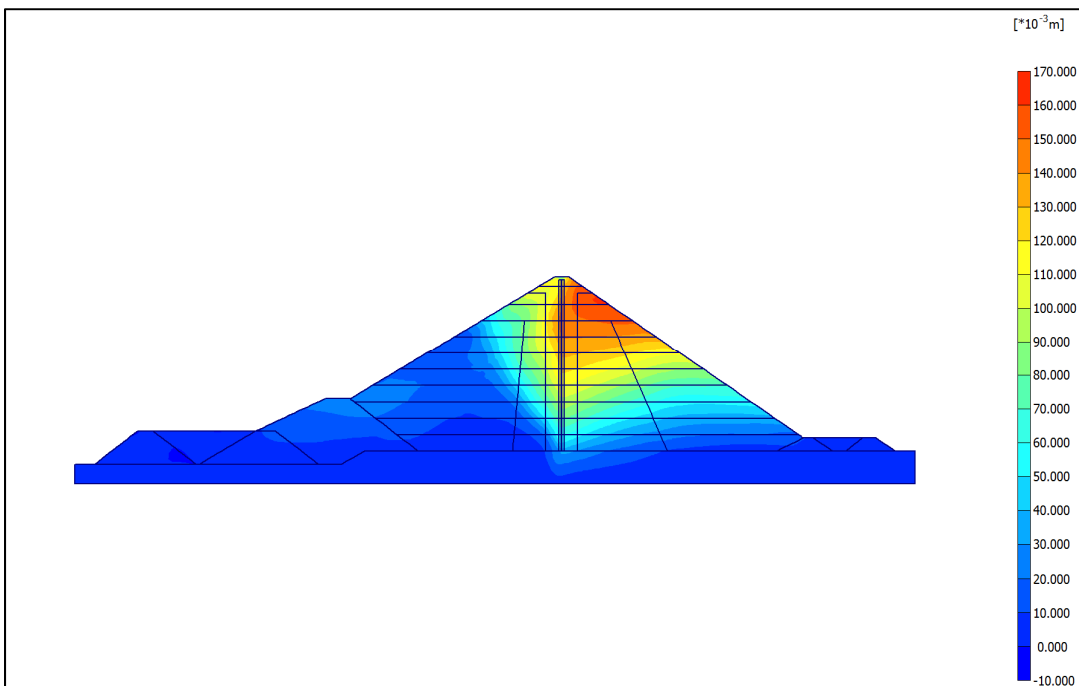


Figure 3.34 Horizontal displacement after watering analyzed based on the Hardening soil model

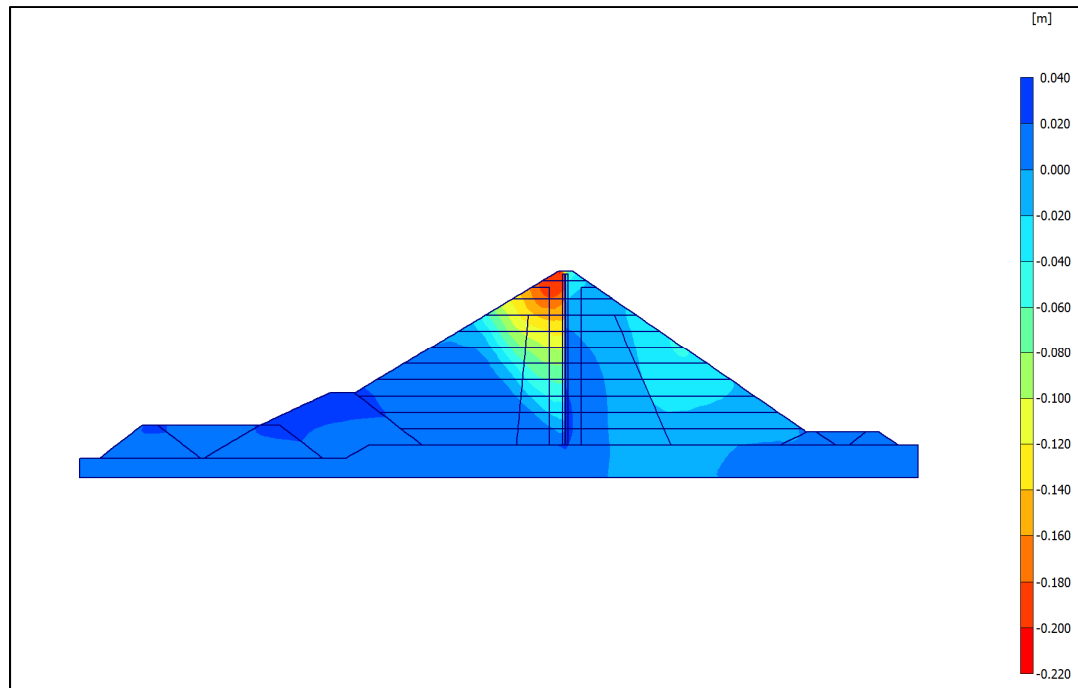


Figure 3.35 Vertical displacement after watering analyzed based on the Hardening soil model

3.12.1 Comparison between measured and computed displacements after impoundment (inclinometer INV-01)

Generally, the following results were observed because of the increase in water level behind the dam:

- 1) Horizontal displacements toward the downstream side as a result of the hydrostatic pressure (figure 3.37).
- 2) Upward movements within the saturated zone in the upstream side owing to buoyant forces (figures 3.33 and 3.35).
- 3) As a result of the wetting phenomenon discussed in the previous section, settlements (downward movements) within the upstream shell and transition (figure 3.36) (Nobari et Duncan, 1972; Qoreishi, 2013).

As shown in figure 3.36, the post-construction crest settlement is approximately 0.22% of the dam height, which is negligible compared with the dam height. The method of construction, rockfill strength, height of the dam, and other parameters can significantly influence the post-

construction crest settlement. Compacted rockfills have significantly lower crest settlement compared with dumped rockfills (Hunter et Fell, 2003b).

The movements measured by inclinometer INV-01, after reservoir filling, indicate a 25 cm settlement. The maximum predicted settlements using numerical simulations ($\epsilon_v = 0.1\%$) are 24.7 and 20 cm, respectively for the MC and HS soil models as shown in figure 3.36. This could indicate a high resistance, of rock materials used in the dam construction, to the wetting condition (Qoreishi, 2013). Furthermore, in terms of the location of the maximum value, the measured data and simulated values are similar.

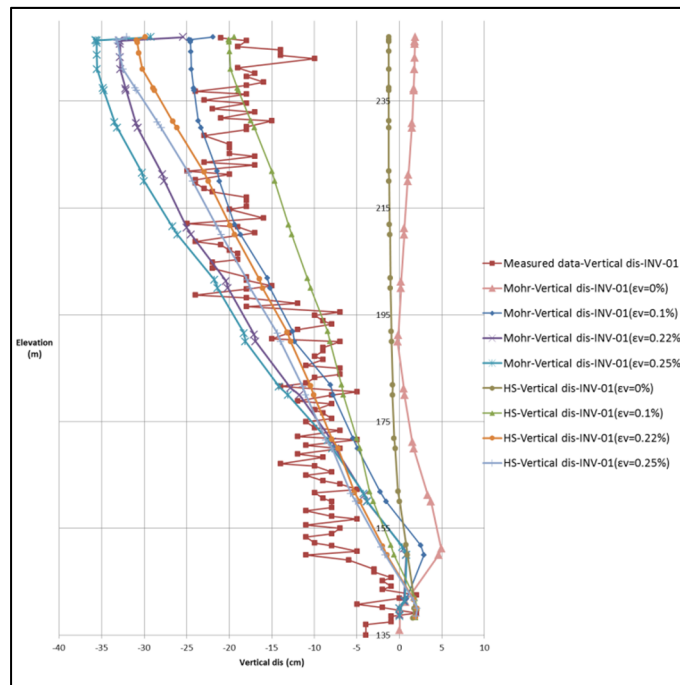


Figure 3.36 Vertical displacements after watering resulted by FE analysis and inclinometer (INV-01)

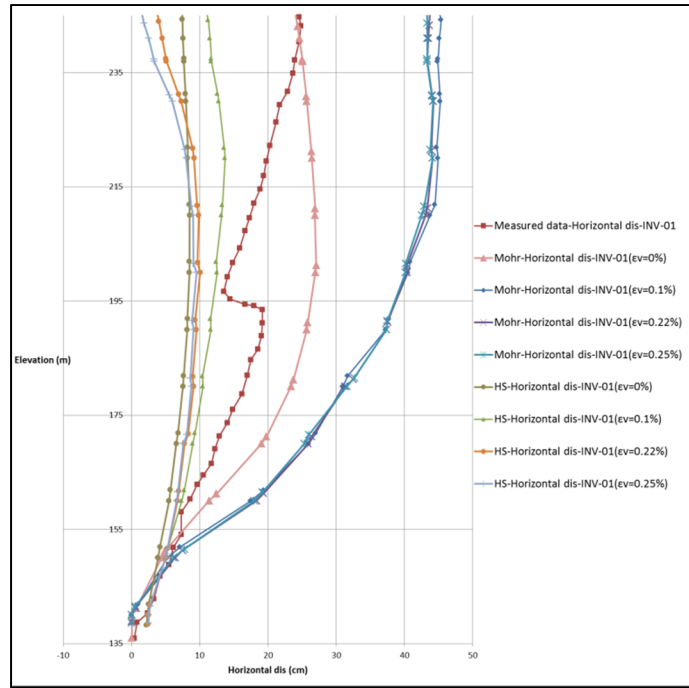


Figure 3.37 Horizontal displacements after watering resulted by FE analysis and inclinometer (INV-01)

Table 3.11 Absolute maximum horizontal and vertical displacement resulted by FE analysis at section INV-1

Soil model	Imposed volumetric strain (%)	Absolute maximum vertical displacement (cm)	Absolute maximum horizontal displacement (cm)
M-C	0	4.9	27
	0.1	24.7	45
	0.22	33.1	43.3
	0.25	35.5	43.3
HS	0	1.24	9
	0.1	20.5	13.7
	0.22	30.8	10.05
	0.25	33.1	9.49
Measurement	-	24.9	24.3

3.12.2 Comparison between measured and computed displacements after impoundment (inclinometer INV-02)

A comparison between the measurements obtained from inclinometer INV-02 and numerical simulation results are shown in figures 3.38 and 3.39. The inclinometer (INV-02) recorded small values of less than 10 cm settlement, which is in fair agreement with the simulation results calculated based on the HS soil model ($\epsilon_v = 0.1\%$ and 0%). However, the MC model ($\epsilon_v = 0.1\%$) predicts some swelling movements of approximately 10 cm as shown in figure 3.38. Since the simulation model behaves as a continuum, rotation towards the downstream or upstream as a result of displacement pattern can be observed (Qoreishi, 2013). In addition, the maximum recorded horizontal displacement at the crest is 32 cm. This value is computed as 14 cm for the HS soil model and approximately 45 cm for the MC model ($\epsilon_v = 0.1\%$) as shown in figure 3.39.

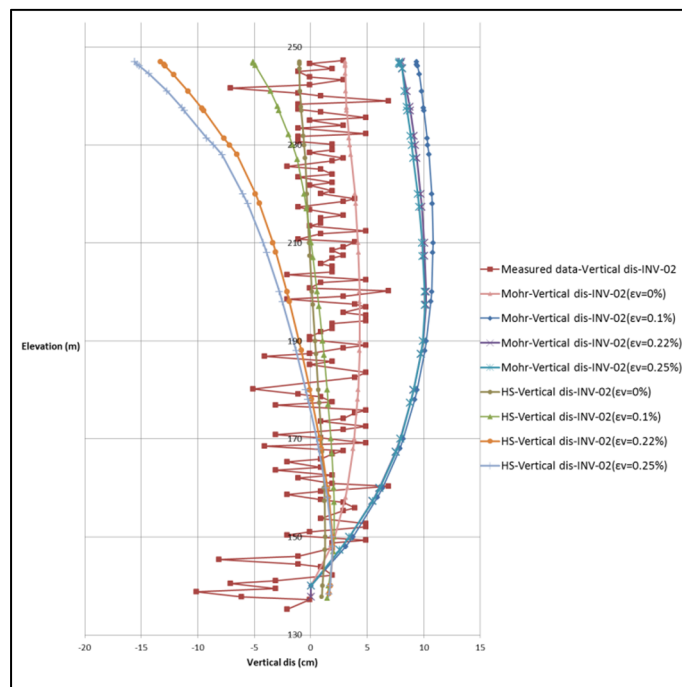


Figure 3.38 Vertical displacements after watering resulted by FE analysis and inclinometer (INV-02)

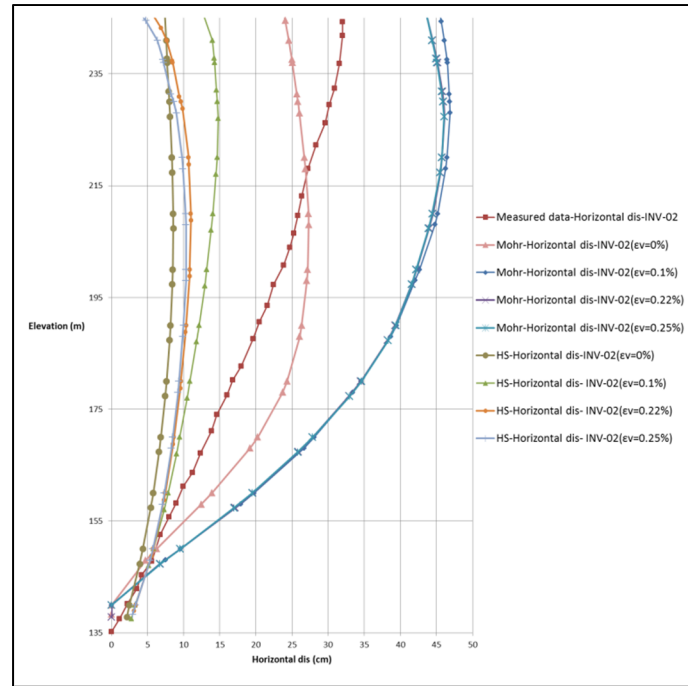


Figure 3.39 Horizontal displacements after watering resulted by FE analysis and inclinometer (INV-02)

Table 3.12 Absolute maximum horizontal and vertical displacement resulted by FE analysis at section INV-2

Soil model	Imposed volumetric strain (%)	Absolute maximum vertical displacement (cm)	Absolute maximum horizontal displacement (cm)
M-C	0	3	27
	0.1	10.7	46.7
	0.22	10.09	45.7
	0.25	10.09	45.7
HS	0	1.2	8.3
	0.1	5.09	14.5
	0.22	13.3	11
	0.25	15.5	10.29
Measurement	-	10	32

3.12.3 Comparison between measured and computed displacements after impoundment (inclinometer INV-03)

The measured vertical and horizontal displacements at the end of watering are shown in figures 3.40 and 3.41, respectively. The measured vertical displacement at section INV-3 in the downstream embankment varies around zero. The maximum settlement obtained by the HS soil model ($\varepsilon_v = 0.1\%$) is estimated to be 1.6 cm, while the MC model predicts some swelling movements in this section, approximately 7 cm (figure 3.40).

By raising the water level up to elevation 240 m, the measurement at INV-03 section shows a 30 cm horizontal displacement. The numerical simulation for $\varepsilon_v = 0\%$ is computed to be 8 cm for the HS soil model and approximately 26 cm for the MC model as shown in figure 3.41.

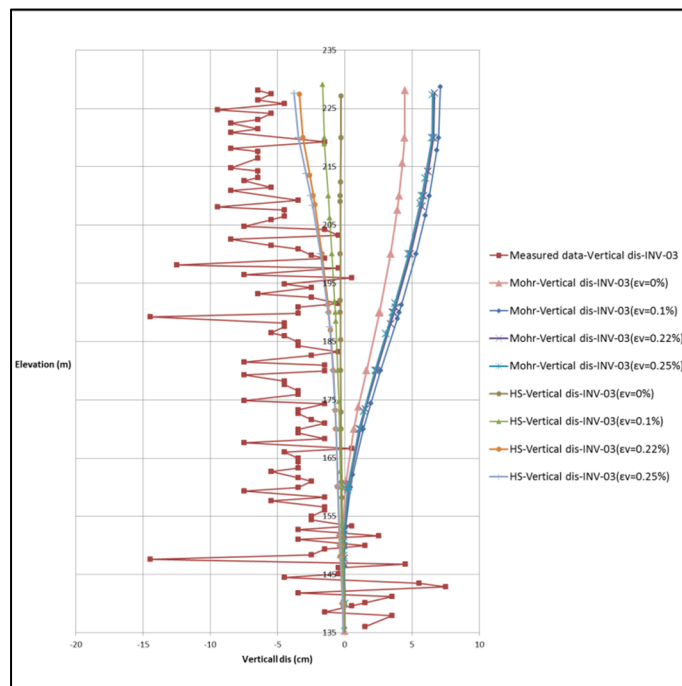


Figure 3.40 Vertical displacements after watering resulted by FE analysis and inclinometer (INV-03)

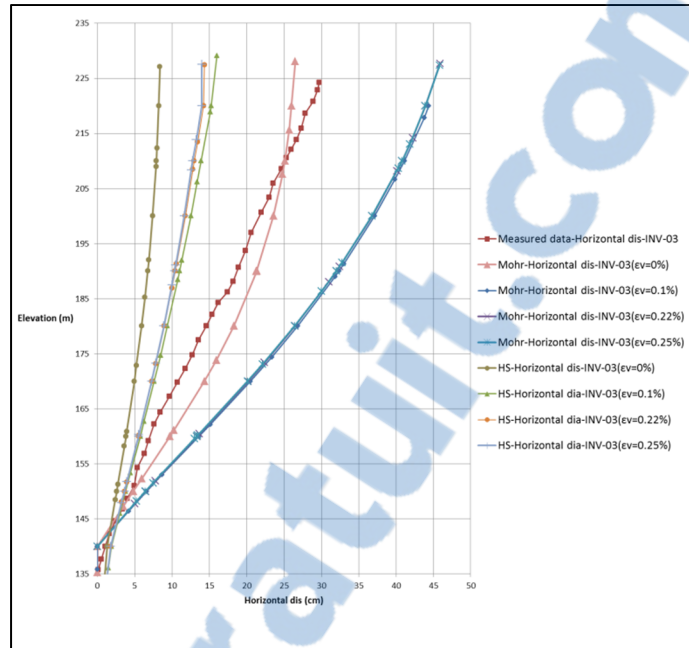


Figure 3.41 Horizontal displacements after watering resulted by FE analysis and inclinometer (INV-03)

Table 3.13 Absolute maximum horizontal and vertical displacement resulted by FE analysis at section INV-3

Soil model	Imposed volumetric strain (%)	Absoloute maximum vertical displacement (cm)	Absoloute maximum horizontal displacement (cm)
M-C	0	4.46	26.4
	0.1	7.11	45.8
	0.22	6.68	45.8
	0.25	6.68	45.8
HS	0	0.27	8.37
	0.1	1.6	16
	0.22	3.37	14
	0.25	3.77	14
Measurement	-	14.4	29.7

3.12.4 Comparison between measured and computed displacements after impoundment (inclinometer INH-01)

Figure 3.42 illustrates the vertical displacements measured using inclinometers INH-01, placed in the shell (zone 3O and 3P). The measurements agree closely with the computation using the HS soil model; however, there is poor agreement for the MC soil model. The calculated vertical displacement based on the HS soil model (4 cm) is less than the measured displacement (10 cm). The disagreement for the MC soil model could be the result of the dam rotation toward the downstream side by not considering the unloading stiffness.

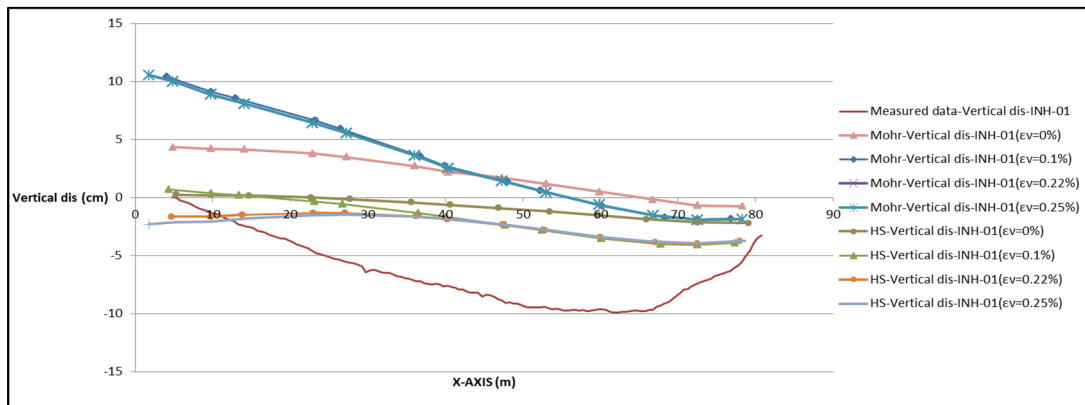


Figure 3.42 Vertical displacements after watering resulted by FE analysis and inclinometer (INH-01)

Table 3.14 Absolute maximum vertical displacement resulted by FE analysis at section INH-1

Soil model	Volumetric strain (%)	Absolute maximum vertical displacement (cm)
M-C	0	4.89
	0.1	10.5
	0.22	10.5
	0.25	10.5
HS	0	2.19
	0.1	3.95
	0.22	3.95
	0.25	3.95
Measurement	-	9.8

3.13 Shear wave velocity measurement

This part of the research follows the work done in previous section; however, it deals with the rockfill stiffness readjusted at different elevations of the dam as indicated in tables 3.15 to 3.20. The multi-modal analysis of surface wave or MMASW test is a nondestructive test and assists to designate the material stiffness based on the obtained wave velocity (Daniel Verret, 2013; Hunter et Crow, 2012). In this test, an impact at the ground surface stimulates a surface wave in most cases; a 60 kg hammer dropping from a height of 1.8 m generates the impact, and a series of 16 sensors positioned on the ground surface monitor the wave velocity. A tomographic presentation of the test results can be obtained from determined Vs profiles as shown in figure 3.43 (Vannobel, 2013).

3.13.1 Material properties for zone 3O and 3P

Equation 3.20 shows the relationship between the shear wave velocity measured using the MMASW test and initial Young's modulus used in the Duncan-Chang model (Karry, 2014).

In fact, this equation shows a relationship between K (modulus number in the Duncan-Chang model) and V_{s1} , and n (the exponent in the Duncan-Chang model) and V_{s1} .

$$E_i = 21.6e^{0.012V_{s1}}P_a \left(\frac{\sigma_3}{P_a}\right)^n, \text{ and } n = 0.0665e^{0.0035V_{s1}} \quad (3.20)$$

where

E_i is the initial tangent modulus, σ_3 is the minor principal stress, P_a is the atmospheric pressure (100 kPa), and V_{s1} is the normalized shear wave velocity

The normalized shear wave velocity can be determined as

$$V_{s1} = V_s \left(\frac{100}{\sigma_3}\right)^{0.25} \quad (3.21)$$

where V_s is the shear wave velocity

Three different soil stiffnesses i.e. E_{50} , E_{ur} , and E_{oed} are defined in the HS and HSS models. E_{50} is the confining stress-dependent stiffness modulus, which can be calculated using equation 3.22.

$$E_{50} = E_{50}^{ref} \left(\frac{c \cos\phi - \sigma_3 \sin\phi}{c \cos\phi + p^{ref} \sin\phi}\right)^m \quad (3.22)$$

as the cohesion is 0, $E_{50} = E_{50}^{ref} \left(\frac{\sigma_3}{p^{ref}}\right)^m$

It is assumed that $E_{50} = E_i$ (Equations 3.20 and 3.22) and $n=m$; therefore,

$$E_{50}^{ref} = 21.6e^{0.012V_{s1}}P_a$$

The following assumptions are made, in the HS and HSS soil models:

$$E_{50}^{ref} \approx E_{oed}^{ref}, \text{ and } E_{ur}^{ref} = 2E_{50}^{ref}$$

Compared to the HS model, the HSS model needs two additional parameters i.e. G_0^{ref} and γ_{70} . All other parameters are the same as in the HS model (Brinkgreve et Broere, 2006).

Small strain shear stiffness, G_0 is defined as

$$G_0 = G_0^{\text{ref}} \left(\frac{c \cos \varphi - \sigma'_3 \sin \varphi}{c \cos \varphi + p^{\text{ref}} \sin \varphi} \right)^m \quad (3.23)$$

$$G_0 = \frac{E_0}{2(1+\theta)} \quad (3.24)$$

As the cohesion is 0, $G_0 = G_0^{\text{ref}} \left(\frac{\sigma'_3}{p^{\text{ref}}} \right)^m$

where G_0^{ref} is the reference shear modulus at very small strain, and $E_0 = 1.5E_{\text{ur}}$.

$$G_0 = G_0^{\text{ref}} \left(\frac{\sigma'_3}{p^{\text{ref}}} \right)^m = \frac{E_0}{2(1+\theta)} = \frac{1.5 * 2 * 21.6 e^{0.012 V_{S1} P_a} \left(\frac{\sigma'_3}{P_a} \right)^n}{2(1+\theta)} \quad (3.25)$$

$$G_0^{\text{ref}} = \frac{32.4 e^{0.012 V_{S1} P_a}}{(1+\theta)} \quad (3.26)$$

Also, $\gamma_{0.7}$ is the strain level at which the shear modulus has reduced to 70% of the small strain shear modulus, it is defined as $\gamma_{70} = 10^{-4}$.

Table 3.15 Mohr-Coulomb soil model parameters used for rockfill dam simulation at zone 3O

Elevation	V_{S1} (m/s) [240-380]	σ_3 (KN/m ²)	E (MPa)
230-240	280	60.5	56.32174
220-230	280	94	60.88123
210-220	280	115	63.08895
200-210	300	128	81.93162
190-200	300	179	87.3052
180-190	340	217	149.365
170-180	340	339	164.6058
160-170	360	376	218.3791
150-160	360	613	244.7853
140-150	360	839	263.4009

Table 3.16 Mohr-Coulomb soil model parameters used for rockfill dam simulation at zone 3P

Elevation	V_{S1} (m/s) [260-340]	σ_3 (KN/m ²)	E (MPa)
210-220	280	87.5	60.11542
200-210	280	129	64.38238
190-200	280	166	67.31537
180-190	280	208	70.05172
170-180	280	244.5	72.08134
160-170	280	275	73.59391
150-160	280	323	75.71552
140-150	280	393	78.38525

Table 3.17 HS soil model parameters used for rockfill dam simulation at zone 3O

Elevation	V_{S1} (m/s) [240-380]	E_{50}^{ref} (KN/m ²)	E_{ur}^{ref} (KN/m ²)	E_{oed}^{ref} (KN/m ²)
230-240	280	62184.65	124369.3	62184.65
220-230	280	62184.65	124369.3	62184.65
210-220	280	62184.65	124369.3	62184.65
200-210	300	79052.19	158104.4	79052.19
190-200	300	79052.19	158104.4	79052.19
180-190	340	127754.2	255508.4	127754.2
170-180	340	127754.2	255508.4	127754.2
160-170	360	162407.4	324814.9	162407.4
150-160	360	162407.4	324814.9	162407.4
140-150	360	162407.4	324814.9	162407.4

Table 3.18 HS soil model parameters used for rockfill dam simulation at zone 3P

Elevation	V_{S1} (m/s) [260-340]	E_{50}^{ref} (KN/m ²)	E_{ur}^{ref} (KN/m ²)	E_{oed}^{ref} (KN/m ²)
210-220	280	62184.6523	124369.3	62184.6523
200-210	280	62184.6523	124369.3	62184.6523
190-200	280	62184.6523	124369.3	62184.6523
180-190	280	62184.6523	124369.3	62184.6523
170-180	280	62184.6523	124369.3	62184.6523
160-170	280	62184.6523	124369.3	62184.6523
150-160	280	62184.6523	124369.3	62184.6523
140-150	280	62184.6523	124369.3	62184.6523

Table 3.19 HSS soil model parameters used for rockfill dam simulation at zone 3O

Elevation	V_{S1} (m/s) [240-380]	E_{50}^{ref} (KN/m ²)	E_{ur}^{ref} (KN/m ²)	E_{oed}^{ref} (KN/m ²)	G_0^{ref} (KN/m ²)
230-240	280	62184.65	124369.3	62184.65	77730.82
220-230	280	62184.65	124369.3	62184.65	77730.82
210-220	280	62184.65	124369.3	62184.65	77730.82
200-210	300	79052.19	158104.4	79052.19	98815.23
190-200	300	79052.19	158104.4	79052.19	98815.23
180-190	340	127754.2	255508.4	127754.2	159692.8
170-180	340	127754.2	255508.4	127754.2	159692.8
160-170	360	162407.4	324814.9	162407.4	203009.3
150-160	360	162407.4	324814.9	162407.4	203009.3
140-150	360	162407.4	324814.9	162407.4	203009.3

Table 3.20 HSS soil model parameters used for rockfill dam simulation at zone 3P

Elevation	V_{S1} (m/s) [260-340]	E_{50}^{ref} (KN/m ²)	E_{ur}^{ref} (KN/m ²)	E_{oed}^{ref} (KN/m ²)	G_0^{ref} (KN/m ²)
210-220	280	62184.6523	124369.3	62184.6523	77730.82
200-210	280	62184.6523	124369.3	62184.6523	77730.82
190-200	280	62184.6523	124369.3	62184.6523	77730.82
180-190	280	62184.6523	124369.3	62184.6523	77730.82
170-180	280	62184.6523	124369.3	62184.6523	77730.82
160-170	280	62184.6523	124369.3	62184.6523	77730.82
150-160	280	62184.6523	124369.3	62184.6523	77730.82
140-150	280	62184.6523	124369.3	62184.6523	77730.82

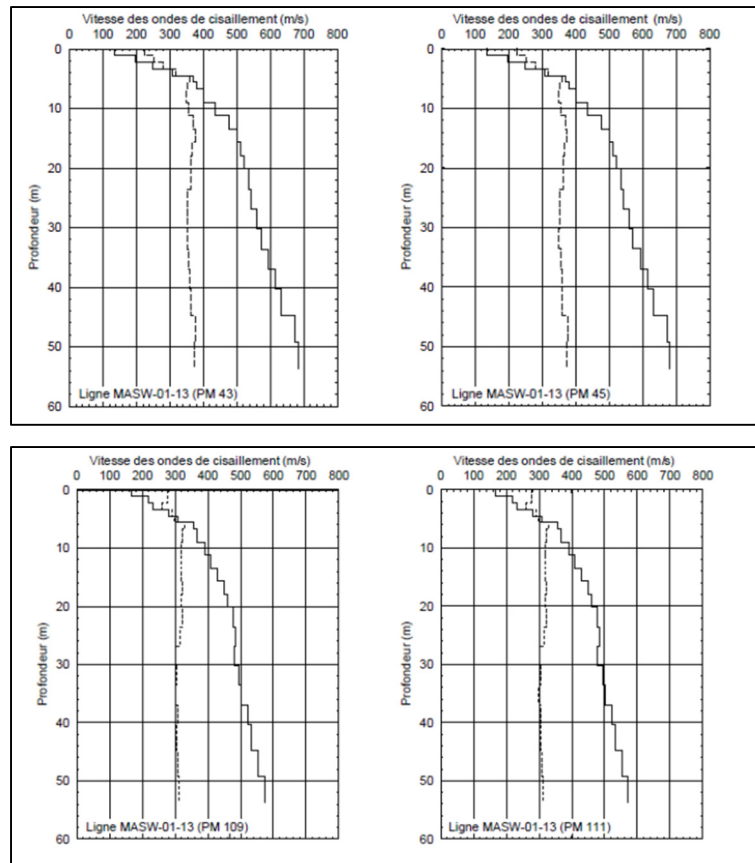


Figure 3.43 Normalized shear wave velocity at zones 3O and 3P(Guy Lefebure, 2014)

3.13.2 Comparison between measured and computed displacements

Figures 3.45 to 3.52 show the results corresponding to vertical inclinometers INV-01, 02, 03 and longitudinal inclinometers INH-01, and 02. In general, the agreement between the measured data and calculated results are acceptable.

It should be noted that, for the same coordinates, inclinometers INV-03, INH-01, and INH-02 record different values (see figure 3.44 for intersection points). It means that the rockfill material properties could change in the out-of-plane direction. Finally, for a better prediction of the dam, we need to define the problem in three-dimensional space or simulate the model for different sections in the z direction.

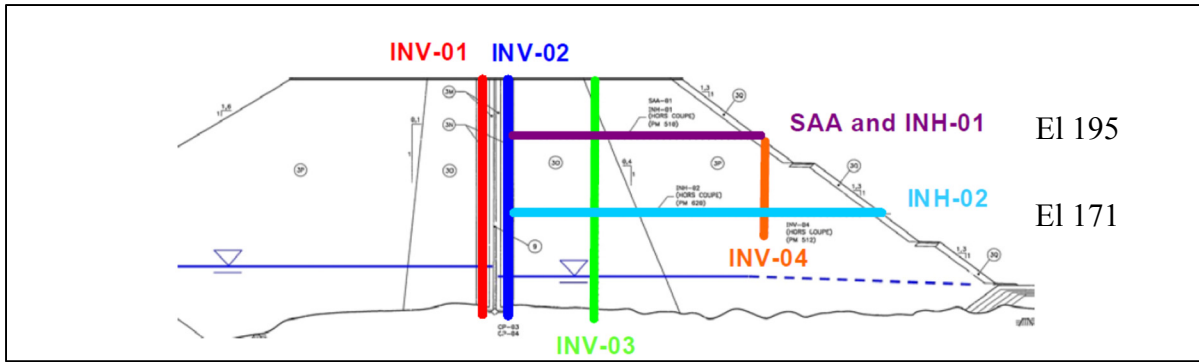


Figure 3.44 Inclinometers placement (Vannobel, 2013)

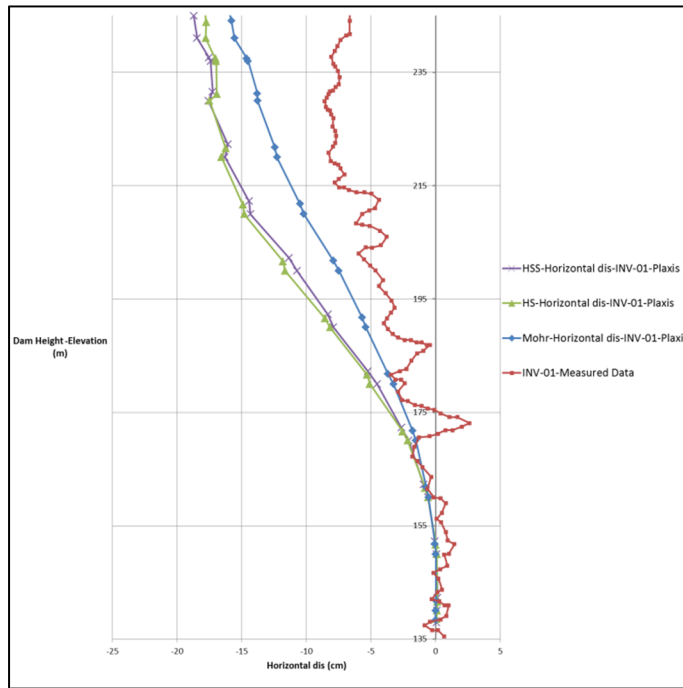


Figure 3.45 Accumulated horizontal displacements at section (INV-01)

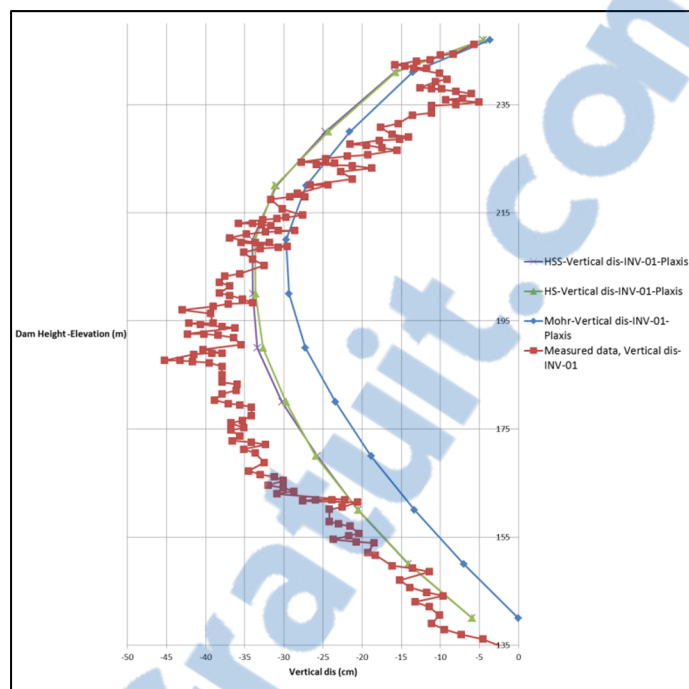


Figure 3.46 Vertical displacements at section (INV-01)

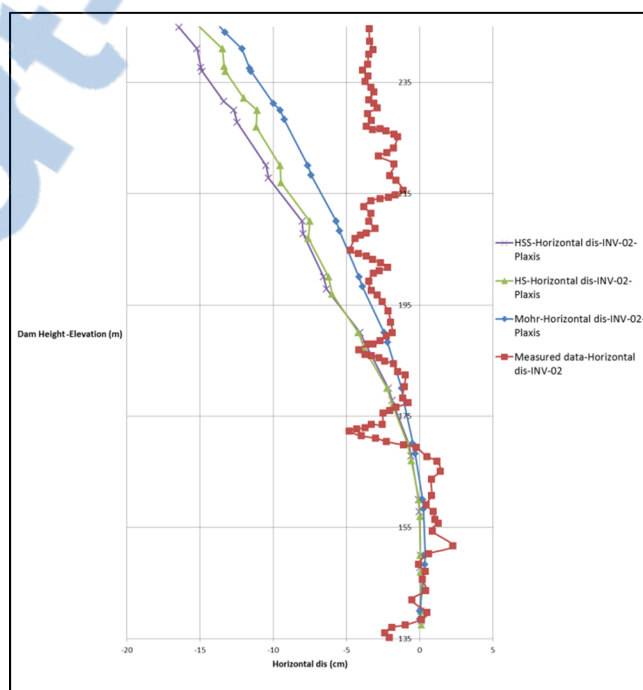


Figure 3.47 Accumulated horizontal displacements at section (INV-02)

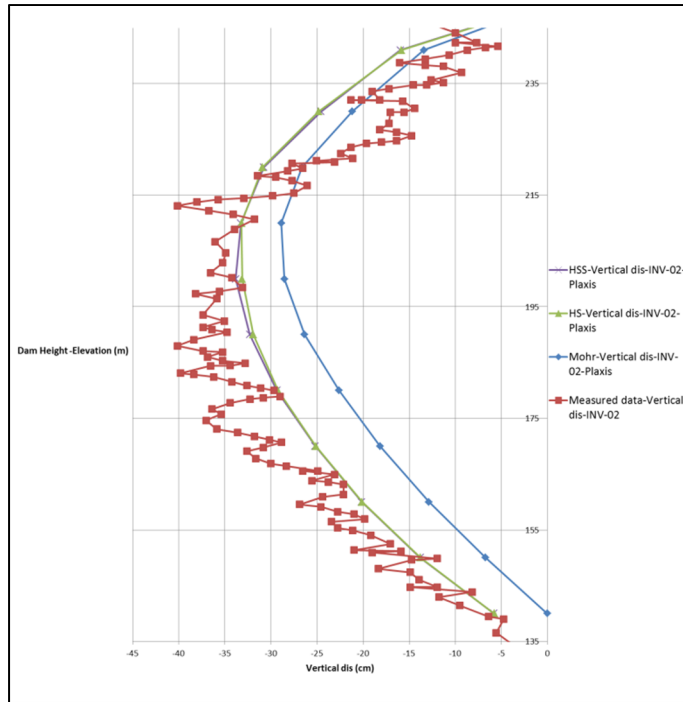


Figure 3.48 Vertical displacements at section (INV-02)

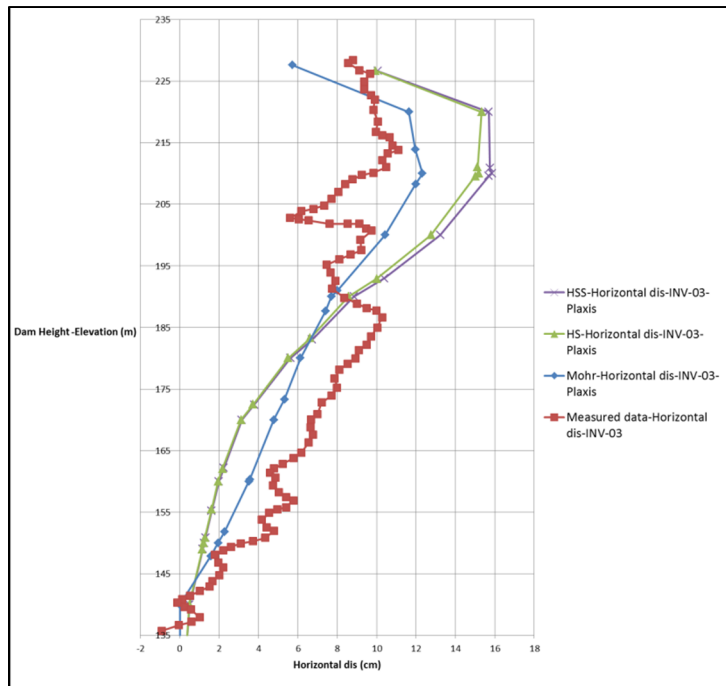


Figure 3.49 Accumulated horizontal displacements at section (INV-03)

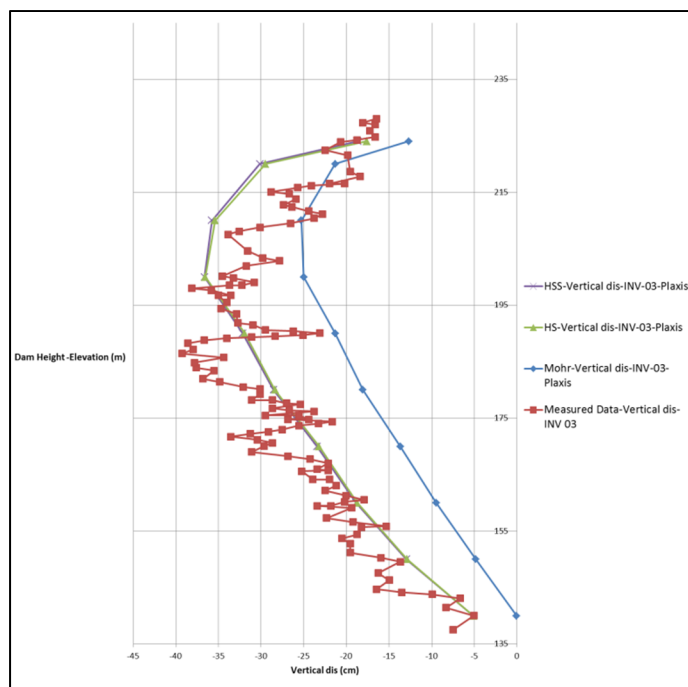


Figure 3.50 Vertical displacements at section (INV-03)

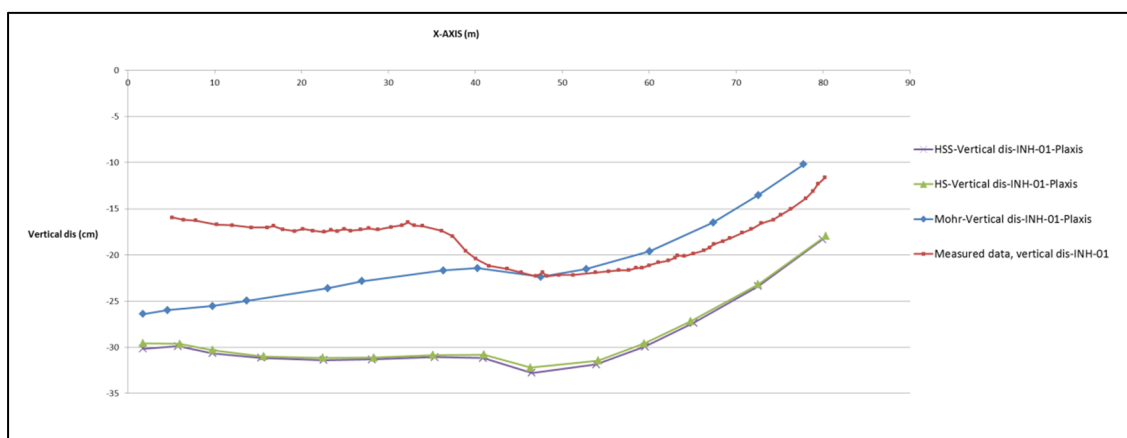


Figure 3.51 Vertical displacements at section (INH-01)



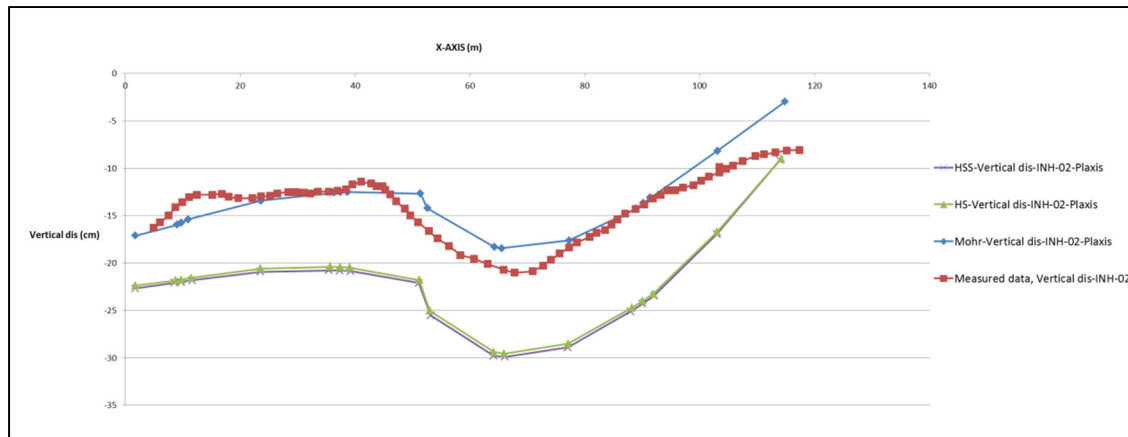


Figure 3.52 Vertical displacements at section (INH-02)

3.14 Concluding remarks

This chapter focuses on the comparison of the measured data from monitoring instruments and the results of numerical analysis of Dam-X. Dam-X is an asphaltic core rockfill dam constructed on a river in the North Shore region of Québec.

The monitoring program in Dam-X comprises vertical inclinometers on both sides of the core (INV-01 and INV0-2), vertical and horizontal inclinometers in the downstream shells (INV-03, INV-04, INH-01, and INH-02). The rockfill dam is analyzed numerically using a finite element commercial software at different stages of construction and after impoundment.

The measured data from the monitoring program indicate the actual response of Dam-X. As the dam was heavily compacted, the movements measured by the inclinometers are small compared with the dimensions of the dam. The numerical analyses using HS and MC soil models can predict the dam performance with fair accuracy before wetting condition. At the end of construction, the settlement profile has the extremum near the mid-height of the dam, and the maximum accumulated horizontal displacement emerges at the crest. This good agreement demonstrates the validity of the numerical simulation.

Generally, the following results were observed because of the increase in water level behind the dam:

- 1) Horizontal displacements toward the downstream side as a result of the hydrostatic pressure
- 2) Upward movements within the saturated zone in the upstream side owing to buoyancy forces
- 3) Downward movements within the upstream shell and transition as a result of the wetting phenomenon
- 4) The anticipated deformation mechanism of the Rankine wedge because of the reservoir pressure on the asphalt core

CONCLUSION

In the first part of this research, data from earlier experiments available in reports (Brinkgreve, 2007; Schanz et Vermeer, 1996) were used to obtain the parameters for modeling and to compare the various constitutive models, i.e., Duncan–Chang, MC, HS, and HSS in Zsoil and Plaxis. The comparison was conducted by modeling a consolidated drained triaxial test. It was shown that a simple linear function as in the MC model is not sufficient to describe the soil stress–strain relation completely. The Duncan–Chang, HS, and HSS provide a better fitting stress–strain curve in comparison with MC; however, they fail to account for softening in dense sand. For the volumetric strain versus axial strain, both HS and HSS have an acceptable accuracy and are better than the MC and Duncan–Chang.

The oedometer experimental results show a permanent strain after each loading and unloading, whereas the Duncan–Chang model displays elastic behavior and deformation that does not comprise irreversible plastic strain. Both the HS and HSS soil constitutive models can reproduce the non-linear original loading portion and differentiate between loading and unloading.

The HS standard model cannot generate hysteretic soil behavior, which can be observed in the experimental test during loading. In contrast, the results obtained indicate that the HSS can produce more precise and consistent estimation of the stress–strain analysis (simulating hysteretic soil behavior).

The second part of this research is focused on the evaluation of the HS, Duncan–Chang, and MC soil models by numerical simulation of the Dam-X. To make a comparison with field data, the soil models were numerically implemented into the finite element programs, Plaxis and Zsoil. The parameters used for the transition zones are chosen based on the recommended Storvatn dam material properties (Benoit Mathieu, 2012). However, for the shell materials, higher stiffness values compared with those of NGI are assumed. In addition, different unloading and reloading stiffness values were assumed for the HS model.

The dam is not perfectly symmetrical; thus, a horizontal displacement towards the upstream side can be observed at the crest. The MC soil model can predict the accumulated horizontal displacement with fair accuracy before watering.

As the rockfill materials are well compacted, the measured and computed vertical displacements are relatively smaller compared with the size of the dam. The MC, HS, and measured data overlap with each other, and provide a better fit when compared with those of Duncan–Chang.

The Justo method was considered to simulate the grain collapse due to wetting. Corresponding to the raised water elevation, a new stiffness is applied to each zone inside the upstream side. However, the stiffness modulus variations do not affect the calculations in Zsoil and Plaxis.

In addition, none of the constitutive soil models, i.e., MC, HS, and Duncan–Chang, used in this study can simulate the strain-softening behavior of geomaterials, collapse settlement (rock breakage), and time dependency.

Finally, as an alternative way to simulate the grain collapse phenomenon due to wetting, a prescribed volume strain was applied to the upstream shoulder cluster during the analyses. A good prediction was achieved for most of the dam movements during the reservoir filling. The simulation results and in situ measurements after reservoir filling indicate that the maximum settlement due to the collapse occurs near the crest at the upstream side. In addition, the maximum horizontal displacement due to the hydrostatic pressure during reservoir filling takes place near the crest at the downstream side of the dam.

RECOMMENDATIONS

- 1- Variations in the volumetric strain should be implemented based on laboratory tests and corresponding stress level. Conducting sufficient experimental tests can be helpful in choosing an appropriate volumetric strain variation corresponding to stresses in each level of the dam.
- 2- None of the constitutive soil models used in this study could simulate the strain softening. To improve the dam prediction after watering, using a constitutive soil model such as Barcelona (Costa et Alonso, 2009), which can model wetting, is essential.

APPENDIX I

Triaxial Test

1.1 Introduction

Plaxis and Zsoil are finite element software applications that have been developed specifically for stability and deformation analysis in geotechnical engineering projects. This appendix contains instructions for simulating a triaxial test in Zsoil and Plaxis. In this appendix, the name of the software menu and the buttons used are **bolted**.

1.2 Zsoil

The images shown in this appendix are taken from the simulation of the triaxial test, which was run by the Zsoil PC 2014 3D student version. The steps are as follows:

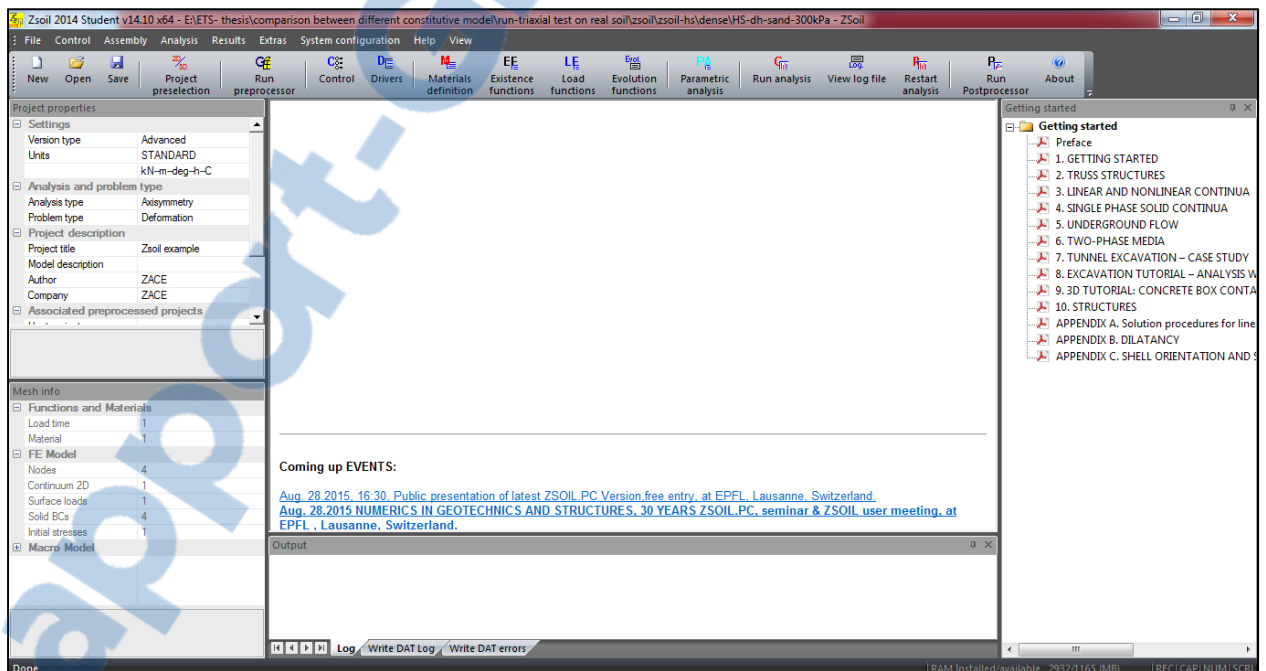


Figure 1.1 The main window in Zsoil

1.2.1 Project Preselection

Once the Zsoil is opened, the **start window** appears wherein, under the **new project** tab, the **axisymmetric model** is selected (figure 1.2). Consequently, the **preselection** window appears in which the details of the project are filled in as shown in figure 1.3. In the project preselection menu, the problem type is set as deformation, and the SI system of units is selected. The name of the project is keyed into the Project title tab (figure 1.3).

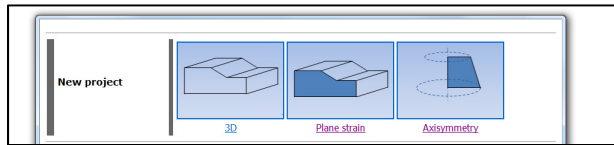


Figure 1.2 Start window

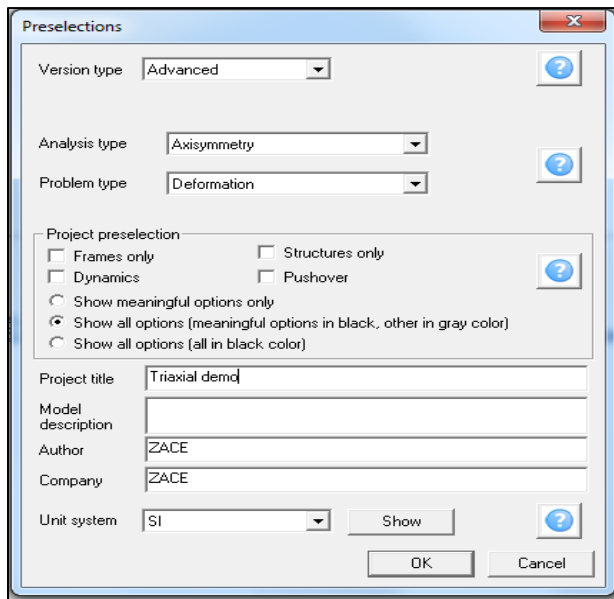


Figure 1.3 Preselection window

1.2.2 Material Definition

The properties of the material are defined in **Assembly/materials** (figure 1.4). By choosing this option, a new dialog box appears (figure 1.5). In the dialog box, the **add** button is selected to define a new material; consequently, another dialog box appears (**Add/Update material**) to choose the material type (figure 1.6). A new material is added to the material list with parameters that can be modified according to the analysis requirement (figure 1.6). To identify the soil type, it can be named as “Hostun sand” in the **Name** box in the **Add/Update material** window (figure 1.6). Various constitutive models can be defined to simulate the soil behavior. The HSS stiffness soil model is chosen from the **material formulation** combo box. The soil weight is not considered in this simulation (figure 1.7); hence, the general properties are left as zero, as shown in figure 1.7. Select **Non-linear** and **Elastic** tabs to

proceed with the material parameters. The parameters pertaining to the selected soil model can be seen in the parameter tab sheet (figures 1.8 and 1.9).

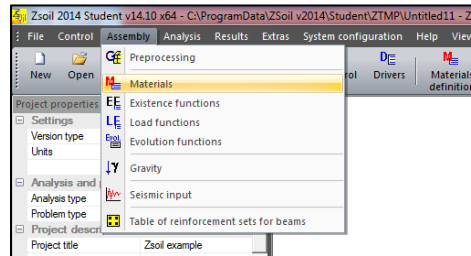


Figure 1.4 Assembly menu, choosing Material

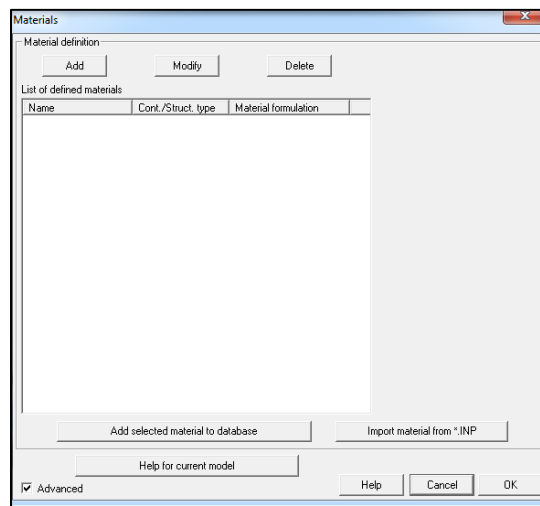


Figure 1.5 Materials window

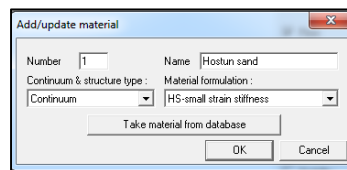


Figure 1.6 Add/update window

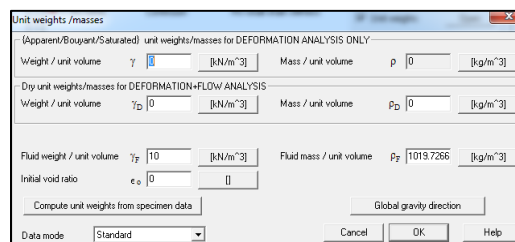


Figure 1.7 Weight window

HS-small strain stiffness

Stiffness setup

Demanded secant reference E modulus at 50% of E_{50}^{ref} 37000 [kN/m²]

Reference stress for Young modulus σ_{ref} 100 [kN/m²]

Shear mechanism

Friction angle ϕ 41 [deg]

Dilatancy angle ψ 0 [deg]

Cohesion c 0 [kN/m²]

Failure ratio R_f 0.9

Tensile cut-off Tensile strength t_t 0 [kN/m²]

Cap (volumetric) mechanism

Hardening parameter H 57882.7 [kN/m²]

Hardening parameter M 1.33559

M, H calculator based on oedometric test

Automatic evaluation of H and M parameters

Given: Oedometric tangent modulus E_{oed}^{ref} 29500 [kN/m²]

Reference vertical stress σ_{oed}^{ref} 100 [kN/m²]

Ko coefficient K_o^{NC} 0.344 Apply Jaky's formula for KoNC

Compute M, H

Setting initial state variables with respect to the initial stress state

Through overconsolidation ratio OCR 1

Through preoverburden pressure POP q 0 [kN/m²]

Historical consolidation setup

Ko coefficient K_o^{SS} 0.344

Ko^{NC} consolidation

Isotropic consolidation

Anisotropic consolidation

Minimum preconsolidation stress p_{co}^{min} 1 [kN/m²]

Advanced Convert standard MC to HS model Help OK Cancel

Figure 1.8 Nonlinear properties

HS-small strain stiffness

Standard HS model setup

Young modulus un./rel. at ref. stress E_{50}^{ref} 30000 [kN/m²]

Reference stress for Young modulus σ_{ref} 100 [kN/m²]

Poisson ratio un./rel. ν_{un} 0.2

Exponent for power law m 0.5

Lower bound stiffness cut-off at stress σ_L 10 [kN/m²]

Small strain extension

Active

Initial Young modulus at ref. stress E_0^{ref} 270000 [kN/m²]

Threshold shear strain $\gamma_{0.7}$ 0.0002

Advanced Help OK Cancel

Figure 1.9 Elastic properties

1.2.3 Load Function

By selecting the **assembly/load function** menu, a new window appears in which a function of time can be defined (figure 1.10). Since, a strain control simulation is considered, the displacement is applied to the top edge nodes, and the load function defined in this section will be used in the boundary condition section (figure 1.19).

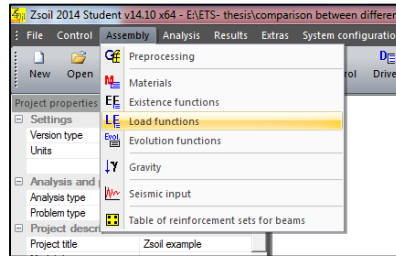


Figure 1.9 Assembly menu, choosing load function

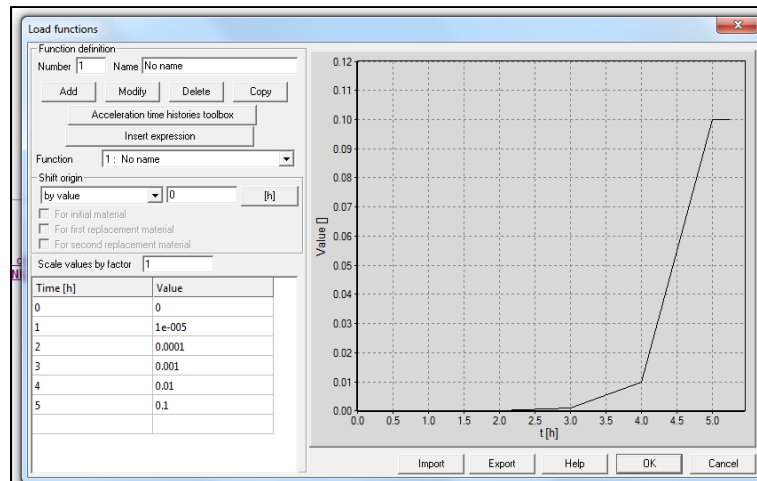


Figure 1.10 Load function

1.2.4 Control/Drivers

Control/drivers is selected from the main menu (figure 1.11). This window contains computational steps that will be carried out during the analysis. Different types of analysis (i.e., stability, time dependent, pushover, and dynamic analysis) can be used to simulate the soil behavior during the test. **Time dependent** analysis is selected from the **driver** combo box (see figure 1.12). The time is defined in the range of 0 to 5 (the maximum time step, which is defined in the previous stage, as shown in figure 1.10). A suitable time step of 0.1 is chosen.

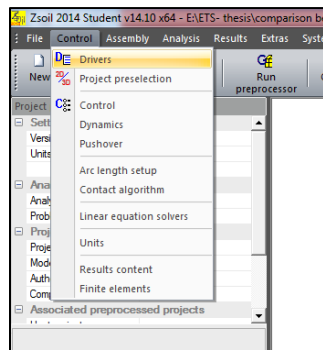


Figure 1.11 Control menu, choosing Driver

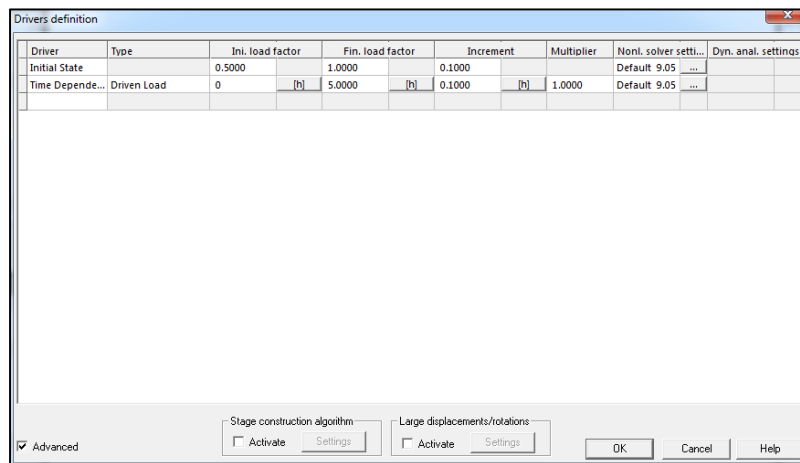


Figure 1.12 Driver definition

1.2.5 Preprocessing

Assembly/preprocessing is selected in the main menu (figure 1.13). A new window opens where the model can be made. In this step, the geometry of the model, mesh, boundary condition, and loading are created (figure 1.14).

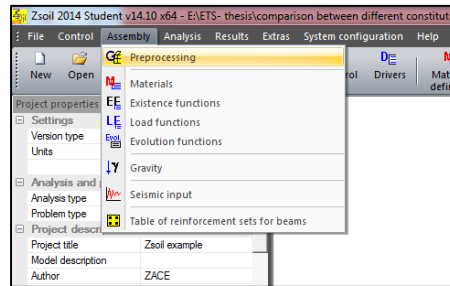


Figure 1.13 Assembly menu, preprocessing

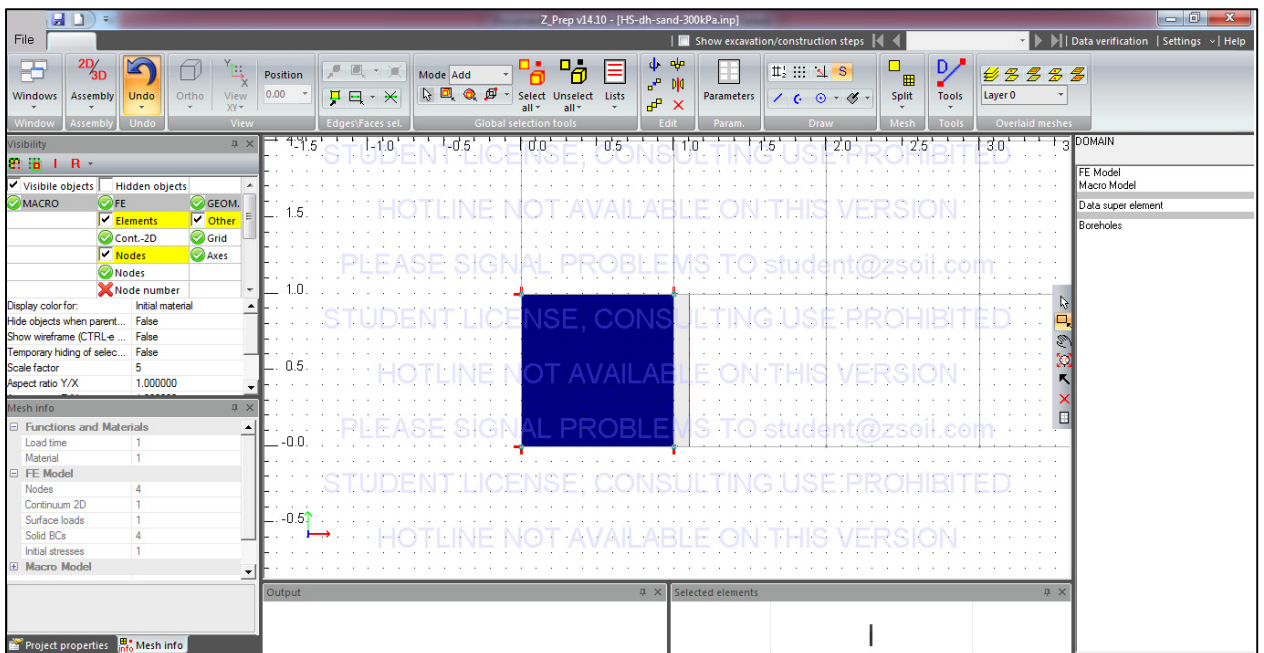


Figure 1.14 Preprocessing window

1.2.6 Geometry

To create the object, the **geometry line** tool is used; the geometry line can be found in the software toolbar. A square of size $1\text{ m} \times 1\text{ m}$ is created by using the draw line tool. Drawing the geometry will be implemented by positioning the cursor at points (0, 0) and moving to points (0, 1), (1, 1), and (1, 0). The geometry lines and points have now been created (see figure 1.15). In the toolbar on the right side, **MacroModel/subdomain/2D continuum inside contour** is selected, and the cursor is clicked inside the box to create a 2D domain inside the contour (figure 1.15).

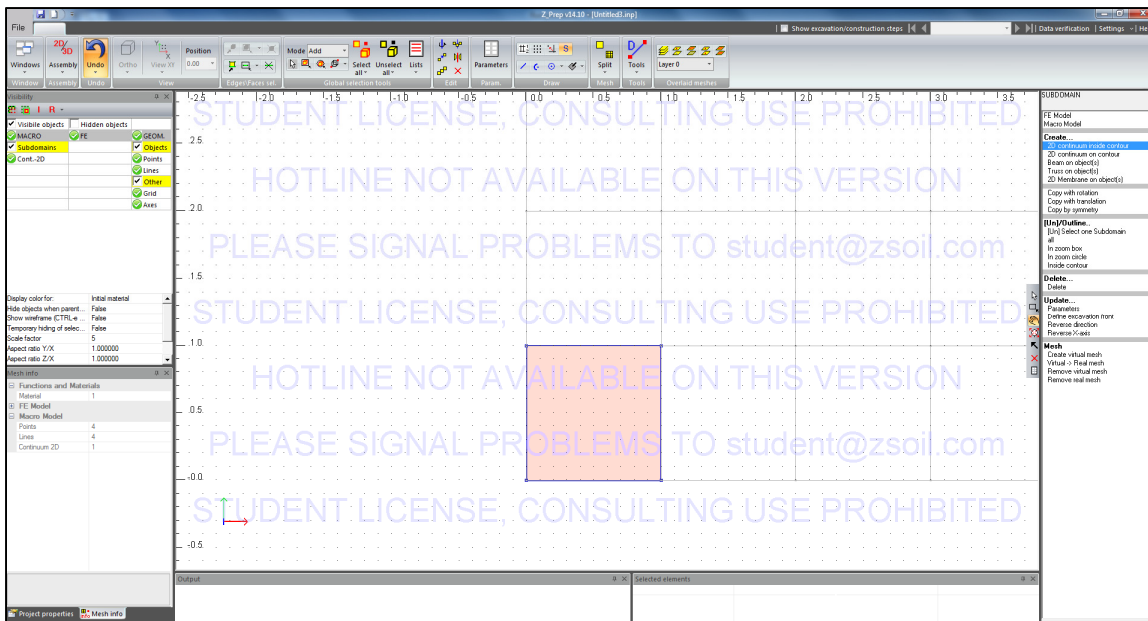


Figure 1.15 Geometry of model

1.2.7 Meshing

The next step is to create the mesh in the obtained subdomain, for which **MacroModel/subdomain/create virtual mesh** is selected and clicked inside the box. The meshing parameters dialog box appears as shown in figure 1.16. A quadrilateral type of mesh is selected. The number of times an edge is to be split can be defined in the menu for two adjacent edges.

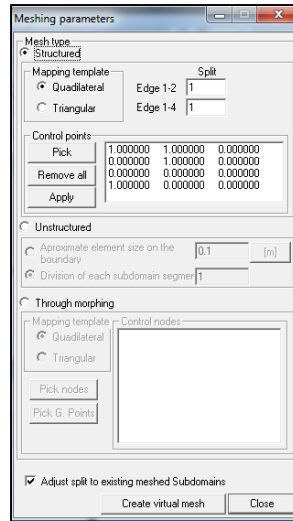


Figure 1.16 Meshing parameters

The virtual mesh is now ready to be changed to a real mesh. Ctrl+A is pressed to select the whole subdomain. **MacroModel/subdomain/virtual/real mesh** is selected to change the virtual mesh to a real mesh.

1.2.8 Boundary Condition

Once the geometry has been created, the boundary condition can be applied. The left and bottom sides of the model are fixed in the horizontal and vertical directions, respectively. The top boundary is assumed to move by the displacement function defined in section 1.2.3. **FE Model/boundary conditions/Solid Boundary condition/Create/on Nodes** are selected and clicked on left nodes to proceed with the horizontal boundary condition (figure 1.17). To assign vertical fixity ($u_y = 0$), **FE Model/boundary conditions/Solid Boundary condition/Create/Nodes** are selected and the bottom nodes are clicked on to proceed with the boundary condition (figure 1.18). In addition, the top nodes are selected to assign the defined displacement function (figure 1.19). Finally, the boundary condition should be similar to that shown in figure 1.20.

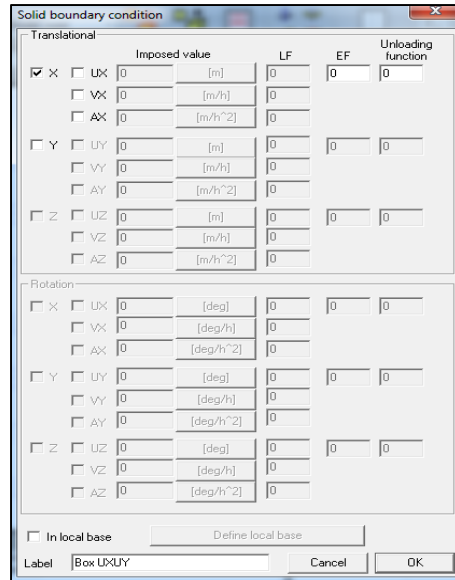


Figure 1.17 Solid boundary condition window, horizontal fixities for left side

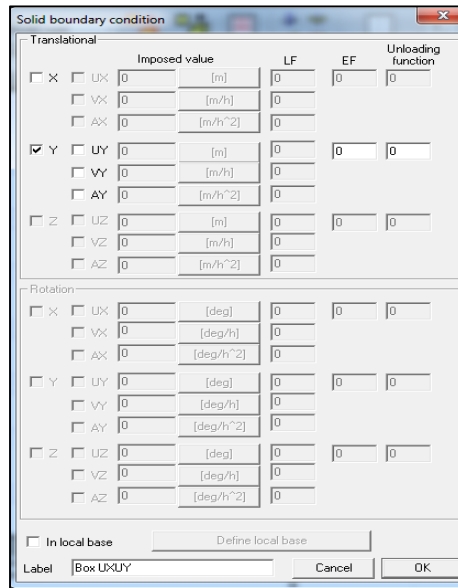


Figure 1.18 Solid boundary condition window, vertical fixities for bottom side

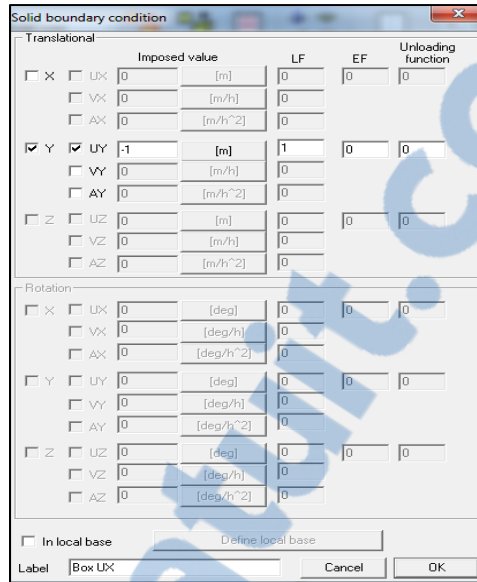


Figure 1.19 Solid boundary condition window, vertical fixities for top boundary

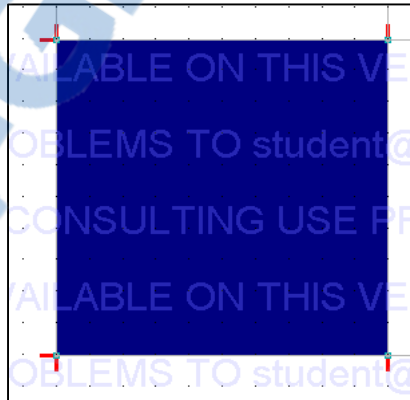


Figure 1.20 Solid boundary condition

To assign the confining pressure, **FE model/initial condition/ initial stresses** (figure 1.21) should be chosen to assign a pressure equal to 300 kPa (figure 1.22).

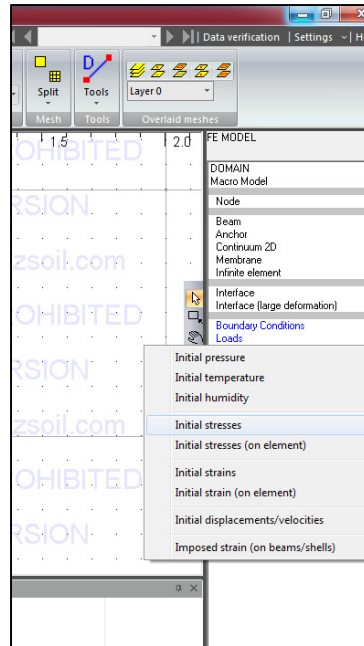


Figure 1.21 Initial Stress

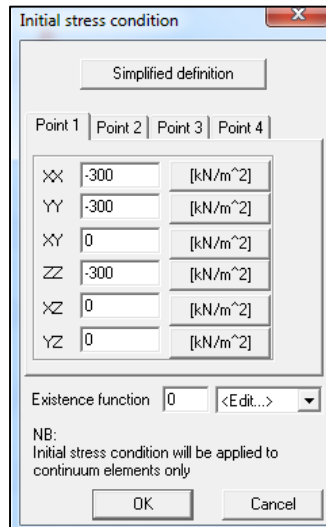


Figure 1.22 Initial stress condition

1.2.9 Loading

To assign the horizontal load, **FE Model/Loads/Surface Loads/ on edge** option is selected. A dialog box appears where the F_y and F_x values are set as 0 and -300 kN/m^2 (figure 1.23). When the model is completed, it should be saved and the preprocessor window is closed. Finally, **Analysis/Run analysis** option is selected (figure 1.25).

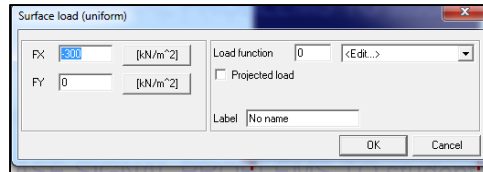


Figure 1.23 Surface load

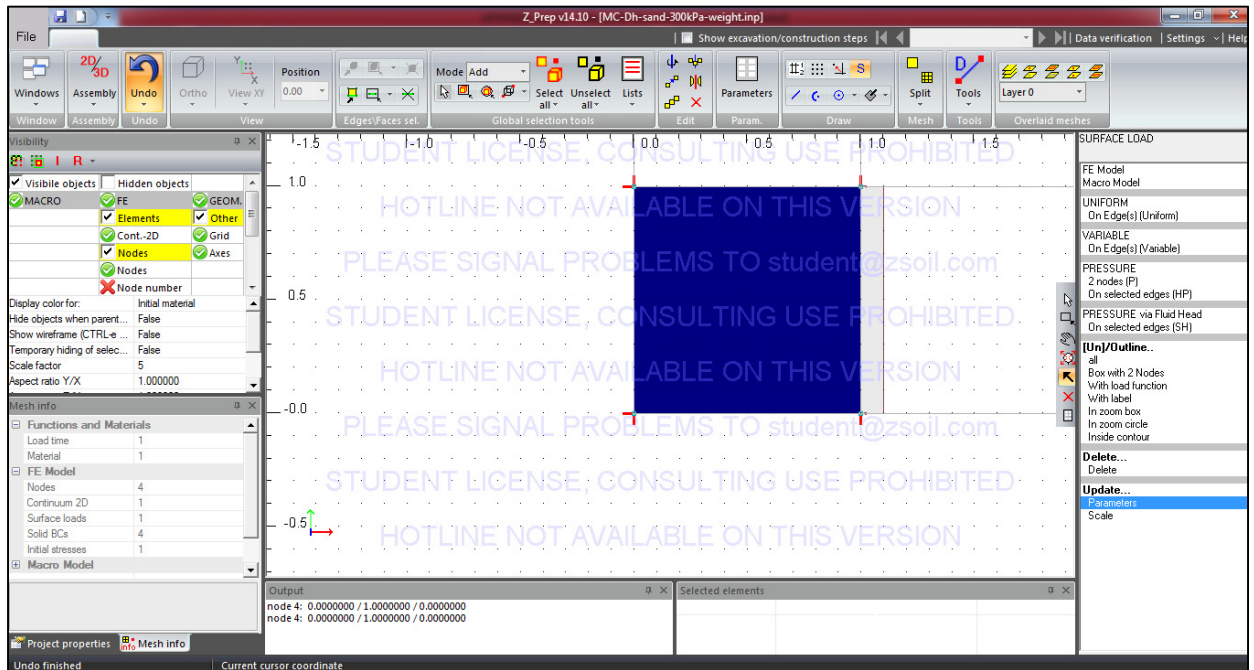


Figure 1.24 Surface load

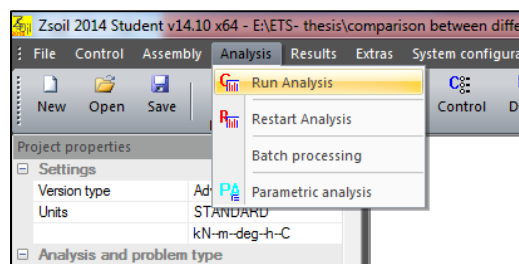


Figure 1.25 Analysis menu, Run analysis

1.2.10. Postprocessing

When the calculation is completed, the results can be seen in **Postprocessing**. In order to draw a stress vs strain curve, the **results/post processing** option is selected (figure 1.26). In the post processing window (figure 1.27), from the top main menu, **Graph options/element time history** option is selected (figure 1.27). Consequently, the **Element list** window (figure 1.28) appears, in which the elements of the project can be chosen. Consequently, **settings/graph** can be used to change the type of graph as shown in figure 1.29.

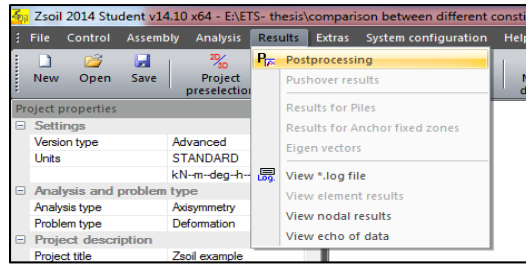


Figure 1.26 Result menu, postprocessing

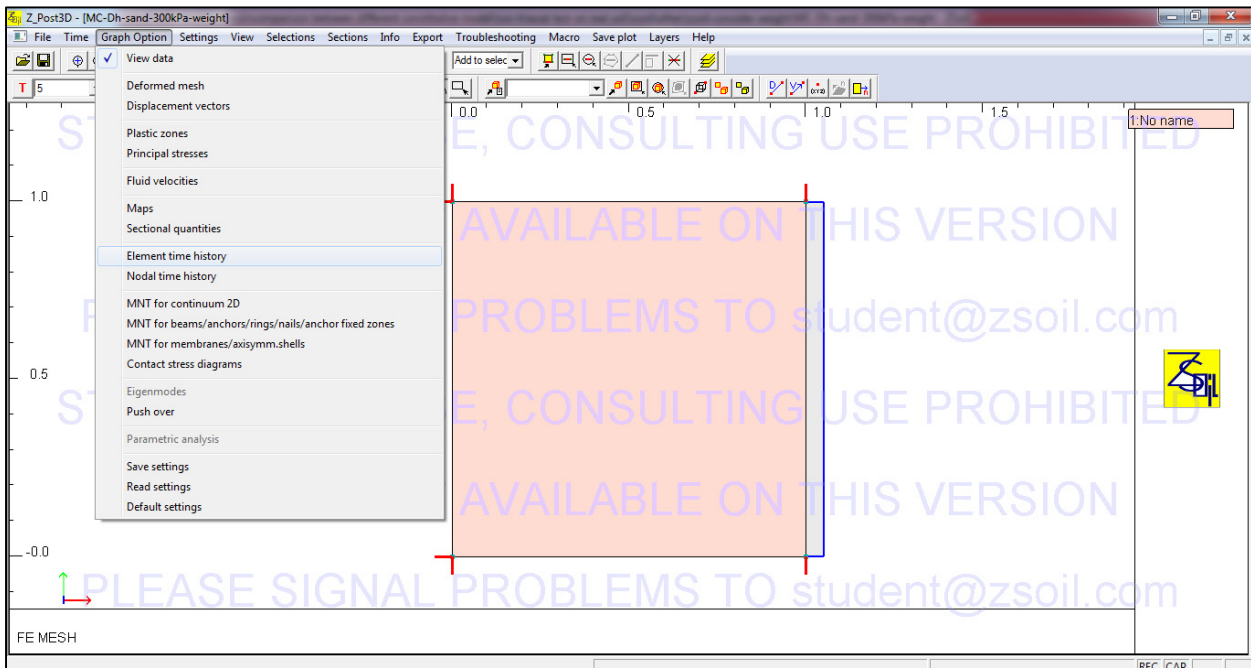


Figure 1.27 Post processing window

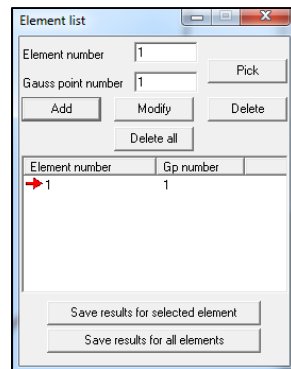


Figure 1.28 Element list

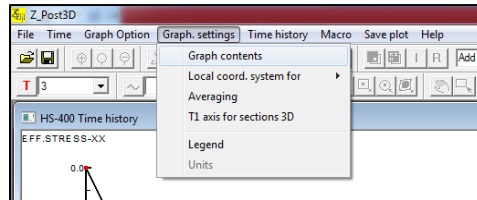


Figure 1.29 Graph contents

1.3.1 Plaxis Procedure

This appendix describes the basic input procedures that are used to simulate the triaxial test. In this appendix, the name of the software menu and the buttons used are bolted. The main menu and toolbar options can be seen in figure 1.30.

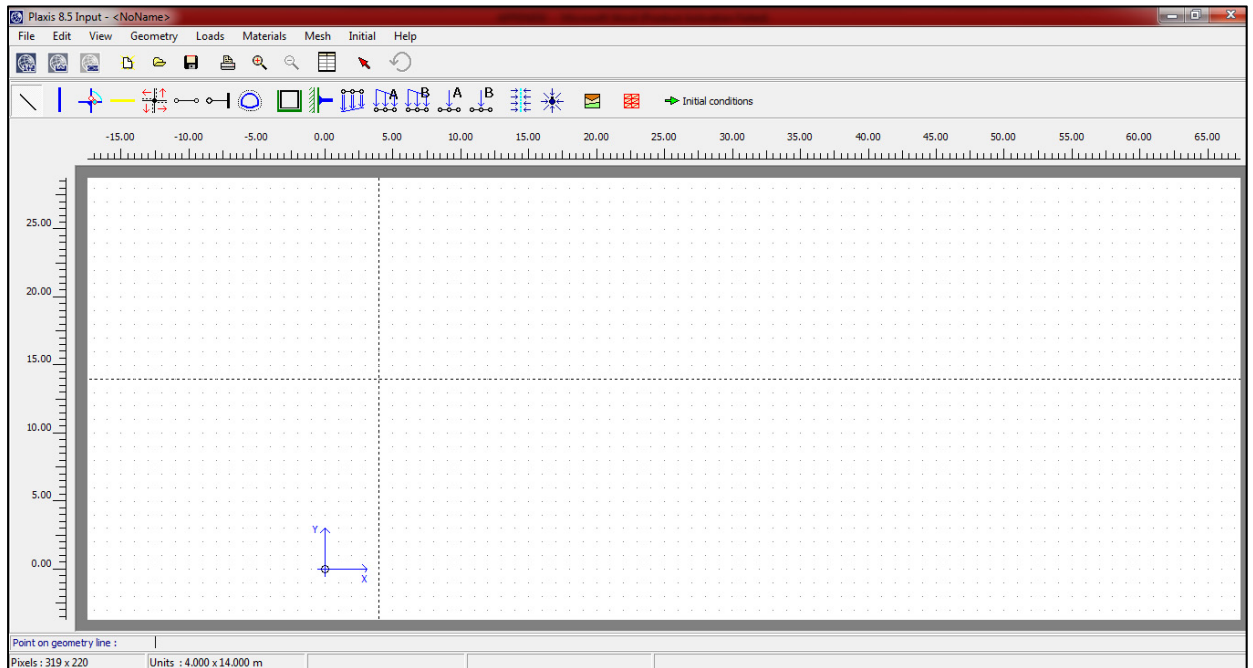


Figure 1.30 The Input program in Plaxis V8.5

1.3.1.1 General Setting

Plaxis V8.5 is used to simulate this test. It starts working by double clicking on **INPUT** program (the input program window is shown in figure 1.30). By starting the program, **create/open** project dialog box becomes accessible as shown in figure 1.31. **NEW PROJECT** is chosen to start a new project and OK is clicked (see figure 1.31). Consequently, the **GENERAL SETTING Window** will appear. It consists of two specific tabs, **Project** and **Dimension** (figure 1.32). As explained in chapter 2, the axisymmetric model and fifteen-node triangular element are used.

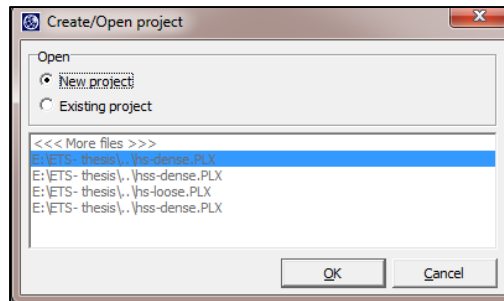


Figure 1.31 The Create/Open project dialog box

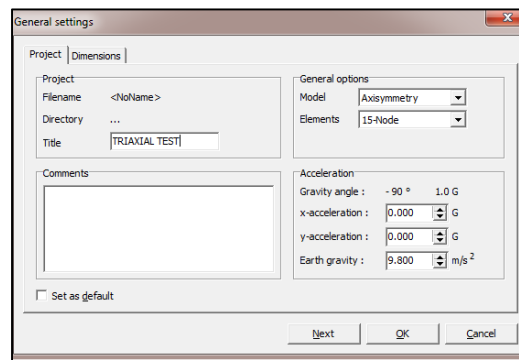


Figure 1.32 The General setting dialog box

In the **Dimension** tab sheet (figure 1.33), the units used for force, time, and length are kilonewton (kN), day, and meter (m), respectively. The required draw area is allocated at the **geometry dimension** box. Dedicated numbers are shown in figure 1.33. It should be noted that Plaxis adds a small margin; hence, the geometry would be fitted to the draw area (Brinkgreve, 2007). The grid space is the space between the dots. These dots make drawing the model geometry more convenient. The distance between grids is taken as 0.1 m (figure 1.33).

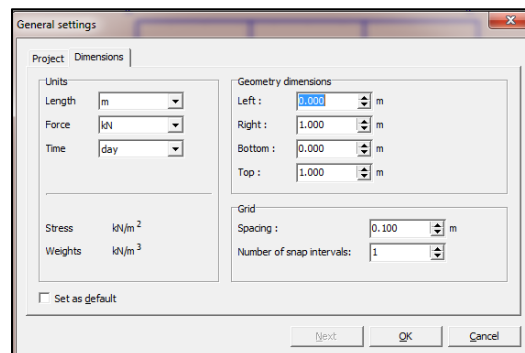


Figure 1.33 The General setting dialog box

1.3.1.1 Geometry of model

Once the general setting has been allocated, the draw area will appear and the geometry can be created. To create the object, the **geometry line** tool is used; the geometry line can be found in the software toolbar and geometry main menu (figure 1.34). Drawing the geometry will be implemented by positioning the cursor at points (0, 0) and moving to points (0, 1), (1, 1), and (1, 0). The geometry lines and points have now been created (see figure 1.35). It should be noted that Plaxis would detect a cluster (closed area by geometry lines) and present it with a light color (see figure 1.35) (Brinkgreve, 2007).

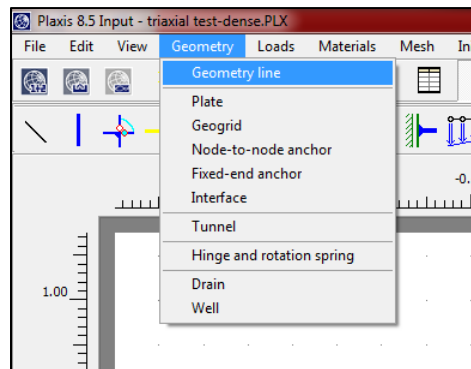


Figure 1.34 Geometry menu, selecting geometry line

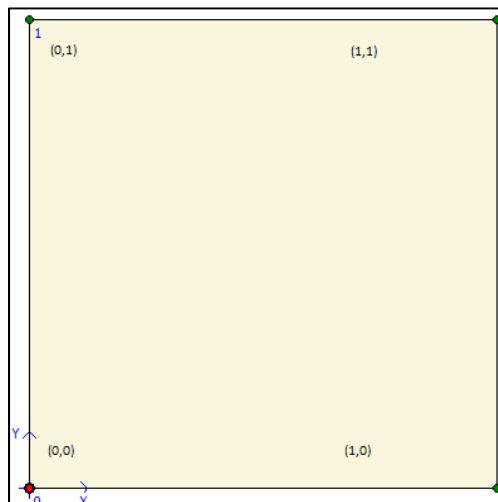


Figure 1.35 The model geometry

1.3.1.2 Boundary Conditions

Once the geometry has been created, the boundary condition can be applied. The boundary condition can be seen in the loads main menu and software toolbar tabs (figure 1.36). The left and bottom sides of the model are fixed in the horizontal and vertical directions, respectively. The rest of the boundaries are assumed free to move. The vertical fixity ($u_y = 0$, $u_x = \text{free}$) from loads toolbar button or by means of options available in loads menu is selected to assign the vertical fixed boundary (figure 1.36). It will be implemented by positioning the cursor at points (0, 0) and moving to point (1,0). To assign horizontal fixity ($u_x = 0$, $u_y = \text{free}$), the horizontal fixities from loads toolbar is selected and then moved from point (0, 0) to point (0, 1) (figure 1.36). It is shown in figure 1.37 that Plaxis has generated the horizontal and vertical fixities for the left side and base, respectively.

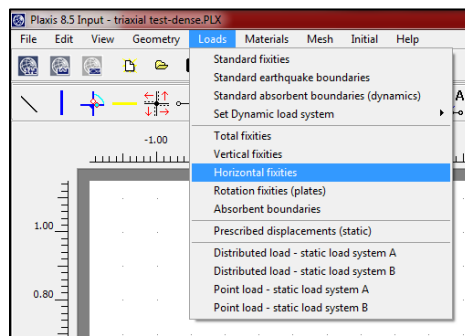


Figure 1.36 Loads menu, selecting horizontal and vertical fixities

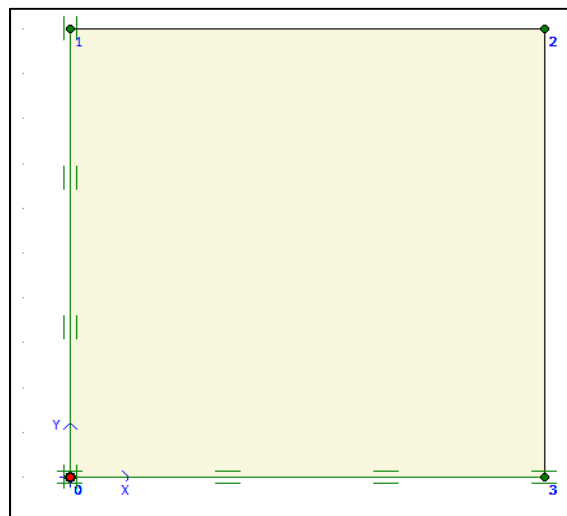


Figure 1.37 The boundary conditions

To simulate the confining pressure (σ_3) and principal load (σ_1), distributed loads (B) and (A) are used, respectively, in the input program (figure 1.39). From the available options in loads menu (**Distributed load – static load system A**) load A is chosen in order to assign the vertical load A (figure 1.38). It can be done by positioning the cursor at points (0, 1) and

moving to point (1, 1). Similarly, to assign the horizontal load B, the **Distributed load – static load system B** from **loads toolbar** button is selected and then it is moved from point (1,1) to point (1,0) (figure 1.38).

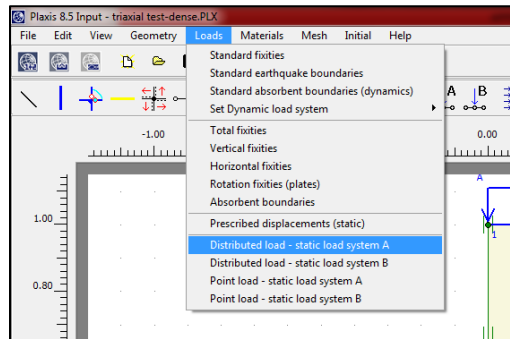


Figure 1.38 Loads menu, selecting distributed load A and B

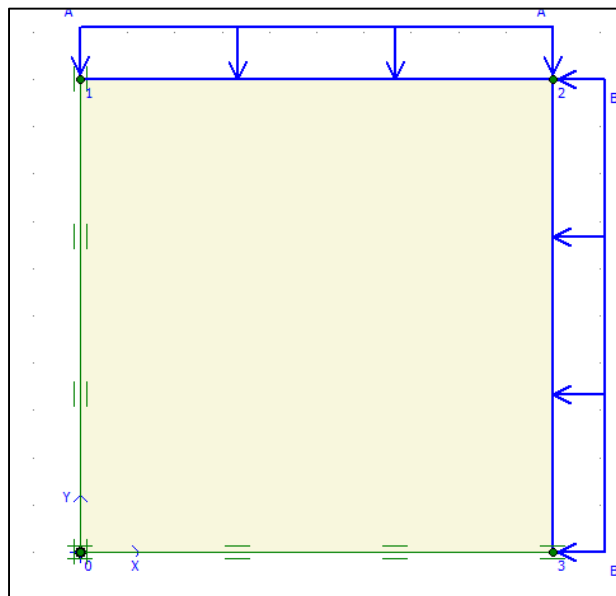


Figure 1.39 The confining pressure and principal stress applied on the model

1.3.1.3 Material data

Generally, the creation of material data is performed after generating the geometry and boundary condition. Before mesh generation, it is essential to define material sets and assign them to clusters. To simulate the soil behavior, various constitutive soil models are created. The input material data can be chosen by using **material sets** button on the toolbar or by means of materials menu (figure 1.40) (Brinkgreve, 2007). The material set button on the toolbar is selected, as shown in figure 1.40.

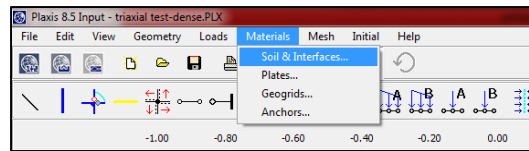


Figure 1.40 Material menu, selecting soil and interface

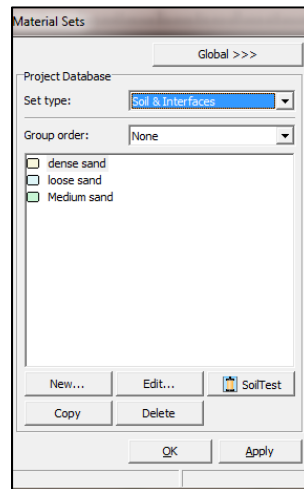


Figure 1.41 Material sets

New materials can be created by clicking on the **New** tab button (figure 1.41). To identify the soil type, it can be named as “Hostun sand” in the **identification** box in the **material set box** of the **general** tab (figure 1.42). Various constitutive models can be defined to simulate the soil behavior. The HS model is chosen from the material combo box, and the drained behavior is selected from material type. The soil weight is not considered in this simulation; hence, the general properties are left as zero, as shown in figure 1.42. Select **parameter** tab to proceed with the material parameters. The parameters pertaining to the selected soil model can be seen in the parameter tab sheet (figure 1.43).

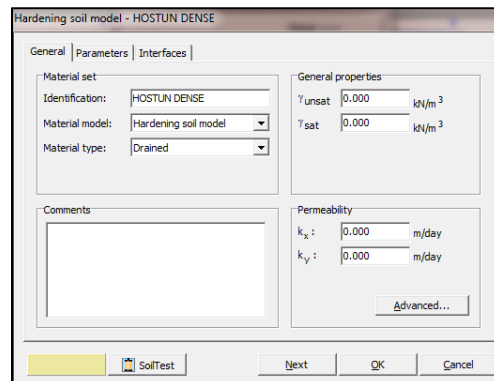


Figure 1.42 General tab sheet of the soil

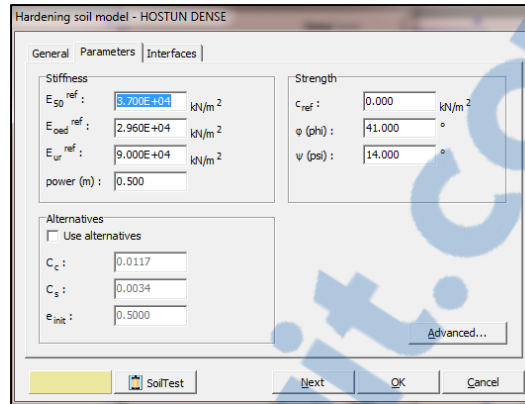


Figure 1.43 General tab sheet of the soil

1.3.1.4 Mesh Generation

After creating the geometry, the next step is to generate the mesh. This is done automatically by Plaxis. To create the mesh, the **Generate** option from the **mesh menu** should be selected (figure 1.44). By selecting it, a new window opens in which the mesh can be seen (figure 1.45). It is possible to go back to the previous window (the geometry input mode) by clicking the **Update** button. Once the mesh is implemented, the finite element model is completed. Generally, the initial condition should be calculated in Plaxis before starting the calculation. The initial condition consists of the groundwater condition and the initial effective stress. In the current simulation, neither water condition nor soil weight is considered. Therefore, it is possible to start the calculation analysis.

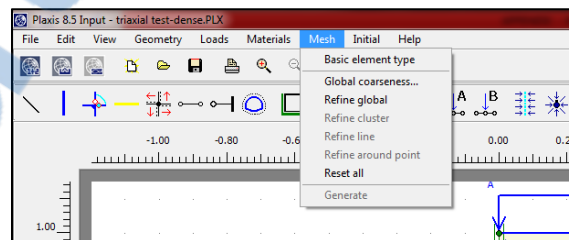


Figure 1.44 Mesh menu

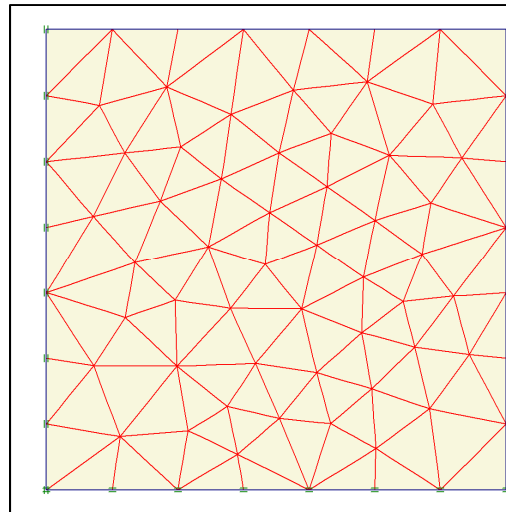


Figure 1.45 Plot of mesh

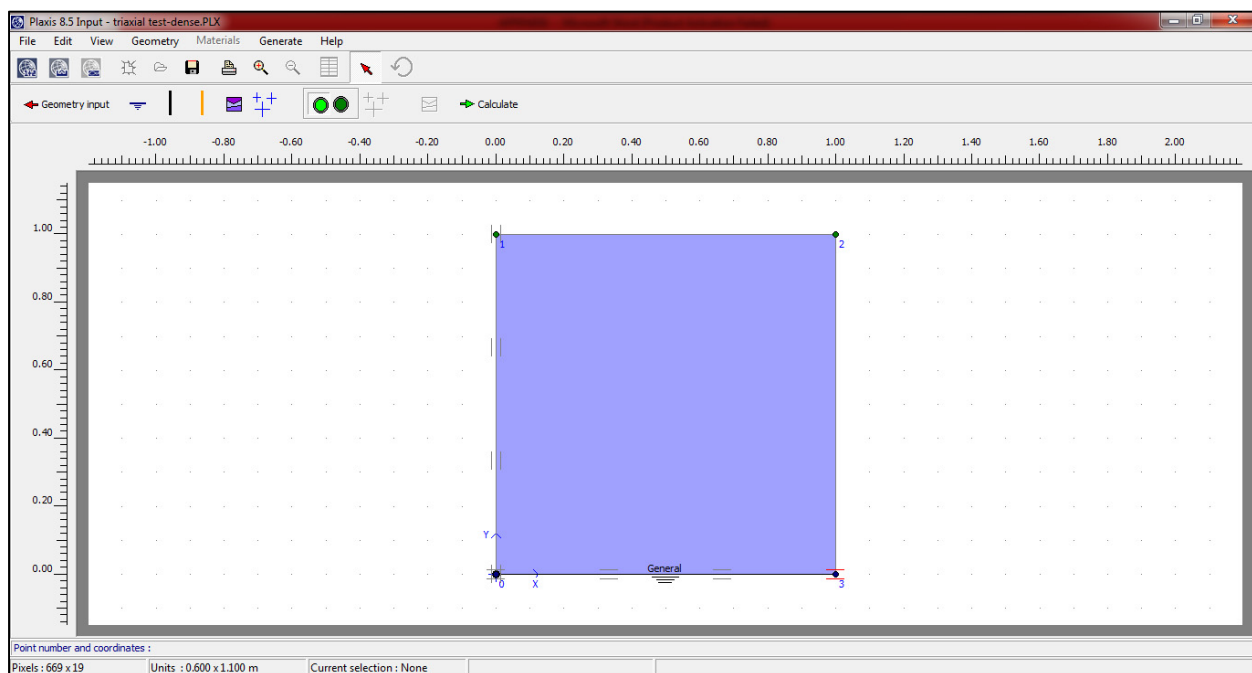


Figure 1.46 The initial condition window

1.3.1.5 Performing the calculation

After clicking on the **calculate** button (figure 1.46), the input program closes and the calculation starts (figure 1.47). When the program starts, an initial calculation phase is considered automatically. Various types of analysis (i.e., plastic analysis, consolidation analysis, phi-c reduction analysis, and dynamic analysis) can be used to simulate the soil behavior during the test. Plastic analysis is selected from the **calculation type** combo box (see figure 1.47). By clicking on the **parameter** tab (figure 1.47) and **define** button (figure 1.48), the **staged construction window** appears. By choosing the distributed loads, we can

assign the confining pressure (-300 kPa) for both loads A and B (figure 1.49). Another phase should be defined by clicking on the next button (see figure 1.47) in which the values of loads A and B should be -1400 kPa and -300 kPa, respectively. Finally, by clicking on **calculate** button (figure 1.47), the calculation is carried out.

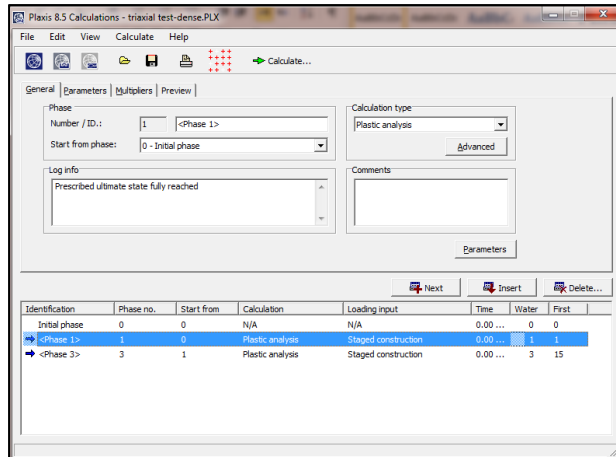


Figure 1.47 Calculation window-General tab

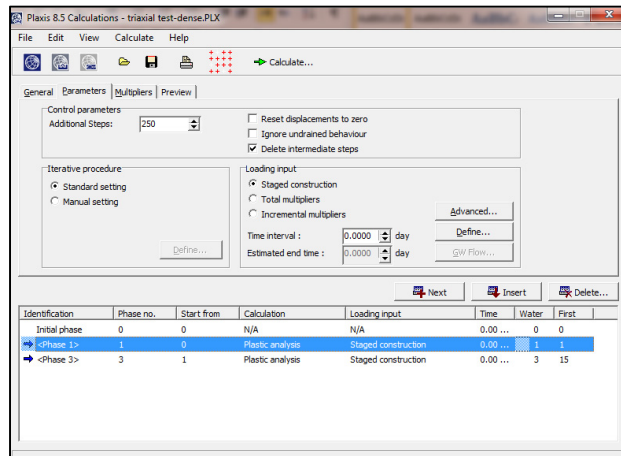


Figure 1.48 Calculation window-parameter tab

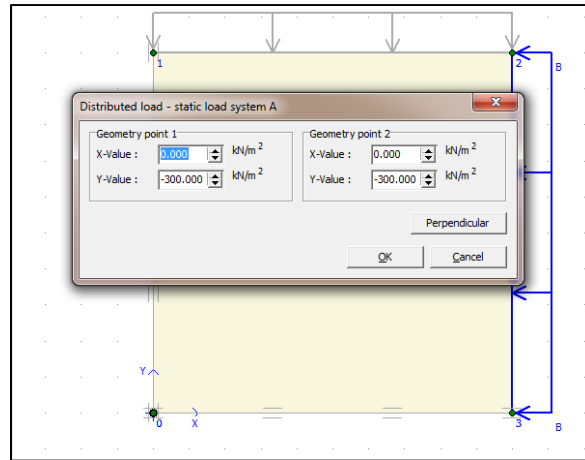


Figure 1.49 Assigning the load through the stage construction window

1.3.1.6 Curves and output results

When the calculation is completed, the results can be seen in the **output program** or **curve program**. In order to draw a stress vs strain curve, the following steps should be carried out. First, the **curve program** button is selected (it is shown in figure 1.47 at the upper left side). Once the program starts, the **create/open project** dialog box can be seen (figure 1.50). After selecting **New chart**, a curve generation window appears (figure 1.51). This window comprises two columns (x-axis and y-axis). For the x and y axes, strain and stress are selected respectively to draw a graph as shown in figure 1.52.

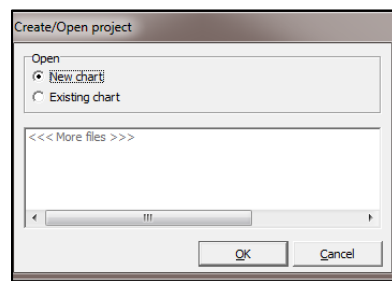


Figure 1.50 The Create/Open project dialog box

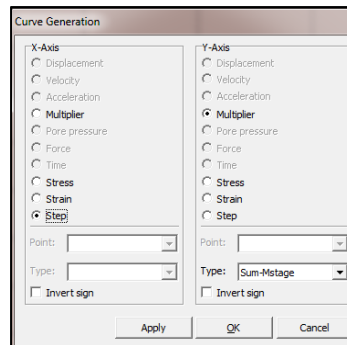


Figure 1.51 The curve generation window

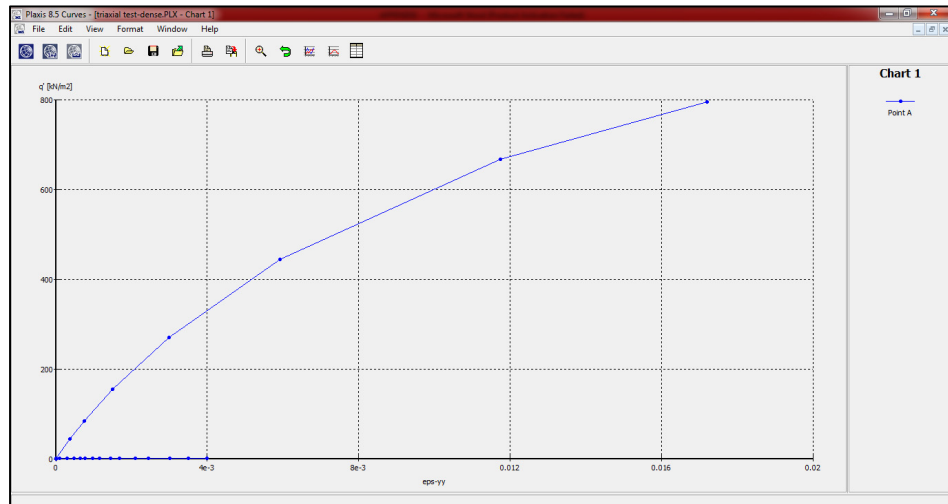


Figure 1.52 The curve window

APPENDIX II

Oedometer Test

2.1 Introduction

This appendix describes the basic input procedures that are used to simulate the oedometer test in Zsoil. In this appendix the name of software menu and the used buttons are **bolded**. The main menu and toolbar options are shown in figure 2.1. The Zsoil PC 2014 3D student version is used to simulate this test.

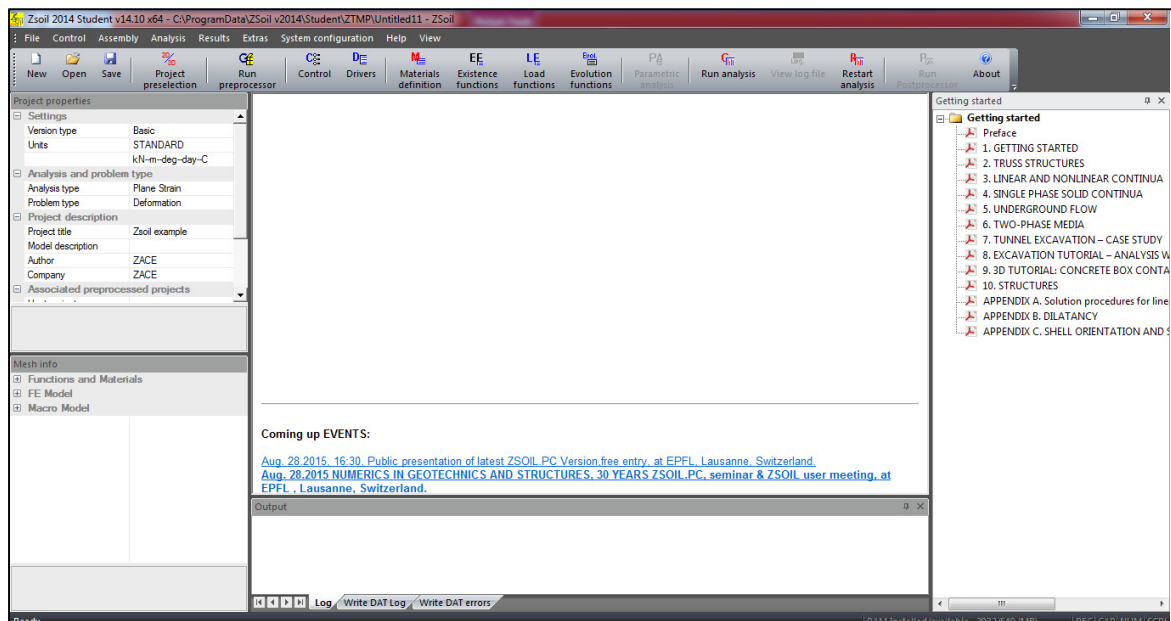


Figure 2.1 The main window in Zsoil

2.2 Project Preselection

Once the Zsoil is opened, the **start window** appears in which under the **new project** tab, **axisymmetric model** is chosen (figure 2.2). Consequently, the **preselection** window appears in which the details of the project are filled in as shown in figure 2.3. In the project preselection menu, the problem type is set to deformation, and the SI system of units is selected. The name of the project is written in the Project title tab (figure 2.3).

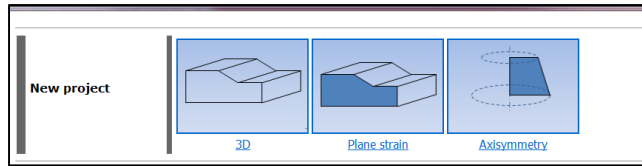


Figure 2.2 Start window

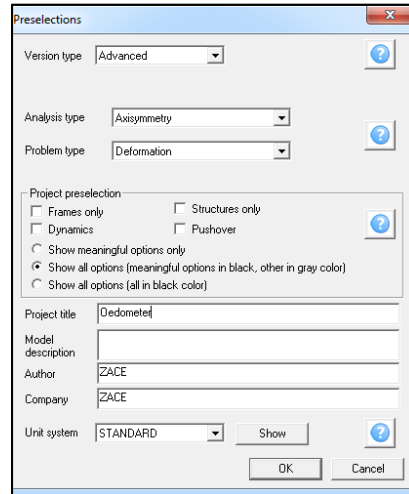


Figure 2.3 Preselection window

2.3 Material

The properties of the material are defined in **Assembly/materials** (figure 2.4). By choosing this option, a new dialog box appears (figure 2.5). In the dialog box, **add** button is selected to define a new material; consequently, another dialog box appears and **Add/Update material** is selected to choose the material type (figure 2.6). A new material is added to the material list with parameters that can be modified according to the analysis requirement (figure 2.6). To identify the soil type, it can be named as “Hostun sand” in the **Name** box in the **Add/Update material** window (figure 2.6). Various constitutive models can be defined to simulate the soil behavior. The HSS stiffness soil model is chosen from the **material formulation** combo box. The soil weight is not considered in this simulation; hence, the general properties are left as zero, as shown in **unit weight window** in figure 2.7. Select **Non-linear** tab to proceed with the material parameters. The parameters pertaining to the selected soil model can be seen in the parameter tab sheet (figure 2.8).

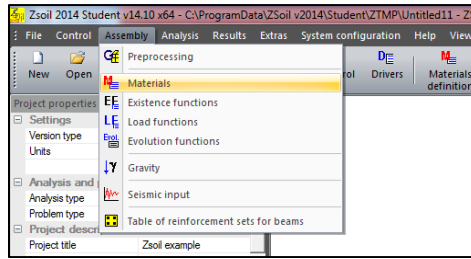


Figure 2.4 Assembly menu, choosing material

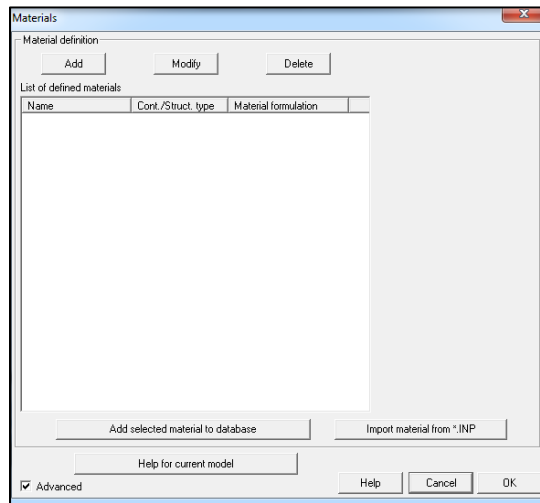


Figure 2.5 Materials window

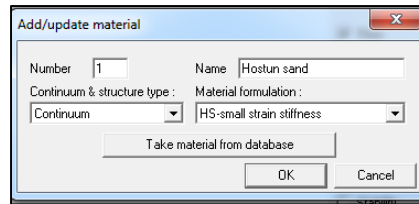


Figure 2.6 Add/update window

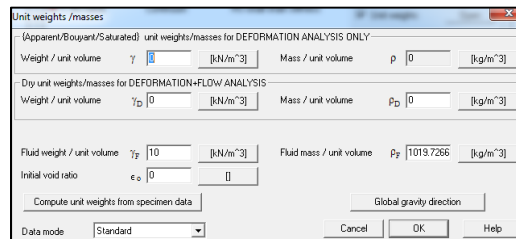


Figure 2.7 Weight window

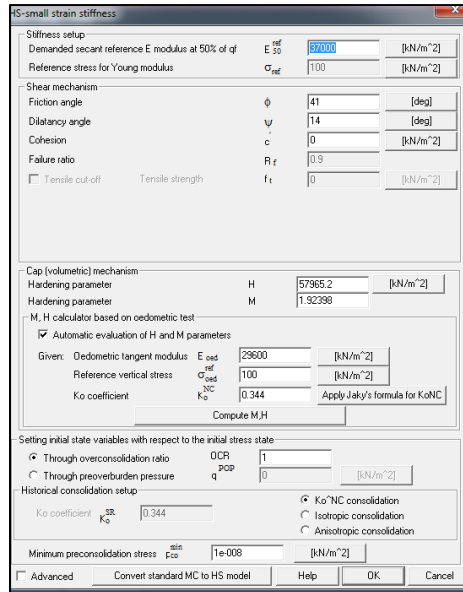


Figure 2.8-a Nonlinear properties

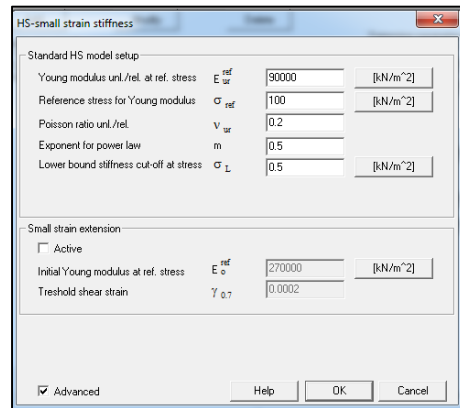


Figure 2.8-b Elastic properties

2.4 Load Function

By selecting the **Assembly/load function** menu, a new window appears in which a function of time can be defined (figure 2.9). The model is loaded at 50 kPa, 100 kPa, 200 kPa, and 400 kPa, consecutively. After each loading, the model is unloaded (figure 2.10).

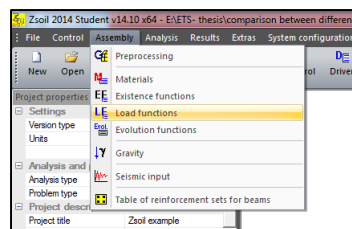


Figure 2.9 Assembly menu, choosing load function

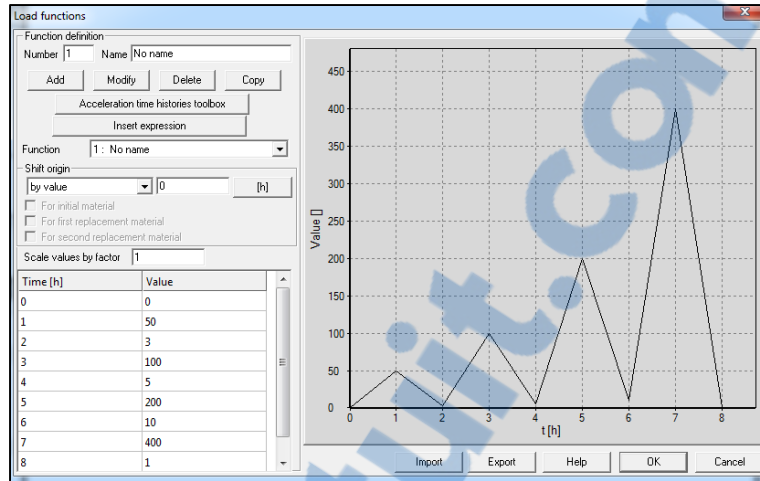


Figure 2.10 Load functions

2.5 Control/Drivers

Control/drivers is selected from the main menu (figure 2.11). This window contains computational steps that will be carried out during the analysis. Various types of analysis (i.e., stability, time dependent, pushover, and dynamic analyses) can be used to simulate the soil behavior during the test. **Time dependent** analysis is selected from the **Driver** combo box (see figure 2.12). The time is defined in the range of 0 to 8; the maximum time step is defined in the previous stage. A suitable time step of 0.1 is chosen.

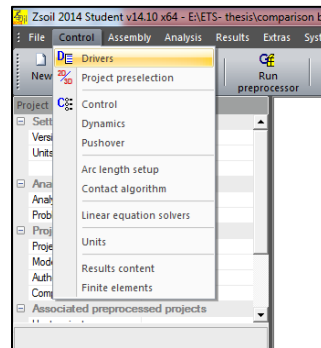


Figure 2.11 Control menu, choosing driver

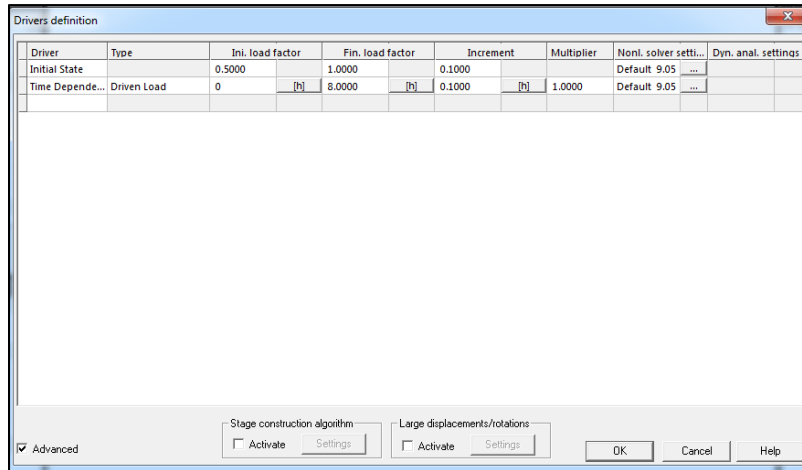


Figure 2.12 Driver definition

2.6 Preprocessing

Assembly/preprocessing is selected in the main menu as shown in figure 2.13. A new window opens, where the model can be made (figure 2.14). In this step, the geometry of the model, mesh, boundary condition, and loading are created.

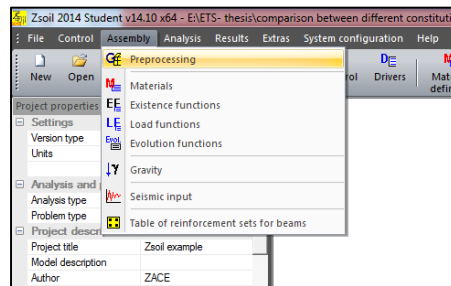


Figure 2.13 Assembly menu, preprocessing

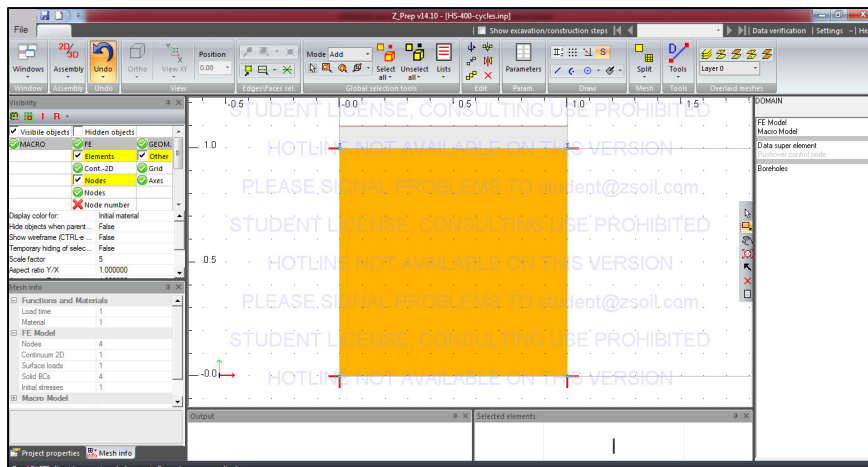


Figure 2.14 Preprocessing window

2.7 Geometry

To create the object, the **geometry line** tool is used; the geometry line can be found in the software toolbar. A square of size $1\text{ m} \times 1\text{ m}$ is created by using the draw line tool. Drawing the geometry will be implemented by positioning the cursor at points (0, 0) and moving to points (0, 1), (1, 1), and (1, 0). The geometry lines and points have now been created (see figure 2.15). In the toolbar on the right side, the **MacroModel/subdomain/2D continuum inside contour** is selected, and the cursor is clicked inside the box to create a 2D domain inside the contour (figure 2.15).

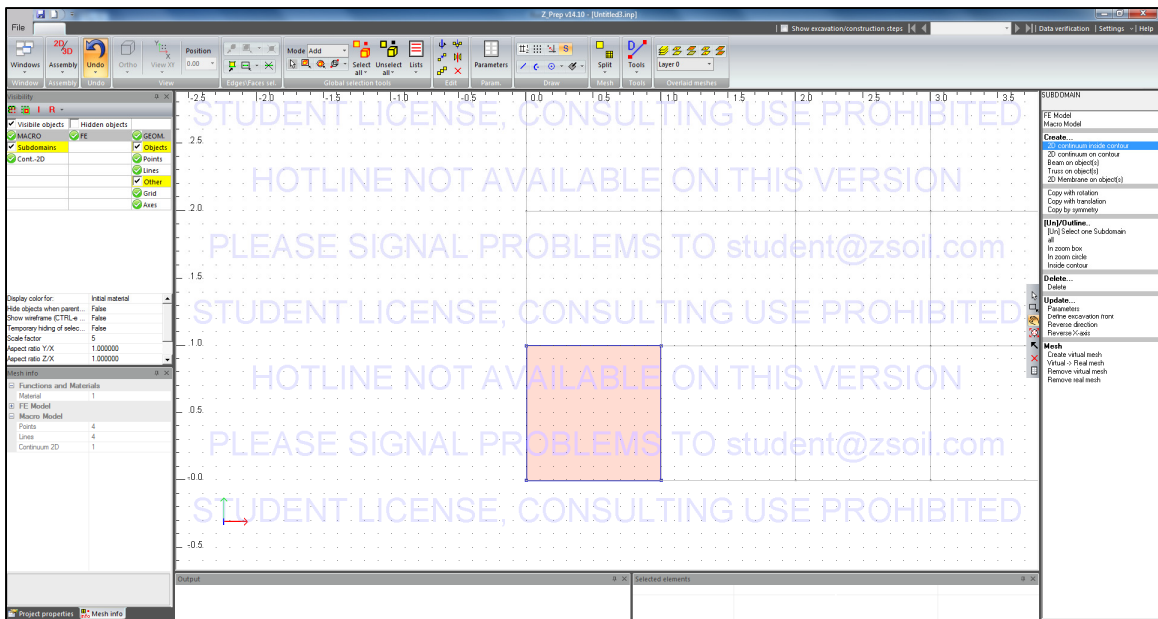


Figure 2.15 Geometry of model

2.8 Meshing

The next step is to create the mesh in the subdomain for which **MacroModel/subdomain/create virtual mesh** is selected and clicked inside the box. The meshing parameters dialog box appears as shown in figure 2.16. A quadrilateral type of mesh is selected. The number of times an edge is to be split can be defined in the menu for two adjacent edges.



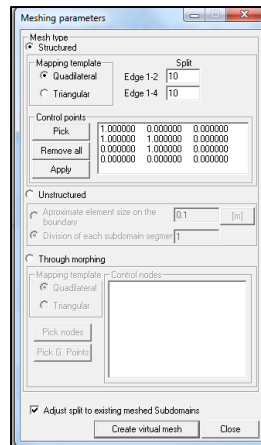


Figure 2.16 Meshing parameters

The virtual mesh is now ready to be changed to a real mesh. Ctrl+A is pressed to select the whole subdomain. **MacroModel/subdomain/virtual/real mesh** is selected to change the virtual mesh to real mesh.

2.9 Boundary Conditions

Once the geometry has been created, the boundary condition can be applied. The left, right, and bottom sides of the model are fixed in the horizontal and vertical directions. The top boundary is assumed free to move. Select **FE Model/boundary conditions/Solid Boundary condition/on box** to proceed with the boundary condition (figure 2.17).

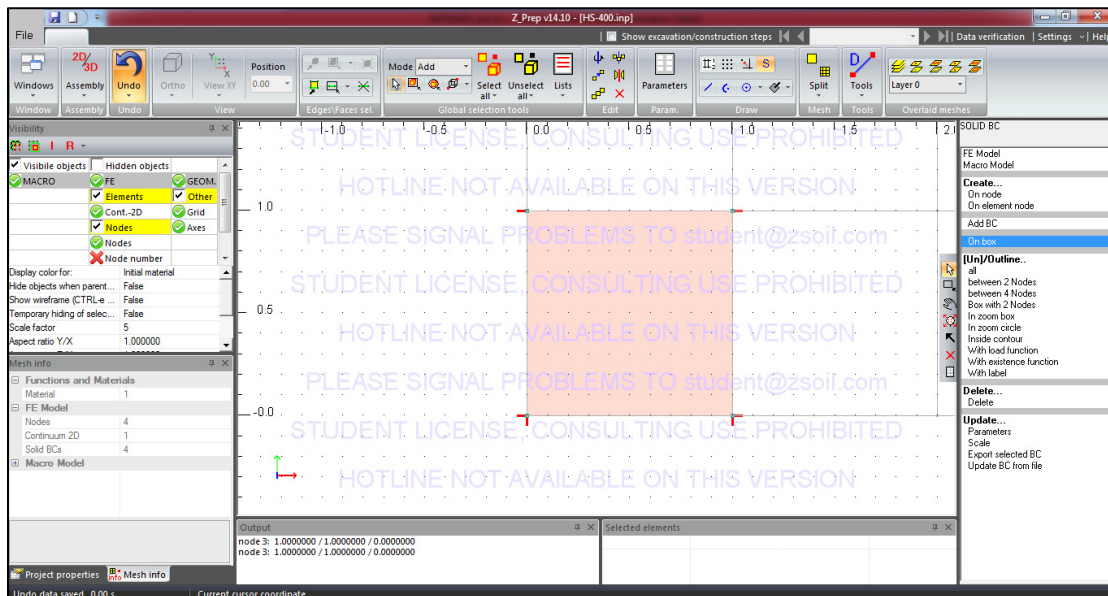


Figure 2.17 Boundary conditions

2.10 Loading

FE Model/Loads/Surface Loads option is selected to assign the vertical load (figure 2.18). A dialog box appears (figure 2.18) where F_y and F_x values are set as -1 and 0 kN/m^2 , respectively, and the load function is assigned to the function defined in section 2.4 (figure 2.18). When the model is completed, it should be saved, and the preprocessor window is closed. Finally, the **Analysis/Run analysis** option is selected (figure 2.19).

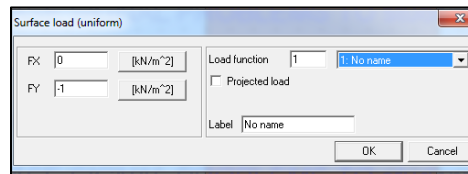


Figure 2.18 Surface load

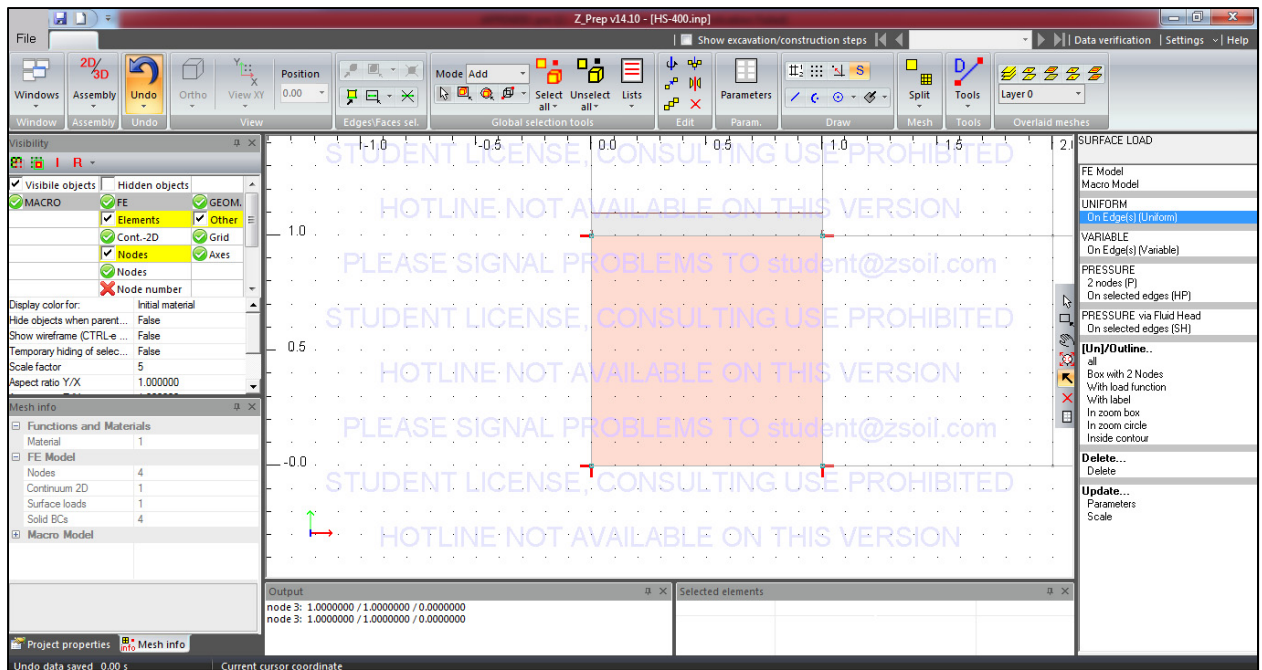


Figure 2.18 Surface load

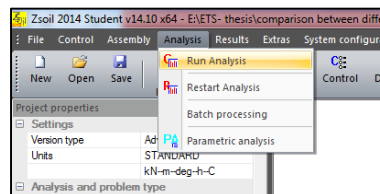


Figure 2.19 Analysis menu,
Run analysis

2.11 Postprocessing

When the calculation is completed, the results can be seen in **Post processing**. In order to draw a stress vs strain curve, the **results/post processing** option is selected (figure 2.20) in the post processing window (figure 2.21). From the top main menu, the **Graph options/element time history** option is selected (figure 2.21). Consequently, the **Element list** window (figure 2.22) appears in which the elements of the project can be chosen. Consequently, **settings/graph** can be used to change the type of graph as shown in figure 2.23.

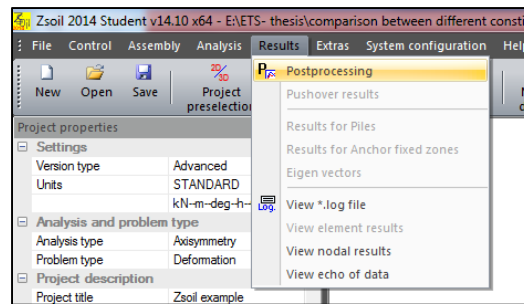


Figure 2.20 Result menu, postprocessing

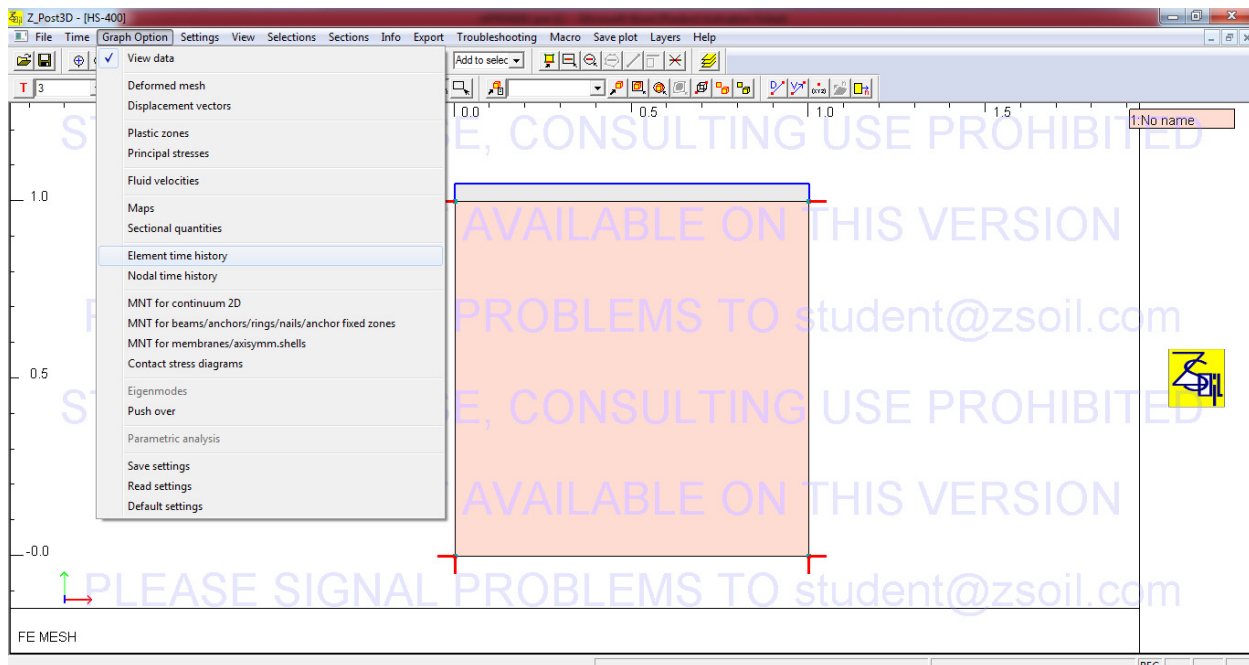


Figure 2.21 Post processing window

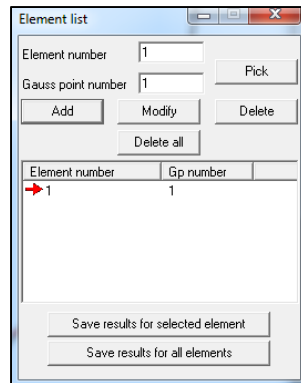


Figure 2.22 Element list

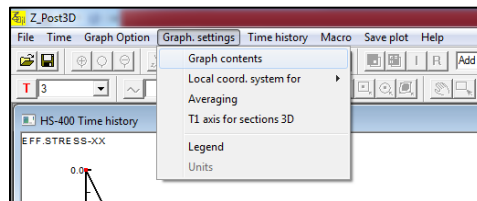


Figure 2.23 Graph contents

BIBLIOGRAPHY

- Akhtarpour, A, et A Khodaii. 2009. « Nonlinear Numerical Evaluation of Dynamic Behavior of an Asphaltic Concrete Core Rockfill Dam (A Case Study) ». *Journal of Seismology and Earthquake Engineering*, vol. 11, n° 3, p. 143.
- Al-Shayea, N, S Abduljawwad, R Bashire, H Al-Ghamedy et I Asi. 2001. « Determination of parameters for a hyperbolic model of soils from the eastern province of Saudi Arabia ». *Geotech. Eng*, vol. 149, n° 4, p. 1-14.
- Alicescu, V, JP Tournier et P Yannobel. 2008. « Design and construction of Nemiscau-1 Dam, the first asphalt core rockfill dam in North America ». In *Proc. of CDA 2008 Annual Conference, Canadian Dam Association*. p. 1-11.
- Atkinson, John. 2007. *The mechanics of soils and foundations*. CRC Press.
- Benoit Mathieu, Hugo Longtin, Simon Grenier. 2012. *Aménagement hydroélectrique de la Romaine-2, Lots R2-06-04 et R2-06-05 Barrage et digues RAPPORT DE CONCEPTION*. Hydro-Quebec.
- Benz, Thomas. 2007. *Small-strain stiffness of soils and its numerical consequences*. Univ. Stuttgart, Inst. f. Geotechnik.
- Brinkgreve, R. 2007. « PLAXIS 2D. Version 8.5 finite-element code for soil and rock analyses ». *Complete set of manuals*.
- Brinkgreve, RBJ, et W Broere. 2006. « Plaxis material models manual ». *Delft:[sn]*.
- Costa, LM, et EE Alonso. 2009. « Predicting the behavior of an earth and rockfill dam under construction ». *Journal of geotechnical and geoenvironmental engineering*, vol. 135, n° 7, p. 851-862.
- Craig, Robert F. 2004. *Craig's soil mechanics*. CRC Press.
- Creegan, Patrick J, et Carl L Monismith. 1996. « Asphalt-concrete water barriers for embankment dams ». In. ASCE.
- Daniel Verret, Simon Grenier, Hugo Longtin, Redha Kara. 2013. « Romaine 2 Hydro electric Project: Large scale test fills for ACRD dam and dikes design ». In *CANADIAN DAM ASSOCIATION*. (Montréal, Québec).
- Das, Braja M, et Khaled Sobhan. 2013. *Principles of geotechnical engineering*. Cengage Learning.

- Duncan, James M, et Chin-Yung Chang. 1970. « Nonlinear analysis of stress and strain in soils ». *Journal of Soil Mechanics & Foundations Div.*
- Duncan, James Michael, Kai S Wong et Yoshio Ozawa. 1980. *FEADAM: a computer program for finite element analysis of dams*. University of California, Department of Civil Engineering.
- Duncan, JM, Kai S Wong et Phillip Mabry. 1980. « Strength, stress-strain and bulk modulus parameters for finite element analyses of stresses and movements in soil masses ». In *Geotechnical engineering*. University of California.
- Feizi-Khankandi, Siamak, Abbas Ghalandarzadeh, Ali Asghar Mirghasemi et Kaare Hoeg. 2009. « Seismic analysis of the Garmrood embankment dam with asphaltic concrete core ». *Soils and Foundations*, vol. 49, n° 2, p. 153-166.
- Gopi, Satheesh. 2010. *Basic civil engineering*. Pearson Education India.
- Guy Lefevre, Mourad Karry, Yannic Ethier. 2014. *Relevés MMASW au barrage Romaine-2 essais sur le chemin d' acces a la crete recharge du cote aval*. Hydro-Quebec.
- Höeg, K, T Valstad, B Kjaernsli et AM Ruud. 2007. « Asphalt core embankment dams: recent case studies and research ». *International Journal on Hydropower and Dams*, vol. 13, n° 5, p. 112-119.
- Hoeg, Kaare. 2005. *Earthquake Resistance of Asphalt core Dams*. Norwegian Geotechnical Institute.
- Höeg, Kaare. 1993. *Asphaltic concrete cores for embankment dams*. Norwegian Geotechnical Institute.
- Hunter, Gavan, et Robin Fell. 2003a. *The deformation behaviour of embankment dams*. University of New South Wales, School of Civil and Environmental Engineering.
- Hunter, Gavan, et Robin Fell. 2003b. « Rockfill modulus and settlement of concrete face rockfill dams ». *Journal of Geotechnical and Geoenvironmental Engineering*, vol. 129, n° 10, p. 909-917.
- Hunter, JA, et HL Crow. 2012. « Shear wave velocity measurement guidelines for Canadian seismic site characterization in soil and rock ». *Geological Survey of Canada, Open File*, vol. 7078, p. 227.
- Janbu, Nilmar. 1963. « Soil compressibility as determined by oedometer and triaxial tests ». In *Proceedings of the European conference on soil mechanics and foundation engineering*. Vol. 1, p. 19-25.

- Jansen, Robert B. 2012. *Advanced dam engineering for design, construction, and rehabilitation*. Springer Science & Business Media.
- Justo, JL. 1991. « Collapse: Its importance, fundamentals and modelling ». In *Advances in Rockfill Structures*. p. 97-152. Springer.
- Karry, Mourad. 2014. *Relation entre la vitesse des ondes de cisaillement et le module initial de duncan-chang pour les enrochements de la Romaine 2*. Hydro-Quebec.
- Kim, Yong-Seong, Min-Woo Seo, Chung-Won Lee et Gi-Chun Kang. 2014. « Deformation characteristics during construction and after impoundment of the CFRD-type Daegok Dam, Korea ». *Engineering Geology*, vol. 178, p. 1-14.
- Kondner, Robert L. 1963. « Hyperbolic stress-strain response: cohesive soils ». *Journal of the soil mechanics and foundations division, ASCE*, vol. 89, n° 1, p. 115-143.
- Lambe, T William, et Robert V Whitman. 2008. *Soil mechanics SI version*. John Wiley & Sons.
- Nahabadi, Ghanooni. 2002. « Seismic analysis and design of asphaltic concrete core embankment dams ». *International Journal on Hydropower & Dams*, vol. 9, n° 6, p. 75-78.
- Naylor, DJ. 1975. *Criteria and Assumptions for Numerical Analysis of Dams: Proceedings of an International Symposium Held at Swansea, UK, 8-11 September 1975*. Department of Civil Engineering, University College, Swansea.
- Nobari, ES, et James Michael Duncan. 1972. *Effect of Reservoir Filling on Stresses and Movement in Earth and Rockfill Dams. A Report of an Investigation*. DTIC Document.
- Obrzud, R. 2010. *The Hardening Soil Model: A Practical Guidebook*. Zace Services.
- Obrzud, Rafał F, et GeoMod Consulting Eng. 2010. « On the use of the Hardening Soil Small Strain model in geotechnical practice ». *Numerics in Geotechnics and Structures*.
- Ozawa, Y, et James Moyer Duncan. 1973. *ISBILD: A computer program for analysis of static stresses and movements in embankments*. University of California.
- Plaxis. 2014. « How does the option volumetric strain work? ». < <http://kb.plaxis.com/tips-and-tricks/how-does-option-volumetric-strain-work> >.

- Pramthawee, Pornthap, Pornkasem Jongpradist et Warat Kongkitkul. 2011. « Evaluation of hardening soil model on numerical simulation of behaviors of high rockfill dams ». *Sonklanakarin Journal of Science and Technology*, vol. 33, n° 3, p. 325.
- Qoreishi, Seyed Mehdi. 2013. « Numerical Modeling of the Behavior of Rockfill Dams During Construction and Impoundment ». Université Laval.
- Roscoe, K H_, ANn Schofield et CP Wroth. 1958. « On the yielding of soils ». *Geotechnique*, vol. 8, n° 1, p. 22-53.
- Saxegaard, H. 2003. « Crack self-healing properties of asphalt concrete: laboratory simulation ». *International Journal on Hydropower & Dams*, vol. 10, n° 3, p. 106-109.
- Schanz, T, et PA Vermeer. 1996. « Angles of friction and dilatancy of sand ».
- Schanz, T, PA Vermeer et PG Bonnier. 1999. « The hardening soil model: formulation and verification ». *Beyond 2000 in computational geotechnics*, p. 281-296.
- Seed, H Bolton, JM Duncan et IM Idriss. 1975. « Criteria and methods for static and dynamic analysis of earth dams ». *Criteria and assumptions for numerical analysis of dams*, vol. 5644588.
- Simon Grenier, Pascal Garand, Hugo Longtin. 2010. *Amenagement hydroelectrique de la Romaine-2, Lot d'ingenierie R2-00-94, Etudes specialises sur le comportement des ouvrages ACRD Hydro-Quebec*.
- Soos, P von, et J Bohac. 2001. « Properties of soils and rocks and their laboratory determination ». *Geotechnical Engineering Handbook, Ernst und Sohn, Berlin*, p. 116-206.
- Stateler, Lead Author, Manoshree Sundaram 2013. *Routine Instrumented and Visual Monitoring of Dams Based on Potential Failure Modes Analysis*. United States Society on Dams.
- Surarak, Chanaton, Suched Likitlersuang, Dariusz Wanatowski, Arumugam Balasubramaniam, Erwin Oh et Hong Guan. 2012. « Stiffness and strength parameters for hardening soil model of soft and stiff Bangkok clays ». *Soils and Foundations*, vol. 52, n° 4, p. 682-697.
- Ti, Kok Sien, Bujang BK Huat, Jamaloddin Noorzaie, Mohd Saleh Jaafar et Gue See Sew. 2009. « A review of basic soil constitutive models for geotechnical application ». *Electronic Journal of Geotechnical Engineering*, vol. 14, p. 1-18.

- Towhata, Ikuo. 2008. *Geotechnical earthquake engineering*. Springer Science & Business Media.
- Vannobel, Marc Smith, Guy Lefebvre, Mourad Karray, Yannic Ethier. 2013. « Control of rockfill placement for the Romaine-2 Asphaltic core dam in Northern Quebec ». In *Canadian dam association* (Montreal, Quebec).
- Varadarajan, A, KG Sharma, K Venkatachalam et AK Gupta. 2003. « Testing and modeling two rockfill materials ». *Journal of Geotechnical and Geoenvironmental Engineering*, vol. 129, n° 3, p. 206-218.
- Wong, Kai Sin, et James Michael Duncan. 1974. *Hyperbolic stress-strain parameters for nonlinear finite element analyses of stresses and movements in soil masses*. College of Engineering, Office of Research Services, University of California.
- Xing, Hao-Feng, Xiao-Nan Gong, Xiao-Guang Zhou et Hai-Feng Fu. 2006. « Construction of concrete-faced rockfill dams with weak rocks ». *Journal of geotechnical and geoenvironmental engineering*, vol. 132, n° 6, p. 778-785.